Photoelectron Spectroscopic Analysis of Solution-Processed Nickel Oxide: Surface Modification and Interfaces in Organic Solar Cells

Zur Erlangung des akademischen Grades Doktor-Ingenieur (Dr.-Ing.)
genehmigte Dissertation von M.Sc. Florian Ullrich aus Bad Soden am Taunus
Februar 2020 – Darmstadt – D17

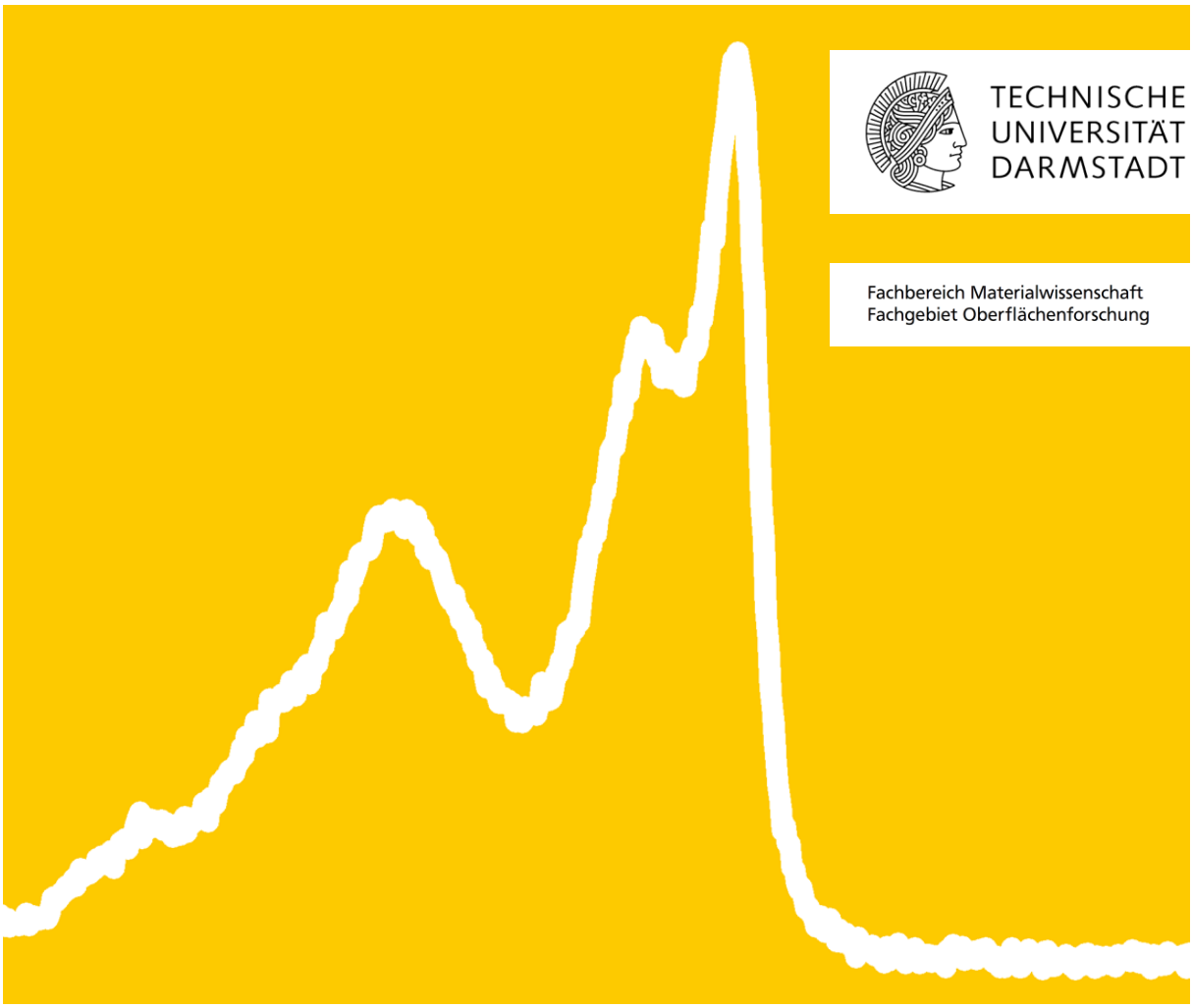

TECHNISCHE UNIVERSITÄT DARMSTADT

Fachbereich Materialwissenschaft
Fachgebiet Oberflächenforschung

Photoelectron Spectroscopic Analysis of Solution-Processed Nickel Oxide:
Surface Modification and Interfaces in Organic Solar Cells

Genehmigte Dissertation von M.Sc. Florian Ullrich aus Bad Soden am Taunus

1. Gutachten: Prof. Dr. Wolfram Jaegermann
2. Gutachten: Prof. Dr. Robert Stark

Tag der Einreichung: 17.10.2019
Tag der Prüfung: 30.01.2020

Darmstadt — D 17

Erklärung zur Dissertation

Hiermit versichere ich, die vorliegende Dissertation ohne Hilfe Dritter nur mit den angegebenen Quellen und Hilfsmitteln angefertigt zu haben. Alle Stellen, die aus Quellen entnommen wurden, sind als solche kenntlich gemacht. Diese Arbeit hat in gleicher oder ähnlicher Form noch keiner Prüfungsbehörde vorgelegen.

Darmstadt, den 15.02.2020

_____

(Florian Ullrich)

Table of Contents

1. Introduction

Electronic devices such as computers, mobile phones, tablets or televisions have become an indispensable part of modern life. Similar to solar cells, which make a decisive contribution to energy generation in many places, most electronic components are currently exclusively based on inorganic material combinations such as silicon or gallium nitride. In the 1970s, Alan J. Heeger, Alan G. MacDiarmid and Hideki Shirakawa took a decisive step towards the usability of organic materials by discovering and developing electrically conductive polymers. For their work they were awarded the Nobel Prize in 2000 [1]. This brought a number of potential advantages of organic electronics, also referred to as plastic electronics, within tangible reach: the specific manipulability of chemical and physical properties of molecules and substances, the usability of a multitude of different, even flexible substrates, and the processability from solution and thus potentially cost-effective production by printing processes. Even fabrication of semitransparent solar cell modules is possible and the installation at skyscraper facades is about to be realized [2,3].

In the years following the discovery of conductive polymers, enormous efforts were made to better understand the basic properties of organic materials like charge carrier transport mechanisms in order to better exploit the advantages of organic electronics [4–6]. In spite of the resulting gain in comprehensive understanding, many chemical and physical processes, especially at component-internal interfaces, are not yet fully understood or controllable. As organic devices like organic light-emitting diodes (OLEDs) or organic photovoltaic cells (OPVs) are usually composed of a stack of different functional layers, in each device several different interfaces exist. These interfaces are crucial to charge injection, extraction, separation and recombination and can lead to efficiency losses, if not properly designed [5]. Therefore, understanding and controlling interface properties are decisive for the functionality of organic devices, or to quote the Nobel Prize winner Herbert Kroemer: "Often, it may be said that the interface is the device."

In particular interesting in a time of constantly growing energy demand and the slowly, however, constantly rising awareness for the destructive, even fatal, impact of fossil fuel-based energy conversion on the climate and the environment is the possibility to convert solar light into electricity. Even though OPVs cannot keep up with currently established technologies like silicon-based solar cells in terms of power conversion efficiency [7], above-mentioned features of organic electronics, in general, also apply to OPVs and provide convincing advantages. Early versions of OPVs date back to the 1970s and 1980s and had a single-layer architecture, in which a single light-absorbing (photoactive) organic material was processed between two different metal electrodes [8]. In such devices, charge carrier separation depended on the electric field induced by the difference in work function between the electrodes. A major break-through was achieved by C. W. Tang in 1986 [9], who used a double-layer of photoactive materials instead, called donor and acceptor, respectively. Thereby, charge carrier separation was shifted to and determined by the internal interface of the double-layer and was thus substantially enhanced. Additionally, the new architecture enabled individual tuning of both layers. Further improvement was achieved by interface engineering at the electrodes to reduce efficiency losses due to energetic misalignment, recombination sites and missing charge carrier selectivity.

In general, there are two major strategies to adjust the properties of electrodes. One is the functionalization with self-assembled monolayers (SAMs), which consist of molecules being chemisorbed onto the surface. For these highly ordered layers, the inherent dipole moments of the molecules induce an electric field similar to a plate capacitor, which leads to a lowering or an increase of the work function, respectively. Thus, energetic offsets between the electrodes and adjacent organic layers can be adjusted. In addition, the functional head group determines the surface energy, an important parameter for subsequently solution-processed adlayers.

A second strategy is the implementation of thin functional layers, so-called hole (or electron, respectively) transport layers (HTLs or ETL, respectively). At the anode side, which will be in the

focus of the present work, popular materials are molybdenum oxide (MoO_3) and nickel oxide (NiO). While MoO_3 exhibits very high work functions [10,11], being beneficial for energy level alignment with deep lying hole transport levels of typical donor materials, the work function of NiO is - depending on the specific fabrication method - not high enough [11]. However, it can be raised by oxygen plasma (OP) treatment [12]. A crucial advantage of NiO in comparison to MoO_3 is the small electron affinity (EA) [13], which is responsible for superior electron blocking abilities. Moreover, NiO can be solution-processed (sNiO), which is a strong plus regarding low-cost, large-area manufacturing. When solution-processed, the precursor material is deposited from solution on a substrate and subsequently converted into nickel oxide by thermal annealing. Compared to the standard solution-processed HTL PEDOT:PSS, it does not suffer from acidity or hygroscopicity, which is beneficial for operational stability [11,14–16]. For these reasons, sNiO is a highly attractive alternative for the usage as HTL and has already been successfully implemented in OLEDs [17,18], OPVs [13,16,19–25] and more recently also in perovskite solar cells (PVSCs) with photon conversion efficiencies in the order of 20 % [26–34]. Still, many properties of solution-processed NiO are poorly understood and especially the adjustment of sNiO surface properties to different donor materials is not possible yet, although desirable to optimally exploit the benefits of sNiO HTLs.

In this work, the chemical composition and electronic properties of this practically relevant metal oxide are analyzed in dependency on processing parameters, and the impact of surface modifications in form of oxygen plasma treatment and SAM functionalization is studied in detail. The obtained data is correlated to characteristics of organic solar cells, and conclusions on interface engineering are deduced. Thus, this work contributes to the understanding and controlling of surface properties of solution-processed nickel oxide, which is crucial for optimal application of sNiO films in electronic devices.

The next chapter gives a more detailed insight into the existing literature and develops the scientific issues addressed in this work.

2. The Scientific Question and How to Address It

As mentioned above, one way to improve the performance of NiO-based solar cells is to use OP treatment, as shown by Berry et al. in 2010 for OPVs [12]. In the aftermath, the beneficial effect of this oxidizing treatment was proven multiple times [13,21], for example by Ratcliff et al. who demonstrated an increase of the photon conversion efficiency by almost 40 % [13]. The authors attributed this enhancement mainly to an increased hole-selectivity caused by a decreased electron affinity. As origin of this decrease the formation of nickel oxyhydroxide (NiOOH) was proposed. According to their interpretation NiOOH induces a dipole on the surface and thus increases the work function of the film. However, in a later study by Steirer et al. [35] it was observed that films annealed at different temperatures, and therefore presumably with different work functions [36], exhibit similar work functions after the OP treatment. This annealing temperature dependent increase of the work function cannot be explained by the commonly accepted model by Ratcliff et al., where OP treatment simply causes a certain additional surface dipole. This example shows that the effects of OP treatment of NiO are still not fully understood. Additionally, the peak assignments of recent photoelectron spectra often contained inconsistencies which require further careful and detailed examination.

Therefore, the first goal of this work is to clarify the chemical and electronic changes caused by the OP treatment of solution-processed NiO. For this purpose, state-of-the-art sNiO without further surface treatment is thoroughly characterized as a function of annealing temperature with several analytical methods, first and foremost photoelectron spectroscopy (PES). In a second step, the samples' properties after OP treatment are investigated. As unambiguous statements about the chemical composition of mixed, non-stoichiometric NiO samples only based on surface sensitive PE spectra prove to be very delicate, the data set is completed with bulk sensitive infra-red (IR) spectroscopy measurements. The study comprises investigations of films reannealed in different environments and comparisons to vacuum-processed samples in order to assess the quality of sNiO films and the transferability of observations. This is the topic of Chapter 5.

The second goal is to understand how solar cell performance is affected by the treatment (Chapter 6). For this purpose, the beneficial effect of OP treatment of sNiO HTLs on the performance of OPVs is confirmed by building F_4ZnPc-based solar cells via evaporation in UHV conditions. To find reasons for the improvement, interfaces of sNiO with and without OP treatment to the donor material F_4ZnPc are studied in detail with both PE and IR spectroscopy. Information thus obtained, like energy level alignment or band bending are discussed in terms of existing theories on organic-inorganic interfaces and related to respective OPV characteristics.

The third goal results from the limited possibilities to precisely adjust surface properties through OP treatment [21]. This can be circumvented by proper functionalization of surfaces with self-assembled monolayers (SAMs), which provides the possibility to vary the work function of metal or metal oxide surfaces in a wide range [37–39]. It has been demonstrated that functionalization through SAMs can alter energy level alignment and that performance of organic electroluminescent devices [40] or organic solar cells [41,42] can thus be improved. However, only few reports on the functionalization of nickel oxide [41,43–45] and even less on the impact on device performance exist [41]. For the functionalization of sNiO only one report, which does not offer insight into the binding mechanism, was found [45]. For these reasons, the third goal is to examine whether solution-processed NiO (sNiO) can be functionalized with SAMs, in particular phosphonic acids (PAs), and whether an improvement of device performance can be achieved (Chapter 7). The functionalization is systematically monitored for differently prepared sNiO substrates. The binding mechanism and charge transfer at the SAM-to-sNiO interface is evaluated and discussed. Moreover, OP treatment of the sNiO films is tested as a mean to tune SAM coverage. Here, a critical question is, how films react to the solvent in which SAMs are dissolved, which is an important issue even beyond the application of SAMs, for example when it comes to spin-coating or printing of layers on top of NiO.

Before showing and discussing the results, relevant theoretical and experimental background knowledge will be reviewed in the next two Chapters 3 and 4.

3. Theoretical Background

Nickel oxide is an inorganic semiconductor. To understand the experimental data on nickel oxide, the understanding of the properties of this crucial material class is important. Therefore, this chapter provides the most important information on semiconductor properties and related effects like band bending and photovoltage. Afterwards, different types of oxidized nickel, like single-crystalline and defective NiO, $Ni(OH)_2$ and NiOOH are introduced and discussed. Finally, also the basics of organic (carbon-based) electronic materials are provided and the principle of organic solar cells is explained.

3.1. Inorganic semiconductors

Inorganic semiconductors are all semiconducting materials which are not based on carbon, such as Si or Ge or III-V semiconductors like GaN and InP. As these materials have been under investigation for decades, their properties are very well known and understood. Here, only the most relevant properties will be revised. For more detailed information the reader is referred to standard references like "Physics of Semiconductor Devices" by S. M. Sze and Kwok K. Ng [46] or "Festkörperphysik" by Siegfried Hunklinger [47].

3.1.1. General properties and charge transport

When two atoms approach, the outer atomic orbitals overlap and interact. Thus, new hybrid orbitals are formed. The two interacting atomic orbitals split up into one bonding and one anti-bonding molecular level. The new levels can be calculated by a linear combination of the atomic orbitals (LCAO).

In a solid, the situation is similar. Here, a high number of atoms in the order of 10^{23} interact. Therefore, in a solid consisting of only of one atomic species, e.g., silicon, the former equal 10^{23} atomic orbitals split into two sets of ½ 10^{23} levels. As the energy levels in each of both sets lie very close to each other, they form quasi-continuous ensembles, so-called bands. The lower band is called valence band (VB), the upper band is called conduction band (CB). The energetic distance in-between, i.e., the distance between the lowest CB level E_{CBM} (CBM, for CB minimum) and the highest level of VB E_{VBM} (VBM, for VB maximum) is referred to as band gap E_{G}. In the case of silicon with [Ne]$3s^2 3p^2$ configuration, the 3s and the three 3p orbitals form four equal sp^3 hybrid orbitals in a solid. In a solid with N silicon atoms, the $4N$ hybrid orbitals split up into valence and conduction band with each $2N$ energy levels, i.e., $4N$ possible states for electrons. As the involved atomic orbitals contain $4N$ electrons, at a temperature $T = 0$, the valence band is fully occupied, and the conduction band is empty. The Fermi level E_{F}, which is the electrochemical potential of electrons in the material, lies in the middle of the band gap. This is the definition of a semiconductor, or – for band gaps larger than ~3 eV – an insulator. As fully occupied bands do not contribute to charge transport, semiconductors are electrical insulators at $T = 0$ K.

For finite temperatures, however, the densities n and p of negative and positive mobile charge carriers are not zero and can be calculated according to Boltzmann statistic as

$$n = N_{\mathrm{C}}\, e^{-\frac{E_{\mathrm{CBM}}-E_{\mathrm{F}}}{k_{\mathrm{B}}T}} \quad \text{and} \quad p = N_{\mathrm{V}}\, e^{\frac{E_{\mathrm{VBM}}-F_{\mathrm{F}}}{k_{\mathrm{B}}T}}, \tag{3.1}$$

where k_{B} is the Boltzmann factor and N_{C} and N_{V} are the effective densities of states of the conduction and the valence band, respectively. Note that the equations are only valid for $E_{\mathrm{CBM}} - E_{\mathrm{F}} \gg k_{\mathrm{B}}T$ and $-E_{\mathrm{VBM}} + E_{\mathrm{F}} \gg k_{\mathrm{B}}T$, respectively.

For an intrinsic semiconductor, each electron which is excited from the valence band to the conduction band leaves a hole in the valence band. Therefore, $n = p$ applies. With this condition it follows for the position of the Fermi level in intrinsic semiconductors:

$$E_F = \frac{E_{\mathrm{CBM}} + E_{\mathrm{VBM}}}{2} + \frac{k_{\mathrm{B}}T}{2} \ln \frac{N_{\mathrm{V}}}{N_{\mathrm{C}}} \tag{3.2}$$

Often, semiconductors are not perfectly clean, but contain intended or unintended impurities and lattice defects, which lead to additional states in the band gap. These defect states sensitively influence the position of the Fermi level and can lead to Fermi level pinning if the density of states is high enough. The act of installing impurities on purpose is called doping. Thus, the Fermi level can be shifted towards to valence band (p-doping) or towards the conduction band (n-doping). This is accomplished by replacing atoms with elements possessing one valence electron more or less, to induce n- and p-type doping, respectively.

3.1.2. Band bending and photovoltage

If defect states are located at the semiconductors' surface, which is, e.g., the case for an in vacuo cleaved single crystal due to the breaking of bonds, a band bending can occur. The origin is a filling (or emptying) of the surface states until thermodynamic equilibrium is reached (Figure 3.1(a)). The induced spatial separation of charges leads to a space charge region near the surface and thus a band bending (Figure 3.1(b)).

In this case, illumination can lead to a surface photovoltage (SPV), whose characteristic properties will be explained exemplary for an n-type semiconductor. For a p-type semiconductor the situation is equivalent but inverted. If such a sample is illuminated with light having a photon energy similar to or larger than the band gap ("super-bandgap SPV"), electrons are excited from the valence band into the conduction band (Figure 3.1(c)). Due to the electric field within the space charge region, excitons created there will be dissociated: electrons are pushed toward the bulk and holes are moved to the surface (Figure 3.1(d)) where they recombine with electrons in the surface states. Thus, a counter field is established and therefore the original band bending is reduced by screening (indicated in grey). This light-induced change of surface band bending is defined as SPV. It should be emphasized that SPV does not consider possible changes of a surface dipole. Thus, only when the surface dipole is unaffected, the SPV is directly reflected in the change of the work function. As excitons will not be separated anymore when the bands are totally flattened, which is the case when the magnitude of the SPV E_{SPV} is equal to the initial BB E_{BB}, the following condition is fulfilled:

$$|E_{SPV}| \leq |E_{\mathrm{BB}}| \tag{3.3}$$

If one measures a light-induced core level shift exceeding the magnitude of the initial band bending, this would be a clear evidence against an SPV or for the presence of an additional effect.
The magnitude of the SPV depends on the intensity of the irradiation [48]: without illumination it is obviously zero and in general approaches a saturation value the stronger the intensity becomes.
As the SPV is an electronic process, it occurs at timescales below 1 µs and thus can be seen as instantaneous, e.g. in PES experiments. Additionally, it is reversible: after switching off the light source, the band bending relaxes back into the initial state.
Finally, it should be mentioned that SPV refers to a surface related phenomenon while a photovoltage, in general, can also occur at buried interfaces [48]. This is, e.g., the case in solar cells. The mechanism is the same in both cases.

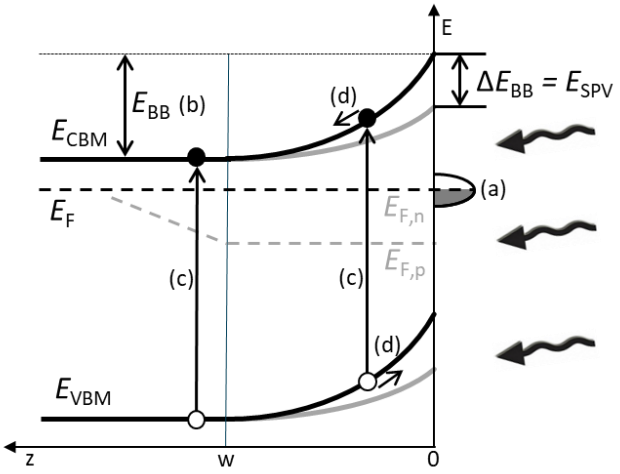

Figure 3.1: Schematic band diagram explaining the processes involved in a surface photovoltage. E_F is the Fermi level in thermodynamic equilibrium, which separates into the quasi Fermi levels $E_{F,n}$ and $E_{F,p}$ under illumination. The latter are depicted schematically in the flat quasi-Fermi levels approximation. E_{VBM} and E_{CBM} are the valence band maximum and the conduction band minimum, E_{BB} is the band bending without illumination and E_{SPV} the light-induced change of E_{BB}. See text for further explanations and Kronik et al. [48] for additional details.

3.2. Nickel oxide

This chapter provides background information on the material which is in the focus of the work, the transition-metal oxide (TCO) nickel oxide (NiO). Besides the information on NiO, also information on higher oxides of nickel will be important to identify the components of the samples.

3.2.1. Single crystalline NiO: bulk and surface properties

NiO single crystals consist of equal amounts of Ni^{2+} and O^{2-} ions. The ions are arranged in a rock salt structure, which has a face-centered cubic unit cell with a diatomic basis. Thus, each ion is octahedrally coordinated to six ions from the opposite type. The lattice constant, i.e., the distance between two neighboring nickel ions, amounts to 4.18 Å [49], which results in a density of 6.67 g/cm³ [50]. While NiO in a stoichiometric form appears greenish, non-stoichiometric samples are rather black [51]. The band gap can range from 3.1 to 4.3 eV, depending on the definition [52–54]. Due to the complicated electronic structure, the determination of the band gap has been a topic of scientific discussion for many years [55–59]. The work function of NiO is generally quite large, but certainly depends on the specific surface and preparation conditions: For NiO made by oxidation of metallic Ni, e.g., the work function was measured between 5.2 and 6.7 eV. Solution-processed NiO usually exhibits smaller values [13,60].

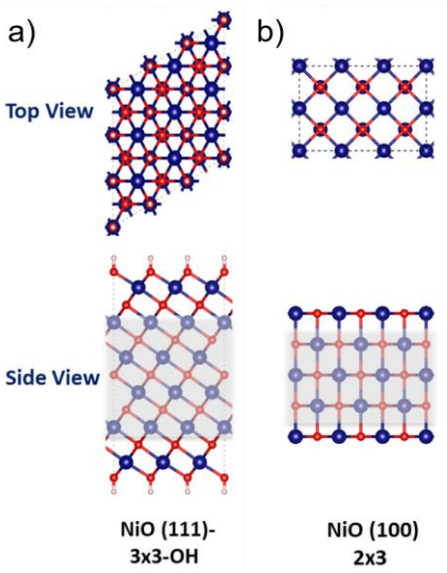

Figure 3.2: Illustration of the atomic arrangement in a NiO single crystal in two different orientations. The surface of the (111) orientation in (a) is fully hydroxylated, the surface of the (100) orientation in (b) is free of OH groups. Red: oxygen, blue: nickel, white: hydrogen. Illustration created by Dr. Shuangying Ma.

The crystallographic orientation is typically either (100) or (111) and has a crucial influence on the properties of the surface. While epitaxially grown films of both orientations are prone to hydroxylation (even in UHV, by reaction with the residual gas atmosphere), the hydroxylation of (111) surfaces was found to be significantly more pronounced than the hydroxylation of (100) surfaces [61]. This behavior was explained by the polar, and thus instable nature of a perfect (111) surface [62].

In contrast, surfaces of NiO(100) single crystals, which are stable without reconstruction [62], have been measured without any OH groups after cleavage in vacuo [63]. Still, after exposure to ambient air, even these surfaces exhibited OH groups.

Figure 3.2 shows NiO clusters in both orientations. The (111) surface in Figure 3.2a is reconstructed by full hydroxylation, which corresponds to a surface density of 13 nm^{-2}.[1] The (100) surface in Figure 3.2b is free of OH groups.

3.2.2. Defective NiO: Ni_2O_3

Often NiO tends to be non-stoichiometric, which means that the O:Ni ratio exceeds unity. If the defect density in NiO reaches a certain level, people speak of defective NiO or Ni_2O_3. Ni_2O_3 is to the present day, not very well characterized [64] and unknown as pure substance [65]. According to Greiner et al., the discussion about the existence of Ni_2O_3 goes back to the 1930's [66]. The ambiguity basically traces back to the fact that oxygen in $Ni(OH)_2$ has the same or at least very similar binding energy as in Ni_2O_3 [66,67]. Some important work worth to be mentioned in this respect was done in the 1970's. In 1972, Kim et al. [68] claimed to have produced Ni_2O_3 by oxidizing metallic nickel at low temperatures in air. While oxidation at room temperature seemed to lead to the formation of Ni_2O_3

[1] Based on a simple geometric calculation for an fcc lattice in (111) with a lattice constant of 4.18 Å.

with rather bulk character (layer thickness of at least 5 nm), the one formed at 250 °C was concentrated at the surface with a thickness below one monolayer. Two years later the same group rather relied on in-situ exposure of evaporated nickel to oxygen at low pressure in the same temperature range, to keep the water level low and exclude the formation of OH groups, with similar conclusions regarding the temperature dependency [67]. Furthermore, they found O_2^+ bombardment of metallic Ni (and also NiO) at temperatures between -80 and 200 °C to be very effective in producing Ni_2O_3, whereas the Ni_2O_3 content was largely reduced at higher temperatures. They concluded that "the stability of Ni_2O_3 decreased as the temperature increased" and that "the bulk Ni_2O_3 structure is not energetically favorable". Furthermore, they noted that the final composition is strongly dependent on the starting conditions: If nickel was already oxidized to NiO, way less Ni_2O_3 was found.
In 1977, Norton et al. [69] found that the existence of Ni_2O_3 is impossible in the presence of water, but agreed on the formation of defective oxide by heating metallic or oxidized nickel crystals in-situ with pure oxygen at low temperatures of ~200 °C. Moreover, they could prove the existence of protonated species by nuclear microanalysis when Ni or NiO films were exposed to air or moist oxygen.
In 1980, Wagner et al. [70] came to the conclusion that especially the damage in nickel crystals induced by Ar^+ sputtering leads to the formation of Ni_2O_3 when such films were treated with O^{2+}. Thirty years later, Greiner et al. [66], could not see any clear evidence in literature that Ni_2O_3 is thermodynamically stable and concluded that in case it exists or it is formed in one of the processes described, it is not in equilibrium and in particular not stable in atmosphere.
After all, there seems to be a general agreement that Ni_2O_3 can only be formed under certain conditions, which include rather low temperature, i.e. below ~250 °C, and a dry environment. It's formation by oxidation of nickel is preferred in comparison to the formation by oxidation of NiO and a very effective way for the production is the treatment of damaged Ni with O^{2+}.

3.2.3. Other oxidation states: hydroxides and oxyhydroxides

Way better characterized are the hydroxidic forms of nickel, nickel hydroxide ($Ni(OH)_2$) and nickel oxyhydroxide (NiOOH). Both types play a major role in Ni-based batteries, where they are used as cathode materials. Furthermore, hydroxidic nickel exhibits strong electrocatalytic properties and has huge potential for water splitting [71]. Therefore, it has now been subject of research for decades. Even back in 1966, when Bode et al. published a comprehensive model of the processes happening during battery charging and discharging [72], the authors talked about ongoing research for more than 50 year. They differentiated two pseudopolymorphous types of $Ni(OH)_2$, which where denoted with α and β, respectively. Similarly, β- and γ-NiOOH where identified as the main types of nickel oxyhydroxide. These different compounds and how they translate into each other where summarized into a common picture (see Figure 3.3a).
Both α- and β-$Ni(OH)_2$ consist of identical sheets of stoichiometric $Ni(OH)_2$, but differ in the interlayer-distance and the orientation of the layers with respect to each other (Figure 3.3a,b and c). The well-ordered structure with a small interlayer distance of 4.61 Å is referred to as β-$Ni(OH)_2$. It can crystallize in a brucite structure [73,74] (Figure 3.3b), but also exists with rotational or translational disordered layers, whereas the interlayer-distance stays the same. As no atoms or ions are intercalated, β-$Ni(OH)_2$ is stoichiometric in a pure appearance. α-$Ni(OH)_2$, in contrast, has water intercalated between the layers, which increases the interlayer distance to approximately 8 Å [72,75,76]. Furthermore, the chemical formula turns into α-$Ni(OH)_2 \cdot xH_2O$ with x being typically indicated from 0.4 to 0.7 [77,78]. Due to the water, the layers have almost no tendency to interact and thus are randomly oriented. Therefore, this structure is also called "turbostratic". Figure 3.3c displays this structure for x = 0.67, corresponding to 3 Ni : 2 H_2O.
Also the β phase can contain water, however only with x up to 0.4 and a weak association of the water molecules with Ni cations. Hydrogen bonds with lattice OH are not formed. Therefore, even incorporated water can be removed at quite low temperatures of ~160 °C [79–82]. Surface water

desorbs at already 80 to 90 °C. In contrast, the water incorporated in the structure of α-$Ni(OH)_2$ can only be removed at higher temperatures of 240 to 300 °C [79,80,83]. Both hydroxide types can be further reduced to NiO, whereas for α-$Ni(OH)_2$ the process is simultaneous to the removal of interlayer water [80]. For β-$Ni(OH)_2$, literature is not totally consistent, but there seems to be an agreement that most of the decomposition takes place in a temperature range from 200 to 300 °C [80,84], thus similar to the decomposition of α-$Ni(OH)_2$, however starting at lower temperatures and happening over a broader temperature range. Kober et al. even reported a saturation only at 525 °C [84].

Also a transformation into β-$Ni(OH)_2$ is possible. This process, for which not necessarily such high temperatures are needed, is also called "aging" [85,86]. Another way to form β-$Ni(OH)_2$ is the oxidation of NiO e.g. in an electrochemical cell [87,88], or simply by the presence of water on the surface [89]. From electrochemistry it is also known that β-$Ni(OH)_2$ can be further oxidized to β-NiOOH [50,90–93]. The oxidation process basically is realized by the removal of one hydrogen atom per nickel ion, which is accompanied by a transition from Ni^{2+} to Ni^{3+} [76], as illustrated in Figure 3.3d and e. For this reason, β-NiOOH also has brucite structure with only slightly altered distance parameters compared to β-$Ni(OH)_2$. The distance between two nickel atoms is reduced from 3.13 to 2.81 Å due to the reduced ionic radius and the c lattice parameter is slightly increased from 4.61 to 4.84 Å [71,75,94], accompanied by a tilting of the lattice. The exact structure, especially whether it is a mixture of Ni^{2+} and Ni^{3+} ions as suggested e.g. by Biesinger et al. [95], a mixture of Ni^{2+} and Ni^{4+} ions [96] or only consists of Ni^{3+} ions [97,98] has long been under debate. Recently, a conclusive theoretical study was published by Tkalych et al., who came to the result that the most stable structure only contains Ni^{3+} ions [71] and has the structure shown in Figure 3.3e. During the oxidation process the Ni^{2+} ions are oxidized to a final charge of +3, although in experimental reality the full Ni^{3+} oxidation is not always reached due to residual $Ni(OH)_2$ amounts [79,95,99]. Similarly to β-$Ni(OH)_2$, β-NiOOH decomposes in a temperature range between 150 and 280 °C with NiO as decomposition product [84,100].

Another type of NiOOH mentioned in literature is referred to as γ-NiOOH. γ-NiOOH can be produced by overcharging of the hydroxide cathode [72,90] and consequently has higher nickel oxidation states of up to +4 [76,101]. Similar to the difference in α- and β-$Ni(OH)_2$, γ-NiOOH consists of β-NiOOH sheets with water and/or alkali cations intercalated into the structure [102]. Interlayer distances are reported with values of about 7 Å [75,76].

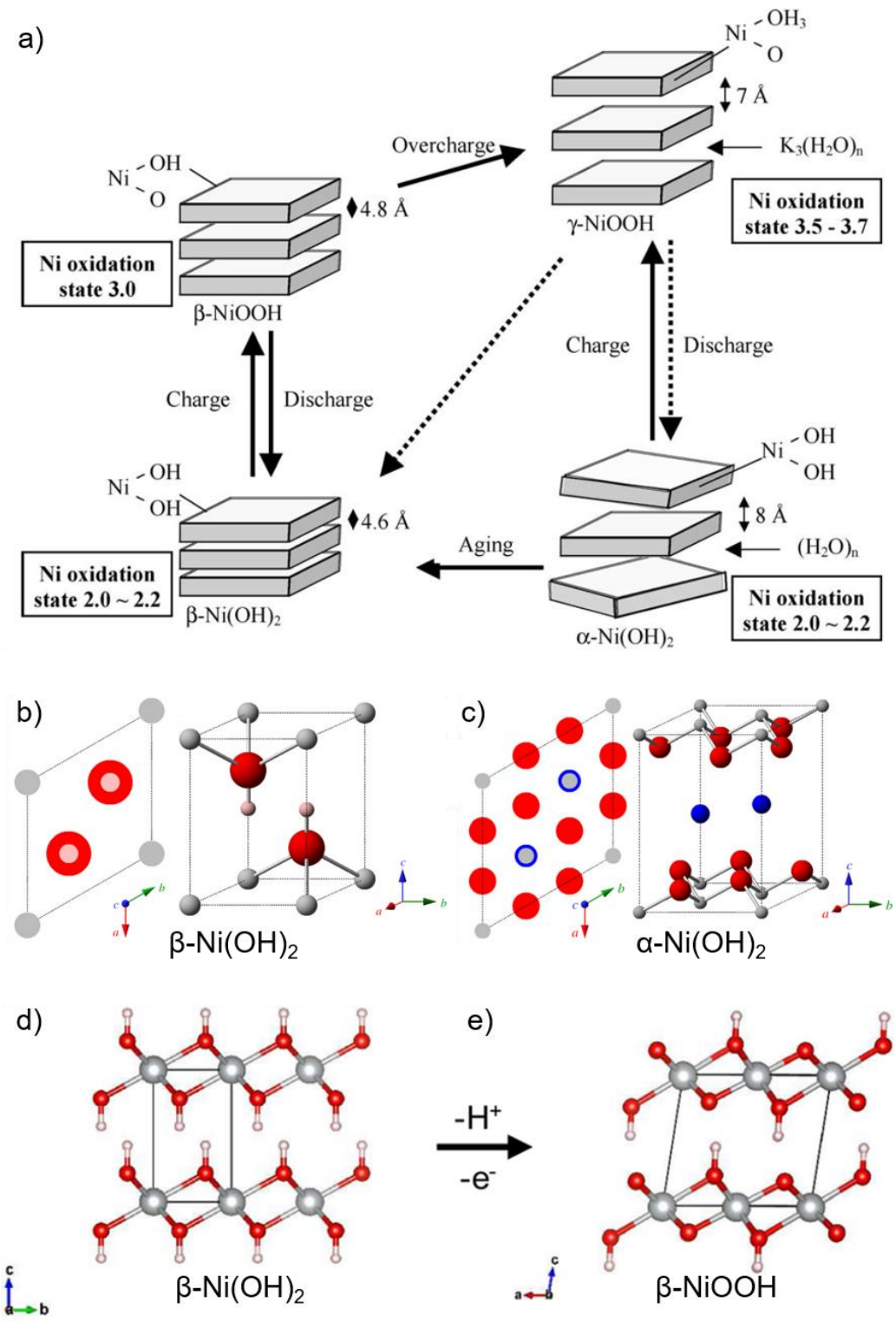

Figure 3.3: Bode diagram [72], illustrating the different types of hydroxidic nickel and their relation to each other. Reprinted from [76]. (b,c) Crystal structure of α- and β-$Ni(OH)_2$, respectively. Grey balls indicate nickel ions, red balls indicated oxygen ions, light red balls indicate hydrogen and blue balls indicate water molecules. Reprinted from [75]. (d,e) Most stable structures of β-$Ni(OH)_2$ and β-NiOOH in (001) direction according to Tkalych et al. [71]. Reprinted from [71].

3.2.4. Fabrication of NiO

Nickel oxide can be produced in several ways, for example by thermal oxidation of metallic Ni in air [50,67,68] or in oxygen atmosphere [61,103]. Besides, films can be deposited via sputtering [104–108], pulsed laser deposition [19,109] or electron-beam evaporation [110]. Single crystals are usually grown via epitaxy [49,111]. Especially for the use in solar cells solution-processed NiO is very popular. Here, solutions with NiO nanoparticles exist [31,112] or such based on a precursor, e.g. nickel acetate [23] or nickel nitrate [28].
The different fabrication methods lead to more or less stoichiometric nickel oxide, in fact in most cases stoichiometry is not provided. Such non-stoichiometric NiO will be denotes as "NiO_x" hereafter. The abbreviation "sNiO" refers to the way of fabrication, namely processed from solution. It is non-stoichiometric in general. The term "stoichiometric NiO" actually is redundant, however it will be used sometimes for clarity reasons, as "NiO" can be understood as abbreviation for (not necessarily stoichiometric) nickel oxide in general.

3.3. Organic semiconductors

An important application of NiO thin films is the usage as functional layer in organic electronic devices like OPVs. As basis for the interface experiments between NiO and the organic material F_4ZnPc and the discussion of the impact on sNiO-based OPV performance in Chapter 6, the specialties of organic semiconductors (OSCs) and the working principle of organic solar cells are discussed in the following.

3.3.1. General properties and charge transport

The fundament of organic compounds is the carbon atom. Similar to silicon, it has four valence electrons ([He]$2s^2 2p^2$), from which two are located in the 2s and two are located in the 2p orbital. When carbon atoms form chemical bonds, the outer orbitals hybridize. Three types of hybrid orbitals are possible: sp for two σ-bound binding partners, sp^2 for three σ-binding partners and sp^3 in case of four σ-binding partners. The latter is the binding type of carbon atoms in diamond.
For organic electronics the sp^2 hybridization is most important. Here, the three hybrid orbitals arrange in a plane with an angular distance of 120° in between, as illustrated in Figure 3.4a. Each sp^2 hybrid orbital contains one electron. The remaining electron is left in the p_z orbital, which is perpendicular to the plane of sp^2 hybridized orbitals. In a carbon-based molecule, two sp^2 hybrid orbitals from different atoms overlap, exchange electrons and form a strongly localized σ-bond (Figure 3.4b). Also the perpendicular oriented p_z orbitals interact and form a so-called π-bond. Thus, the typical carbon double bonds are formed. In carbon chains (like polyacetylene) or ring structures (like benzene), the double bonds and single bonds alternate. Due to the small overlap of the p_z orbitals, π-bonds are weak and rather delocalized over the whole molecules.
Similar to the inorganic case, the overlap of two atomic orbitals leads to a splitting of the resulting energy levels of the molecule. In the case of the π-bond, beside the bonding, fully occupied π-orbital also an antibonding, empty π*-orbital exists (Figure 3.4d,e). These orbitals are called highest occupied molecular orbital (HOMO) and lowest unoccupied molecular orbital (LUMO), respectively.

In a solid, the interaction between organic molecules usually has van der Waals character, which implies a weak coupling between the π-orbitals of different molecules such that charge carriers are strongly localized to the respective molecule. Thus, the intermolecular mobility is low and charge transport cannot be described in term of delocalized bands. In 1993, Bässler presented a model to describe charge transport in OCSs by hopping transport [4]. The idea is that charge carriers have a certain probability to "hop" from one molecule to the next, driven by thermal activation. The hopping probability, or the intermolecular charge transport, respectively, depends on overlap of the wavefunctions. This can lead to anisotropic mobilities. Due to the sp^2 hybridization, π-electrons are located on both sides of the molecular plane (Figure 3.4b). As illustrated in Figure 3.4c, π-electrons from different (planar) molecules in a molecular crystal can only overlap when the molecules are stacked "face-to-face". In this case, electrons can be exchanged between two molecules, whereas perpendicular to this direction, the electronic interaction and thus mobility is weak.
Due to the high degree of disorder in molecular crystals, or even absence of order in the amorphous OSCs, not all HOMOs and LUMOs of all molecules are located at exactly the same energy. The consequence is an energetic disorder of HOMO and LUMO levels, which is often approximated by a Gaussian distribution. This ensemble of molecular energy levels is usually referred to as "the HOMO" and "the LUMO" of a molecular material (Figure 3.4). This is also the terminology used in this work. The energetic distance of the HOMO to vacuum level is called ionization potential (IP) and the energetic distance of the LUMO to the vacuum level is call electron affinity (EA). As point of reference both the middle of the distribution, which is the energetic position with the highest density of states (DOS), and the onset of the DOS can be used. In the present work, IP and EA refer to the onset of the DOSs. The HOMO can be seen as the organic analog of the inorganic valence band, in the sense that both are responsible for hole conduction. The same applies to the LUMO of a material and the

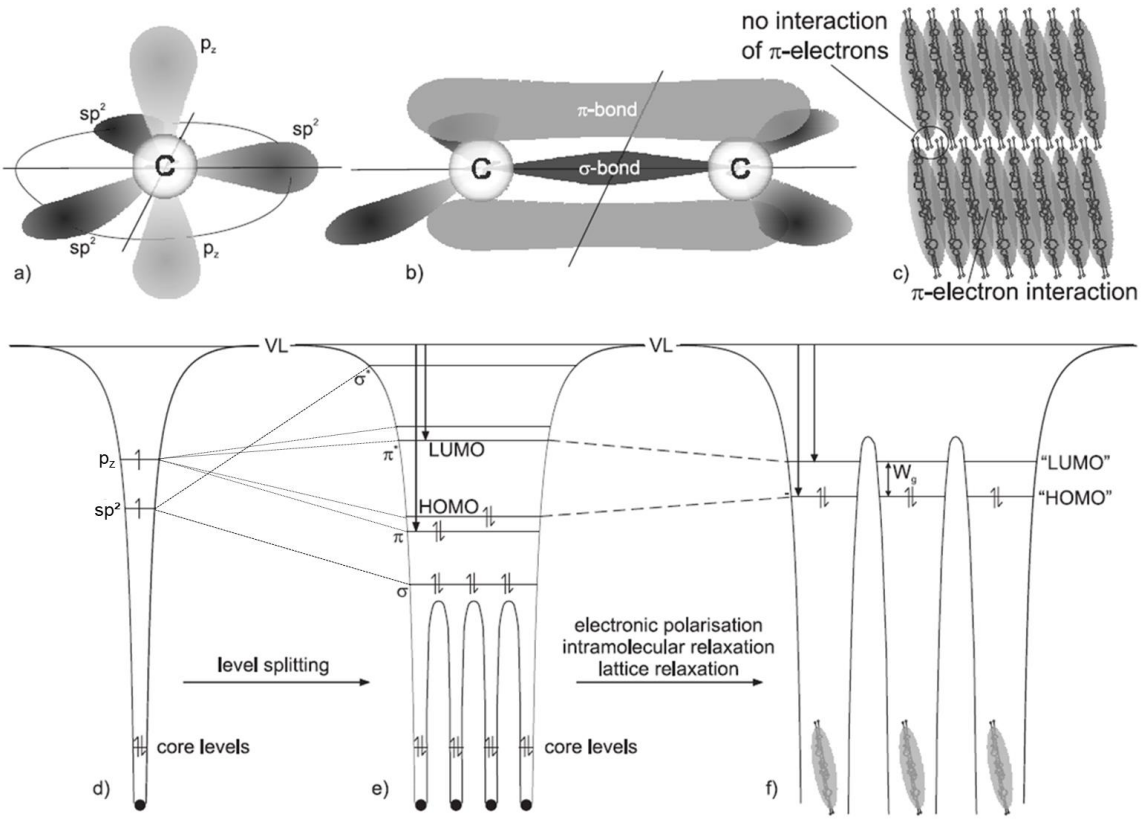

Figure 3.4: Illustration of the chemical bond between two carbon atoms and of the electronic interaction between organic molecules. (a) Carbon atom with three hybridized sp^2 orbitals in a plane and one p_z orbital perpendicular to the plane. (b) Double bond between two carbon atoms. Two sp^2 orbitals from the different atoms form a strong σ-bond, the p_z orbitals form a less localized π-bond. (c) Sketch of the electronic interaction in a molecular crystal. (d-f) Simplified energy level diagrams of an sp^2 hybridized carbon atom (d), a model organic molecule (e), and a model molecular crystal (f). Reprinted from [308].

conduction band regarding electron transport. The hopping transport in OSC implies the existence of ionized molecules. These polarons polarize the molecules in the vicinity (electronic relaxation). Additionally, the bond lengths are changed (intramolecular relaxation) as well as the molecular lattice positions (intermolecular relaxation) [113,114]. These three processes lower the energetic gap between HOMO and LUMO by 1 to 1.3 eV [115] compared to the energy gap of a single isolated molecule $E_g^{molecule}$. Hereby, electronic relaxation has by far the strongest contribution (>1 eV), intramolecular relaxation is in the order of 100 meV and intermolecular relaxation only in the range of 10 meV [113,114]. This "new" band gap due to the polaronic relaxation is called transport gap E_g^{transp}.

A similar situation is created when a molecule is ionized during photoelectron spectroscopy (see Chapter 4.1.1). However, due to a lower time constant of photoionization processes (~10^{-14} s), intermolecular relaxation with a time constant of about 10^{-12} to 10^{-13} s is not registered during the measurement, which is why the photoionization gap E_g^{photo} is larger than the transport gap. Electronic relaxation occurs on a time scale of 10^{-16} s and thus contributes to photoionization measurements, while intramolecular relaxation happens on a time scale of 10^{-14} s, which is in a similar range than photoionization processes.

The smallest band gap is usually the optical gap E_g^{opt}. This is due to the high binding energy $E_{bin}^{exciton}$ of excitons in organic semiconductors (Frenkel excitons), which is the difference between $E_g^{transport}$ and E_g^{opt} and was measured between 0.4 to 1.4 eV [114].

Thus, in general the following inequation is valid:

$$E_g^{molecule} > E_g^{photo} > E_g^{transp} > E_g^{opt}. \quad (3.4)$$

3.3.2. Organic solar cells – structure and working principle

A solar cell uses the energy of photons to generate electrical power. Its electrical behavior can be approximated by the equivalent circuit depicted in Figure 3.5a. Although this circuit is only valid in good approximation for inorganic solar cells, where the series and shunt resistance are independent of the voltage, it is helpful for the understanding and interpretation of organic J-V curves as well and is therefore presented in the following. The circuit consists of a current source (I_{ph}) accounting for the photogenerated charge carriers, a diode (I_d), a parallel resistance (also called shunt resistance R_{SH}) and a series resistance R_S. Thus, in the dark, a solar cell shows the behavior of a diode. Under illumination, the additional photocurrent I_{ph} shifts the J-V curve in negative y-direction (red line in Figure 3.5b). Important quantities of the J-V characteristics are the following: the short circuit current J_{SC} is the intersection of the curve with the y-axis and is the current generated by an illuminated cell with shorted contacts. J_{SC} is approximately proportional to the illumination intensity. The open circuit voltage V_{OC} is the intersection of the curve with the x-axis and is the maximum possible voltage, which is reached when the electrodes of the cell are not electrically connected. If a load is attached to the cell, $J(V)$ will take on values between zero and J_{SC} (V_{OC}). The product is the electrical power $P = JV$ generated by the cell. Only when operated in the fourth quadrant, the solar cell can provide electrical power, which reaches the highest value at the so-called maximum power point (MPP), P_{MPP}. The quotient of P_{MPP} and the product of J_{SC} and V_{OC} is the fill factor

$$FF = \frac{J_{MPP}\, V_{MPP}}{J_{SC}\, V_{OC}}. \tag{3.5}$$

The power conversion efficiency (PCE) of a solar cell is defined as the quotient of the power generated at the MPP and the solar power input P_{in}:

$$PCE = \frac{P_{MPP}}{P_{in}} = FF\, \frac{J_{SC}\, V_{OC}}{P_{in}}. \tag{3.6}$$

In reality, solar cells have both a series and a shunt resistance. The series resistance

$$R_S = \left[\frac{dJ}{dV}\,(V = V_{OC})\right]^{-1} \tag{3.7}$$

is defined as the inverse slope of the J-V curve at $V = V_{OC}$. To avoid losses and obtain optimized fill factors, R_S should be as small as possible. The shunt resistance

$$R_{SH} = \left[\frac{dJ}{dV}\,(V = 0)\right]^{-1}, \tag{3.8}$$

which is a parallel resistance, should be as large as possible. R_{SH} is related to leaking paths, e.g., caused by pinholes in the active laver between the electrodes.

Figure 3.5c illustrates the energy level alignment of the simplest OPV architecture for different important points of the J-V curve. The model OPV consists of an organic (low-conductive) active layer, which is sandwiched between two metal electrodes with different work functions. It is related to the metal-insulator-metal (MIM) model [116]. It should be emphasized that this picture is highly idealized and that the J-V curve of such single-layer OPV will clearly deviate from the one shown in Figure 3.5b. Still, it helps to relate J-V characteristics to the energetic situation in an OPV.

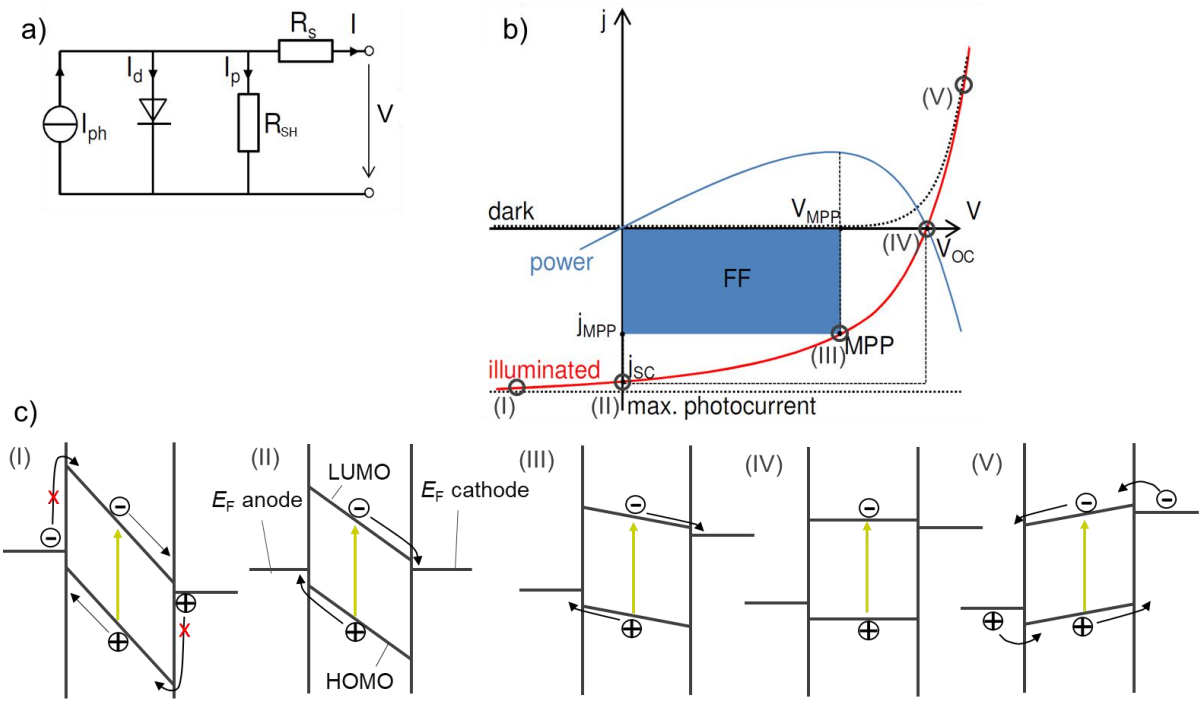

Figure 3.5: Basics of solar cell characteristics. (a) Equivalent circuit diagram of a solar cell consisting of a current source (I_{ph}) accounting for the photogenerated charge carriers, a diode (I_d), a parallel resistance (or shunt resistance, respectively) R_{SH} and a series resistance R_S. The idealized j-V curve in (b) can be obtained by variation of the voltage V and simultaneously measuring the current j. (c) Illustration of idealized energy level diagrams of a single-layer OPV (according to the metal-insulator-metal model) for different important points of the j-V curve. (a,b) Reprinted from [309].

If the cell is operated at negative voltages (Figure 3.5c(I)), a strong field exists in the active layer, which dissociates photogenerated excitons. Thus, a revers current is created. Ideally, charge carriers at the electrodes are not able to pass the injection barriers, even at high negative voltages V. This is related to a high shunt resistance. For $R_{SH} = \infty$, an ideal diode behavior and no losses, the reverse current corresponds to the photocurrent. For $V = 0$ (Figure 3.5c(II)), the situation is similar, except for a lower field in the active layer, which reduces the exciton dissociation efficiency and thus the generated photocurrent. As the Fermi levels of both electrodes are aligned (thermodynamic equilibrium), no power can be gained. This changes when V is further increased (Figure 3.5c(III)). For $V = V_{OC}$ (Figure 3.5c(IV)), flat-band condition is reached. Thus, excitons cannot be dissociated at all, and the photocurrent is zero. If V is further increased, the direction of the current is reversed and consists of photogenerated charge carriers, as well as of injected carriers, which easily can overcome the small barriers between anode (cathode) and HOMO (LUMO).
As mentioned above, this picture is highly idealized. The biggest deviation originates from the high binding energy of excitons in organic materials, which is the reason why high fields in the order of 10^6 Vcm^{-1} [117,118] are necessary for the dissociation. This is not well provided, especially not in the working regime in the fourth quadrant and a major reason for the poor efficiency of OPVs with a single-layer architecture.

This is why double-layer cells, also called flat-hetero junction (FHJ) cells, have been introduced by Tang et al. [9]. In this design, the active layer consists of two different organic materials, the donor and the acceptor, respectively, as illustrated in Figure 3.6. The exciton is typically created in the donor and diffuses within the layer. When it reached the donor/acceptor interface, it dissociates with a certain probability. The advantage of an FHL design is an enhanced charge carrier separation and the uncoupling of the dissociation process from the field across the active layer. Furthermore, the interface can be adjusted by tuning or replacing the donor and acceptor material. In general, a large energetic

offset between the LUMO onset of the acceptor $E_{\mathrm{LUMO}}^{\mathrm{acceptor}}$ and the HOMO onset of the donor $E_{\mathrm{HOMO}}^{\mathrm{donor}}$ is desirable, since these levels define the effective band gap

$$E_{\mathrm{g}}^{\mathrm{eff}} = E_{\mathrm{LUMO}}^{\mathrm{acceptor}} - E_{\mathrm{HOMO}}^{\mathrm{donor}}, \tag{3.9}$$

which gives an upper limit for the maximum achievable V_{OC} [119–121].

In order to increase device efficiency, additional functional layer, called hole and electron transport layer (HTL and ETL), are added between the active layer and the electrodes. In literature, the layers are sometimes also referred to as hole/electron extraction or blocking layers, whereas the usage is not always entirely consistent. The main function of these layers is twofold and will be explained for the HTL, i.e., the anode side. First, energetic offset between the anode's Fermi level and the HOMO onset of the donor layer should be small to reduce energetic losses. However, in order to avoid losses due to energetic barriers, it also has to be ensured that the VBM (or the HOMO onset in case of an organic HTL), is close to the HOMO onset of the donor. This distance is referred to as hole *injection* barrier for $E_{\mathrm{VBM}}^{\mathrm{HTL}} - E_{\mathrm{HOMO}}^{\mathrm{donor}} > 0$ and as hole *extraction* barrier for $E_{\mathrm{VBM}}^{\mathrm{HTL}} - E_{\mathrm{HOMO}}^{\mathrm{donor}} < 0$. Second, a large band gap, i.e., a low electron affinity, blocks electrons in the donor material and thus helps to inhibit recombination with holes in the anode. Such leakage current would reduce the generated photocurrent.

The FHJ architecture can be improved by mixing donor and acceptor in the active layer. The so-called bulk-hetero junction (BHJ) has a largely increased donor/acceptor interface, which increases the dissociation probability of excitons and thus, PCE.

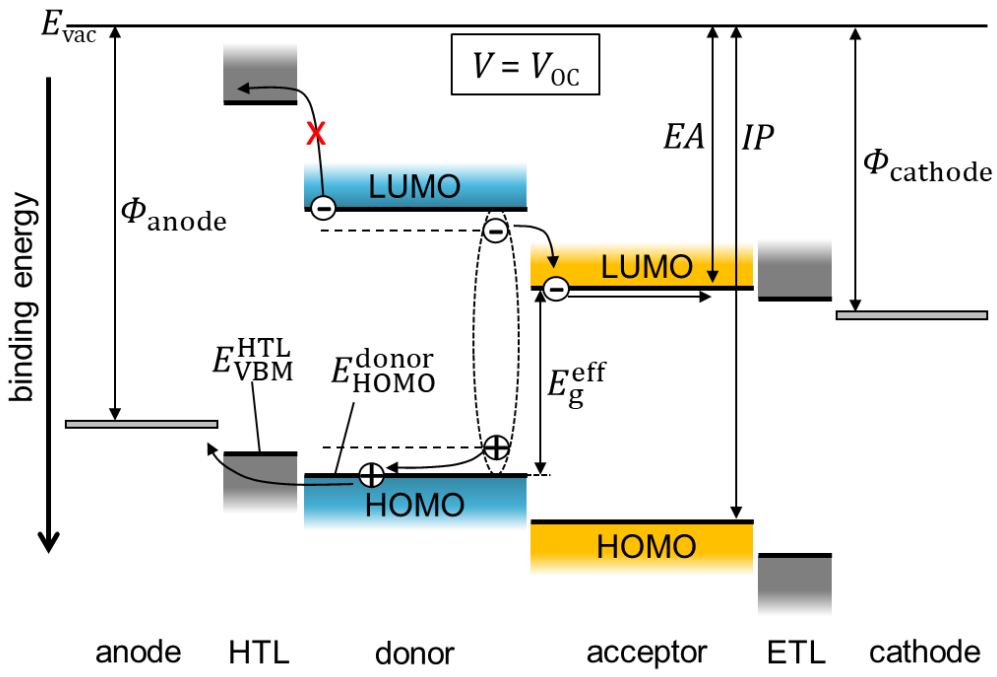

Figure 3.6: Schematic energy level diagram of a bilayer solar cell at open-circuit condition. The photogenerated excitons dissociate at the donor/acceptor interface. Afterwards, the separated charge carriers are extracted to the respective electrode.

4. Experimental Background

The purpose of this chapter is to provide information about the experimental background. The chapter starts with the presentation of the analytical techniques and the explanation of measurement and working principles in general. Details on the specific setups are provided. Information about experimental setups, which were used during the experiments but do not generate data, follow and, finally, important materials and processing steps are introduced.

4.1. Analytical techniques

The analytical techniques of this work comprise spectroscopic methods like photoelectron and infrared spectroscopy and microscopic techniques like atomic force and scanning electron microscopy. Finally, it is explained how solar cells were characterized.

4.1.1. Photoelectron spectroscopy

A very common and powerful technique for the analysis of surfaces and the main analytic method of this work is the photoelectron spectroscopy (PES). PES is based on the external photoelectric effect, which was first explained by Einstein in 1905 [122] for which he was awarded the Nobel prize in 1921 [123]. The principle of the effect is the following: when a photon hits a sample, it can transfer its energy to an electron in the target. If the photon energy $h\nu$ is high enough, the electron can be released from the material (illustrated in Figure 4.1). By measuring the kinetic energy of the photoelectron, the original binding energy can be determined. Based on this information, conclusions about the chemical composition, the position of the Fermi level at the surface or the work function of the sample can be drawn.

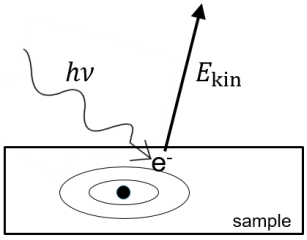

Figure 4.1: Illustration of the basic principle of the external photoelectric effect.

This concept is now explained in more detail. To leave the sample, the excited electrons have to overcome the binding energy E_B, which is defined with respect to the Fermi level E_F, and the work function of the sample Φ_{sample}. The remaining energy is converted into kinetic energy ($E_{kin,sample}$). According to the energy conservation, the process can be described as

$$h\nu = E_{bin} + \Phi_{sample} + E_{kin,sample}. \tag{4.1}$$

Thus, by knowing the energy of the incoming photons and the work function of the sample, the original binding energy of the photoelectrons can be calculated by measuring their kinetic energy. This principle is illustrated in Figure 4.2.

However, a priori neither the work function of the sample Φ_{sample} nor the kinetic energy of the photoelectrons at the sample's surface $E_{kin,sample}$ are known. Therefore, the sample is conductively connected to a spectrometer, which measures the photoelectrons' kinetic energy in the spectrometer $E_{kin,spec}$. Due to the electrical connection, the Fermi levels of sample and spectrometer are equalized, and photoelectrons are accelerated (or decelerated) on their way from the sample's surface into the spectrometer by the electric field induced by the contact potential difference between sample and spectrometer ($\Phi_{sample} - \Phi_{spec}$). Therefore, the sum of work function and kinetic energy is preserved according to

$$\Phi_{sample} + E_{kin,sample} = \Phi_{spec} + E_{kin,spec}. \tag{4.2}$$

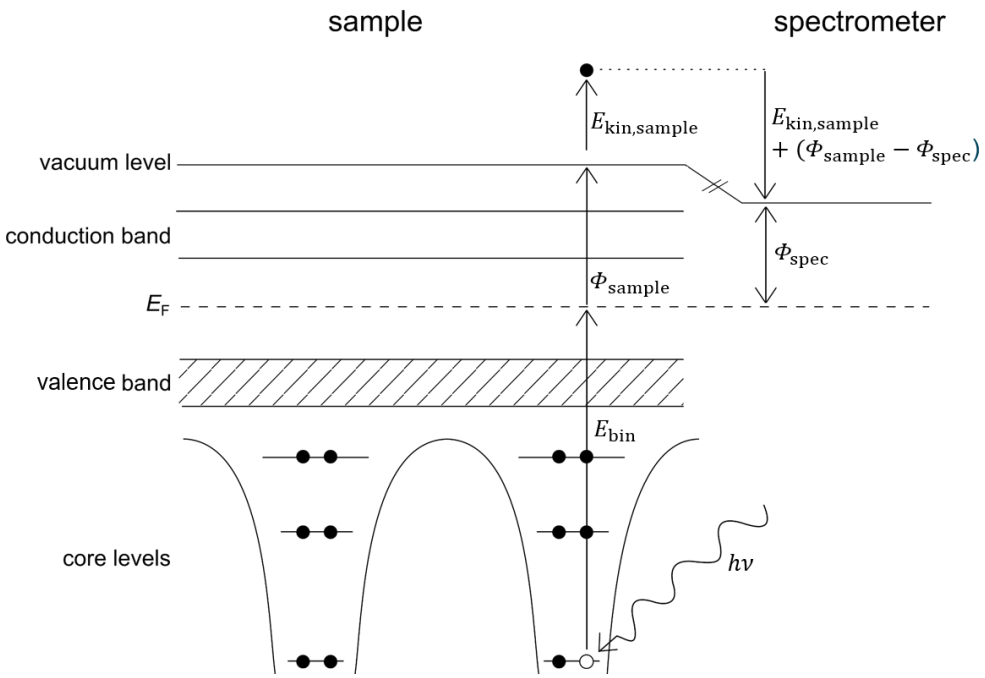

Figure 4.2: Energy level diagram illustrating the measurement principle of photoelectron spectroscopy. Reprinted and adapted from [239].

By combining with Equation (4.1), the binding energy

$$E_{\mathrm{bin}} = h\nu - \Phi_{\mathrm{spec}} + E_{\mathrm{kin,spec}} \tag{4.3}$$

is obtained. The only unknown quantity left is the work function of the spectrometer Φ_{spec}, which is determined by measuring $E_{\mathrm{kin,spec}}$ of photoelectrons stemming from the Fermi edge of a metallic sample, as here the binding energy E_{bin} is zero, per definition. Thus, Φ_{spec} can be calculated and each measured kinetic energy $E_{\mathrm{kin,spec}}$ can be translated into a binding energy E_{bin} of the photoelectron prior to the ionization process.

For the determination the kinetic energy, several types of spectrometers exist. Most common are cylindrical and hemispherical analyzers, of which the latter was used in this work. It consists of two hemispheres with different radii but a common center. Therefore, both hemispheres form a curved capacitor. By applying a voltage between both hemispheres, a certain energy is defined. Only electrons with this specific kinetic energy can pass the analyzer, which is why this energy is called pass energy. After the analyzer, an electron multiplier detects each arriving electron by converting the kinetic energy into an electric signal and sending it to a computer. On way to obtain counts for different binding energies, and thus to obtain a spectrum, is to vary the pass energy. As each pass energy (and thus kinetic energy) corresponds to a certain binding energy, the result is a histogram which shows the number of photoelectrons detected within a certain time frame for each binding energy. Figure 4.3 exemplarily depicts such a photoelectron spectrum of a sputter-cleaned silver sample. It shows the full accessible range and is therefore called survey spectrum. To ensure the same resolution over the whole binding energy range, not the pass energy of the hemispherical analyzer itself is varied during a scan, but a retardation potential, which is applied in front of the analyzer's entrance slit and decelerates arriving electrons.
However, it can also be useful to adjust the pass energy. As slower electrons are "more easily deviated" the resolution for lower pass energies is higher, but the intensity is lower. Therefore, for detail spectra with a higher resolution (e.g., of a certain orbital), the pass energy is set to a smaller value. In turn, the spectrum has to be measured several times to provide a sufficient signal-to-noise ratio. The final

spectrum is an average of all recorded ones. Thus, doublet structures and even smaller features as chemical shifts are resolvable.
In general, photoelectron spectroscopy is classified into ultraviolet (UPS) and X-ray photoelectron spectroscopy (XPS), according to the respective wavelength regimes used for the excitation. Additionally, also excitation via synchrotron radiation is possible, but as this excitation source was not used within the frame of this thesis, it will not be discussed in the following.

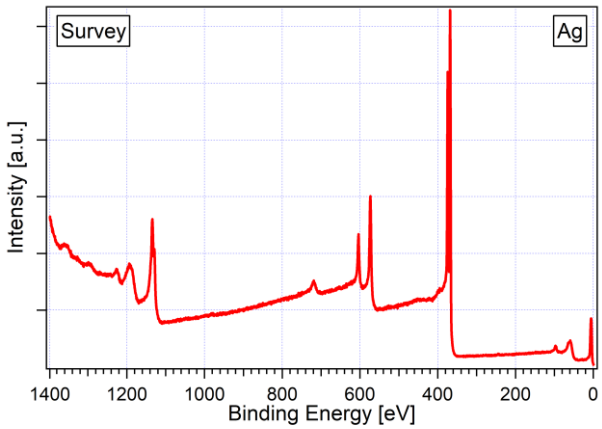

Figure 4.3: Example for a photoelectron survey spectrum. For each binding energy (corresponding to a kinetic energy) the amount of photoelectrons detected within a certain time is indicated.

Ultraviolet photoelectron spectroscopy

For UPS usually a gas discharge lamp is employed. The two main lines feature energies of 21.22 eV (He I) and 40.60 eV (He II), respectively. Therefore, it is especially suitable to study the valence region. Advantages are a high resolution due to a small line width (~2 meV [124]), a low signal-to-noise ratio due to a high intensity and a strong surface sensitivity (see Figure 4.5).
Additionally, UPS usually is used for the determination of the work function via the so-called secondary electron cutoff (SEC). This is the feature in the survey spectrum at the highest binding energies, i.e. lowest kinetic energies. For electrons with even lower kinetic energies in the material $E_{\mathrm{kin,in\_sample}} < \Phi_{\mathrm{sample}}$, the energy is too small to overcome the work function and leave the sample. Thus, they cannot be detected. Electrons with a kinetic energy being just large enough to leave the sample will have zero kinetic energy at the surface ($E_{\mathrm{kin,sample}} = 0$) and thus appear in the spectrum at the binding energy of the SEC, $E_{\mathrm{bin}}(SEC)$, for which the following equation applies:

$$h\nu = E_{\mathrm{bin}}(SEC) + \Phi_{\mathrm{sample}}. \tag{4.4}$$

This is on the one hand apparent from Figure 4.4, illustrating the described process, and on the other hand evident from Equation (4.1) for $E_{\mathrm{kin,sample}} = 0$. Thus, the work function of the sample can be calculated. For this purpose, the linear range of the SEC is extrapolated and the intersection with the x-axis is determined as demonstrated in Figure 4.8. In order to increase the signal of electrons with a kinetic energy close to zero, an acceleration voltage between sample and spectrometer is applied. This causes a shift of the spectra, which has to be considered during evaluation.

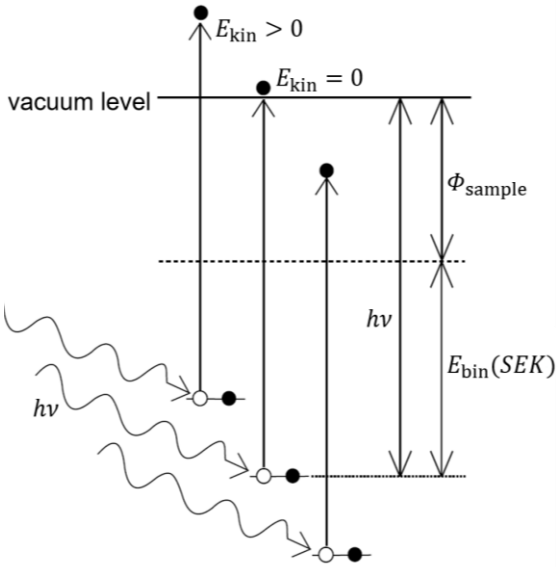

Figure 4.4: Illustration of the principle of the work function measurements using photoelectron spectroscopy.

X-ray photoelectron spectroscopy

In the case of XPS, either magnesium or aluminum anodes are used for the creation of excitation radiation with photon energies of 1253.6 and 1486.6 eV, respectively. Thus, also deeper core levels of different atoms are accessible. As core level binding energies are characteristic for each atomic species, the chemical composition of a sample including atomic ratios can be determined. Furthermore, different oxidation states of a certain element are distinguishable based on chemical shifts. In most cases, the binding energy of a core level is larger when the ion is more positively charged as the electric field of the core is less screened, e.g., $E_{bin}^{2p}(Ni^{2+}) > E_{bin}^{2p}(Ni^{0})$ and $E_{bin}^{1s}(O^{0}) > E_{bin}^{1s}(O^{2-})$ [125]. Another example for a chemical shift is the dependence of the binding energy of a certain element (e.g., carbon) on the binding partner in a molecule as the electron density around a considered atom is influenced by the electronegativity of the binding partners. In the case of a more electronegative partner (e.g., F), binding energies are generally increased due to less screening and in the case of a less electronegative partner (e.g., P) binding energies are generally lowered due to a stronger screening. Thus, differently bound atoms of the same element can be distinguished, which is especially helpful in organic molecules. However, care should be taken. Although very often these rules provide a good qualitative estimation of the physical reality, exceptions do exist and a careful comparison with literature values is necessary for a reliable attribution.
Compared to UPS, the linewidth of exciting photons is much larger, but can be reduced to below 300 meV when a monochromator is used [124].

Inelastic mean free path and the determination of layer thicknesses

A further important application of XPS is the determination of adsorbate layer thicknesses. If a sample is covered with an adsorbate layer, the intensity of any sample line of the uncovered sample will be reduced, as the photoelectrons are inelastically scattered by the covering atoms. In a first approximation it is assumed that the damping in each infinitesimal small layer is proportional to a factor $1/\lambda$, where λ is the inelastic mean free path (IMFP) of electrons in the covering layer. Then, the intensity I_0 of a substrate line of an uncovered sample is damped according to

$$I_d = I_0 \exp^{-\frac{d}{\lambda}} \tag{4.5}$$

where d is the thickness of the covering layer. By measuring the intensity of a line before (I_0) and after coverage (I_d), the thickness

$$d = \lambda * \ln\left(\frac{I_0}{I_d}\right) \tag{4.6}$$

can be calculated.
It is important to mention that the as-calculated layer thickness is a nominal layer thickness, which only corresponds to the "real" layer thickness if the layer is perfectly even. As soon as the adsorbate layer is rough or not fully covering, the nominal layer thickness will be smaller than the average layer thickness:

$$d_{\text{nom}} \leq d_{\text{av}}. \tag{4.7}$$

Of course, d_{nom} can only be determined if the adlayer is sufficiently thin. Otherwise the substrate lines vanish in the noise and cannot be measured with sufficient precision.
Also, the intensity of adlayer lines

$$I_{\text{ads}}(d) = I_\infty\left(1 - \exp^{-\frac{d}{\lambda}}\right) \tag{4.8}$$

depends on the thickness d. I_∞ is the intensity of the respective line for thick layers ($d \gg \lambda$) and limited by scattering processes. For thin layer with $d \ll \lambda$ (and thus in particular for submonolayers), the exponential function can be approximated by $1 - d/\lambda$ and $I_{\text{ads}}(d)$ is proportional to d:

$$I_{\text{ads}}(d) \sim d \quad , d \ll \lambda. \tag{4.9}$$

It follows from Equation (4.6) that the knowledge about λ is necessary for the estimation of d_{nom}. It was shown experimentally that λ follows a similar dependence on the kinetic energy of photoelectrons for most material (Figure 4.5), whereas some characteristics of the curve like vertical position or incline can depend on the density or the type (organic or inorganic) of the material. The curve reaches a minimum around 50 eV with a value of 0.5 nm. For smaller kinetic energies it increases to several nm

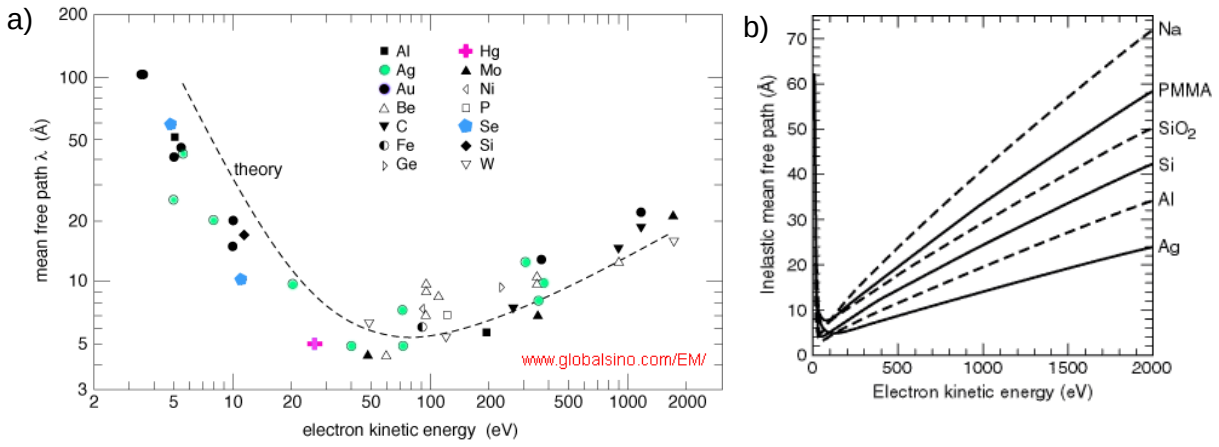

Figure 4.5: "Universal" dependence of the mean free path on the kinetic energy of electrons in different elements (a). (b) Shows deviations in the course of the function for different compounds. Reprinted from [310].

(e.g., 1 nm for He I with 21.22 eV) and for higher values of λ, it follows a square root behavior. In the keV range (XPS) it goes up to 1-3 nm.

For the determination of a nominal layer thickness, a suitable value of λ for the respective core level line (and thus kinetic energy) has to be estimated. Several formulas with different advantages and disadvantages for specific applications have been developed [126–129]. Most commonly the G1 formulas of Gries [127] on the one hand and the TPP-2M formula of Tanuma, Powell and Penn [128] on the other hand are used. In this work, TPP-2M is employed as it less dependent on the density and thus, is more suitable for organic compounds where the exact density often is unknown.

Information depth

The information depth is a measure for the depth from which the detected signal stems and is determined by the scattering mechanisms and thus the IMFP. The deeper the atom from which the photoelectron is released is located, the higher is the probability that it is scattered on its way to the surface: in a depth of 1λ, only 37 % of the electrons which are emitted in the direction of the surface normal will be able to escape. Electrons from the surface region up to this depth contribute 63 % to the total signal. For a depth of 3λ, only 5 % of the perpendicularly emitted electrons will reach the surface. This depth is defined as the information depth d_i. With IMFPs in the nm range, these considerations illustrate that PES is an extremely surface sensitive method.

Usually, a takeoff angle Φ of 90° is used, which means that the analyzer detects electrons which leave the sample perpendicular to the surface. By tilting the sample, the surface sensitivity can be further increased, since the information depth

$$d_\mathrm{i}(\Phi) = d_{\mathrm{i},90°} \cos(\Phi) \tag{4.10}$$

is proportional to the cosine of Φ. The principle is illustrated in Figure 4.6a.

This dependence can be used to obtain information about the location of a certain species. Upon reducing the takeoff angle, the signal of species which located closer to the surface are less damped than the signal of bulk species (see Figure 4.6). Thus, the intensity ratio between surface and bulk signals are increased. This technique is called angle-resolved XPS (ARXPS).

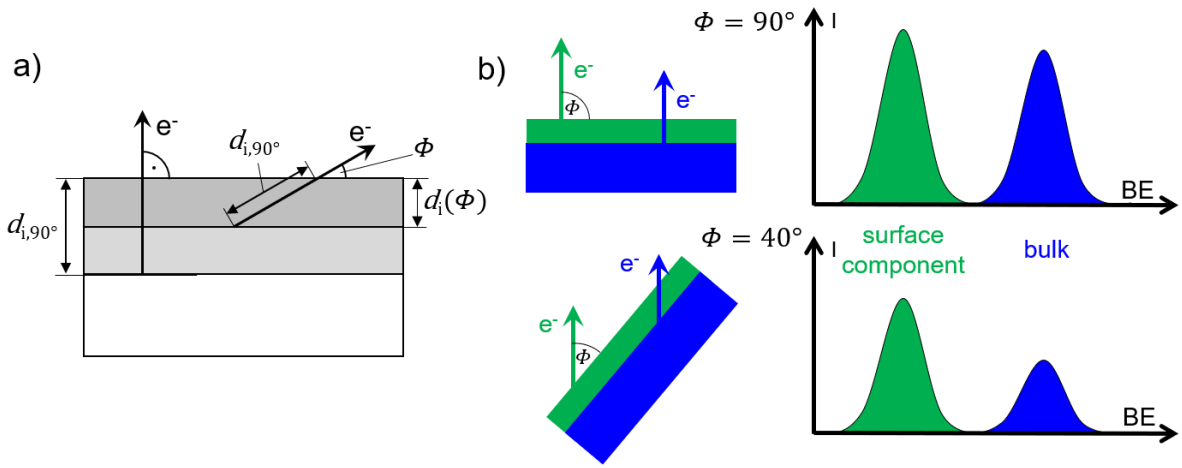

Figure 4.6: Illustration of the principle of ARXPS measurements. (a) Demonstrates how the information depth is reduced when a smaller takeoff angle is chosen, and (b) depicts the impact on spectral components of a two-layer sample: bulk components are damped more strongly than surface components.

Background

The inelastic scattering processes lead to an inevitable background underlying the actual signal, as can be seen in the exemplary survey spectrum in Figure 4.3. For the calculation of a line intensity (e.g., for layer thickness determination), this background has to be properly subtracted. For this purpose, according to Shirley [130] three assumptions are made.

i. A continuous excitation spectrum: all possible energy losses during a scattering process (zero to E_{kin}) are possible.
ii. All cross-sections for aforementioned scattering processes are the same and therefore, all energy losses during a scattering process are equally likely.
iii. Multiple scattering is neglected.

Under these strongly simplified conditions, the background of a hypothetical material with only one thin emission line would be a constant (see Figure 4.7a). In a more realistic case with a finite linewidth, the background at each kinetic energy E_X under the line is proportional to the amount of photoelectrons having a higher kinetic energy (marked in grey), since each of these photoelectrons has the same probability to experience an energy loss which leaves it with the energy E_X (see Figure 4.7b). Similarly, the background at a certain position in a spectrum is the sum of all scattered electrons from lines with higher kinetic energy. Thus, in the model, the background under each peak consists of a constant value from other lines and the non-constant background of the respective peak (Figure 4.7c). In reality, the situation is much more complex, but for practical application, the model of Shirley is totally sufficient and therefore used in this work.

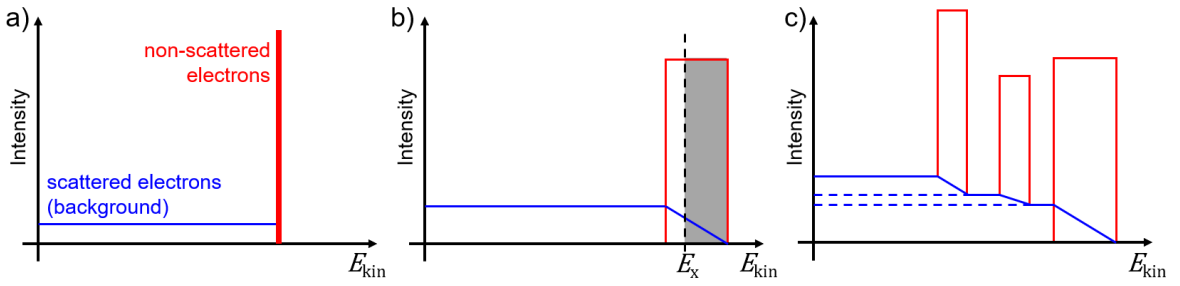

Figure 4.7: Illustration of the background according to Shirley. (a) A hypothetical line of non-scattered electrons leads to a constant background of scattered electrons. (b,c) Illustrate the proportionality of the background at a certain kinetic energy to the total number of electrons with higher kinetic energy (prior to scattering processes).

Sensitivity factors

The knowledge of the background is especially important in terms of the calculation of atomic ratios for which the intensities of the respective lines are needed – of course without distorting contributions from the background. However, the ratio of the measured intensities of two lines from two species in general does not correspond to the actual atomic ratio, since several non-constant (and non-equal) factors contribute to the finally recorded signal intensity. These factors are summarized as sensitivity factors and depend on the atomic species and the specific orbital, but also on the specific experimental setup.

The following equation lists all factors which contribute to the final signal intensity

$$I_{AX} = A\,\phi\,G_\theta\,\varepsilon_T\,\varepsilon_D\,\sigma\,\lambda\,n_A \tag{4.11}$$

that is measured for an orbital X from an atom of the species A. In Equation (4.11), A is the surface area of the samples from which photoelectrons are detected and ϕ is the photon flux of the X-ray source. Both quantities are constants for a specific setup. This also applies for the angular efficiency factor G_θ, however only for a setup with an angle of 54.7° ("magic angle") between the direction of

incoming X-rays and the direction of photoelectrons moving toward the detector. For other angles the quantity depends on the respective orbital [131]. ε_T is the transmission function of the specific analyzer setup and depends on the kinetic energy of the photoelectron and thus on AX. ε_D is the detection efficiency, which is in general as well a function of the kinetic energy, unless the system is operated with a constant pass energy. σ is the cross-section, i.e., the probability for the photoionization of a certain atomic orbital AX by an incoming X-ray photon with a certain energy. It is also called relative sensitivity factor (RSF or RSF_{AX}, respectively). Values are tabulated in literature for different X-ray energies [132]. λ is the inelastic mean free path of photoelectrons in the samples (as discussed before) and of course also a function of AX, unless the investigated film is a monolayer. n_A is the density of the atomic species A in the sample. Usually, not all quantities are available in absolute values with enough precision to determine the atomic density based on the measured line intensity I_{AX}. However, Equation (4.11) can be used to calculate relative atomic ratios:

$$\frac{n_A}{n_B} = \frac{I_{AX}/ASF_{AX}}{I_{BX}/ASF_{BX}} \tag{4.12}$$

Here, all prefactors were summarized to the atomic sensitivity factor

$$ASF_{AX} = A\ \phi\ G_\theta\ \varepsilon_T\ \varepsilon_D\ \sigma\ \lambda = f(AX)\ RSF_{AX}\ \ \lambda_{AX} \tag{4.13}$$

The ASFs have to be determined empirically for each type of XPS system. In some cases, for example when the desired value is not listed, it is useful or even necessary to use RSF_{AX} values instead. However, to do so, $f(AX)$ has to be constant. This is only provided for a setup with $\theta = 54.7°$, which is operated with constant pass energy and for a known (or considered) transmission function. Additionally, for bulk samples, λ_{AX} has to be estimated, as described earlier.

Determination of the work function: UPS vs XPS

It was mentioned earlier that usually UPS is used for the measurement of work functions. However, work function values can also be obtained with XPS. The principle is identical to the determination with UPS, however, calibration is not realized via the XPS Fermi edge, since this would involve the risk of inaccuracy due to the large energetic distance between SEC and Fermi level. Thus, calibration is accomplished by determining the work function of a sputter cleaned Ag sample with UPS. For the same sample, the XPS SEC is recorded and the binding energy at the SEC is linked to the work function.

The usage of XPS has some advantages. Most important: it is less prone to both charging and photovoltage effects. The former is due to lower intensities compared to UPS and the latter is due to smaller cross-sections for band-to-band transition.

In terms of precision, using XPS has no drawbacks compared to UPS. Repetition accuracy at the very same spot gives standard deviations below 1 meV for both XPS and UPS, respectively. The standard deviation of several measurements at different spots of the same sample lies in the meV range and even seems to be slightly higher for XPS than for UPS (see Figure 4.8).

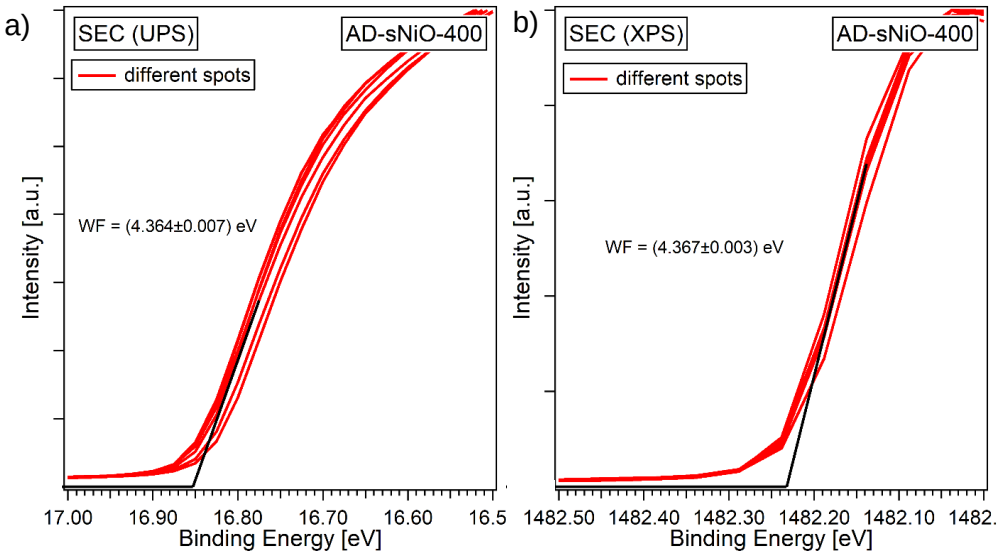

Figure 4.8: Measurement of the SEC of a NiO test sample with UPS (a) and XPS (b), respectively, for the comparison of the standard deviation for several measurements at different spots of the same sample.

Determination of the valence band maximum

In this work, the valence band maximum (VBM) was determined according to the leading edge. Here, the steepest incline of the valence band's leading edge is extrapolated and the binding energy at the intersection with the extrapolated background is defined as the VBM. An example for a VBM measured with XPS is given in Figure 4.9. Note that reliable values may in general only be expected for XPS valence band spectra, while the onset extracted from UPS measurements may be affected by band dispersions and the linear approximation has to be done at lower binding energies. Valence band spectra are always presented normalized if not stated otherwise.

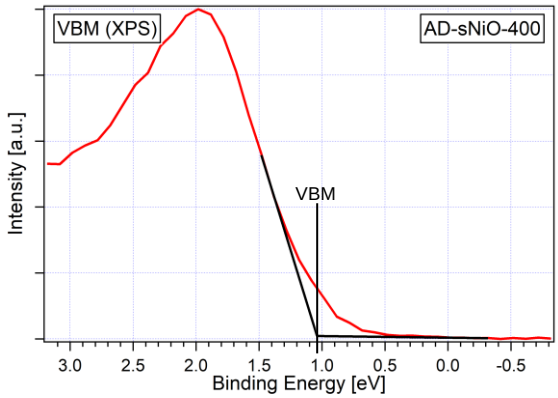

Figure 4.9: Example of a valence band spectrum and the determination of the VBM.

Charging

One of the most common artifacts in PES of solid-state samples is the shift and/or distortion of the spectral signal due to charging of the sample. This happens when the sample is not sufficiently conductive. The higher the flux of exciting photons (X-ray or UV) the more electrons leave the sample. If not enough electrons can be provided through the electrical connection between sample and sample holder and through the samples itself, a positive charging of the sample is the consequence. Especially

for the He lamp used in our system the flux is quite high such that many samples show charging issues with UPS but not with XPS.
Charging of a sample is seen as a shift of the whole spectrum to higher binding energies (lower kinetic energies), caused by the electrostatic attraction of the negatively charged photoelectrons by the positively charged surface region of the sample. This shift usually is accompanied by a deformation of the spectrum. To work around this issue a high-intensity UV LED (365nm) has been installed by Maybritt Kühn [133]. For semiconductors with a smaller band gap than 3.4 eV (according to 365nm wavelength) the resistivity of a sample can be reduced by photoconductivity, such that the sample can be measured without parasitic influences from charging. However, care must be taken as other effect can be induced, like surface photovoltage or photovoltages at buried interfaces.

Sputtering

Sputtering is a technique in which accelerated ions are focused onto the surface of a sample. It is basically used for two purposes. The first is to clean the surface from contaminants like, e.g., hydrocarbon. This feature is used every time before calibration measurements on the silver sample to ensure the same condition of the reference for each calibration. The second is to ablate parts of a sample's surface in order to obtain depth profiles.
For this work, an argon gun was used. For the cleaning of the silver reference, ions were accelerated to 3 keV and shot onto an area of 8x8 mm^2 for usually 4 min. Whenever sputtering is used in another context the respective parameters will be given.

Satellites

Satellites occur when photoelectrons loose energy on their way toward the sample's surface, for example by interacting with other electrons in the sample. The most common loss mechanisms are the excitation of electrons into higher states, so-called shake-up processes, and the excitation of electrons into vacuum, so-called shake-off processes. In a typical shake-up process, a valence electron is excited into the conduction band while the photoelectron loses the necessary part of its kinetic energy and appears in the spectrum at accordingly higher binding energies.

Instrumentalization of this work

All PES measurements in the frame of this thesis were performed using a PHI Versa Probe II system equipped with a monochromatized Al Kα anode as X-ray source (1486.6 eV), an Omicron HIS 13-helium discharge lamp as ultraviolet source (21.22 eV), and a concentric hemispherical analyzer for the measurement of kinetic electron energies. The angle between the analyzer and the X-ray source was 54.7°. Survey spectra were recorded with a pass energy of 187.85 eV, detail spectra of the core level lines were measured with 11.75 eV, valence bands were taken with 23.5 eV, and for the secondary electron cutoff either 2.95 or 5.85 eV were chosen. The spectra are referenced in binding energy with respect to the Fermi edge and the core level lines of in-situ cleaned Ag, Au, and Cu foils. Some spectra are referenced via the position of their main peaks. Details are indicated in each case. The base pressure of the measuring chamber during all experiments was kept in the 10^{-9} mbar regime. If not indicated otherwise, the takeoff angle was 90°. XPS fits were performed using Voigt profiles after subtraction of a Shirley background [130].

4.1.2. Infrared spectroscopy

Working principle

Fourier-transform infrared (FTIR) spectroscopy is an optical analytical method in which absorption of infrared light is used to obtain information about molecular vibrations, lattice vibrations (phonons) or electronic vibrations like plasmons. Depending on the frequency range, different absorption types prevail. In the mid-infrared (MIR) range (here 700–4000 cm^{-1}) mainly molecular vibrations are visible. From according absorption modes, conclusions about the chemical composition and changes of molecular structures can be drawn by comparison with DFT calculations and reference spectra. Absorption modes of phonons are located in the far-infrared (FIR) range (here 250–700 cm^{-1}) and provide information on the structural order like crystallinity or grain sizes.

An FTIR spectroscope is equipped with a broadband emission source, which is a heated silicon carbide rod in the present case. The emitted light is coupled into a Michelson interferometer and afterwards led through the sample. Finally, it is registered by a detector, which measures the intensity I, integrated over all frequencies. For the measurement of a spectrum, the interferometer is used to create a difference Δx between the two beam paths inside the interferometer and thus constructive or destructive interference. By variation of Δx, an interferogram $I(\Delta x)$ is created and recorded by the detector. To obtain the intensity as a function of the wavenumber $\tilde{\nu}$, $I(\Delta x)$ is fourier-transformed into the spectrum $I(\tilde{\nu})$.

FTIR spectroscopy can be operated in two different modes: reflection and transmission. Here, all measurements were performed in transmission if not stated otherwise. In this case, always intrinsic silicon (i-Si), which provides enough transparency in the IR region, was used as substrate. To avoid artefacts of the measurement system and to separate the signal of the film from the signal of the i-Si substrate, all samples (i.e., films of interest on i-Si) were measured with respect to a clean i-Si reference sample. As the properties of i-Si depend on the processing steps like, e.g., annealing, for each sample an equally treated reference sample was used. The final (relative) transmission spectrum

$$I_T(\tilde{\nu}) = \frac{I_T^{sample}(\tilde{\nu})}{I_T^{ref}(\tilde{\nu})} \tag{4.14}$$

was obtained as the quotient of the transmission spectrum of the sample $I_T^{sample}(\tilde{\nu})$ and the transmission spectrum of the reference $I_T^{ref}(\tilde{\nu})$.

Another important application of FTIR is the estimation of molecular orientations. This technique is based on the coupling of the linearly polarized infrared light with the transition dipole moments of molecules in or on the sample. For the transition dipole moment $\vec{M}$ of a certain mode, the intensity I_m of this absorption mode is proportional to $\left|\vec{E} \cdot \vec{M}\right|^2$, where $\vec{E}$ is the oscillating electric field of the incident IR beam.

Now consider a planar molecule which is oriented perpendicular to the surface as illustrated in Figure 4.10. Assume it has an in-plane (ip) and an out-of-plane (oop) dipole moment ($\vec{M}_{ip}$ and $\vec{M}_{oop}$, respectively). The incoming light is p-polarized, that is the electric field $\vec{E}$ oscillates in the plane of incidence. For an angle of incidence of 0° w.r.t the surface normal, $\vec{E}$ only couples to $\vec{M}_{oop}$ and not to $\vec{M}_{ip}$, as here the projection is zero ($\vec{E} \cdot \vec{M}_{ip} = 0$, Figure 4.10a). However, when the sample is tilted by Θ, the scalar product becomes positive as $\vec{E} \cdot \vec{M}_{ip} \propto \cos(\Theta) > 0$ and part of the light will be absorbed by the ip dipole moment (Figure 4.10b). When the sample's tilt angle Θ is further increased, also the absorption of the ip mode increases while the absorption of the oop mode decreases until it reaches zero for $\Theta = 90°$ (Figure 4.10c). Here, $\vec{E} \cdot \vec{M}_{ip}$ is maximal. Thus, two functions, $I_{\mathrm{ip}}(\Theta)$ and $I_{\mathrm{oop}}(\Theta)$, describing the absorption of the ip and the oop mode, respectively, in dependence on the tilt angle of

the sample, are obtained. As these functions depend on the orientation of the molecules in or on the sample, an average value for the molecular orientation can be calculated. This technique is called angular-resolved IR measurement.

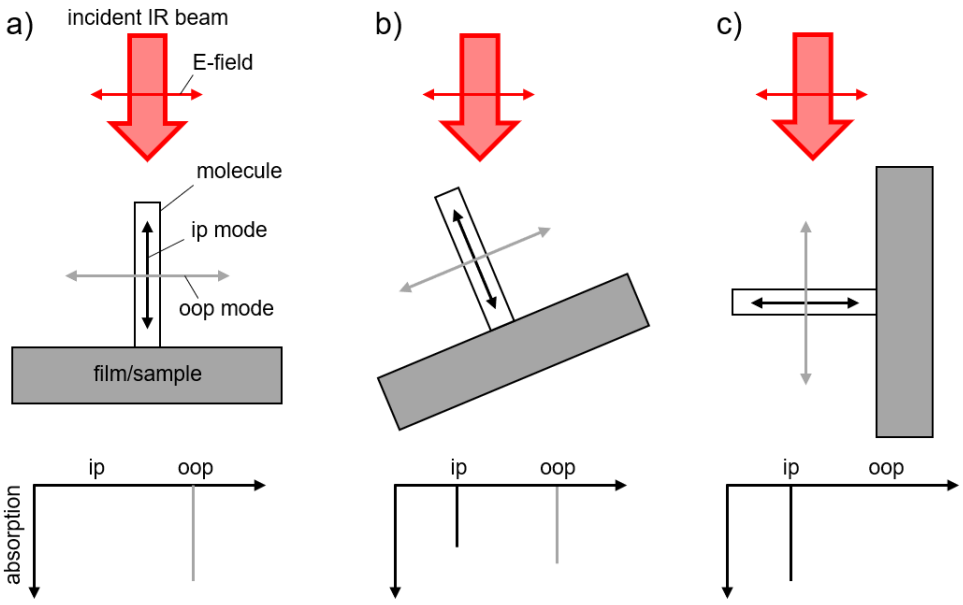

Figure 4.10: Principle of angle-resolved IR measurements. Only modes with non-zero projection of the dipole moment on the E-field can couple to incoming IR photons and lead to absorption. In the case of metallic samples the "metal-surface selection rule" has to be considered.

Instrumentalization of this work

IR transmission spectra were recorded with a Fourier-transform IR spectrometer Vertex 80v (Bruker) in the nitrogen-filled sample compartment. The spectrometer was located in the cleanroom of the InnovationLab, see Chapter 4.2.1. All spectra were taken with p-polarized light and are relative spectra with respect to the cleaned bare silicon wafer, if not indicated otherwise. A nitrogen cooled mercury cadmium telluride (MCT) detector was used in the MIR range, and a DLaTGS (deuterated L-alanin doped triglycine sulfate) detector in the FIR range, both with resolution of 4 cm^{-1}. In the MIR, final spectra were averaged over 200 scans, whereas spectra in the FIR were averaged over 2500 scans.
All IR data presented in this work were taken by Dr. Sabina Hillebrandt or Valentina Rohnacher from the Kirchhoff-Institute for Physics in Heidelberg.

4.1.3. Atomic force microscopy

A common method for the measurement and investigation of topographies in the nanometer range is the atomic force microscopy (AFM). It is based on the interaction between a tip located on a vibrating plate, the cantilever, and the sample's surface. To obtain an image the tip is moved over the surface and for each pixel the z-deviation and thus the height is determined. This regulation can be realized in different operation modes, most important for this work the amplitude-modulated and the peak-force tapping mode. With typical tip sizes between 10 and 20 nm, resolutions in the sub-nm range can be reached [134].
In the amplitude-modulated tapping mode the cantilever is excited by a piezo with a certain frequency close to resonance. A laser points onto the cantilever and the reflection is detected. Thus, the actual frequency and amplitude can be logged. If the tip is close enough to the surface, any change of the distance results in a change of these values. In the present case, only the amplitude is important and is used to adjust the tip-sample distance to a constant value via a feedback loop. The final image then is based on this information. Measurements for this work were performed with an AFM from DME (DS

95 SPM) at the InnovationLab in Heidelberg with tip radii of about 8 nm or at Princeton University with a DI Dimension 3000 SPM from Bruker [135].
While the amplitude-modulated tapping mode is classified as non-contact mode, in the peak-force mode the tip touches the surface. For each pixel it is recorded how far the tip has to be approached in order to experience a certain repulsion from the surface. Measurements with this technique were performed at the KIP in Heidelberg by Dr. Sabina Hillebrandt and Valentia Rohnacher. The instrument was a Nanoscope IV from Bruker. Cantilevers had a resonance frequency of 325 kHz and a tip radius below 10 nm.

4.1.4. Scanning electron microscopy

Scanning electron microscopy (SEM) is an imaging method in which a focused electron beam is scanned over a sample. For each beam position, the intensity of either backscattered (primary) or secondary electrons are detected and processed to an image. Compared to optical microscopy, higher resolutions are accessible due to the small de-Broglie wavelength of high-energy electrons. For the images of the present work, an acceleration voltage of either 0.5 or 5 keV was applied, resulting in a de-Broglie wavelength and thus, a theoretical resolution limit of λ_e = 0.6…0.2 nm. The experimental resolution was indicated as 1.2 nm.
The kinetic energy of the electron beam furthermore determines the depth from which electron are detected. For 5 keV, this depth was estimated to 5-10 nm [136].
Images were taken at a base pressure below $1x10^{-5}$ mbar via recording secondary electrons.

4.1.5. Solar cell characterization

Solar cells were characterized with a LOT LS0816-H solar simulator by Jakob Bombsch from the TU Braunschweig. It was equipped with a 1000 W xenon arc lamp as solar source, which simulated a standard terrestrial spectrum of AM 1.5G. A certified silicon solar cell (RR106O, Radboud University, Nijmegen) was used for calibration of the emission intensity of 100 mW cm^{-2}. Current-voltage characteristics were recorded with a Keithley 2601B source meter (2-wire configuration). Prior to the actual measurements, test runs under illumination were performed to minimize deviations due to temperature.

4.2. Experimental setups

Most of the experimental work has been carried out in the clean room of the InnovationLab in Heidelberg. Here, a vacuum system with different preparation and analysis chambers is located. This so-called clustertool is presented in the first part of this chapter. Afterwards, oxygen plasma treatment, an important technique in the field of surface science and in the present work, is explained.

4.2.1. The clustertool

The clustertool is an UHV system operated with a base pressure in the 10^{-6} mbar regime. It connects several analytical methods like PE and IR spectroscopy as indicated in the sketch in Figure 4.11. Additionally, samples can be prepared in a nitrogen-filled glovebox and directly transferred into the UHV system, for the deposition of metal layers and/or organic molecules. Here, the solar cells investigated in the Chapters 6 and 7 were built, and the layers for the interface experiment in Chapter 5 were evaporated. After evaporation, samples can be analyzed in-situ with the different analytic techniques.

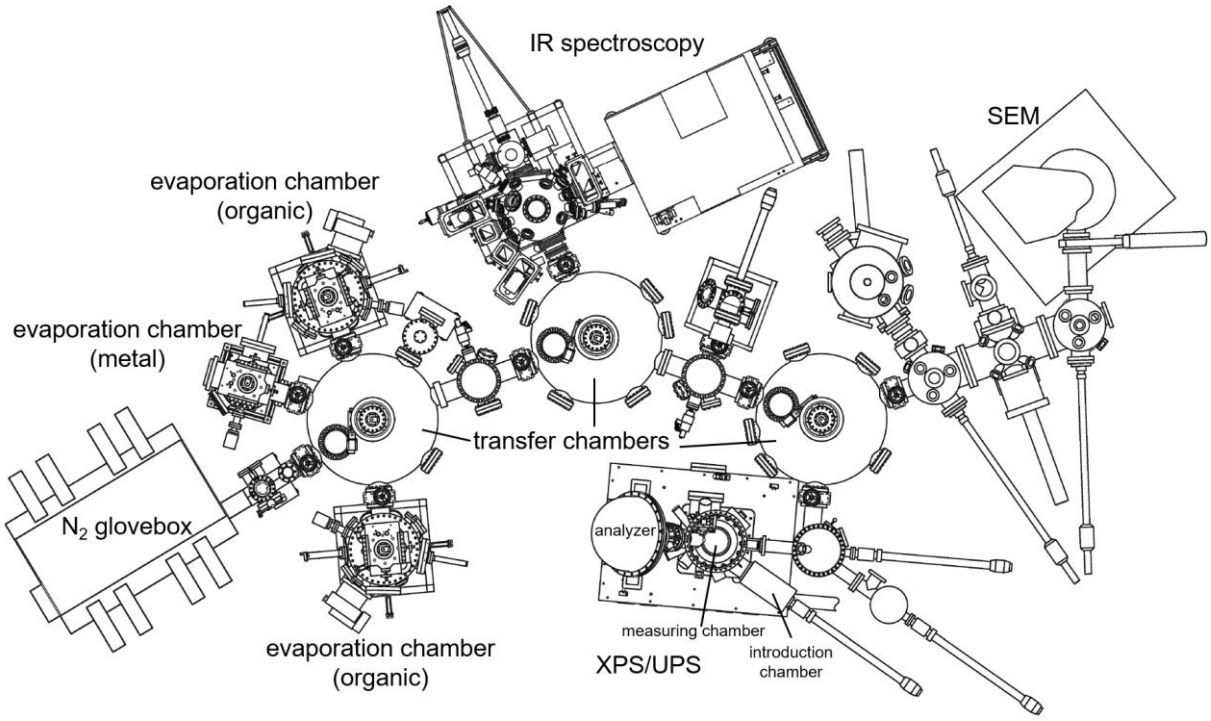

Figure 4.11: Sketch of the UHV system at the InnovationLab in Heidelberg called clustertool. Reprinted and adapted from [311].

4.2.2. Oxygen plasma oven

Oxygen plasma (OP) treatment is a common tool for the cleaning of surfaces and for increasing the surface energy and thus wettability and printability. The plasma is created in an oven, which is evacuated to a pressure of about 1/1000 atm, and refilled with a gas, usually argon or oxygen. Then, a high-frequency voltage is applied to ionize the gas atoms and initiate the plasma. In the case of oxygen gas, the plasma consists of the following species: $O^{(+/-)}$, $O_2^{(+/-)}$, O_3 and free electrons [137,138], whereas according to Steirer et al. O^- and O^{2+} are the main reactive components [21]. Finally, the oven is vented, and the OP treated samples can be taken out.
The oven used in this work was a model called Tetra from Diener Electronics. OP was applied for 1 min with a power of 900 W and a base pressure of 0.3 mbar. When samples for IR analysis were OP treated, the reference i-Si sample was put onto another piece of a silicon wafer to ensure that only one side is affected by the plasma.

4.3. Materials and sample preparation

In this Chapter, all relevant materials are introduced. The focus is on the origin of the materials and basic properties and procession steps.

4.3.1. Silicon substrates

In the course of the work the following silicon substrates were used:

Table 4.1: Survey on the silicon substrates used for this work. All wafers had a native oxide surface layer.

label	resistivity [Ωcm]	dopant	supplier
i	>5000	P	Sil'tronix Silicon Technologies
n	10-20	P	Active Business Company GmbH
n^+	0.008-0.018	P	Sil'tronix Silicon Technologies
n^{++}	0.001-0.005	P	Sil'tronix Silicon Technologies
p	1-3	B	Sil'tronix Silicon Technologies
p^{++}	0.001-0.002	B	Sil'tronix Silicon Technologies

Prior to further processing, substrates were cut into pieces, typically about 1x1 cm^2, and cleaned in an ultra-sonic bath with acetone and 2-propanol for 15 min each. Finally, substrates were dried with gaseous nitrogen.

4.3.2. Solution-processed NiO

Solution-processed NiO films were spin-coated from a precursor solution of nickel(II) acetate tetrahydrate (NiAc) (99.998 % trace metal basis) and monoethanolamine (MEA) (< 98 %). Both materials were purchased from Sigma-Aldrich and dissolved in anhydrous ethanol from VWR International GmbH. Reagents were used without further purification.

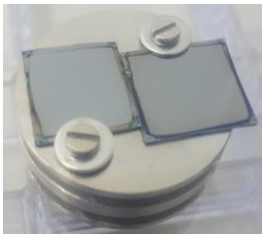

Figure 4.12: Picture of two spin-coated NiO films mounted onto a sample holder.

The precursor materials NiAc and MEA were dissolved in ethanol (0.2 M). The molar ratio between nickel ions and the stabilizing MEA was kept 1:1 [23]. The solution was stirred at 50 °C overnight prior to deposition by spin-coating onto the silicon substrates (2000 rpm for 60 s, acceleration: 2000 rpm/s), both in N_2 atmosphere. The films were then thermally annealed in ambient clean room atmosphere to convert the deposited precursor material into nickel oxide. Afterwards, samples were transferred to the respective measurement setups within the shortest time possible. A detailed thermogravimetric analysis of the thermal decomposition of NiAc powder in air including reaction equations can be found in [139]. Briefly, in a first step, crystallized water evaporates at a temperature of slightly above 100 °C. The actual conversion to NiO_x takes place in a range between 310 – 370 °C and is complete at about 380 °C. Afterwards the TGA signal stays about constant. XRD measurements showed only the typical reflection peaks of pure NiO at 37°, 43° and 63° [140] for annealing temperatures of 300 °C and above. Similar reflection patterns were observed for solution-processed films based on NiAc, indicating the presence of the two main orientations (111) and (100) [141].

In the following, a sample annealed at a certain temperature, e.g. 400 °C, will be referred to as "sNiO-400". As-deposited samples obtain the prefix AD, OP treated samples obtain he prefix OP. Thus, "OP-sNiO-400" denotes an sNiO sample which was annealed at 400 °C and afterwards treated with oxygen plasma.

Pre-experiments for the optimization of production parameters have been carried out by Florian Friedrich [142]. The author also likes to thanks Valentina Rohnacher for the fabrication of many samples for the analytical examination.

4.3.3. F_4ZnPc

The donor material fluorinated zinc phthalocyanine (F_4ZnPc) was provided by BASF SE. The molecular structure is depicted in Figure 4.13. For interface experiments, it was deposited via evaporation in UHV. Further details on the deposition procedure may be found in [143,144].

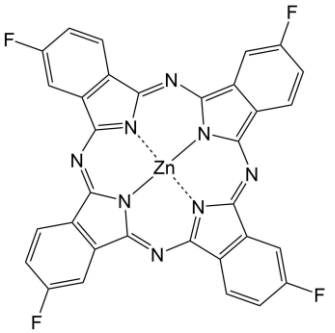

Figure 4.13: Molecular structure of F_4ZnPc [232].

4.3.4. C_{60}

The acceptor material C_{60}, also known as buckminsterfullerene, is a popular acceptor material in organic solar cells with high electron mobilities [145,146]. C_{60} has been purchased from American Die Society (purity > 99.9 %) and deposited via evaporation in UHV. Further details on the deposition procedure may be found in [143,144].

4.3.5. CYNOPPA

CYNOPPA is the abbreviation for 4-cyanophenylphosphonic acid with the chemical formula ($C_7H_6NPO_3$). It was purchased at Manchester Organics with a purity of 96 %. The phosphonic acid was further purified via recrystallization by Max Ackermann from the Institute of Organic Chemistry in Heidelberg. In a final nuclear magnetic resonance spectrum nothing but the molecular components where detectable, according to M. Ackermann.

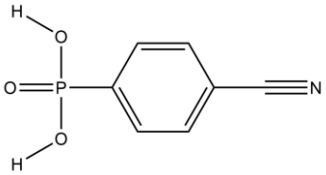

Figure 4.14: Molecular structure of 4-cyanophenylphosphonic acid (CYNOPPA).

Purified CYNOPPA was dissolved in anhydrous ethanol purchased from VWR (≥ 99.8 %) in a concentration of 1 mM and stirred for 4 h prior to each usage. Afterwards, sNiO samples were left in the solution in a nitrogen-filled glovebox overnight at 50 °C to ensure agglomeration of the molecules on film surfaces. In this step, it is important to properly cover the petri dish containing the solution to prevent evaporation of the solvent. To activate the bonding, samples were annealed at 140 °C for 3 h. Also this step took place in nitrogen atmosphere. Subsequently, potential multilayers were removed by sonication in a heated ultrasonic bath for 20 min. Finally, samples were blown dry with nitrogen and heated again to 120 °C for about 10 min to clean the surfaces from residual solvent. This procedure is based on recipes from literature [147,148].

5. Solution-Processed Nickel Oxide and the Impact of Oxygen Plasma Treatment

This chapter is dedicated to the experimental characterization of solution-processed NiO films. First, as-deposited (AD) films without any further surface treatment are investigated. The chemical composition as well as the spatial distribution of the components and electronic implications are discussed. Afterwards, changes induced by oxygen plasma (OP) are analyzed and correlations between chemical and electronic properties are examined. Parts of these results have been published in [149]. Subsequently, further influences on film properties are evaluated and attempts to increase the quality of solution-processed films in terms of stoichiometry are described. Finally, both the films and the impact of different treatments are compared to vacuum-processed NiO samples.
The results of this chapter are crucial for the following ones, in which the interface of sNiO to other materials is investigated. Before discussing the results of spectroscopic analysis, basic spectral features of single crystalline NiO photoelectron spectra are provided as their features can easily be confused.

5.1. Basics of nickel oxide photoelectron spectra in literature

Figure 5.1 shows the Ni 2p detail XP spectrum of a NiO reference from literature [125]. It can be divided into two parts: the $2p_{1/2}$ region for binding energies higher than ~870 eV and the $2p_{3/2}$ emission lines below this value. In both parts two main features are visible. The ones at lower binding energies are the actual core level emission lines and the ones at higher binding energies are satellite structures [49,67,150]. As the $2p_{1/2}$ region does not provide any new information, spectra within this work only have been taken in the $2p_{3/2}$ region. Thus, also the following discussion will be limited only to this part of the spectrum.
The main feature at roughly 854 to 855 eV is uncontroversial. It originates from the Ni^{2+} species of stoichiometric NiO [13,49,63,67,68,151–154]. The adjacent region at about 1.5 to 2 eV higher binding energies around the side peak is much more complex and often leads to confusion. This holds especially for mixed systems where additionally to nickel oxide also hydroxides and oxyhydroxides contribute to the signal. Nevertheless, already for single crystals, the interpretation of the side peak is far from trivial. In the following, an insight into the current understanding is provided and various possible contribution are discussed.

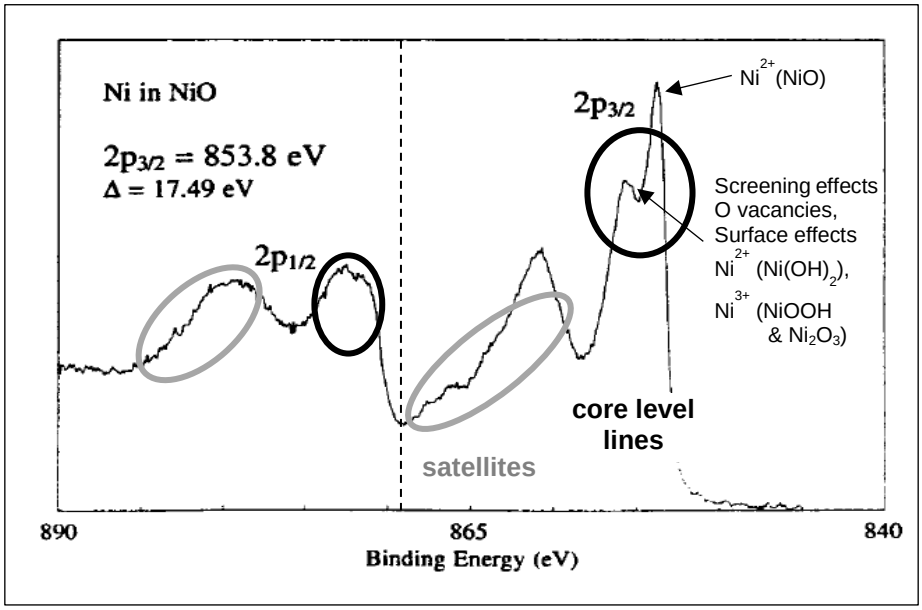

Figure 5.1: Example for the Ni 2p region of NiO, reprinted and adapted from [125]. Aside from the doublet structure, features of satellite, intersite and surface effects render this spectrum quite complex.

A fundamental question is whether the side peak already exists in perfect (defect-free) single crystals, and if so whether it is a bulk or a surface feature.
A clear answer was given by Uhlenbrock et al. in 1992 [63]. As Figure 5.2a shows, even a freshly in-situ-cleaved NiO(100) single crystal features such a side peak. As it does not show an angular dependency, it cannot originate from the surface or at least has to have a strong contribution from the bulk. However, in a similar experiment with a softly sputtered sample, Uhlenbrock et al. observed an angular dependency of a component at exactly the same position. The authors concluded that this feature is a superposition of contributions from both the bulk and sputter-induced Ni^{3+} states near the surface. The bulk contribution was only vaguely explained by "correlation effects".
In 1993, van Veenendaal and Sawatzky were able to give a more detailed explanation [150]. By calculating spectra of differently designed clusters, the authors drew conclusions about the different contributions from defects in the bulk, from the bulk itself as well as from the surface. A first important - although not too surprising - result was that a cluster of a single NiO_6 unit does not exhibit a peak splitting, as shown in Figure 5.2b. However, screening effects are responsible for the satellite features at binding energies of 6 and 9 eV, respectively. In contrast, in the spectrum based on a larger cluster which takes into account the six nearest neighboring units (Ni_7O_{36}), an additional feature close to the side peak of experimental data appears (Figure 5.2c). The authors' explanation is a charge transfer from a neighboring NiO_6 unit to the nickel site with the core hole, instead of a transfer from an adjacent oxygen ion. After this screening process, the interaction of the holes from both units lead to the splitting. The effect is referred to as nonlocal or intersite charge transfer screening. In additional calculations, possible influences of the surface on the one hand and defect states in the bulk on the other hand were investigated. The calculation of the surface's influence is based on a cluster similar to the large Ni_7O_{36} cluster, only that one NiO_6 unit is missing (see inset in Figure 5.2d). To estimate the

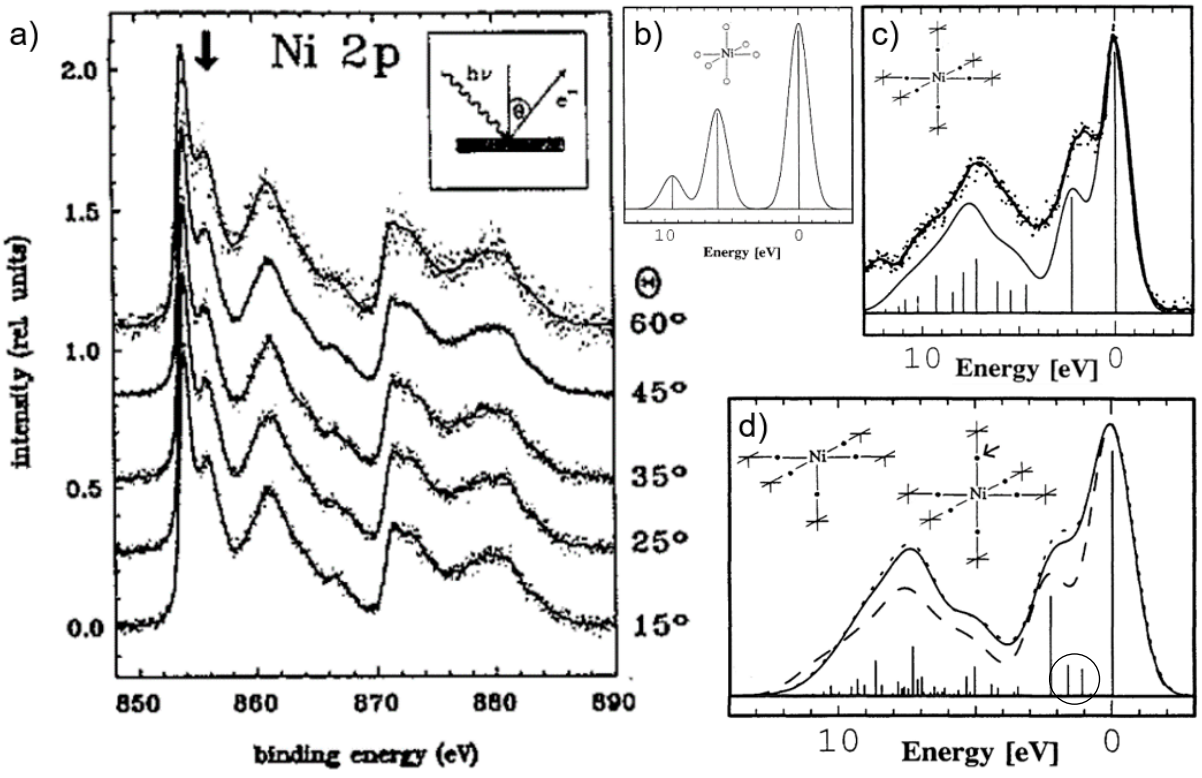

Figure 5.2: Literature examples for Ni 2p spectra of NiO single crystals. (a) ARXPS measurements from Uhlenbrock et al. of a freshly cleaved NiO(100) single crystal [63]. (b) Calculation based on a single NiO_6 cluster. (c) Calculation based on a Ni_7O_{36} cluster (lower line) in comparison to experimental data from Uhlenbrock et al. [63]. (d) Addresses the question of the influence of the surface by calculating a spectrum of a Ni_6O_{30} cluster in which the upper NiO_6 part was omitted to simulate the surface (solid line). The influence of oxygen deficiencies (dotted line) was investigated with the same the cluster as in (c), but without the oxygen atom indicated by the arrow. The dashed line is a replication of the calculation result in (c). Figured (b)-(d) are reproduced from van Veenendaal and Sawatzky [150].

impact of a defect states, again the large cluster was used, however, with one oxygen atom less. As shown in Figure 5.2d, both scenarios lead to a line in the region of the side peak, however at slightly lower binding energies.

In conclusion, it is seen as proved that the side peak is an inherent feature of single crystalline bulk NiO [153,155–157], but also contains contributions from oxygen deficiencies in the bulk and surface effects like incomplete octahedral structures or sputter-induced Ni^{3+} ions.

A similar question arises for the O 1s spectrum. While it is known for NiO(111) that the surface at room temperature is always hydroxylated due to hydroxyl groups bonding to regular sites [61,103,158], NiO(100) can be prepared such that only one single peak (caused by O^{2-} ions) is visible [49,61,63]. An example is given in Figure 5.3a, trace a. Consequently, in contrast to Ni 2p spectra, O 1s spectra of pure single crystalline NiO do not exhibit an inherent side peak, nor do surface effects lead to a splitting: all other features which may be seen in those O 1s spectra are due to ad- or chemisorbed species or imperfections.

According to Langell et al. the intensity of the side peak in O 1s spectra of epitaxially grown NiO(111) thin films is about 25 to 35 % of the total intensity and is caused by surface hydroxide which is "singly coordinated to a Ni^{2+} site" and covers 65 to 85 % of the surface [158].

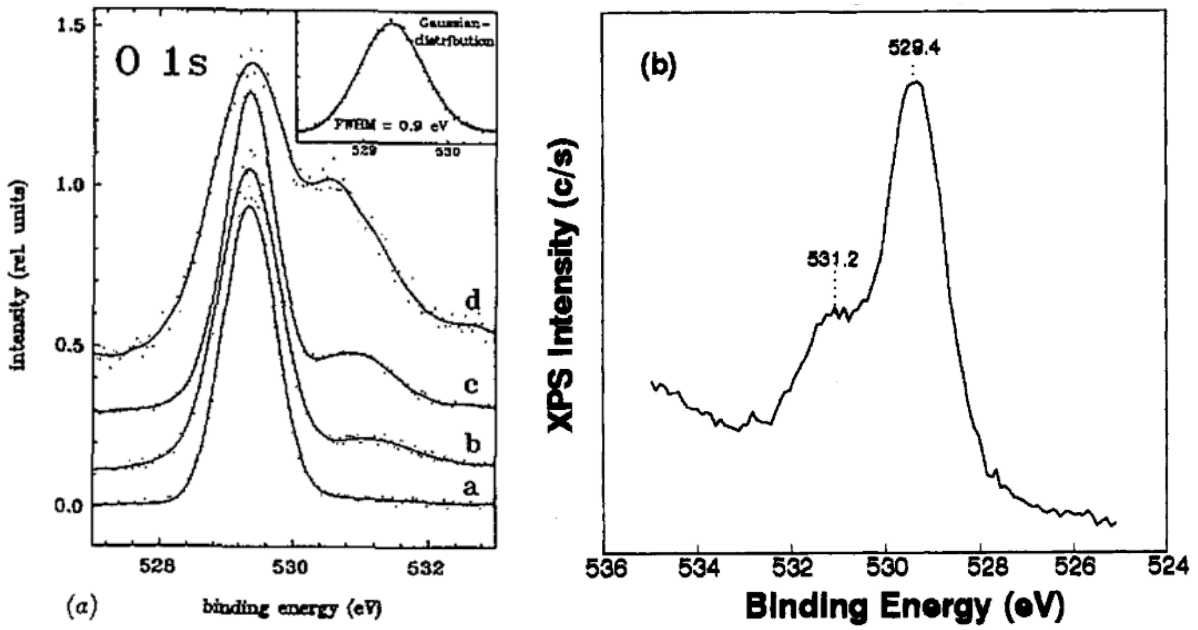

Figure 5.3: Literature examples for O 1s spectra of NiO: (a) NiO(100) single crystal, reprinted from [63]. Trace a was recorded on a fresh surface after cleavage in vacuo. A side peak at higher binding energies can be produced by sputtering (trace b), exposure to ambient conditions (trace c) or a combination of both (trace d) (b) Expitaxially grown NiO(111) thin film on a Ni(100) single crystal subtrate, reprinted from [158]. Note that expitaxially grown NiO(100) also exhibits a side peak. It is, however, smaller in general.

Confusion in current literature

The described effects render the interpretation of both Ni $2p_{3/2}$ and O 1s XP spectra pretty difficult. If one does not proceed very carefully, a wrong interpretation can easily be the result. Despite the ongoing research over decades, still ambiguities exist, and faults have been established in recent years, especially for mixed samples. A very common example is the too trivial peak fitting of the Ni $2p_{3/2}$ core level lines with only two components, which usually are attributed to Ni^{2+} from NiO and Ni^{3+} from Ni_2O_3, respectively. Since even spectra of pure NiO samples show two peaks, as discussed above, this procedure appears to be questionable. However, even without this knowledge clear contradictions result from this interpretation of the spectra, which will be demonstrated in the following for a recent literature example. In 2015, a work was published in Science [33], where the ratio of Ni^{3+} to Ni^{2+} ions based on the Ni $2p_{3/2}$ spectrum would be close to one according to the false interpretation (see Figure 5.4a). The O 1s spectrum is fitted similarly with two components, which are attributed to the corresponding oxygen species in Ni_2O_3 (blue) and NiO (red). If the ratio of Ni^{3+} to Ni^{2+} ions was indeed about 1, the ratio of the two corresponding oxygen species – O in Ni_2O_3 and O in NiO, respectively - should be 1.5:1. However, undoubtedly the ratio is well below 1 and thus contradicts the conclusion based on the Ni $2p_{3/2}$ spectrum.

Still, the fitting of the Ni $2p_{3/2}$ spectrum with simple components attributed to Ni^{2+} and Ni^{3+} is very common [36,159,168–172,160–167], even in high-impact journals such as Nature [28,30] or Advanced Materials [173–175] and is used for the calculation of atomic ratios and the interpretation of the data.

The examples demonstrated that assignments in recent literature are often not reliable. Therefore, in this work, special care has been taken and the assignments are traced back to reference spectra as far as possible. Furthermore, interpretations are crosschecked by complementary IR measurements.

The following section shows the results of measurements with both spectroscopic techniques and further analytical methods on AD-sNiO films.

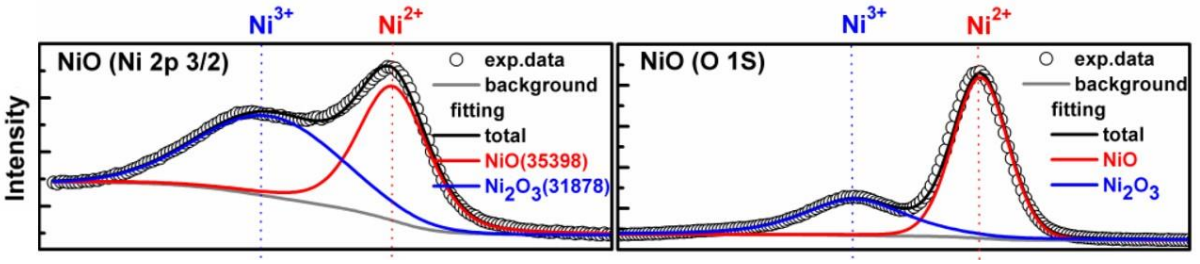

Figure 5.4: Literature examples for inconsistencies due to inadequate simplification of photoelectron spectra of a NiO containing sample. Reprinted from [33].

5.2. Characterization of solution-processed nickel oxide

As described in Chapter 4.3.2, an annealing step is needed to convert the precursor into NiO_x. The annealing temperature T_a crucially influences the final chemical composition, and thus the film and potential device properties [17,24,36,176–178]. Therefore, in a first step the impact of T_a was examined. For this purpose, samples were annealed at temperatures between 275 °C, where the conversion is sufficiently complete for optoelectronic applications [17,24], and 400 °C, where the efficiency of OPVs exhibits a maximum [24]. Unless otherwise specified, n-doped silicon with a native oxide layer was used as substrate. Samples without any further treatment are referred to as AD (as-deposited). This chapter starts with surface characterizations of the produced thin films, including AFM, SEM, XPS and KP measurements. Thereafter, bulk characterizations by UVvis ellipsometry, IR and UVvis spectroscopy follow. The results are then comprehensively discussed and compared to literature.

5.2.1. Surface properties

A first rather qualitative but revealing technique is the scanning electron microscopy (SEM). Figure 5.5 displays SEM images of the surface region of an AD-sNiO film annealed at 400 °C (AD-sNiO-400) in different magnifications, taken by Dr. Jean-Nicolas Tisserant from the TU Braunschweig at the InnovationLab in Heidelberg. With the lowest magnification in the submillimeter range, the sNiO film looks smooth and compact and covers the complete surface without any visible cracks or pinholes (Figure 5.5a). With a larger magnification, a few potential pinholes and grains in the submicron range appear (Figure 5.5b). Additionally, a certain structure emerges, which becomes clearly visible with an even larger zoom (Figure 5.5c): the structure contains features with lateral sizes in the range of 20 nm.

Atomic force microscopy (AFM) is suitable for a more quantitative evaluation. Measurements on a similar sample (e.g., AD-sNiO-400) in amplitude-modulated mode confirm a low surface roughness with RMS values below 1 nm and peak-to-valley values for single grains of typically about 2 nm (Figure 5.6). Spherical grains with sizes between 10 and 20 nm (~17 nm in average) are homogenously distributed. These findings were also confirmed by Valentina Rohnacher using peak-force mode, whereas grain heights and thus RMS values were slightly larger due to a higher accuracy of this measurement mode (see Figure A.1a). Additional measurements on films annealed at 325 and 275 °C showed slightly smaller grain sizes and RMS values than films annealed at 400 °C (see Figure A.1c). Under consideration of layer thicknesses of more than 20 nm (see Chapter 5.2.2), the films showed no

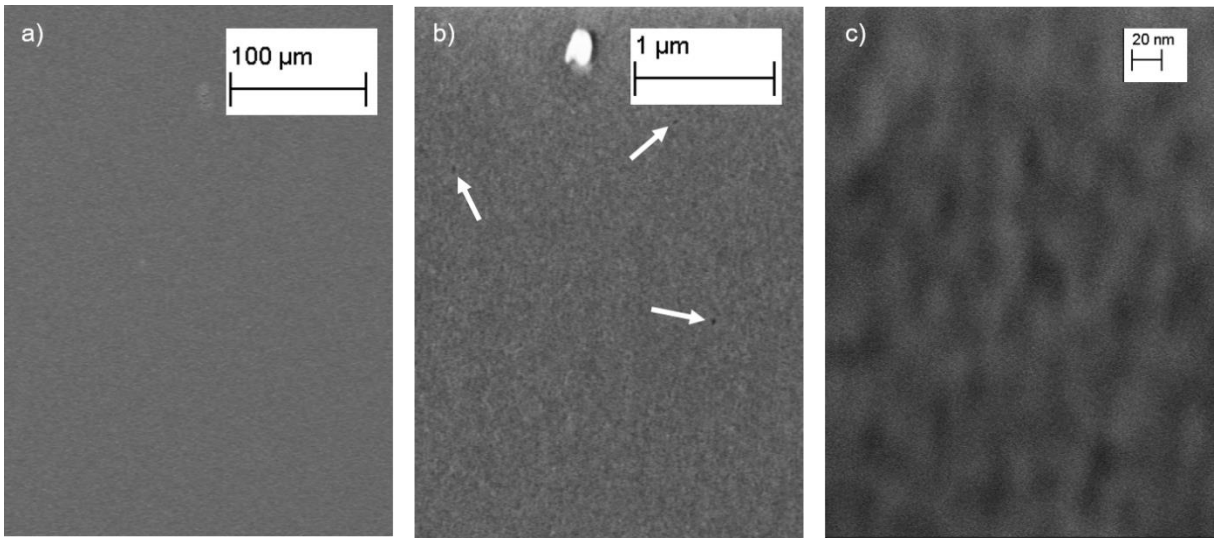

Figure 5.5: SEM image of an AD-sNiO-400 film on a silicon substrate, taken by Jean-Nicolas Tisserant @ 5 kV.

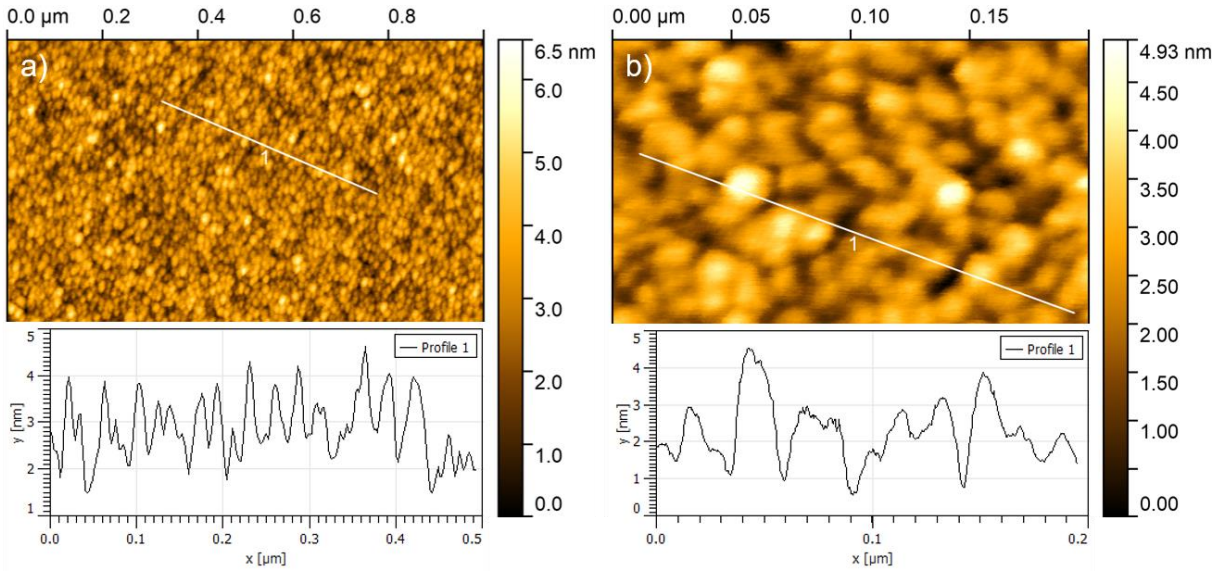

Figure 5.6: (a) and (b) AFM images of an AD-sNiO-400 sample measured in amplitude-modulated mode. (a) 1x1 µm² and (b) 0.2x0.2 µm² with heigth profiles in the insets. Grain sizes between 10 and 20 nm are visible. RMS values are around 0.7 nm. Layer thicknesse is about 23 nm.

sign of incomplete coverage, although on the basis of the present AFM images it cannot be ruled out that some pinholes extend to the substrate as overall peak-to-valley values can reach 13 nm (shown in inset in Figure A.1a).

Still, the amount of such potential pinholes cannot be significant as silicon from the substrate was not detected by XPS (Figure 5.7a), witnessing a nominal layer thickness of at least 10 nm. In fact, no other signals than those from the expected species Ni and O were found in the survey spectra, except for tiny amounts of chlorine in some of the samples.O 1s detail spectra (Figure 5.7c) exhibit basically two features. A main peak, which is referenced in binding energy to 529.6 eV [13] for better comparability, and a side peak around 531.4 eV.[2] As discussed in the previous section, the main peak is due to the oxygen of stoichiometric NiO (O^{2-}) [13,49,61,67,69,95,103] (see Table A.1 for BE values from literature). The side peak, in contrast, cannot be attributed this unambiguously since many different oxygen species can contribute to the signal in this region. Most import to name are nickel hydroxides (α-, β-, oxy- and surface-) [13,61,67,69,103,154,179,180], defective or adsorbed oxygen [95,154,156] and dinickel trioxide (Ni_2O_3) [67–69,154].

As discussed in Chapter 3.2.2, Ni_2O_3 can only be formed under certain conditions, including a dry environment and rather low temperatures, i.e. below ~250 °C. Besides, formation by oxidation of metallic Ni is much more effective than the formation by oxidation of NiO [67]. However, at no point in the solution-based process of this work metallic Ni is involved. Instead, $Ni(OH)_2$ is directly converted into NiO [67,68], which significantly reduces the probability of Ni_2O_3 formation. Additionally, due to the solution-processing in ambient conditions and annealing temperatures starting from 275 °C the prerequisites for Ni_2O_3 formation are not fulfilled for samples of this work. Moreover, XP and IR data indicate water, at least in the samples annealed at lower temperatures, and an annealing temperature of 400 °C is certainly too high for the formation of Ni_2O_3. Thus, one must conclude that Ni_2O_3 cannot exist in the present sNiO films. A final evidence might be the absence of a characteristic peak at 653.5 eV (E_{kin} = 833.1 eV) in the LMM Auger lines, identified by Kim et al. [67] (see Figure 5.16). Under the given ambient and thus moist conditions, it is much more likely that Greiner et al., who have come to the conclusion "that the peak commonly attributed to Ni_2O_3 in ex-situ-prepared samples is actually from $Ni(OH)_2$" [66], are correct. This interpretation is backed by IR measurements (shown in Chapter 5.2.2), where strong hydroxide signals are detected. Furthermore, these signals correlate with the size of the side peak in the O 1s spectra. Therefore, it is highly likely

[2] The relative position of the Fermi level will be discussed in Chapter 5.3.2.

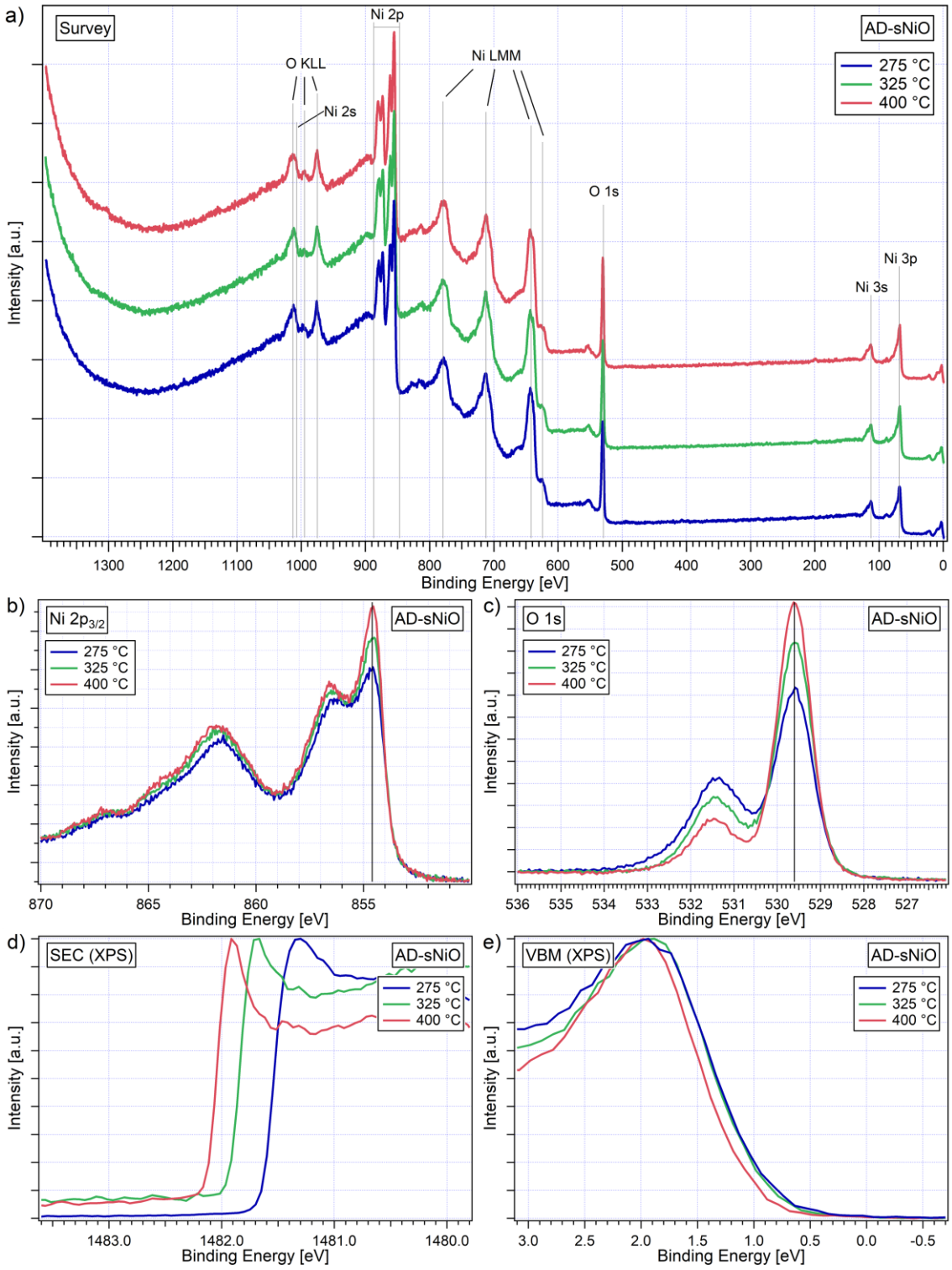

Figure 5.7: XP spectra of the AD films annealed at three different temperatures. (a) Survey spectra, (b) Ni $2p_{3/2}$ detail spectra referenced in binding energy to 854.7 eV [50], and (c) O 1s detail spectrum referenced in BE to 529.6 eV [13].

that the side peak in the present case is mainly due to hydroxidic species. Small amounts of adsorbed or defective oxygen cannot be ruled out but are considered to be negligible. Details of the different hydroxide contributions will be discussed later. The considerations about Ni_2O_3 are important beyond the scope of this work since this topic is far from unambiguous until today and many groups still assign peaks in spectra of solution-processed NiO films to Ni_2O_3 [31,36,165,181].

Additionally, at higher binding energies around 533 to 534 eV, interstitial or adsorbed water [13,63,95,154,179] on the one hand and adsorbed oxygen [4,11,49,60] on the other hand may

contribute to the signal. For T_a = 400 °C such species can be widely excluded, as the spectrum does not show any significant signal in this range. The spectrum for T_a = 275 °C, in contrast, shows a clear tail toward higher binding energies, which is attributed to water in agreement with IR measurements. Finally, carbon-oxygen compounds like alcohol (-COH), carbonyl (-CO-) or ester (-COO-) groups can contribute to the signal in this range above 531.5 eV [95,154,180]. However, as no carbon contamination is detectable in the survey spectra (Figure 5.7a) and even detail spectra only in some cases exhibit a peak which was distinguishable from noise (Figure A.3), such contributions can be neglected here.
In summary, XP spectra indicate that in the surface regions of the samples only NiO, hydroxidic nickel and small amounts of water are present. Regarding the temperature dependency, for higher annealing temperatures the O 1s main peak becomes more pronounced, while the side peak undergoes a reduction. Based on the explanations above, the following statements can be drawn: higher annealing temperatures provide for a more complete conversion of the hydroxide-containing precursor film into stoichiometric NiO. Water seems to be present at 275 °C while no sign for it is found for 400 °C.
These trends are also supported by the Ni $2p_{3/2}$ spectra (Figure 5.7b). The intensities in regions indicative for Ni^{2+} from stoichiometric NiO (854.7 eV and 856.5 eV, see Table A.2) increase at higher annealing temperatures. At the same time, the valley between both lines at approximately 855.7 eV deepens slightly, which is consistent with the previous conclusion from O 1s spectra, as $Ni(OH)_2$ is known to exhibit features in this region (see Table A.2). Furthermore, formation of NiO explains the increase of integral intensity, since the volume density of Ni ions in NiO is about twice as high as the one in $Ni(OH)_2$ while the inelastic mean free path, and thus the information depth, is about the same for both materials [50]. This is why higher $Ni(OH)_2$-to-NiO ratios result in a smaller integral intensity of the Ni 2p spectrum. The same holds for NiOOH [50]. For an annealing temperature of 400 °C, the described changes result in a spectrum which shows no significant differences to reference samples of crystalline NiO from literature [153,154,158,180] (see also Figure A.2).

These changes should also influence the O:Ni ratios of the samples, since stoichiometric forms of the hydroxide species $Ni(OH)_2$ and NiOOH exhibit an atomic ratio of 2:1, while stoichiometric NiO has a ratio of 1:1. These values were experimentally confirmed by Payne et al. [154,180]: 1.9 was determined for NiOOH and 2.0 for $Ni(OH)_2$, although some $Ni(OH)_2$ samples had values of only 1.5-1.6. For NiO powder samples mostly a ratio of 1.1 was found. For the sample of the present work, the following O:Ni ratios were determined: 1.50, 1.26 and 1.20 for 275, 325 and 400 °C, respectively. Thus, the ratio drops for higher annealing temperatures in agreement with the observed reduction of hydroxide species. The ratios were determined by integration of the O 1s and the Ni $2p_{3/2}$ spectra after correction for Shirley background [130] and were calibrated to measurements on a single crystal, as will be explained in Chapter 5.6.2.
As shown in Figure 5.7d, work functions vary from 4.5 to 5.0 eV for 275 and 400 °C, respectively, in good agreement with ambient KP measurements (Figure A.4) and typical values from literature [13,16,22,36,60,182,183].
Valence band maxima are located about 1 eV below the Fermi level for 400 °C and slightly closer (~100 meV) to it for 327 and 275 °C. Considering (optical) band gaps of almost 4 eV (see next Section), the samples show the expected p-type character, even though not strongly pronounced.[3]

In summary, films showed an increasing conversion for higher annealing temperatures. Less hydroxide species were detected and more stoichiometric NiO instead. These changes lead to lower work functions, whereas the Fermi level was only slightly affected. The results will be discussed quantitatively in Chapter 5.3.2.

[3] The p-type behavior seems to be slightly stronger for lower annealing temperatures. However, as will be shown in Chapter 5.4.2, this shift is accompanied by a band bending in the silicon substrate in the range of the observed variation of the Fermi level. A priori, it is not clear whether the band bending in the Si substrate just follows the intrinsic Fermi level of sNiO. Therefore, a dependence of the Fermi level on the annealing temperature cannot be clearly stated.

Remarks on lateral homogeneity and reproducibility

The lateral homogeneity was probed via the work function, as it is very sensitive to all kinds of changes at the surface. For five measurements of the SEC at different spots of a certain sNiO film within an area of about 1 mm^2, the standard deviation was typically below 10 meV (see also Figure 4.8b). This is comparable to the homogeneity of a sputtered silver sample.

A similar measurement on an AD-sNiO-275 sample using KP revealed a certain dependency of the work function on the position on the sample: spots closer to the edges tend to exhibit higher values (Figure 5.8). Still, the average value over all data points yields a standard deviation of only 13 meV. Thus, although XPS measurements were usually performed close to the center of the sample, deviation from this procedure would have a rather negligible influence.

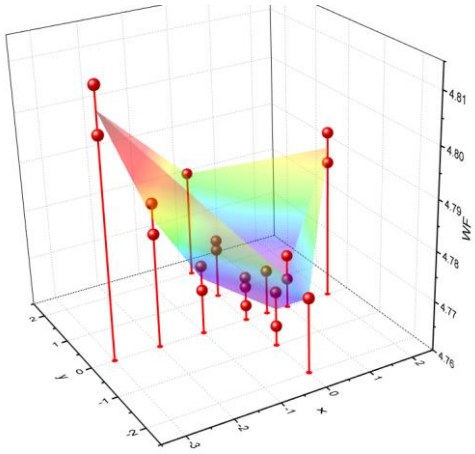

Figure 5.8: Work function distribution of an AD-sNiO-275 sample. The xy-plane shown here roughly corresponds to the whole sample size of 1x1 cm^2.

Within a batch, samples were typically very similar to each other. However, batch-to-batch variations (i.e., standard deviation) for both the work function and also the Fermi level, were in the range of 50 to 100 meV, even with proper control of all processing parameters, whereas the exact procedure of the annealing step seemed to have the biggest influence (see Chapter 5.4.4). Outliers with larger deviations also existed. Interestingly, the accuracy also depends on the annealing temperature: it was observed throughout the work that samples annealed at 325 °C were somewhat less reproducible compared to samples annealed at 275 or 400°C. Work functions of AD-sNiO-325 samples, e.g., varied significantly more (~200 meV). A possible reason is the rapid conversion of NiAc precursor in this temperature range [139], and thus an increased sensitivity to the actual temperature of the hotplate. Additionally, it is reported that also the decomposition of surface OH takes place between 320 °C [158] and 330 °C [61].

5.2.2. Bulk properties

A first insight into the bulk structure can be gained by SEM imaging of a cross-sectional fracture. Figure 5.9 shows such a cross-section of an AD-sNiO-400 film spin-coated onto a silicon substrate. As expected based on the SEM and AFM images discussed earlier, the layer covers the substrate homogeneously. The layer thickness appears to be slightly above 20 nm [136]. Again, a grainy structure is visible, whereas the grains have an elongated shape perpendicular to the surface. Actually, the layer mostly consists of a densely packed monolayer of these grains with widths between 10 and 20 nm.

Ellipsometry confirmed this layer thickness for AD-sNiO-400 with a value of 23 nm. For lower annealing temperatures of 325 and 275 °C, respectively, layers are somewhat thicker (26 and 36 nm, respectively), which can be explained by the less complete conversion of $Ni(OH)_2$ into NiO, as water is

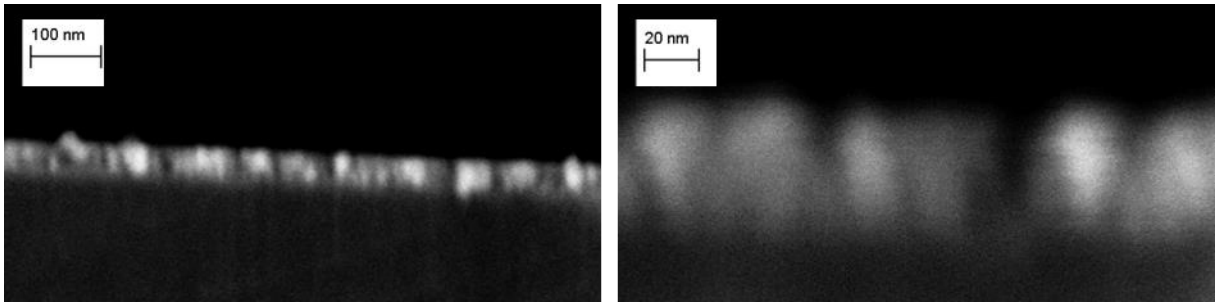

Figure 5.9: Cross-sectional SEM image of an AD-sNiO-400 sample on silicon, taken by Jean-Nicolas Tisserant @ 0.5 kV.

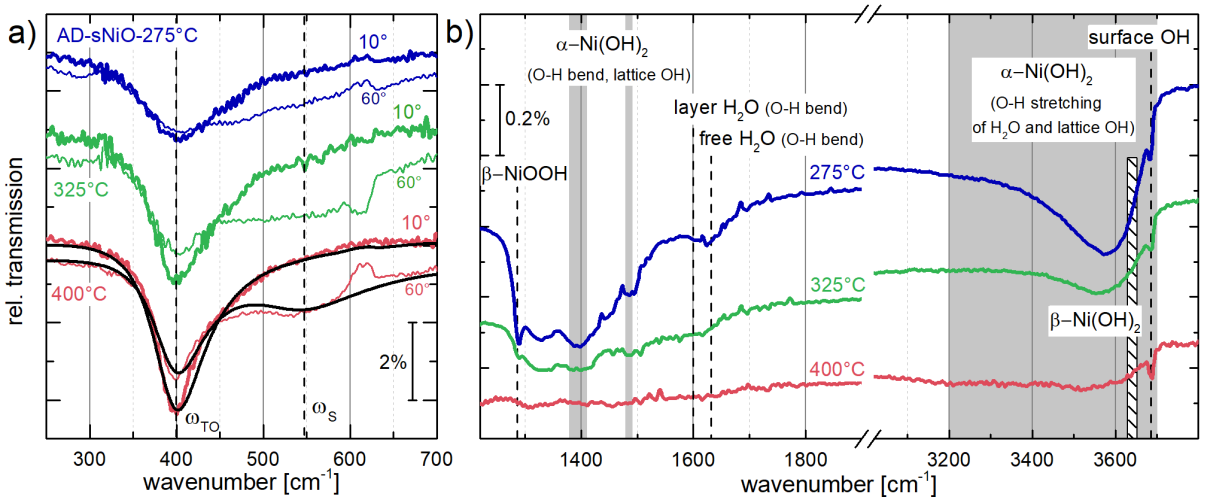

Figure 5.10: (a) FIR and (b) MIR spectra of AD-sNiO samples annealed at 275, 325 and 400 °C, respectively. Indicated mode positions are based on a review by Hall et al. [75]. Measurements were performed by Valentina Rohnacher and Dr. Sabina Hillebrandt.

released during the conversion and the mass density of NiO is larger. For a specific sample no significant inhomogeneity of the thickness could be found with ellipsometry.

Another powerful analytical technique for the investigation of bulk properties, particularly the chemical composition and structural order, is IR absorption spectroscopy. In contrast to XPS, IR spectroscopy probes the complete depth of a sample instead of only the surface region. However, the precision of the instrumentation also allows to resolve changes in the order of magnitude of single atomic layers [184–186]. As explained in Chapter 4.1.2, the absolute spectra were divided by reference spectra of pure i-Si to eliminate modes from the substrate. Thus, all spectra discussed in this work ideally only contain information about the layers of interest, which of course includes the surface region. Considering that about 63 % of the XPS O 1s signal stems from a depth of up to 2 nm (≈ IMFP) and a film thickness of slightly above 20 nm, the overlap of IR and XPS information is not negligible.

Figure 5.10 displays representative IR absorption spectra of sNiO samples, which were annealed at the three temperatures 275, 325 and 400 °C. In contrast to XPS, IR provides the possibility to distinguish between the two different nickel hydroxide species described in Chapter 3.2.3: α-$Ni(OH)_2$, which has water incorporated between the layers, exhibits broad absorption bands between 3200 and 3700 cm^{-1} and several smaller modes between 1300 and 1750 cm^{-1} [75,86]. β-$Ni(OH)_2$, both ordered and disordered, only has one predominant sharp absorption between 3630 and 3650 cm^{-1} due to OH stretching vibrations [75,86]. In this range none of the samples showed a clear feature. However, there are some reports that β-$Ni(OH)_2$ can also exhibit an absorption mode between 3680 and 3690 cm^{-1} [85,94,187,188]. Mostly, this absorption has been related to a mode on grain surfaces, which also explains the higher frequency due to less damping. This surface OH mode is clearly visible in the spectra presented in Figure 5.10b. The intensities are roughly the same for all three temperatures. Unfortunately, as the peak is rather weak and superimposed by the α-$Ni(OH)_2$ signal, a more quantitative analysis for this species is not possible [149]. In the case of α-$Ni(OH)_2$, in contrast, the amount is strongly reduced for higher annealing temperature. This is still true, when the layer thickness is taken into account, which also shows a small temperature dependency.[4] In other words, not only the overall amount of α-$Ni(OH)_2$ in the probed volume decreases, but also the concentration in the films. For 400 °C, also the characteristic shape of the broad α-$Ni(OH)_2$ mode changes.

[4] As IR probes the whole sample depth, the signal intensity of a mode behaves linearly to the layer thickness for a constant film composition. However, here, variations of the thickness are much smaller than the changes of the mode's intensity (see Figure A.5). Therefore, changes of intensity can be ascribed to differences in film composition.

Furthermore, both O-H bending modes of water at about 1600 and 1630 cm^{-1}, respectively, which are clearly visible for 275 °C, are not detectable for 400 °C anymore. As α-$Ni(OH)_2$ inherently has water incorporated in the structure, the term "α-like $Ni(OH)_2$" may be more appropriate in this case. This α-like $Ni(OH)_2$ phase is assumed to be located at the grain boundaries and to consist of randomly oriented sheets of $Ni(OH)_2$ with a larger distance to each other than in β-$Ni(OH)_2$ but with no or little water in-between. The result that sNiO-400 films contain no water seems to be reasonable considering the tendency of α-$Ni(OH)_2$ to dehydrate at elevated temperatures of about 240 to 300°C [79,80,83]. One further mode in the MIR spectra can be identified as β-NiOOH at 1286 cm^{-1} [143,149]. For this mode a qualitatively similar trend as for α-$Ni(OH)_2$ is observed: sNiO-275 features the strongest signal and sNiO-400 the lowest. In the latter case it is below the detection limit.
Modes of carbon-containing species, e.g. C-O or C-H, were registered for some samples, but usually sNiO films were free of such signals when measured in nitrogen atmosphere.

The FIR region (Figure 5.10a) holds information about optical phonons, whose modes strongly depend on the crystalline quality of the sample, e.g., the grain size or the stoichiometry. The most prominent feature in this region is the TO phonon mode around 400 cm^{-1} [189]. Its intensity increases from 2 % for 275 °C to more than 4 % for 400 °C. This increase is accompanied by a narrowing of the mode. Both trends are indicative for a higher structural order. Under an AOI of 60° an additional mode appears between 500 and 600 cm^{-1}. With the help of a fit model, the exact position was determined to be at 547 cm^{-1} [149]. It is known that NiO films exhibit a TO mode in this range which is crucially influenced by the surface structure. Whereas measured values for NiO single crystals are reported to lie between 564 and 586 cm^{-1} [103,158,189], the mode tends to shift to lower values if the surface is imperfect or grainy [190,191]. Therefore, values found for NiO films grown by oxidation of single crystalline Ni films have slightly lower wavenumbers of 544 to 557 cm^{-1}, which agrees very well with the value of 547 cm^{-1} found for the samples of this work. This result again witnesses the order in the samples and in particular in the vicinity of the surface.
Thus, IR spectroscopy confirms the XPS results for the bulk of the samples including the surface region: stoichiometric NiO grains are formed and the crystallinity of the films increases for higher annealing temperatures while both the NiOOH and the α-$Ni(OH)_2$ content, existent in minor phase concentrations, decrease. For 400 °C no free water can be detected anymore.

To estimate the band gap, UVvis measurements were performed. The band gap determined by UVvis absorption is the optical band gap, however, for inorganic materials it is typically close to the electronic band gap due to small binding energies of excitons ("Mott-Wannier excitons") [47]. To increase the absorption, sNiO layers were spin-coated several times, with only a short annealing step between the spin-coating cycles. FTO glass was chosen as transparent substrate rather than ITO as the latter is known to degrade at elevated temperatures [192]. The final layer thicknesses were around 120 nm. The spectra were plotted as Tauc plots (Figure 5.11), where the absorption is written as $(\alpha h\nu)^{1/r}$, with $r = ½$ for direct allowed transitions [193]. α is the measured absorption coefficient. Extrapolation of the linear regime to $y = 0$ results in values of around 3.9 eV for 275 and 325 °C annealing temperature. These results agree very well with

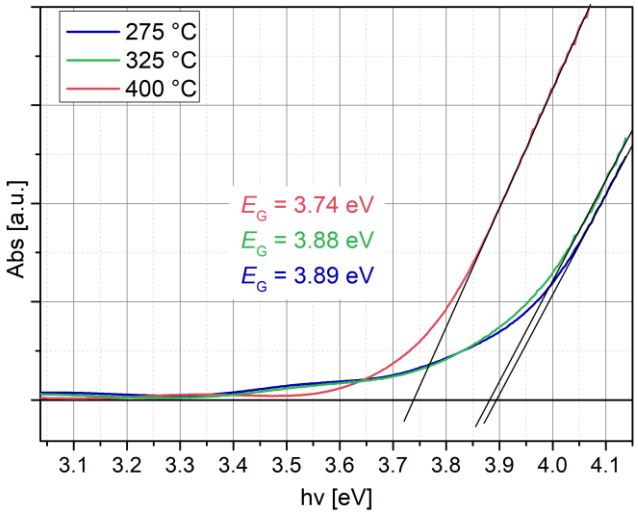

Figure 5.11: UVvis spectra of sNiO samples on FTO substrates. To increase the absorption, layer thicknesses were increased by spin-coating multiple time.

the 3.8 eV measured by Manders et al. for samples prepared with the same precursor recipe and an annealing temperature of 275 °C [23] and also with the values measured by Steirer et al. for annealing temperatures of 250 and 300 °C using a different precursor (3.9 eV) [35]. Ratcliff et al. found an optical band gap of 3.8 eV for films spin-coated from a nickel-formate precursor (T_a = 300 °C) [13].
For 400 °C the band gap lowers to 3.7 eV, which agrees to the band gap of (solution-processed) NiO nanoparticles [31] and is similar to the one found for NiO films deposited by pulsed laser deposition (3.6 eV) [19,109]. Recently, a value of 3.7 eV has also been measured for electron-beam evaporated nickel oxide [110] and 3.6 eV have been found for NiO produced by molecular beam epitaxy [111]. For single crystalline samples even lower values of 3.5 eV were found [53].[5]
These results suggest that more stoichiometric and more crystalline NiO samples exhibit lower band gaps and that hydroxidic components increase it. At least for NiOOH this has already been observed [13,22].

5.2.3. Integration of the results into a common picture

The purpose of this section is to discuss the results presented before and combine them to a coherent picture. The focus is on the localization of the different species.

OH in AD-sNiO-400

With IR spectroscopy, a surface OH mode of β-$Ni(OH)_2$ was detected. If part of the OH is indeed located at the film surface, the O 1s side peak should show an angular dependency when measured with ARXPS, as explained in Chapter 4.1.1. An according measurement is shown in Figure 5.12b. Indeed, an angular dependency is visible: the side peak increases relative to the main peak when the takeoff angle is reduced. One has to conclude that part of the hydroxide is located at the surface. This interpretation is in line with further experiments which showed that most of the hydroxide can be removed by sputtering. The hydroxide signals in the IR and XP spectra may stem from Ni^{2+}-O-H units in which surface OH is singly coordinated to Ni^{2+} sites. For a possible (111) orientation of a NiO grain, such structure is isomorphic to the surface of a β-$Ni(OH)_2$ grain and would explain why in IR spectra, the surface mode of β-$Ni(OH)_2$ is visible, but the bulk mode of β-$Ni(OH)_2$ is not (compare Figure 3.2a and Figure 3.3d). This interpretation may also explain the weak angular dependency of

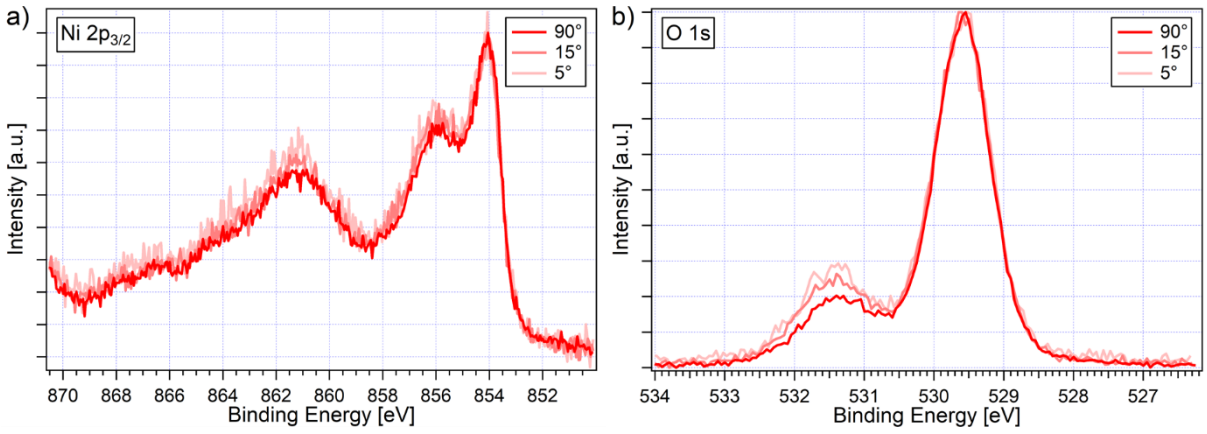

Figure 5.12: Angle-resolved XP spectra of an AD-400 sample, normalized to the main peak. When the take-off angle and thus the surface sensitivity is increased, the ratio of the side peak intensity to the one of the main peak becomes larger. While this is very clear for the O 1s spectra (b), the ratio changes only slightly in the Ni $2p_{3/2}$ region maybe due to the overlap of the surface component with the component due to intersite screening.

[5] Depending on the definition, values based on the data of Powell and Spicer [53] can range from 3.1 to 4.3 eV (see also [58]). 3.5 eV is obtained, when the absorption edge is linearly extrapolated to zero. Thus, this value should be comparable to ones discussed before. The determination of the "real" optical band of single crystalline NiO is highly complex [55–59]: XPS/IPES measurements, e.g., deliver significantly lower values of 3.2 eV (linear extrapolation) [58].

the side peak around 856 eV in the Ni $2p_{3/2}$ region in Figure 5.12a. In any case, it is not surprising to find OH termination for NiO samples which have been exposed to air [61,63,158].
The O 1s spectrum can be used to estimate the amount of hydroxide. For this purpose, two ways exist. The first way is a comparison to literature. Langell et al. stated that for a fully hydroxylated NiO(111) surface (i.e., a coverage of 65 to 85 %) the area ratio between side peak and the main peak (SP-to-MP ratio) lies between 1:4 and 1:2 [103,158]. The SP-to-MP ratio for typical AD-sNiO-400 film of this work, based on two-component Voigt fits, is about 1:3.4 to 1:4.0 and thus would indicate a hydroxylation in the range of one monolayer if all hydroxide is located homogeneously on the surface and is not mostly accumulated at the grain boundaries. As the sample was exposed to air, it seems unlikely that large parts of the surface are not covered with hydroxide [61,89,158]. Therefore, it is concluded that large part of the signal has to stem from a surface hydroxide with a potential minor contribution from the grain boundaries.
A second way is to correlate the integrated intensity signal of the O 1s side peak directly to an atomic surface density. However, in general the correlation factor is unknown. In the course of this work it was possible to estimate this factor, as will be described in Chapter 7.3.1. Thus, an estimation of the atomic surface density of OH groups can be obtained, whereas this estimation gives an upper limit. The real value will be slightly lower. The result in the present case is 24 OH groups per nm^2. This indicates an OH layer thickness of more than a monolayer, since the theoretically calculated surface density of a fully hydroxylated NiO(111) surface is 13 nm^{-2} (based on basic geometric considerations and a lattice constant of 0.418 nm). Thus, using the second method a slightly higher value than with the first method is obtained. However, considering an uncertainty of the correlation factor of at least 15 % and the fact that it rather gives an upper limit, the results of both methods are reconcilable with each other: The OH amount on the film surface is in the range of one monolayer, but certainly below two monolayers. A value which exceeds one monolayer could be caused either by $Ni(OH)_2$ at the surface (which has the double OH areal density than surface OH), or by hydroxide at the grain boundaries.

β -NiOOH in AD-sNiO films

According to IR experiments, the β-NiOOH content of AD-sNiO-275 is almost completely erased by immersion in ethanol. Under the reasonable assumption that ethanol cannot penetrate into the bulk of the film, one has to conclude that the vast majority of β-NiOOH in the 275 °C, and also in the 325 °C sample is located at the surface.

Conclusion

In conclusion, the following results can be recorded. The films consist of a monolayer of NiO grains, whereas order is higher for higher annealing temperatures. Higher annealing temperatures also lead to a reduction in density of both α-$Ni(OH)_2$ and NiOOH. This goes along a reduced work function. NiOOH was found to be located at the surface of samples annealed at 275 and 325 °C, while at an annealing temperature of 400 °C no NiOOH was detected. Here, hydroxide is mostly located at the surface in a thickness of about one monolayer and is mainly surface OH instead of $Ni(OH)_2$. α-like $Ni(OH)_2$ must be predominantly located at the grain boundaries in the sNiO layer. This conclusion is further confirmed in Chapter 5.5.4.

These findings are illustrated in Figure 5.13a for T_a = 275 °C and 400 °C, respectively. Figure 5.13b gives an idea about the atomic structure of a possible surface component. Note that XRD measurements of the films indicate a mixture of different facettes rather than a uniform orientation of grains in agreement with literature on sNiO grown from NiAc solved in ethanol [141].

In the next chapter the influence of OP treatment on these samples will be investigated.

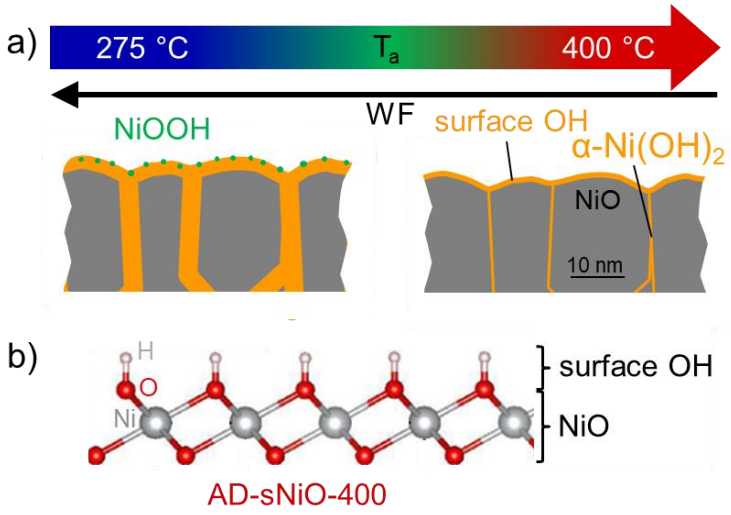

Figure 5.13: (a) Schematic illustration of the structure of sNiO samples. The grey grains indicate stoichiometric NiO and the orange structure is α-$Ni(OH)_2$ and/or surface OH, respectively. Topography and grain sizes are based on experimental data. (b) Illustration of an idealized possible surface facet of an AD-sNiO-400 film. The structure is a fully hydroxylated NiO(111) surface. According to XRD measurements, the grains are not uniformly oriented.

5.3. Impact of oxygen plasma treatment

The first part of this section focusses on the chemical changes which were observed in IR and PE spectroscopy upon OP treatment. IR results are discussed first and then compared to the observations made with XPS. Subsequently, electronic changes are presented and related to chemical changes. Finally, conclusions are validated with I-V measurements.

5.3.1. Chemical changes

IR spectroscopy

Figure 5.14a depicts IR spectra of the three sNiO samples before and after OP treatment. The most striking changes occur in the fingerprint region at 1286 cm^{-1} and in the $Ni(OH)_2$ vibrational modes between 3200 and 3700 cm^{-1}. To enable a more precise evaluation, relative intensity changes of the spectra are shown in Figure 5.14b. Negative peaks (downward) indicate an increase of a mode and the concentration of the corresponding molecular species in the samples. Accordingly, upward peaks indicate a reduction.

Obviously, for the sample annealed at 275 °C, the amount of α-$Ni(OH)_2$ (3000 to 3700 cm^{-1}) is increased upon OP treatment (blue line). For AD-sNiO-325 and -400 no significant changes are observed (green and red lines, respectively). The absorption band at 1286 cm^{-1}, which was attributed to β-NiOOH [143,149], shows an energetic shift for 275 °C, while it increases clearly for 325 and 400 °C. This confirms that NiOOH is formed upon OP treatment of sNiO films, in agreement with earlier propositions by Ratcliff et al. [13]. Although this mode is clearly visible in the spectra of all three samples (Figure 5.14a), a reasonable quantitative comparison of the total β-NiOOH amounts in the treated films is not possible due to superposition with vibrational modes of α-$Ni(OH)_2$, especially in the case of the two lower annealing temperatures. However, it can be stated qualitatively that after OP treatment the amount of β-NiOOH is similar in all films, independent of their annealing temperature and the different compositions before the treatment.

In contrast to oxyhydroxide, the β-$Ni(OH)_2$ surface component (i.e., surface OH at ~3685 cm^{-1}) cannot be detected in any of the OP treated samples: a complete oxidation into β-NiOOH during the OP process stands to reason, according to the Bode diagram (Figure 3.3). However, a closer look at the spectra, especially the one of the AD-400 sample, reveals the formation of an additional mode between 3630 and 3650 cm^{-1} (best seen in Figure 5.14b). As mentioned earlier, this is the wavenumber range which is well known for the characteristic distinct LO and TO modes of β-$Ni(OH)_2$ [75]. It seems like another layer of β-$Ni(OH)_2$ has been formed, presumably below the newly created NiOOH layer as otherwise the surface mode of β-$Ni(OH)_2$ should be visible. Finally, a layer stack in the surface region of AD-sNiO-400 samples similar to NiO/β-$Ni(OH)_2$/β-NiOOH is concluded.

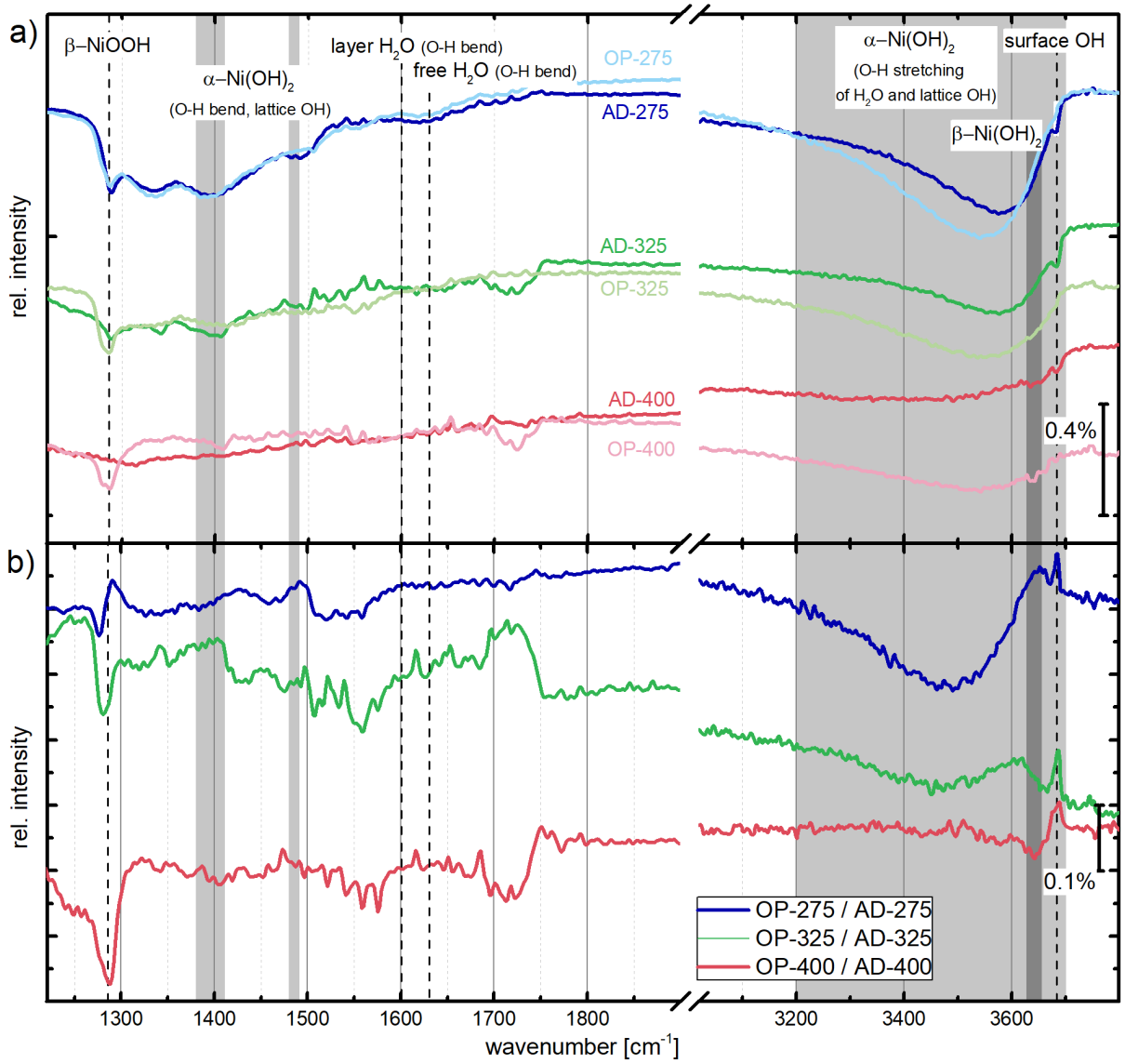

Figure 5.14: (a) IR spectra of sNiO films before and after OP treatment. (b) Relative IR spectra showing the changes induced by the treatment.

PE spectroscopy

Figure 5.15a and b display according core level spectra of the samples with and without OP treatment referenced in binding energy to common values of the main peaks. The most striking change in the Ni $2p_{3/2}$ spectra (Figure 5.15a) is a reduction of the integral intensities for all annealing temperatures. This reduction occurs almost exclusively in the two Ni^{2+} regions (beyond the reduction in the corresponding part of the satellite structure), which conspicuously indicates damping of the NiO signal by an additional surface layer. The formation of an adsorbate layer can be excluded since survey spectra of OP treated samples evidence the absence of any significant contamination (Figure A.6). Furthermore, the conversion of β-$Ni(OH)_2$ into β-NiOOH seen in IR spectra, cannot explain the damping either, as both species have similar IMPFs [50]. Therefore, another reaction has to take place. The only reasonable explanation is that in addition to hydroxide, NiO is also converted. Oxidation of NiO can lead to the formation of $Ni(OH)_2$ and NiOOH, respectively, by the following reactions:

$$NiO + H_2O \rightarrow Ni(OH)_2 \qquad (5.2)$$

and

$$2\ NiO + H_2O + O \rightarrow 2\ NiOOH. \qquad (5.3)$$

Both reactions can explain certain observations. Equation (5.2) describes the increase in the amount of α-$Ni(OH)_2$ as seen by IR spectroscopy during OP treatment of sNiO films annealed at 275 and 325 °C. It also explains the formation of β-$Ni(OH)_2$ seen in the mode between (3630 and 3650 cm^{-1}).
In Equation (5.3) atomic oxygen is supplied during the OP process and water is always present on the AD-sNiO samples at ambient conditions, and even after several minutes in vacuo or nitrogen atmosphere.[6] Based on the standard enthalpies of formation of the species involved, the reaction is exothermic (reaction enthalpy $\Delta_r H^0 < 0$). If the oxygen is ionized instead ($O^+ + e^-$), ΔH_r reaches even lower values. Also reactions of NiO with other oxygen species which are present in oxygen plasma (O^-, O_2, O_2^-, O_2^+, O_3) [137] have negative reaction enthalpies (see Table A.3). Therefore, it is concluded that one or several of these reactions occur during the OP process. This would also explain the filling of the valley between the main and the side peak in the Ni $2p_{3/2}$ spectra (see inset in Figure 5.15a) since – depending on the source and the sample fabrication – NiOOH shows binding energies in this range (see Table A.2 binding energy values). The reaction can furthermore explain the integral intensity reduction of the Ni $2p_{3/2}$ spectra upon OP treatment, as - similarly to $Ni(OH)_2$ - the Ni ion density of NiOOH is about a factor of two smaller than the one of NiO, while the inelastic mean free path and thus the information depth is the same [50].
Moreover, the formation of NiOOH is supported by the shape of the multiplet satellite structure around 862 eV. Upon OP the rather sharp and narrow peaks of AD samples loose intensity and flatten to some extent. Structures on the left shoulder in the range of 861.5 to 869 eV are reduced such that this range becomes more linear. Similar differences were observed by Grosvenor et al. [153] and Payne et al. [154] between spectra of NiO and NiOOH reference samples (Figure 5.15c,e). The satellite structure of $Ni(OH)_2$, in contrast, is quite pronounced (Figure 5.15d) and differs strongly from the corresponding peaks of the OP samples.
Also, the changes of the LMM Auger lines (Figure 5.16) are compatible with the interpretation of generation of NiOOH. According to literature the LMM line of NiO contains two main contributions at around 638 and 644 eV with similar intensities [101,194]. Both are also present in spectra of the AD samples, most clearly for 400 °C in agreement with the previous findings. Upon OP treatment the lower BE feature decreases while the higher BE contribution stays almost unchanged. Thus, the spectra approximate the shape of a LMM line of NiOOH which has only one dominant contribution at a BE of ~643 eV [13,194]. Additionally, the Auger lines give a hint about the type of NiOOH which

[6] Personal communication with Valentina Rohnacher.

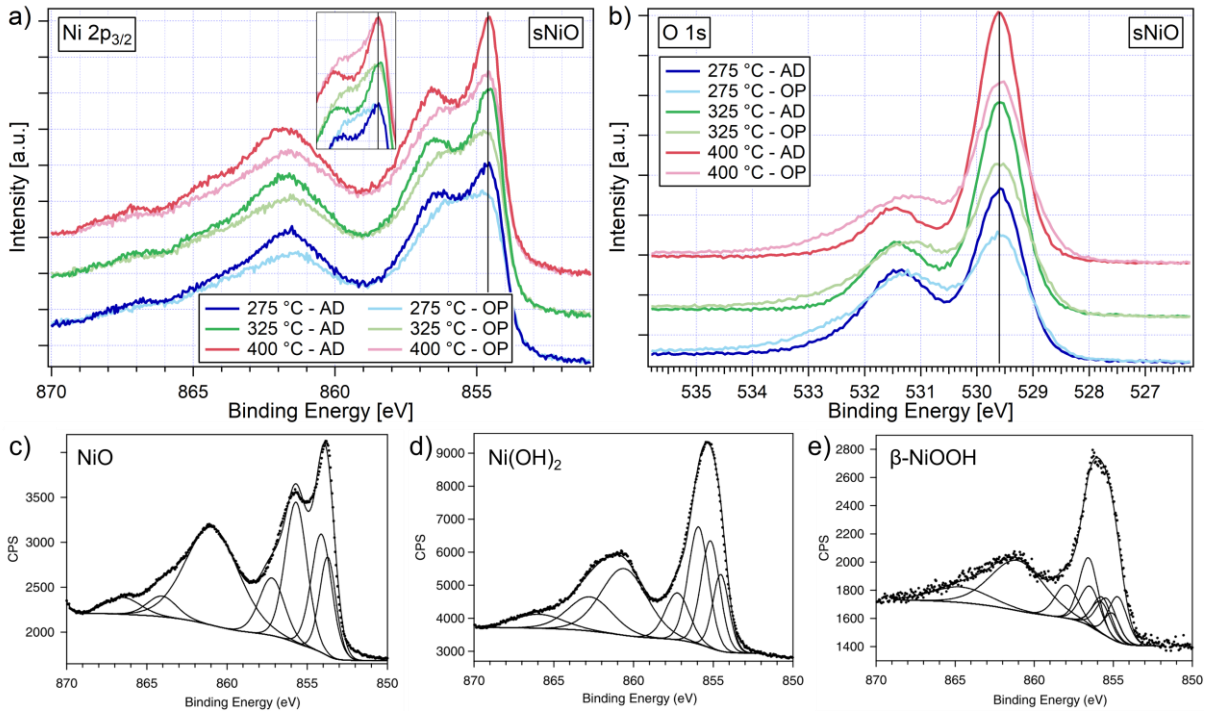

Figure 5.15: (a) and (b) XPS detail spectra of the films before and after OP treatment, referenced in binding energy to 854.7 eV [50] and to 529.6 eV eV [13], respectively, to provide better comparability of the chemical changes upon OP treatment. The inset in (a) shows the peak regions of normalized spectra. (c) to (e) Reference spectra reprinted from literature [153]. Only the spectrum of β-NiOOH in (e) has an almost linear trend in the region between 860 and 870 eV.

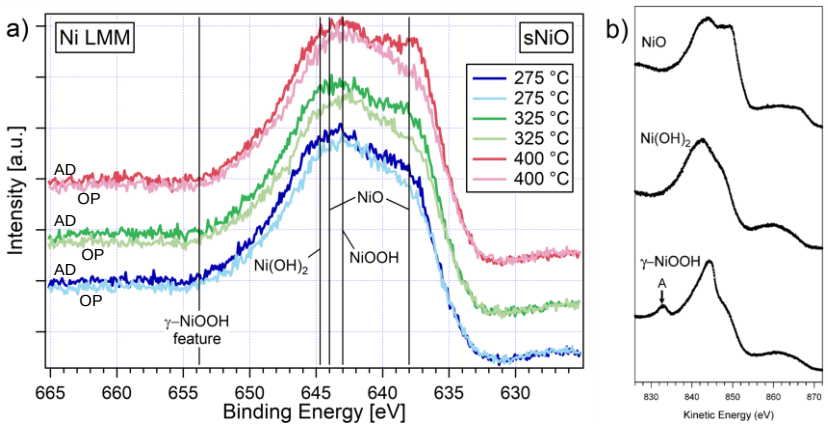

Figure 5.16: LMM Auger spectra of AD- and OP-sNiO films (a) and of reference samples from literature (b), reprinted from [194]. The peak positions from (b) are indicated in (a).

is created: according to Biesinger et al. the γ-NiOOH LMM line contains a characteristic peak at 653.8 eV, corresponding to a kinetic energy of 832.8 eV [194]. This feature does not appear in the spectra presented here, which is consistent with the assumption that β-NiOOH is prevailing and not γ-NiOOH. Admittedly, the shape of the spectra after OP treatment are still much closer to the NiO reference than to the NiOOH reference, which might be explained by the small amount of NiOOH created. Furthermore, spectra rather resemble the $Ni(OH)_2$ reference, which is not surprising considering that in all three cases $Ni(OH)_2$ is formed, for 275 °C rather α- and for 400 °C rather β-$Ni(OH)_2$. Thus, spectra after OP treatment show a superposition of these signals.

A similar reduction as for the Ni $2p_{3/2}$ region is observed in the O 1s spectra for the O^{2-} peak (Figure 5.15b). This again supports the formation of additional OH or OOH which is created during the OP treatment close to the surface, according to Equation (5.2) and/or (5.3). At higher binding energies, adjacent to the side peak of all AD samples, two regions exist where the intensity increases. To exclude the influence of the broadened O^{2-} peak after OP treatment on this observation, the respective O^{2-} peaks were subtracted from the O 1s spectra before and after OP treatment in Figure 5.17b (exemplarily for the sample annealed at 400 °C). Then, the difference between these two adjusted spectra was calculated in Figure 5.17c. This difference spectrum still shows two distinct features, similar to spectra of NiOOH reference samples (see Figure 5.17d,e) with a distance of about 1.5 eV. These features are evidently caused by the species which is obviously formed by oxygen plasma, namely NiOOH. In literature, however, NiOOH in composite films is always considered with only one peak [13,17,31,36,165,177,195–197] and the spectra are usually explained by four contributions: O^{2-} from NiO, OH^- from $Ni(OH)_2$, oxygen from NiOOH, and oxygen from water [13,17].

To test the hypothesis that NiOOH actually has to be taken into account with two components, a five-component fit was used instead of a conventional four-component fit. The fits are displayed in Figure 5.18. For three of the fit components little doubt concerning the assignment exists: the main component located at 529.6 eV refers to O^{2-}, the middle component located at 531.5 eV belongs to

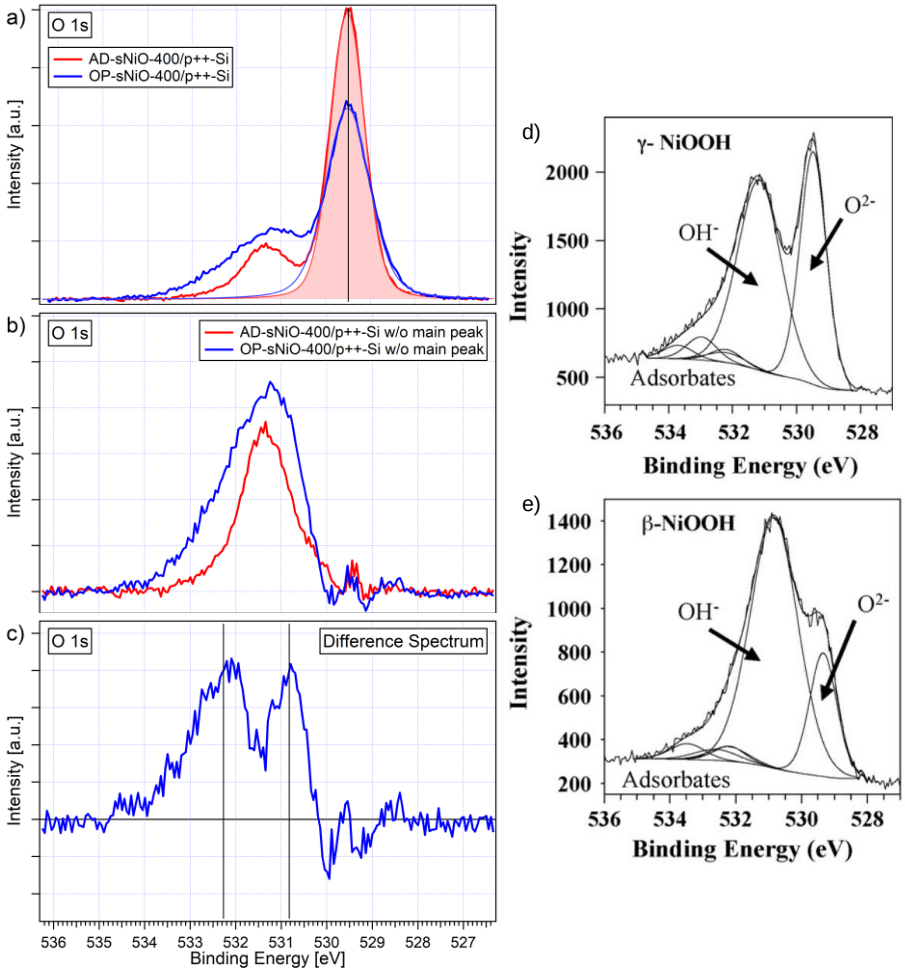

Figure 5.17: O 1s core level spectra of an sNiO-400 sample before and after OP treatment. Spectra in (a) were referenced in binding energy to the indicated position. The main peaks were fitted with Voigt functions. To enable a direct comparison, the fitted main peaks were subtracted from the respective spectra (b). The difference spectrum of these two adjusted spectra is displayed in (c). The shape exhibits two characteristic features and reminds on spectra of NiOOH reference samples (d and e), reprinted from [154].

hydroxide species (α-, β- and surface hydroxide) and the component located at the highest binding energy of 533 - 534 eV is caused by water (see Table A.1 for BE values from literature). The two remaining peaks are located in the regions with the increased intensity after OP treatment. As described earlier, OP treatment of sNiO-400 increases only the IR mode of β-NiOOH and β-$Ni(OH)_2$. Since β-$Ni(OH)_2$ contributes to the middle component, it is reasonable to attribute the two peaks to β-NiOOH. This assignment is furthermore supported by the following arguments. According to Tkalych, the most stable configuration of β-NiOOH contains two inherently different oxygen species, namely O^{2-} and OH^-, as was explained in Chapter 3.2.3. It is plausible to relate the O^{2-} component to the peak at 530.9 eV, and the OH^- component to the peak at higher binding energies around 532.4 eV. The assignment is supported by the study of Payne et al. [154] in which polycrystalline NiOOH powders were investigated by XPS. These spectra showed two main features with a distance of 1.5 - 1.7 eV (see Figure 5.17d,e), which is in line with other studies on NiOOH reference samples (see Table A.1) and in agreement with the value found here.

However, in the spectra of the current work it is prominent that the proposed O^{2-} component of NiOOH has a higher binding energy compared to O^{2-} in NiO. A possible explanation is trivalent character of adjacent nickel ions in NiOOH instead of the bivalent nickel ions in stoichiometric NiO. The shift of the OH^- component compared to hydroxide in $Ni(OH)_2$ may be explained similarly. However, also compared to the reference spectra the binding energies are shifted toward higher values. This might be related to the calibration of the reference spectra or surface or structural effects at the present samples, but a clear conclusive explanation was not found.

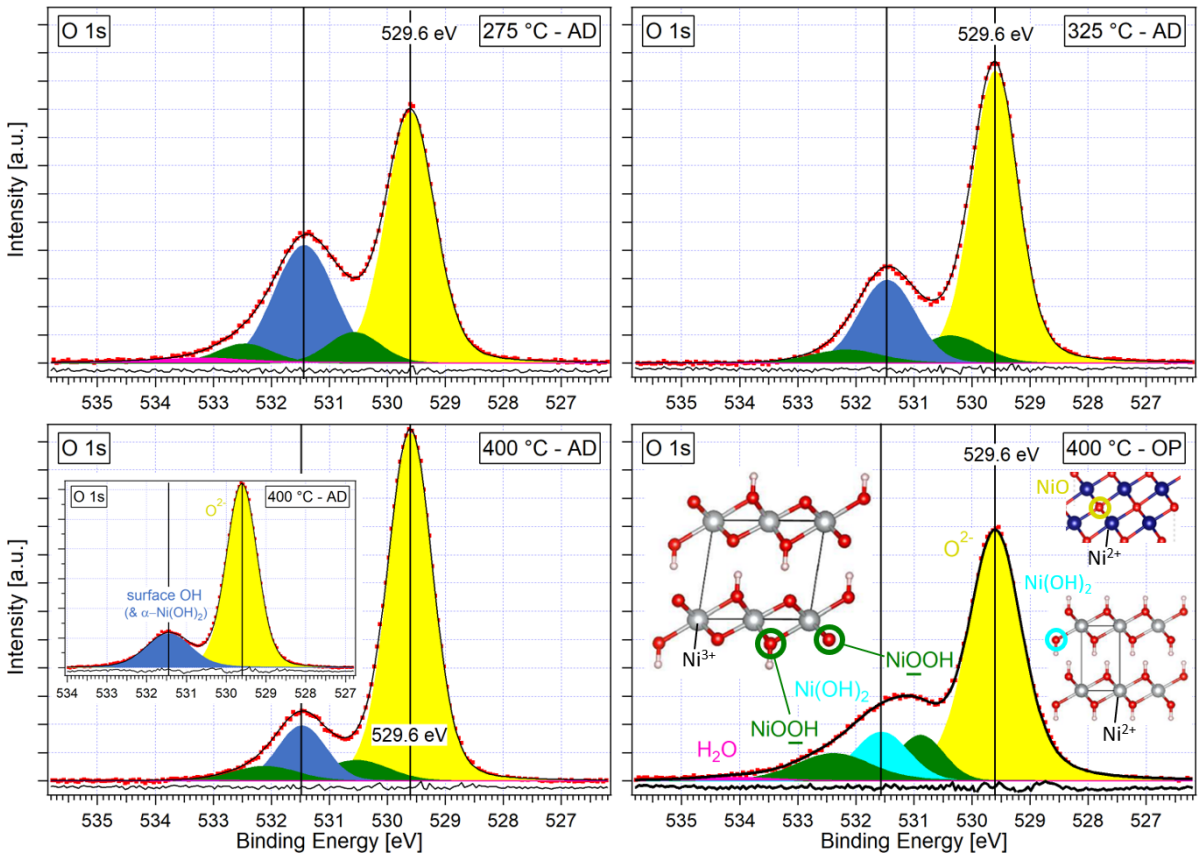

Figure 5.18: Five-component fits of O 1s detail spectra of AD samples and OP-sNiO-400 which consider the two different oxygen species of NiOOH in green (O^{2-} and OH^-). While the trends based on the fit components qualitatively agree with the results from IR spectroscopy, the inset demonstrates the limited reliability of these five-component fits: for the fitting of the AD-sNiO-400 spectrum, already two components are sufficient to describe the data quite well. The insets in the lower right diagram illustrate the structure of the different components. All spectra are referenced via the main peaks to 529.6 eV as indicated by the black lines. The additional lines at about 531.5 eV are located at the positions of the hydroxide components and show a variation in the range of only 100 meV.

Additionally, a further species, namely adsorbed superoxide (O_2^-) could, in general, contribute to the component at 532.4 eV as O_2^- was claimed to exhibit binding exergies in this range [198–200]. O_2^- is an instable and reactive species, best known from oxygen photoadsorption experiments on TiO_2 [201], where it was found to be stable only below ~150 K. Also on silver superoxide has been proven but is only stable until 200 K [198,199]. Therefore, it cannot exist in the present case at room temperature in the dark and after contact to ambient air, especially when consideration that O_2^- has never been evidenced on NiO films at all. Furthermore, the presence of organics leads to the reactive removal of superoxide [201]. As in Chapter 6.4 an OP treated sNiO film is evaporated with an organic molecule and the O 1s spectrum does not change significantly (see Figure A.18), the presence of O_2^- in OP treated sNiO films can be excluded. A final evidence may be obtained by combined experiments with electron paramagnetic resonance, electron energy loss spectroscopy or surface-enhanced Raman spectroscopy.

Regarding the five-component fit, it should be mentioned that the risk of overfitting exists due to the high number of components. Therefore, the results do not necessarily have to reflect physical reality. This can be seen in the fit of the AD-sNiO-400 sample in Figure 5.18 were the XPS fit shows a certain amount of NiOOH, while IR data confirms the total absence of NiOOH for such samples. And indeed, the very same spectrum can be fitted quite well with only two components (O^{2-} and hydroxide) and thus without the two NiOOH components. The example demonstrates that the fit results are not solid enough for the calculation of reliable ratios between the different oxide and hydroxide species. This is also due to the inhomogeneous distribution of the species within the films. As they are partially stacked on top of each other, damping of deeper lying species would distort the calculated ratio. Finally, the uncertainty of this fitting is also manifested in the peak positions, which exhibit some variability from fit to fit. These considerations underline the limited reliability of the five-component fits and demonstrates that it can be potentially misleading.
Nevertheless, the fits provide a semiquantitative insight: for AD samples the NiOOH amount is the lowest for T_a = 400 °C, $Ni(OH)_2$ decreases with increasing T_a while the NiO signal is growing, and, upon application of OP, NiOOH is formed. This result corresponds to the conclusions drawn from the IR spectra.

Furthermore, the fit components of the main peaks can be used to roughly estimate the layer thickness of additionally created OH and OOH species. Again, due to the similarity of the IMFPs, a transformation of $Ni(OH)_2$ into NiOOH is not considered in this approach. In the present case for the sNiO-400 sample the intensity is reduced from 12600 to 11500 counts. With the TPP-2M formula for the O 1s main peak an IMFP of electrons in $Ni(OH)_2$ or NiOOH of 2.2 nm was calculated. Using Equation (4.5) a value of 0.2 nm is obtained. This is even smaller than the lattice constants of $Ni(OH)_2$ and NiOOH in c-direction (0.46 and 0.48 nm, respectively, see Chapter 3.2.1). Of course, the validity of this estimation for such thin layers is discussable, but it definitively shows that the amount of additionally created hydroxide is small and not in the multilayer range.

A further interesting quantity which can be extracted from the data is the O:Ni ratio based on the integrated intensity of O 1s and Ni $2p_{3/2}$ spectra (see Chapter 5.6.2 for details). All values, including the ones extracted for the AD samples, are summarized in Table 5.1.

Table 5.1: O:Ni atomic ratios for all six differently prepared sNiO samples.

	AD	OP	Relativ change [%]
275 °C	1.50	1.67	11
325 °C	1.26	1.46	16
400 °C	1.20	1.46	22

For AD samples a decrease of the oxygen content with increasing annealing temperature is observed, which was explained by the smaller content of $Ni(OH)_2$ and NiOOH. For all annealing temperatures

the oxygen content increases due to the formation of NiOOH and $Ni(OH)_2$ upon OP treatment. This change is the largest for 400 °C in agreement with IR and XP spectra. After the OP treatment, the sNiO-275 sample shows the highest O:Ni ratio. This seems reasonable as the NiOOH layer on the surface is expected to be thinner than the information depth of XPS. Thus, also the unaffected phase beneath the NiOOH, which contains significantly more hydroxide as sNiO annealed at higher temperatures, contributes to the XPS signal.

Finally, also for the OP samples ARXPS measurements were performed and displayed in Figure 5.19. Similar to AD samples, the angular dependency of the Ni $2p_{3/2}$ spectra is still rather weak after OP treatment, but existent (Figure 5.19a). Contrastingly, the angular dependency of the O 1s features (Figure 5.19b) is largely enhanced. This is another evidence that OP treatment has an impact on the surface region. Interestingly, now also the binding energy ranges which were related to NiOOH show an angular dependency. However, still the strongest angular dependency is in the region in between, which is not in agreement with the expectations for a perfect NiOOH layer on the surface. Figure 5.19c and d show the same spectra without normalization for a better comparison of the OP influence on the samples for the different takeoff angles. In Figure 5.19d, for the spectra taken at 20° the intensity reduction due to the smaller takeoff angle is corrected. Here, a slightly stronger increase in the NiOOH regions is visible, which is, however, still weakly pronounced. This may be related to the small thickness of NiOOH or the additional $Ni(OH)_2$ appearing in the IR spectra upon OP treatment. Nevertheless, the data clearly shows that OP treatment alters the very surface of sNiO films. This agrees to the observation that the O^{2-} component in the O 1s spectra is only damped and does not disappear completely as well as to observations in literature [107].

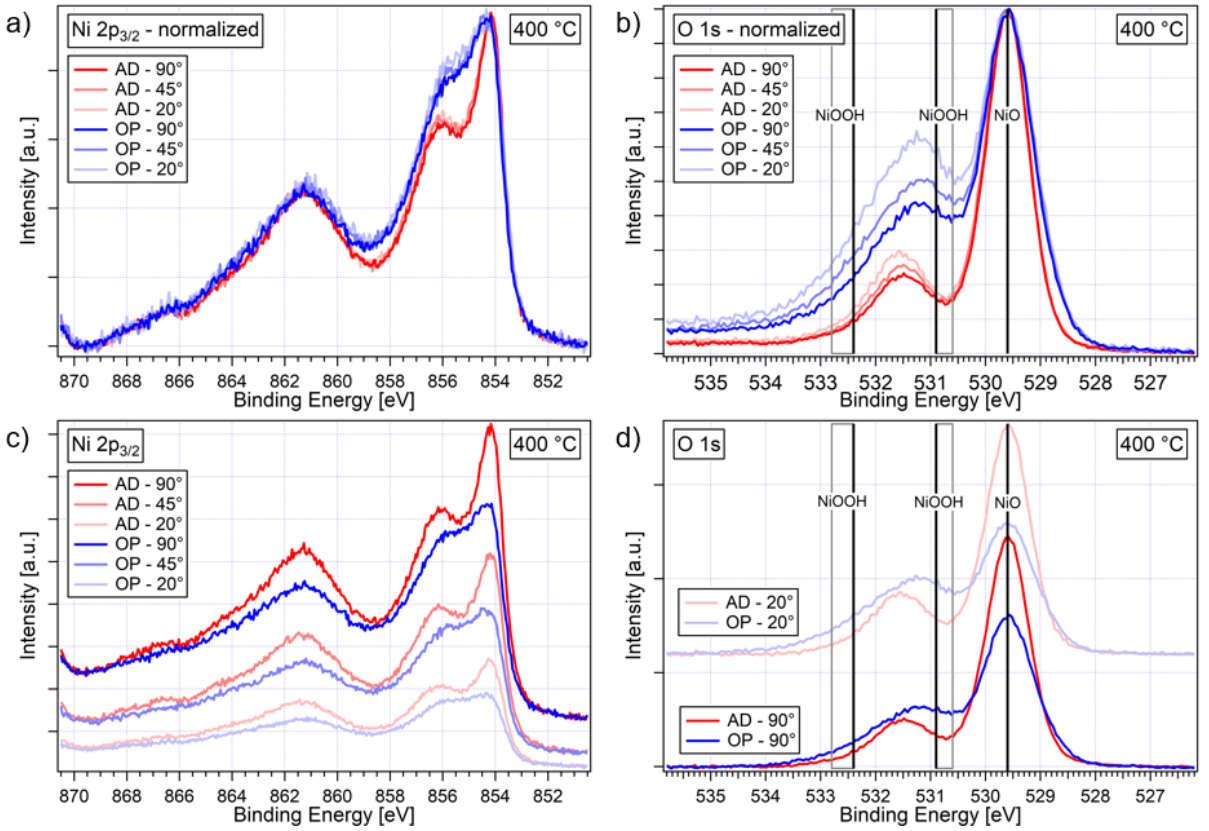

Figure 5.19: ARXPS measurements of an sNiO-400 sample before and after OP treatment. (a) and (c) show the Ni $2p_{3/2}$ region, (b) and (d) the O 1s region. The spectra in (a) and (b) are normalized in intensity, spectra (c) and (d) are without normalization, whereas the spectra in (d) taken at 20° are corrected for the intensity reduction due to the smaller takeoff angle. All spectra of the OP treated sample are corrected in binding energy w.r.t. the one without treatment.

Excursus: Literature examples for inconsistencies when using only one NiOOH component

As mentioned before, the O 1s peak of NiO_x samples nowadays is typically fitted with four components (O^{2-}, OH, OOH and H_2O), which, however, can lead to inherent contradiction, or at least certain peculiarities. Most of these papers justify this step by the work of Ratcliff et al. [13]. But even this work exhibits inconsistencies in the OP treated spectra: all components exhibit clear shifts in different directions, compared to their position in untreated samples (Figure A.7a). For a solution-processed and OP treated sample, this leads to a very large distance of 2.5 eV between the O^{2-} component and the one which is attributed to OOH. For a homemade γ-NiOOH reference the distance is even larger (2.9 eV). A comparison to values which were determined for NiOOH reference samples unveils significantly smaller values of 1.5 to 1.7 eV (see Table A.1). This discrepancy is not discussed or explained and shows that this approach is too simple and the NiOOH reference doubtful.

A very similar example can be found in a recent RCS publication by Kim et al. [18], in which the authors wanted to point out the difference induced by annealing NiO nanoparticles in air instead of in nitrogen (Figure A.7b). Although the spectra look very similar, simply an additional peak which accounts for NiOOH is added to the fit (actually to both core levels). This of course shifts the component attributed to OH to lower binding energy values. The "appearance" of the NiOOH component is seen as prove for a larger NiOOH content of the air annealed samples and their better performance. Similar to Ratcliff et al. this procedure leads to a huge O^{2-}-to-OOH distance of 2.6 eV. Further examples of the same kind are found in [17] (2.3 - 2.4 eV). When only three components are used (because water is neglected), the distance is often even larger: 3 eV [31,36,197], 3.1 [165] and 3.7 eV [196].

Finally, the results of the different fits in literature show a great variability regarding the NiOOH peak position. In some examples like the one just mentioned it is located around 856 - 857 eV at the highest BE end of the feature [31,195], whereas in other publications it rather is located around 855 eV as the middle peak of the three fit components [164].

For these reasons the consideration of NiOOH with a single fit component in the O 1s spectrum does not seem to be appropriate.

Summary of the chemical changes of sNiO films upon OP treatment

IR spectroscopy showed that OP leads to an increased amount of α-$Ni(OH)_2$ in films annealed at a lower temperatures. Additionally, β-$Ni(OH)_2$ at the surface is turned into a NiOOH-like phase, which is similar to β-NiOOH. This process is more pronounced for samples annealed at higher temperatures and thus with a lower NiOOH content before the treatment. After the treatment all samples exhibit similar amounts of NiOOH, which is in the range of a monolayer.

For 400 °C, some bulk-β-$Ni(OH)_2$ is formed, presumably beneath the surface NiOOH layer, through reaction of NiO. Furthermore, a reaction of NiO to NiOOH is possible. Finally, there are hints that the surface component of β-$Ni(OH)_2$ (which is only present in the AD samples) actually has the same IR signature as OH groups on the surface of NiO. The topography of the films is not noticeably changed upon OP treatment, as AFM measurements show (Figure A.1b).

Based on these results, for 400 °C an idealized visualization of the surface structure before and after OP treatment was conceived. As shown in **Fehler! Verweisquelle konnte nicht gefunden werden.**a, t he first layer of OH-terminated nickel is converted into a layer of NiOOH. Underneath, a layer (or semi-layer) of β-$Ni(OH)_2$ is formed. The concluded layer stack is able to explain large parts of the recorded data, which is summarized in **Fehler! Verweisquelle konnte nicht gefunden werden.**b. The m odel of the atomic structure is hypothetical but gives an idea of how the layer stack could be composed. It does not consider the influence of grain boundaries nor structural defects, which have to be present - not at least due to the curvature of the grains.

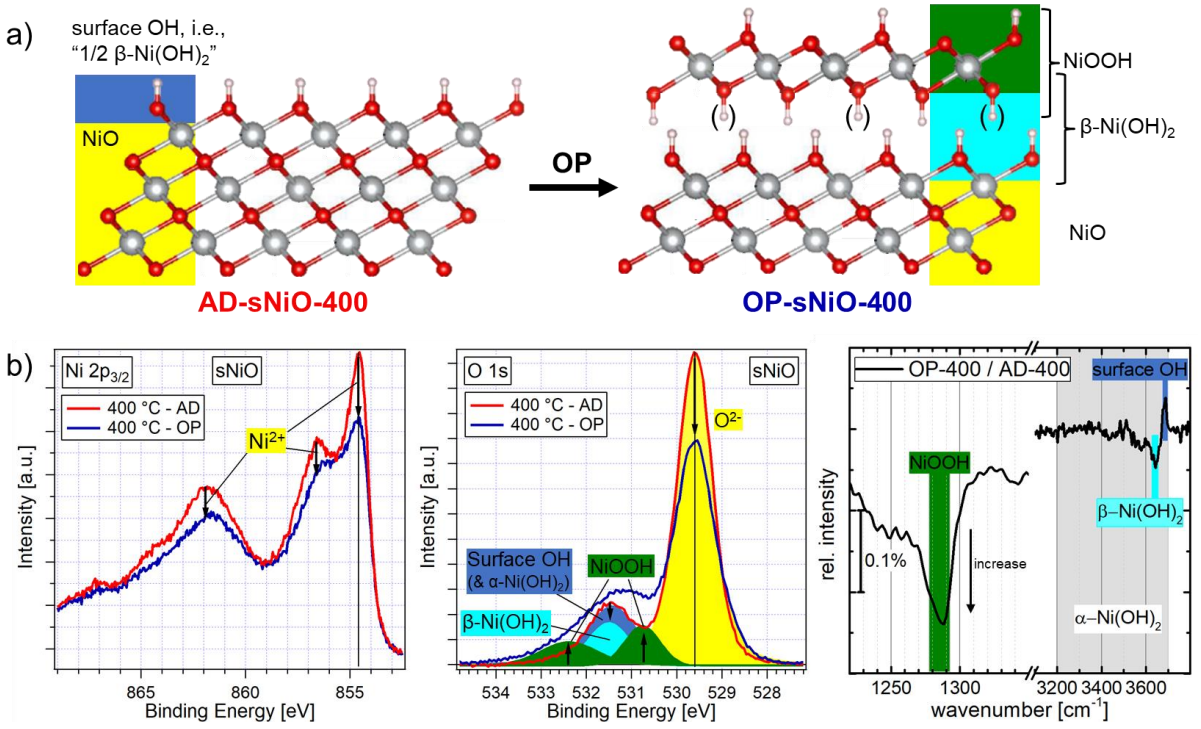

Figure 5.20: (a) Hypothetical surface structure of an sNiO-400 film before and after OP treatment for a surface oriented in (111) direction to visualize the conclusions based on XP and IR spectroscopy measurements, which are summarized in (b). If the second layer of OH rather is NiOOH- or $Ni(OH)_2$-type (i.e., if the hydrogen atoms in brackets are present or not) is unclear.

5.3.2. Electronic changes and correlation to chemical properties

In this section the electronic changes induced by OP exposure are presented. Figure A.8 shows representative valence band and secondary electron cutoff regions of the three different types of samples before and after the treatment. Both features were linearly extrapolated, and the valence band maxima as well as the work functions were extracted as describes in Chapter 4.1.1. For each type of sample, three to five samples were measured. The respective values were averaged and displayed in Figure 5.21a. While for AD samples slight but significant differences between the temperatures exist, the VBM values coincide within uncertainty after OP treatment. In all cases the VBM is shifted toward the Fermi level.

The work function of AD samples ranges from 4.4 to 4.9 eV and decreases with increasing T_a. As this correlates with the concentration of hydroxidic species ($Ni(OH)_2$ and NiOOH), it is concluded that the hydroxidic species increase the WF, while a higher content of stoichiometric NiO leads to lower WF values.

Upon OP treatment, the WF strongly increases. While Shim et al. [202] have previously attributed this increase in work function to the removal of carbon contamination, this can be excluded in the present case as XPS data shows the carbon contamination to be minimal (Figure A.3). Instead, the strong increase of NiOOH species upon OP treatment appears to be the main factor. This conclusion is further supported by the fact that the effect is more pronounced for higher annealing temperatures, where also the increase of NiOOH is larger. Interestingly, a common work function of about 5.5 to 5.6 eV is measured for all OP samples, independent of the initial work function (Figure 5.21a). These values agree with the results of Steirer et al. In this work, the authors investigated the influence of OP treatment duration on the work function of sNiO-250 and observed a saturation in the range of 5.6 to 5.7 eV [21].

The observed work function changes upon OP treatment ΔWF can be divided into two contributions: a change of the Fermi level ΔE_{VBM} at the surface relative to the band edges and a change of the surface dipole $\Delta\delta$. This is expressed by the following formula[7]:

$$\Delta WF = \Delta E_{\mathrm{VBM}} + \Delta\delta. \tag{5.1}$$

ΔWF and ΔE_{VBM} were determined based on the measurements and the difference is attributed to a change of the surface dipole. As indicated in Figure 5.21a, ΔE_{VBM} is in the range of 0.15 to 0.30 eV (positive values indicate a shift of the valence band toward the Fermi level). $\Delta\delta$ starts with 0.5 eV in the case of sNiO-275 and increases to almost 1 eV in the case of sNiO-400.

This saturation of the valence band maximum and of the work function upon OP treatment is ascribed to the formation of the NiOOH layer, which pins the Fermi level. Additionally, it is exerting a surface dipole, which should be comparable for all three temperatures, since all of them show similar amounts of NiOOH. The different changes of the surface dipole lead to the conclusion that AD samples with lower annealing temperatures already had larger surface dipoles prior to OP treatment, which are removed and reestablished or simply increased during OP treatment. The size of the surface dipoles of AD samples is ascribed to the higher NiOOH content of samples annealed at lower temperatures.

These results and considerations are summarized in schematic band diagrams of the surface regions in Figure 5.21b and c. Two assumptions were made: first, the absence of a surface dipole for the AD-400 sample and second, the hypothesis that the surface dipoles after OP treatment are similar in magnitude for all annealing temperatures, based on the conclusion of chemically similar surface layers after OP treatment. The Roman numerals show the order of calculation. Potential band bending in the sNiO film or the substrate is not considered. It will be discussed in Chapter 5.4.

[7] Note that this formula is only valid as long as the valence bands stem from the same orbital before and after treatment, in which case VBM follows the Fermi level. This is given in the present case, see Figure A.9 for details.

Additionally, surface dipoles based on another assumption are indicated in green. Here, instead of assuming the absence of a surface dipole for the AD-sNiO-400 sample, a modified AD-sNiO-400 film with significantly reduced surface OH was used as reference for a surface dipole of zero. Thus, an offset of -0.6 eV is added. The sample was obtained by heating an AD-sNiO-400 film in UHV. Details will be shown in Chapter 5.5.4.

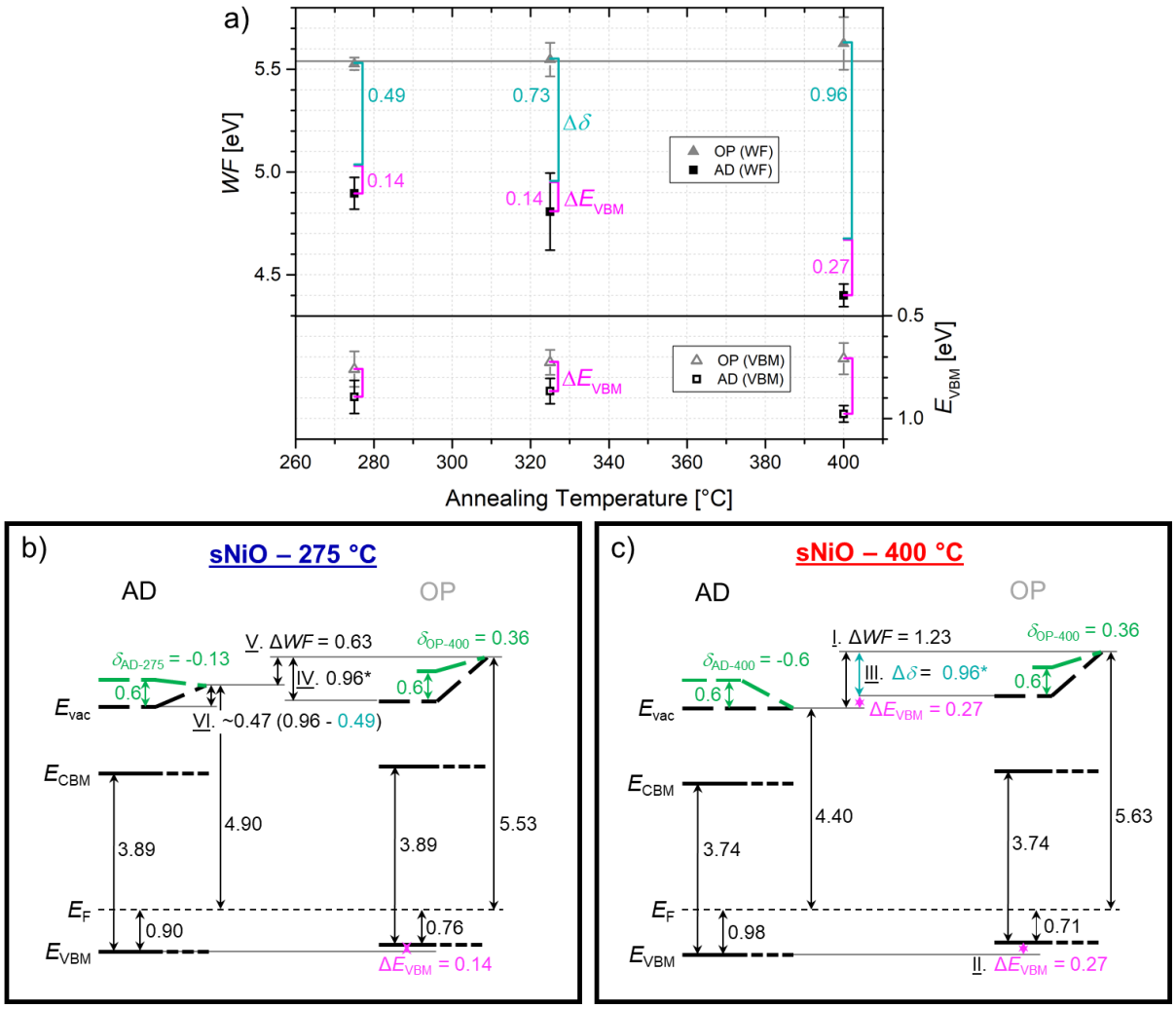

Figure 5.21: (a) Work functions (filled symbols) and valence band maxima (open symbols) of AD- and OP-sNiO for the three annealing temperatures. While the work function for AD-sNiO decreases with increasing annealing temperature, it saturates at a value of about 5.5 to 5.6 eV for OP treated samples. The purple and light-blue bars illustrate the changes of the VBM at the surface (ΔE_{VBM}) and the surface dipole ($\Delta\delta$) upon OP treatment. The data is averaged over several measurements, the values are given in Table A.4. Representative spectra are shown in Figure A.8. (b,c) Schematic band diagrams of the surface regions of average AD and OP samples annealed at 275 and 400 °C, respectively, based on the values depicted in (a). The surface dipoles are drawn under the (somewhat arbitrary) assumption that the surface dipole of AD-sNiO-400 films is zero. Therefore, the absolute value of the dipole of OP-sNiO-400 samples is equal to the measured change of the dipole upon OP treatment $\Delta\delta$ = 0.96 eV. Based on the reasonable assumption that the surface dipoles are similar for all three temperatures due to the chemically similar surfaces, the same value was used for the diagram of OP-sNiO-275 samples (indicated with *). By subtracting the measured change of the dipole $\Delta\delta$ = 0.49 eV, the estimated surface dipole prior to the OP treatment was obtained. The Roman numerals show the order of calculation. Additionally, alternative dipoles are given in green based on a different assumption. As will be shown in Chapter 5.5.4, the surface dipole of an AD-sNiO-400 sample increases by ~0.6 eV when heated to 400 °C in vacuo. During this process the film looses large parts of the surface hydroxides. The green surface dipoles are drawn under the assumption that these OH-reduced sNiO films have a surface dipole of zero. Finally, the optical band gaps from Chapter 5.2.2 are indicated.

5.3.3. Plausibility check by I-V measurements

NiOOH is known to have a much higher conductivity than $Ni(OH)_2$ and NiO [75,203–205]. Therefore, according to given interpretation of data, the resistivity of the surface should be reduced after OP application and reach similar values for all OP samples. To test this, sNiO films were spin-coated on glass substrates and gold contacts with a thickness of 50 nm were evaporated on top of the films. Lateral I-V measurements were performed in inert nitrogen atmosphere at RT, before and after OP treatment of these samples. The extracted resistances for channels with a length of 70 µm are shown in Figure 5.22. Among the AD samples, sNiO-275 has the lowest value. The values of films annealed at 325 and 400 °C are approximately one order of magnitude larger. Upon OP treatment there is a slight decrease in the resistance of the film annealed at 275 °C, and a drastic reduction of about one order of magnitude for films annealed at 325 and 400 °C. The final absolute values are similar for all three temperatures (see Table A.5 for details). As OP treatment was performed after the deposition of the gold contacts, we assume no significant changes of the contact resistance during the oxidation process. Therefore, the changes in overall resistances are attributed to changes in the channel resistances. These observations agree with the previous findings: in the case of AD-sNiO-275, where NiOOH is already present in the films, the channel resistance is low and is only slightly increased upon OP treatment. AD-sNiO-400, in contrast, is free of NiOOH and has a high resistance. Upon OP treatment a large amount of NiOOH is produced and the resistance drops. Finally, OP treatment results in a similar amount of NiOOH for all T_a, which is also reflected in similar resistances. Note that the reduction of channel resistance may also be (partially) related to the change of the Fermi level by NiOOH formation and thus an increase in charge carrier density. These results support the suggested model, that for all three annealing temperatures similar conductive NiOOH surface layers are formed on polycrystalline sNiO upon OP treatment.

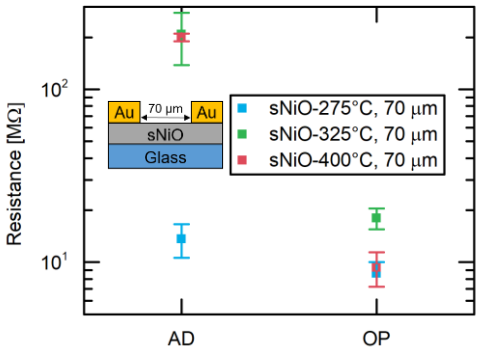

Figure 5.22: Total resistance of sNiO films before and after OP treatment for all three annealing temperatures extracted from I-V measurements with a channel length of 70 µm. Exact values are given in Table A.5.

5.4. Further influences

In this chapter, several further influences of processing parameters and conditions are presented and discussed in order to complete the picture drawn in previous chapters and to give practical advice on which result may or may not be obtained by varying a certain fabrication step. The first section focusses on the impact of the substrate and describes how measurement values are influenced. In this regard also band bending and photovoltage will play a major role.

5.4.1. The influence of the substrate's doping level on sNiO film properties

To estimate the influence of the substrate on sNiO films, differently doped silicon with native oxide was used. Figure 5.23 displays the O 1s binding energies and work functions of AD- and OP-sNiO-400 films as a function of the doping level of the silicon substrate. The comparison was carried out between slightly n-doped silicon (n-Si), which was used by default, and strongly doped (degenerate) p-type silicon (p^{++}-Si, see Table 4.1 for details). Obviously, there is a statistically significant impact: the Fermi level in sNiO on p^{++}-Si is elevated by about 150 meV, although the difference in the work functions of the silicon substrates was barely significant (WF(p^{++}-Si) = (4.20±0.08) eV vs. WF(n-Si) = (4.15±0.03) eV)[8]. After OP treatment the tendency is still visible, although less pronounced, which confirms the already discussed pinning-character of NiOOH. Work functions after OP treatment even coincide within the mutual error bars.

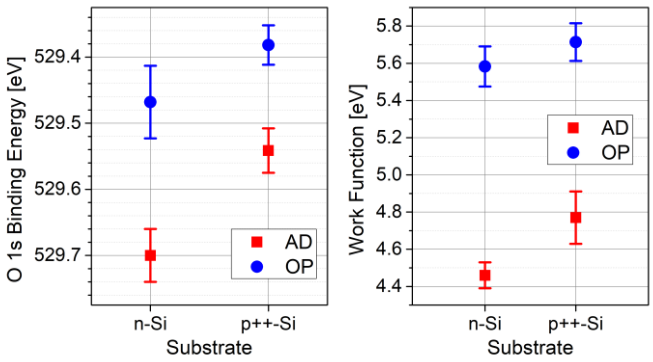

Figure 5.23: O 1s binding energy and work function of AD- and OP-sNiO-400 films as a function of the doping level of the silicon substrate beneath the sNiO films. Each data point is the average of four to nine similar samples, the error bar indicates the standard deviation.

Further substrates were not systematically investigated, however, single experiments with n^{+}- and n^{++}-Si delivered data points in the range between those of sNiO on n-Si and on p^{++}-Si, respectively. For reliable statements, further investigation is necessary, but lies beyond the scope of this work. What can be said, though, is that a systematic impact of the substrate on the spectral shape and thus on the chemical composition at the surface was not observed. This holds in particular for a direct comparison (i.e., within the same batch) of sNiO on n-Si with sNiO on i-Si (see Figure 5.24). As the Fermi levels in the sNiO films are at the same position and even the work functions are identical, it is concluded that the change from intrinsic to slightly n-doped silicon does not influence sNiO film properties.

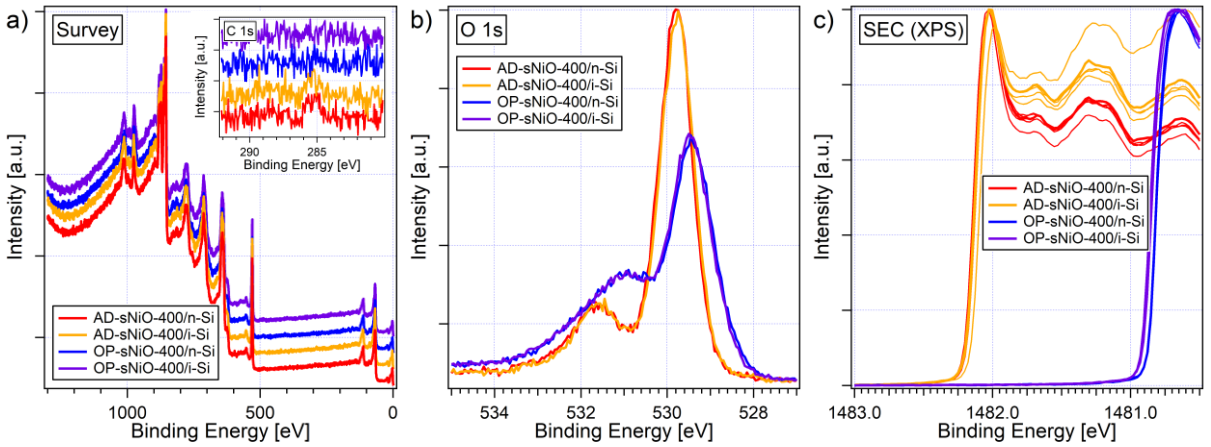

Figure 5.24: XP spectra taken to estimate the difference between sNiO film deposited on intrinsic (i-Si) and n-type (n-Si) silicon substrates.

[8] WF(p^{++}-Si) has been measured by Patrick Reiser, Materials Science Institute in Darmstadt.

5.4.2. Response to illumination – light-induced core level shift

Within a complementary examination, the response of sNiO properties to illumination was investigated, as it has been noticed that the Fermi level position was changed when the lamp inside the UHV XPS measurement chamber was turned on. For this purpose, sNiO films (on n-Si) were illuminated during XPS measurement with a GaN UV LED through a CaF_2 window ($I = 0.65$ A; $U = 15.30$ eV). O 1s core level spectra were recorded in the dark and immediately after turning on the illumination. According spectra are depicted in Figure 5.25. In all cases, except for the AD-sNiO-400 sample, a light-induced energy level shift (LI-ELS) toward higher binding energies is observed, whereas the shift is much more pronounced after OP treatment.[9] Here, it is in the range of about 200 meV. In all cases, illumination seems to shift the spectra toward the position of the AD-sNiO-400 sample at 529.66 eV. At further samples, it was confirmed that the shift similarly occurs in all other spectra (Ni $2p_{3/2}$, VBM and SEC) and is reversible.

Such a behavior can be explained by an upward band bending in the samples, which is screened under illumination due to a surface photovoltage (see also Chapter 3.1.2). It may be tempting to ascribe this effect to a band bending in the sNiO layer. However, there are two aspects causing doubts about this interpretation. On the one hand, it is doubtful whether the purity (or crystallinity, respectively) of sNiO is high enough to feature a band bending, especially over a short range of 20 nm. And on the other hand, the LED has a wavelength of 365 nm, which corresponds to an energy of 3.4 eV. According to UVvis measurements in Figure 5.11, this is not enough to induce interband excitation in the sNiO films. Silicon, in contrast, has a band gap of 1.12 [47] and a good absorption at 3.4 eV [206]. Therefore, a photovoltage in the silicon substrate seems to be more likely.

Hence, n-Si was exchanged by highly conductive, degenerate p^{++}-Si substrate. Although several sNiO-400 films were spin-coated on p^{++}-Si and were investigated with XPS, for none of those samples a spectral reaction to illumination was found: neither for AD films nor for OP treated ones. The same applied for further highly conductive substrates such as n^{++}-Si and fluorine-doped tin oxide (FTO), whereas here statistics was very poor. Nevertheless, these results show that the sensitivity to light depends on the substrate material and strengthens the assumption that the photovoltage measured for sNiO on n-Si substrates drops in the silicon rather than in the sNiO film. This agrees to former findings of our group: Tengeler et al. found band bending upwards in n-type silicon beneath in-situ magnetron sputtered NiO_x layers [105]. Consequently, the effect seems to be a "buried interface effect" [48] rather than a surface photovoltage.

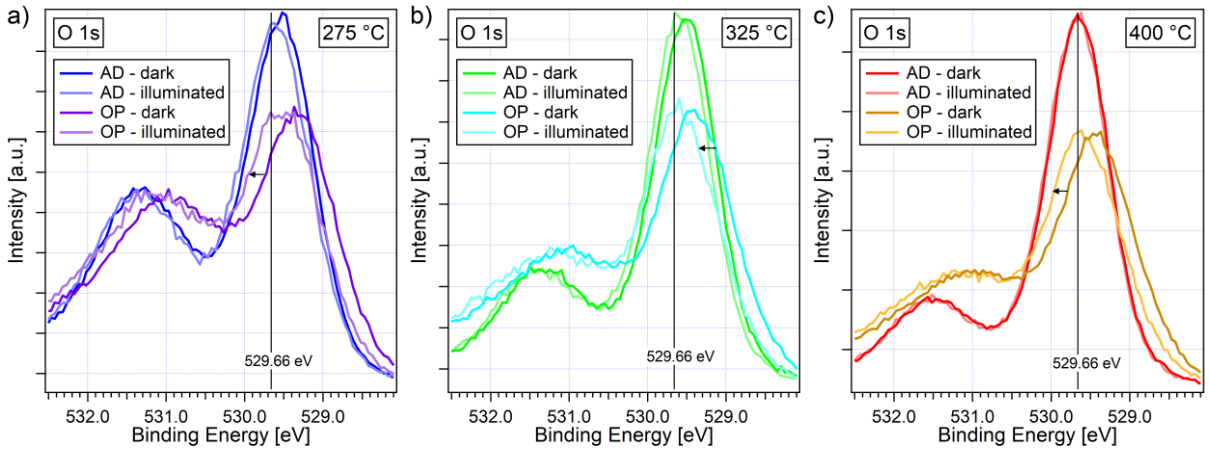

Figure 5.25: O 1s core level spectra of sNiO annealed at different temperatures, before and during illumination with a GaN UV-LED. The position of the main peak of the AD-sNiO-400 film at 529.66 eV is indicated in all three diagrams.

[9] Note that the result was qualitatively confirmed for a similar complete batch (three annealing temperatures, each with both AD and OP) and additionally for further samples. However, for some AD-sNiO-400 samples that were tested in the aftermath, also a non-zero photovoltage of less than 100 meV was observed.

However, as it was shown in Figure 5.23, the binding energy of the O 1s main peak in sNiO is reduced by OP treatment. As a band bending upward of more than 100 meV in degenerate p-type silicon is not to be expect, a certain potential drop must exist within the sNiO layer.

Interestingly, the LI-ELS can be turned off by surface functionalization of sNiO films with a self-assembled monolayer (SAM). Details of SAM functionalization will be discussed in Chapter 7. Most important for now is that core levels of AD- and OP-sNiO do not shift back to a common main peak position upon SAM functionalization (see Figure 5.26). Therefore, at least in some of the samples a remaining band bending is expected. Still, almost no reaction upon illumination is observed anymore. Obviously, the Fermi level is pinned by the functionalization. Although it appears to be interesting to toggle the response to light in the substrate by manipulating the surface of the adsorbate film, the phenomenon was not in the focus of the work and therefore not further studied.

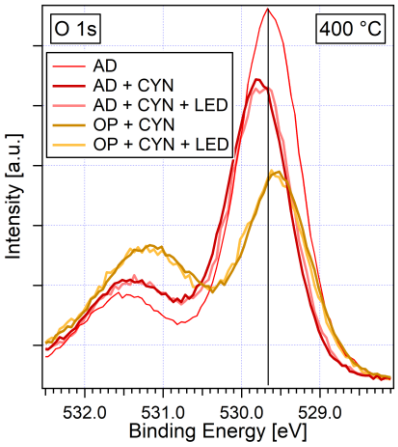

Figure 5.26: O 1s core level spectra of sNiO annealed at 400 °C and functionalized with a SAM, before and during illumination with a GaN UV-LED. The position of the main peak of the non-functionalized AD-sNiO-400 film at 529.66 eV is indicated as reference.

To account for the observed phenomenon and to check the influence on statements given before, the diagram in Figure 5.21a was redrawn under consideration of the light influence and displayed in Figure 5.27. To obtain the adjusted data point, the light-induced ELSs measured at two to three samples were averaged and subtracted from the averaged data points measured in the dark.

As a result, the Fermi levels of the AD samples are now similar for all three annealing temperatures and the difference between AD and OP now only exists for sNiO-400, although much less pronounced. Note that for specific sNiO-400 samples the Fermi levels of illuminated AD and OP samples can coincide. With regard to the work function, statements are essentially the same as for samples measured in the dark: the lowest annealing temperature has the highest work function and vice versa and upon OP treatment, the work functions of all three sNiO film types are clearly increased to a comparable level. After all, unless highly conductive substrates are used, great care must be taken regarding the illumination of sNiO samples to avoid artifacts.

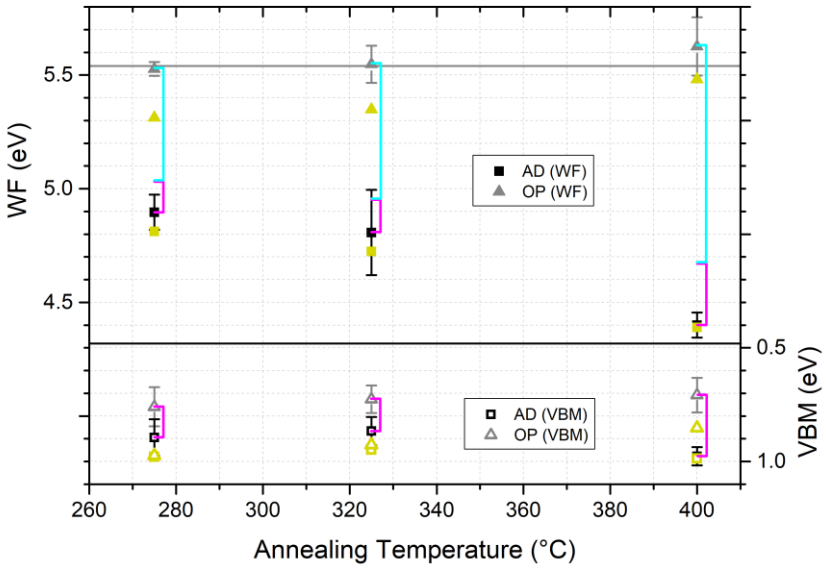

Figure 5.27: Work functions and valence band maxima with respect to to the Fermi level position of the differently prepared sNiO samples without illumination (grey and black) and with illumination (yellow).

5.4.3. The atmosphere while spin-coating

In this section, the influence of the atmosphere surrounding the sample during the spin-coating process is discussed. Two atmospheres are compared: nitrogen and ambient air. All results presented in the Chapters 5.2 and 5.3 were obtained from samples spin-coated in a nitrogen-filled glovebox. As many samples in literature are fabricated in air, and also for practical reasons, the question whether spin-coating in air leads to the same results is interesting. For this comparison all other parameters were kept the same.

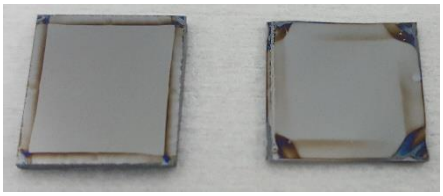

Figure 5.28: Photograph of two AD-sNiO-400 samples spin-coated in nitrogen (left) and in air (right).

A first difference which stands out is a considerably thicker margin of the sample spin-coated in air (see Figure 5.28). Except for this, the samples appear optically identical. Over the course of this work many samples of both types have been investigated with XP and also IR spectroscopy. No significant difference that exceeded the typical sample-to-sample variation was observed. Figure 5.29 shows exemplary XP and IR spectra of two samples from the same batch, one spin-coated in air and the other in nitrogen. Except for minimal differences of the Fermi level position and the surface dipole, the respective spectra are identical. This observation is confirmed by the IR spectra in Figure 5.29c.
Apparently, the atmosphere while spin-coating has no significant influence on the film composition and its properties. Also exposure of the precursor and the precursor solution to air did not have a clear impact.

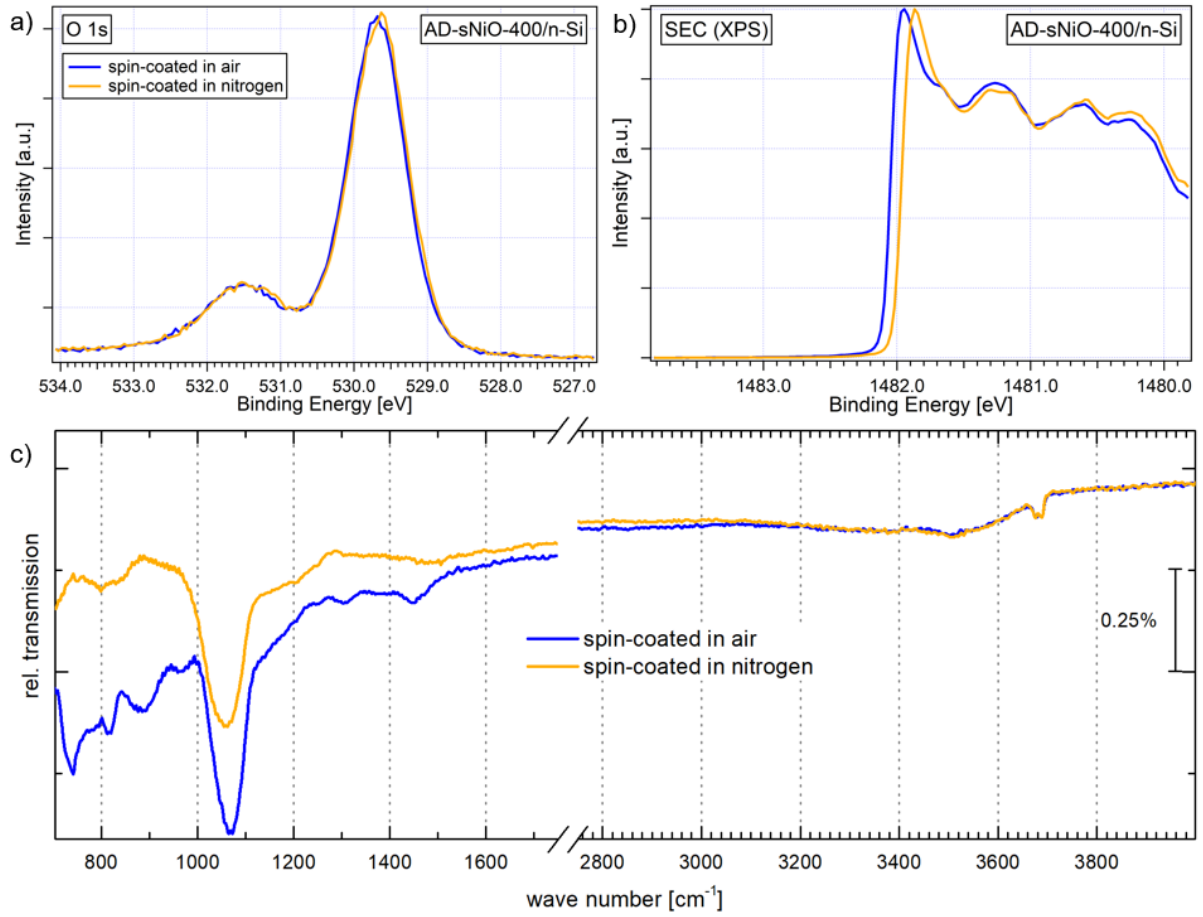

Figure 5.29: Influence of the spin-coating atmosphere on XP spectra (a,b) and on IR spectra (c). The pronounced mode between 1000 to 1100 cm^{-1} is glass mode of the native silicon oxide layer [312].

5.4.4. Specifics of heating conditions

Typically, samples were annealed at a certain temperature in air for 45 min. To enable controllable and reproducible conditions, the hotplates were preheated to the respective temperature. If this procedure was not followed and the sample was placed on the hotplate before the final temperature was reached, differences in the XPS O 1s side peak and the work function were observed. This underlines the strong impact of the annealing temperature and procedure, respectively. Therefore, it is important to follow exactly the right recipe.
Although this sounds quite simple, in laboratory reality unexpected hurdles may appear. During the course of the work there were several issues to deal with: as an example, it turned out that some hotplates suffered from a huge temperature gradient (roughly 10 °C/cm). Other plates did not deliver the temperature indicated. To tackle both issues, aluminum plates were located on top of the hotplates and the temperature was checked with a thermocouple. Thus, a stable and homogenous temperature with a variation of a few degree was achieved. Additionally, it turned out that covering of the sample with a cup leads to an increase in temperature. Therefore, it is important to check the temperature, if a cup is used. For this work the samples usually were annealed uncovered.
In further experiments the influence of the annealing time was investigate. It was found that the film almost reached equilibrium after already 5 min annealing. In the following 40 min only slight changes occurred. It is very likely (although not directly measured) that most of the conversion occurs in the first few seconds, as a clear and sudden color change is observed right after placing the sample on the hotplate.
In summary, the exact annealing conditions are found to be crucial for the film properties. To ensure reproducibility, great care must be taken.

5.4.5. Stability of NiOOH in UHV

This section is about the question whether NiOOH which is created upon OP treatment of sNiO films is thermodynamically stable. To answer the question, two OP treated sNiO-400 samples were introduced into the UHV XPS measurement chamber and measured at a base pressure in the 10^{-9} mbar regime. As can be seen in Figure 5.30, neither the spectral shape nor the Fermi level position changes within 14 h in UHV. Even the work function is almost identical. In conclusion, OP treated sample show no sign of decomposition at room temperature in UHV and are therefore considered to be thermodynamically stable. If a decomposition takes place nevertheless, the time scale is at least several days. For completeness, also a non-treated sNiO sample was investigated similarly, with the same result: within the period examined no changes are visible.

5.4.6. Storage and carbon adsorption

During the course of this work it was noted that sNiO exhibits a strong tendency to adsorb carbon in environments other than UHV, which includes atmosphere and medium vacuum (~3 mbar). Interestingly, while storage in air is possible without adsorption of contamination in a timescale of minutes to an hour, in medium vacuum noticeable amounts of carbon are adsorbed even within a few minutes (see [207] for more details). Even in the controlled atmosphere of a nitrogen glovebox a significant amount of carbon contamination is observed already after two days (see Figure 5.31). Therefore, storage in a nitrogen glovebox is not advised without further measures. However, as also depicted in Figure 5.31, carbon contamination is effectively removed by additional heating for 5 min at 400 °C in ambient atmosphere. Chemically, i.e., based on the spectral shape of XP and IR spectra, and regarding the Fermi level position, reannealed samples were similar to fresh samples.

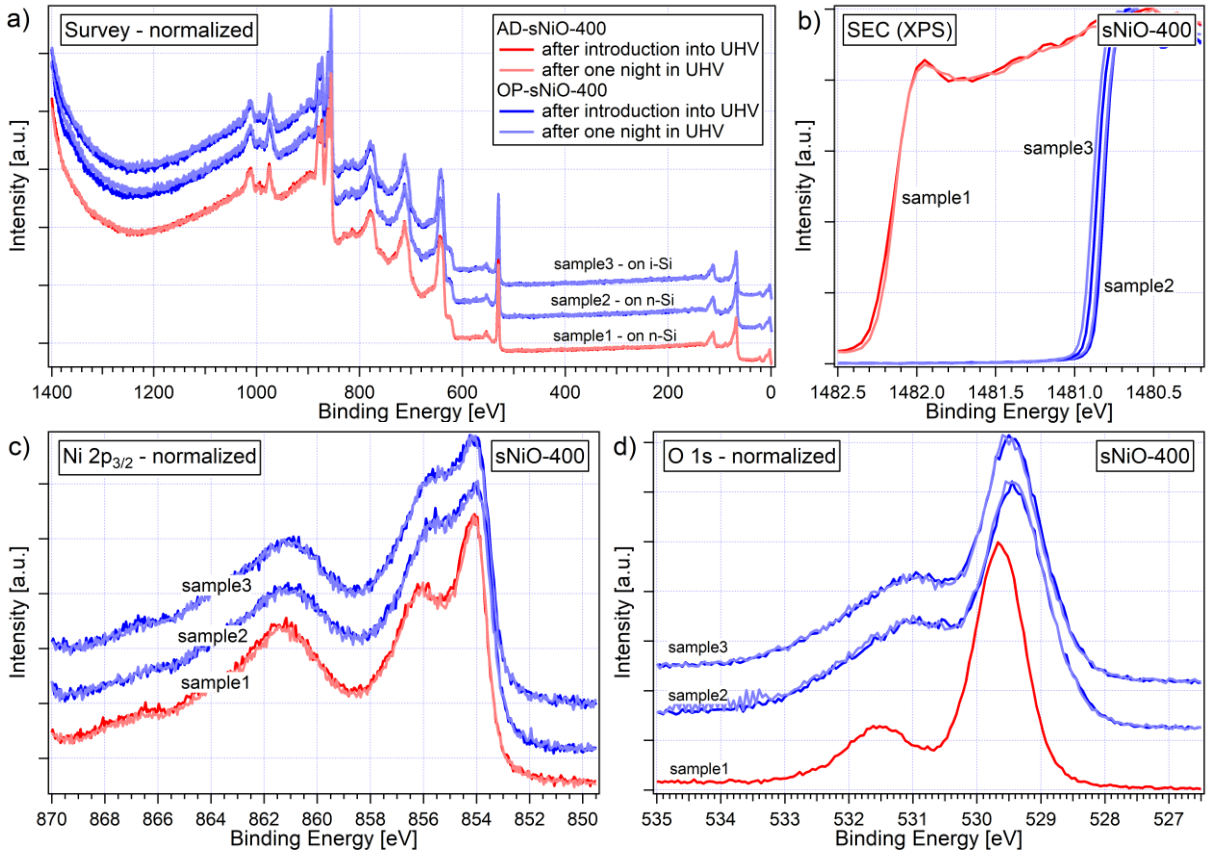

Figure 5.30: Normalized XP spectra of AD- and OP-sNiO thin films after introduction into the UHV system (darker lines) and after one night (lighter lines) to examine the stability of NiOOH in UHV. No changes are observable.

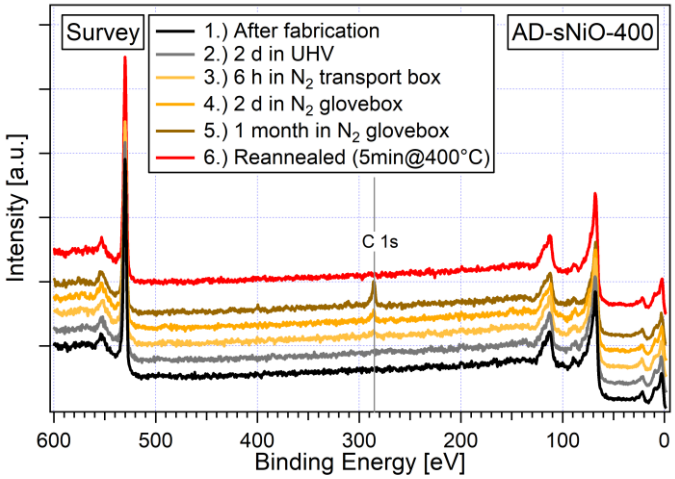

Figure 5.31: Investigation of the storage behavior of AD-sNiO-400 films in nitrogen by XPS measurements.

5.5. Attempts to further increase the quality of solution-processed nickel oxide

In the last sections, a thorough picture of sNiO samples fabricated in a "standard" way and modified by OP was developed, including traps and subtleties of the fabrication process and the measurement. In Chapter 5.2 it was shown that sNiO films annealed at the highest temperature (400 °C) had the lowest content of $Ni(OH)_2$. Here, specific targeted trials to increase the quality of the AD-sNiO-400 films in terms of stoichiometry and grain sizes are described. This also includes the purpose of learning more about the composition and the type and origin of the hydroxide detected.

5.5.1. Annealing in air with temperature ramp

A first attempt was based on the thought that a slower temperature ramp would leave the atoms more time to arrange and thus lead to larger crystallites and a better surface-to-volume ratio. For this purpose, instead of putting the samples directly on a preheated 400 °C hotplate, the temperature initially was left at RT and increased by 50 °C every 10 min. Finally, it was left at 470 °C for about 45 min. The temperature evolution is shown in the inset in Figure 5.32a.
However, AFM reveals no significant increase of the crystallite sizes and the RMS values stay about the same (1.1 nm instead of 1.0 nm, see Figure 5.32a und b). Also XPS cannot find a reduction of the side peak in the O 1s spectrum. Instead, it appeared broader, which might be a sign for NiOOH, as discussed earlier. Another hint for this interpretation is the increase of the region between main and side peak in the Ni $2p_{3/2}$ spectrum (Figure 5.32d), which is where NiOOH exhibits a feature. In agreement to former findings this leads to a higher work function (+0.2 eV), which can be attributed to a larger surface dipole as the Fermi level shift is small (see Figure 5.32c with inset and d).

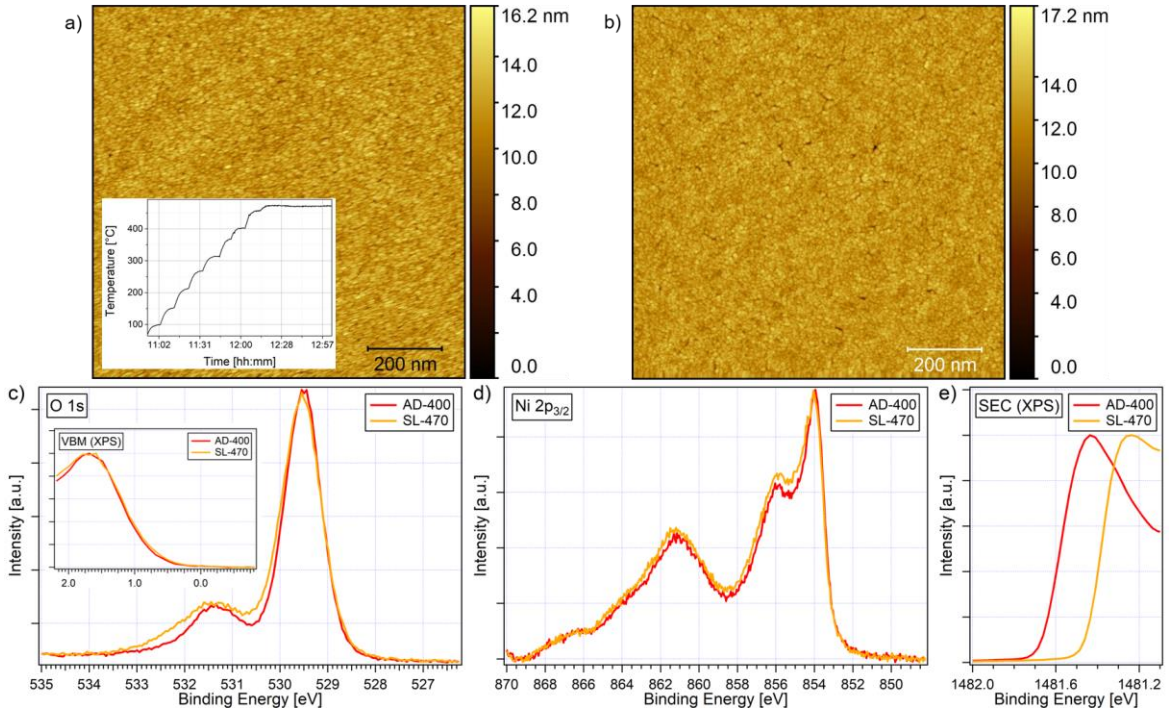

Figure 5.32: Peak-force AFM images of the sample heated with temperature ramp (a) and of a control sample (b). The Images were taken by taken by Dr. Sabina Hillebrandt. (c) – (e) PE spectra of both samples.

5.5.2. Heating in air with quick transfer

Another attempt was inspired by the knowledge that hydroxidic species decompose at temperatures between 250 to 330 °C [61,67,158,197,205,208]. Therefore, during the annealing process samples annealed at 400 °C should not contain any $Ni(OH)_2$ anymore and the hydroxide which is detected in sNiO-400 samples has to be formed only when the sample is cooled down after the annealing step, before the introduction into the vacuum system. Therefore, an AD-sNiO-400 film (here on p^{++}-Si) was mounted on a sample holder and reannealed in air for 15 min at 400 °C. Afterwards, it was directly transferred into the XPS-UHV system while still being attached to the hot sample holder. The pumping process of the introduction chamber was started immediately, and the measurement was initiated about 15 min after the end of the annealing step.
Indeed, this step lead to a decreased hydroxide amount, compared to a sample which had time to cool down before insertion into the system, however, the reduction was very small. Interestingly, spectra were shifted to higher binding energies despite the high conductivity of the p^{++}-Si substrate. After a short exposure to air, the typical size of the O 1s side peak (indicative for hydroxide) was reestablished. This experiment gave a first confirmation that the side peak is related to the exposure to ambient atmosphere.

5.5.3. Heating in nitrogen

Consequently, the idea for the next trial was to inhibit the contact to oxygen or moisture during and after annealing. Therefore, an AD-sNiO-400 sample (again on p^{++}-Si) was annealed for almost 1 h at 400 °C in a nitrogen glovebox. Subsequently, the sample was directly transferred into the adjacent UHV system of the clustertool and into the XPS measurement chamber without air contact. Figure 5.33 depicts the recorded spectra before and after this process. The survey spectrum in Figure 5.33a reveals a significant contamination of the heat-treated sample with carbon and chlorine, which is attributed to the impurity of the atmosphere of the glovebox. These adsorbates also explain the reduction of the O 1s peak's intensity and render the interpretation of the data precarious.
However, the oxygen peak undoubtedly exhibits a reduction of the side peak with a final SP-to-MP ratio of 1:10.6. This proves that at least part of the side peak is indeed due to the contact of annealed samples to ambient atmosphere.
Here again, a shift of the reheated spectrum to higher binding energies occurs.

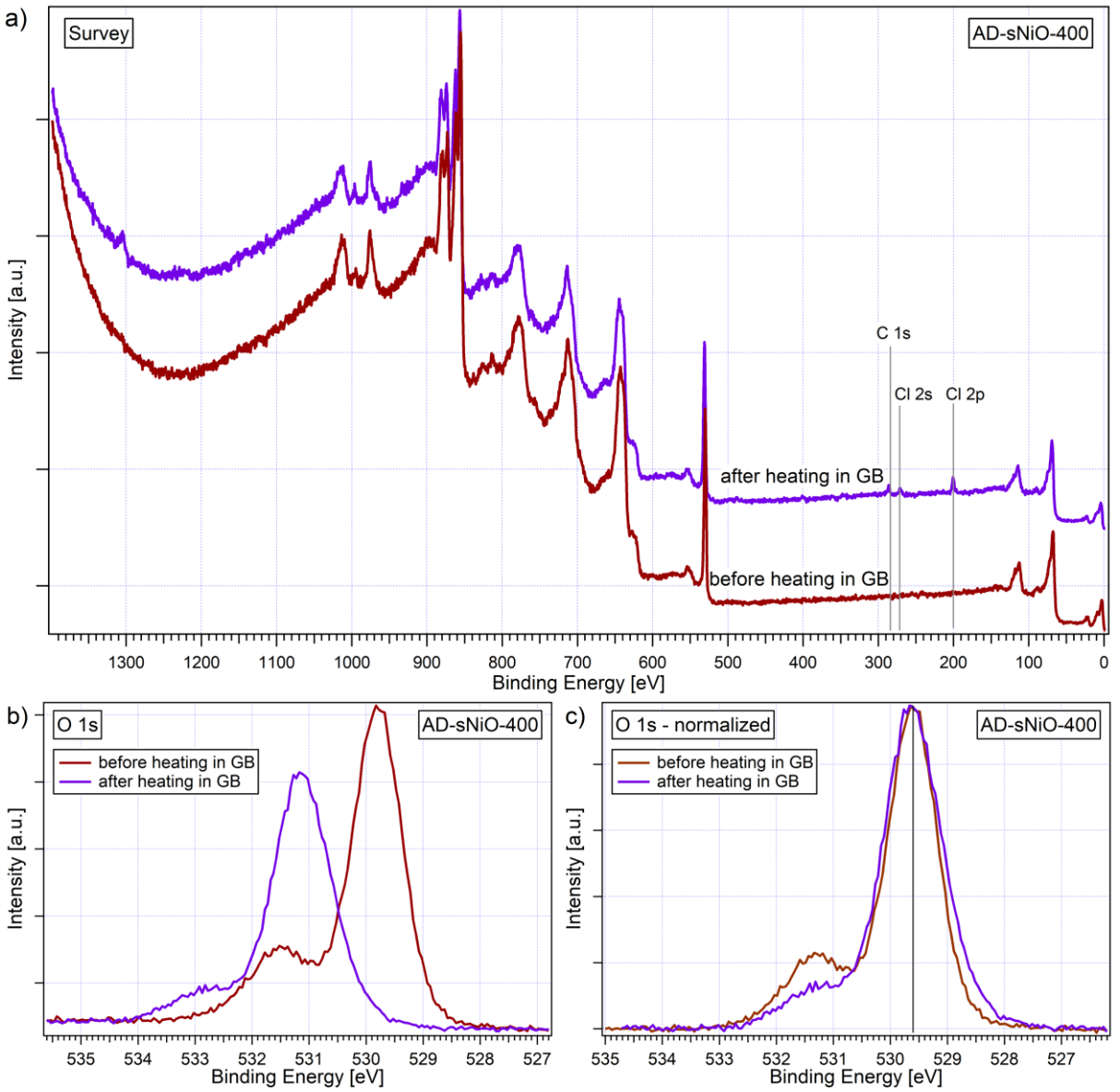

Figure 5.33: XP spectra of an AD-sNiO-400/ p^{++}-Si sample before and after heating to 400 °C in a nitrogen glovebox (GB). During the whole procedure the sample had no air contact. Spectra in (c) are referenced in binding energy to 529.6 eV and a Shirley background [130] was subtracted.

5.5.4. Heating in UHV

The next step was to transfer the heating process into UHV. This measure does not only reduce contamination and possible interaction with the atmosphere, but furthermore provides the possibility to monitor the supposed reduction of hydroxidic species in-situ as a function of temperature, which could shed light on the type of hydroxide based on the different thermal decomposition characteristics of α- and ß-$Ni(OH)_2$ (see Chapter 3.2.3). Using a heatable sample holder, the temperature of an AD-sNiO-400/p^{++}-Si sample was slowly increased while PE spectra were taken at several selected temperatures. For elevated temperatures, the temperature was hold constant for about 5 min prior to each measurement to give the sample time to reach thermal equilibrium. The maximum temperature was 420 °C, which was reached after almost 2 h. Thus, the ramp had an average incline of about 3 °C/min. Subsequently, the sample was cooled down and final spectra were recorded at a temperature of about 50 °C. Survey spectra are shown in Figure 5.34a. Except for a tiny signal from chlorine (~200 eV) no significant contamination is visible.

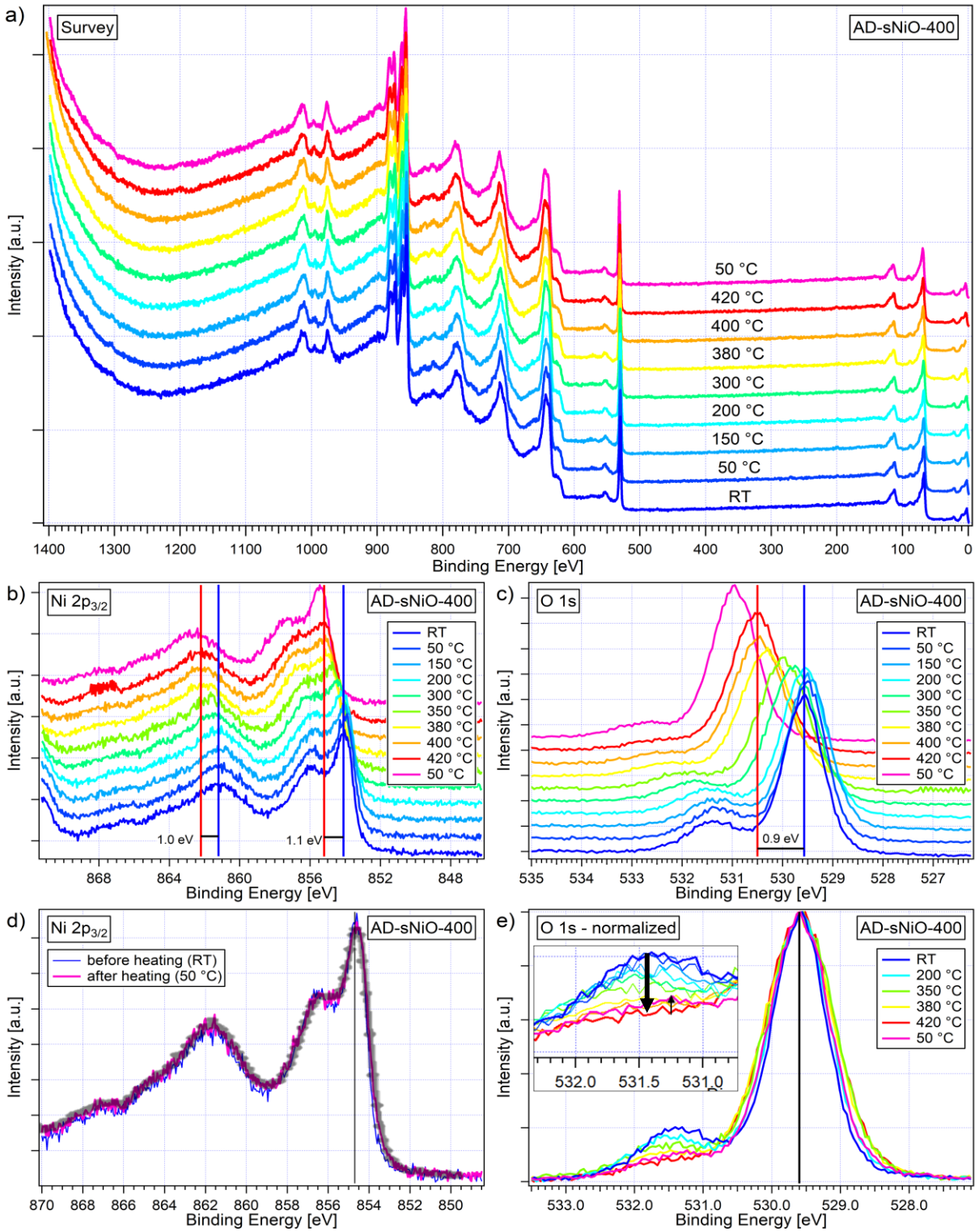

Figure 5.34: XP spectra of an AD-sNiO-400 sample heated in in UHV. Ni $2p_{3/2}$ spectra in (d) are referenced to 854.7 eV and O 1s spectra in (e) are referenced in binding energy to 529.6 eV [13]. Spectra in (d) are superposed by a reference spectrum from literature of a NiO(100) single crystal after cleavage in vacuo without detectable amounts of hydroxide [49]. The inset in (e) magnifies the O 1s side peak region. All spectra in (e) are show after subtraction of a Shirley background [130].

Both detail spectra (Ni $2p_{3/2}$ and O 1s) exhibit a shift of about 1 eV during the heating process and a further shifting of almost 0.5 eV during the cooling down (see Figure 5.34b and c). These shifts may be caused by band bending at the p^{++}-Si/SiO_2/sNiO interface or by an artefact due to charging. The stability of the work function between 400 and 420 °C and after cooling down (85 and 60 °C) (see Figure 5.35 for SECs) may exclude a charging process, as such is often accompanied by an ongoing

shifting or fluctuating of the spectra. Furthermore, a charging usually goes along with a broadening of the peaks. While such broadening indeed happens during the heating process, the opposite occurs during cooling down whereas the core levels still shift further to higher binding energies. This as well excludes charging, and the broadening is more likely to be related to the elevated temperature rather than to charging. After all, neither the origin of the broadening nor the origin of the shifting could finally be clarified, however, based on the data, interesting observations regarding chemical changes can be made and are described in the following.

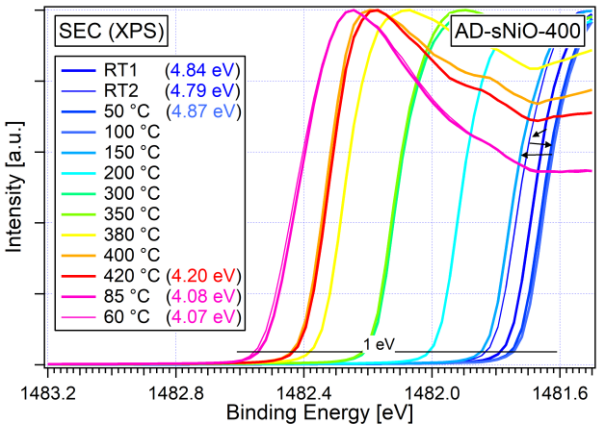

Figure 5.35: Secondary electron cutoffs measured with XPS on an AD-sNiO-400 sample during heating in UHV.

The spectral shape in the O 1s region clearly changes during the heating process: the higher the temperature the smaller becomes the side peak around 531.5 eV. For a better comparability, normalized spectra are displayed in Figure 5.34e. While until 50 °C nothing happens, the side peak has already started to decrease at 150 °C and continues to do so with increasing temperature. Toward the end of the process, between 400 and 420 °C, the process starts to saturate and only a fraction of the initial hydroxide amount is left. The decomposition is rather continuous over large parts of the temperature range tested. This result seems to indicate β-$Ni(OH)_2$ rather than for α-$Ni(OH)_2$, according to reports in literature [75,84]. However, unambiguous statements about the nature of the decomposed $Ni(OH)_2$ in the present samples are not possible due to the small differences of the decomposition characteristics of both hydroxides [80]. Instead, another interpretation is favored by the Ni $2p_{3/2}$ spectra. As shown in (Figure 5.34d), the Ni $2p_{3/2}$ spectrum after the heating process is almost identical to the initial spectrum. As a change of the $Ni(OH)_2$ content should go along with a clear change in the region of the Ni $2p_{3/2}$ side peak, this excludes the presence of "classical" α- or β-$Ni(OH)_2$. A monolayer of surface OH attached to NiO grains is concluded instead, in agreement with the suggestion in Chapter 5.2.
Interestingly, the O 1s side peak is slightly increased after the sample has cooled down from 420 to 50 °C (red and pink line in Figure 5.34e). This is possibly due to a reaction of the sNiO film surface with residual gas in the UHV chamber (such as H_2O) to surface OH. The surface nature of this OH was confirmed by additional sputtering for 2 min at 3 kV, after which most of the side peak was removed again, however, a small signal remained (SP-to-MP ratio of ~1:17). All in all, the SP-to-MP ratio has been reduced from 1:4.0 in the beginning, over a minimum ratio at a temperature of 420 °C of 1:14 to a final value after heating of 1:9.3.
The final Ni $2p_{3/2}$ spectrum (after heating, at 50 °C) is a spectrum which is not distinguishable from a spectrum of a NiO(100) single crystal after cleavage in vacuo without detectable amounts of hydroxide, as illustrated in Figure 5.34.

Finally, it is worth noting that the work function is only reduced by ~0.8 eV during the whole process (including the cooling down) (Figure 5.35) while the O 1s core level shifts by ~1.4 eV. Consequently, the surface dipole is increased by ~0.6 eV. This is a priori surprising for surface OH groups with a negative partial charge, although literature reports exist which state exactly this correlation [66]. However, this observation fits to the conclusion of a monolayer of OH at the surface with partially positively charged hydrogen atoms in the outermost layer, which is destroyed upon heating by separation of hydrogen atoms, instead of by separation of OH groups. This process could explain the observed increased surface dipole upon heating in vacuo.

5.5.5. Comparison and discussion

AD-sNiO-400 samples contain hydroxidic species, which can be effectively removed by heating above 400 °C, both in nitrogen and UHV, in agreement with literature on the thermal decomposition of $Ni(OH)_2$ and surface hydroxides. As the typical changes in Ni $2p_{3/2}$ spectra, which are expected for $Ni(OH)_2$, are missing, it is concluded that the hydroxidic species are surface OH groups rather than bulk-like $Ni(OH)_2$. Only minor parts, which probably stem from a different type of oxygen, like interstitial oxygen, remain after heating and after sputtering. For further clarification, additional combined IR experiments would be helpful. The heating process is in each case accompanied by a strong Fermi level shift, whose origin was not clarified. Arguments against a charging were discussed. A further argument against charging is the similarity of the shifts: The O 1s main peak of all three heated samples (heated in air with quick transfer, heated in nitrogen and heated in UHV) lie in a range of 531.0 and 531.2 eV, which appears to be too similar for being caused by charging. However, an evidence could not be given.

The experiments give strong evidence that the side peak in the O 1s spectrum of sNiO samples is to a large extent caused by interaction of the film with the atmosphere after the samples are taken from the hotplate. During the interaction, OH groups are formed on the surface of NiO grains. Thus, the O 1s side peak is not a remnant of the conversion process of the precursor. This conclusion is also supported by the O:Ni ratio, which is very close to unity during heating in UHV, according to the following tabular.

Table 5.2: SP-to-MP and total O:Ni ratios of several samples discussed in this chapter.

Sample	SP-to-MP ratio	O:Ni ratio
AD-sNiO-400	1:4.0	1.17
Heated in nitrogen	1:10.6	1.19 (contaminated)
Heated in UHV, measured at 420 °C	1:14	1.01
Heated in UHV, measured at 50 °C	1:9.3	1.13

5.6. Comparison to vacuum-processed nickel oxide

So far, only solution-processed NiO was analyzed. This section examines the transferability of the results and conclusions to vacuum-processed NiO films, especially regarding the influence of oxygen plasma treatment. For this purpose, a polycrystalline and a single crystalline sample was investigated.

5.6.1. Polycrystalline NiO

Polycrystalline NiO was oriented in (111) direction and grown at 300 °C on a GaN(0001) substrate by Melanie Budde at the Paul-Drude institute (PDI) in Berlin using plasma-assisted molecular beam epitaxy. The AFM image given in Figure 5.36a reveals a grainy surface structure with lateral grain sizes of about 20 to 30 nm, thus comparable to the grains of solution-processed NiO. The layer thickness was in the range of 20 nm.[10] As the grains in the AFM image are only about 7 nm high, the area in between has to be NiO as well. Apparently, after a layer is complete, NiO nucleates on the surface. XRD proves a certain crystallinity with preferred orientation in (111) direction (Figure 5.36b). In the course of this work the sample was measured with XPS after each step of the following sequence of treatments: as-received, reannealing for 10 min at 400 °C in air, 5 min air exposure and finally OP treatment. The survey spectra in Figure 5.37a show the expected nickel and oxygen lines, but also reveal contamination peaks from indium and carbon. While the former seems to be an inherent part of the sample due to the growth conditions,[11] the latter is effectively removed by the reannealing step in air. Thus, also the main peak in the O 1s region in Figure 5.37c is increased due to less damping, while the side peak is reduced. The latter is attributed to the removal of oxygen-containing carbon compounds on the surface. The ratio of the side peak to the main peak based on a two-component fit now reaches a low value of 1:11, while the O:Ni ratio amounts to 1.11.
During the reannealing step the sample was still mounted onto the sample holder with the intention to reduce surface hydroxylation by insertion of a hot sample (still heated by the sample holder, similarly as in Chapter 5.5.2) into the vacuum of the XPS introduction chamber. In order to check the success of this measure, the sample was brought into contact with air afterwards and measured again. The difference turns out to be rather small: the core level spectra shift by 0.1 eV to lower binding energies and the side peak of the O 1s feature increases slightly. However, SP-to-MP ratio increases clearly to 1:6.6. One must conclude that the introduction on the hot sample holder at least somehow prevents the surface from immediate and complete rehydroxylation.

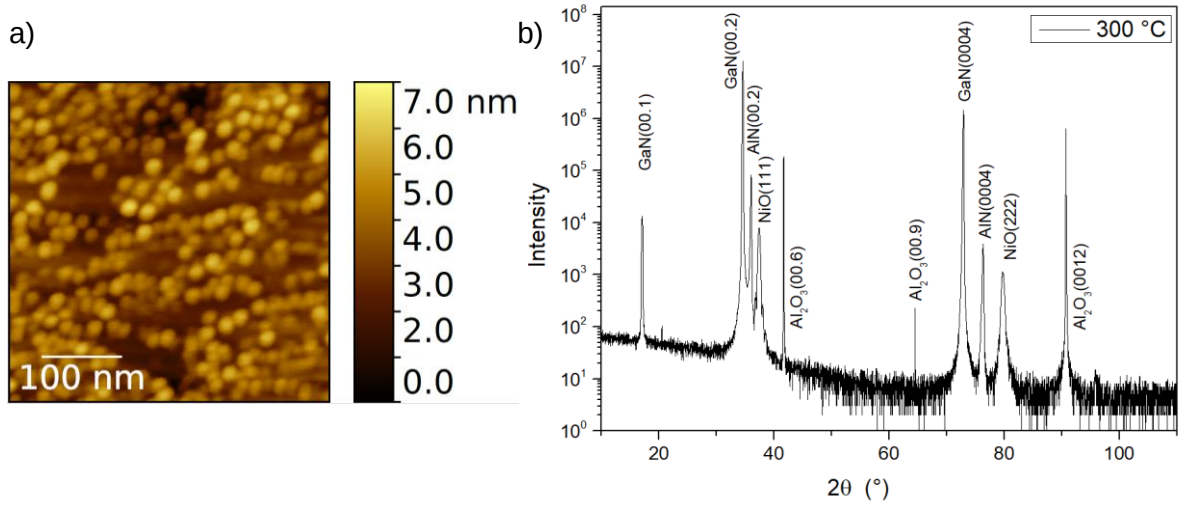

Figure 5.36: Characterization of polycrystalline NiO samples grown at 300 °C. (a) AFM image and (b) X-ray diffractogram. The data was provided by Melanie Budde.

[10] Personal communication with Melanie Budde, PDI in Berlin.
[11] Note that all samples which were received from the PDI contained traces of indium. The one presented here exhibited one of the lowest impurity levels.

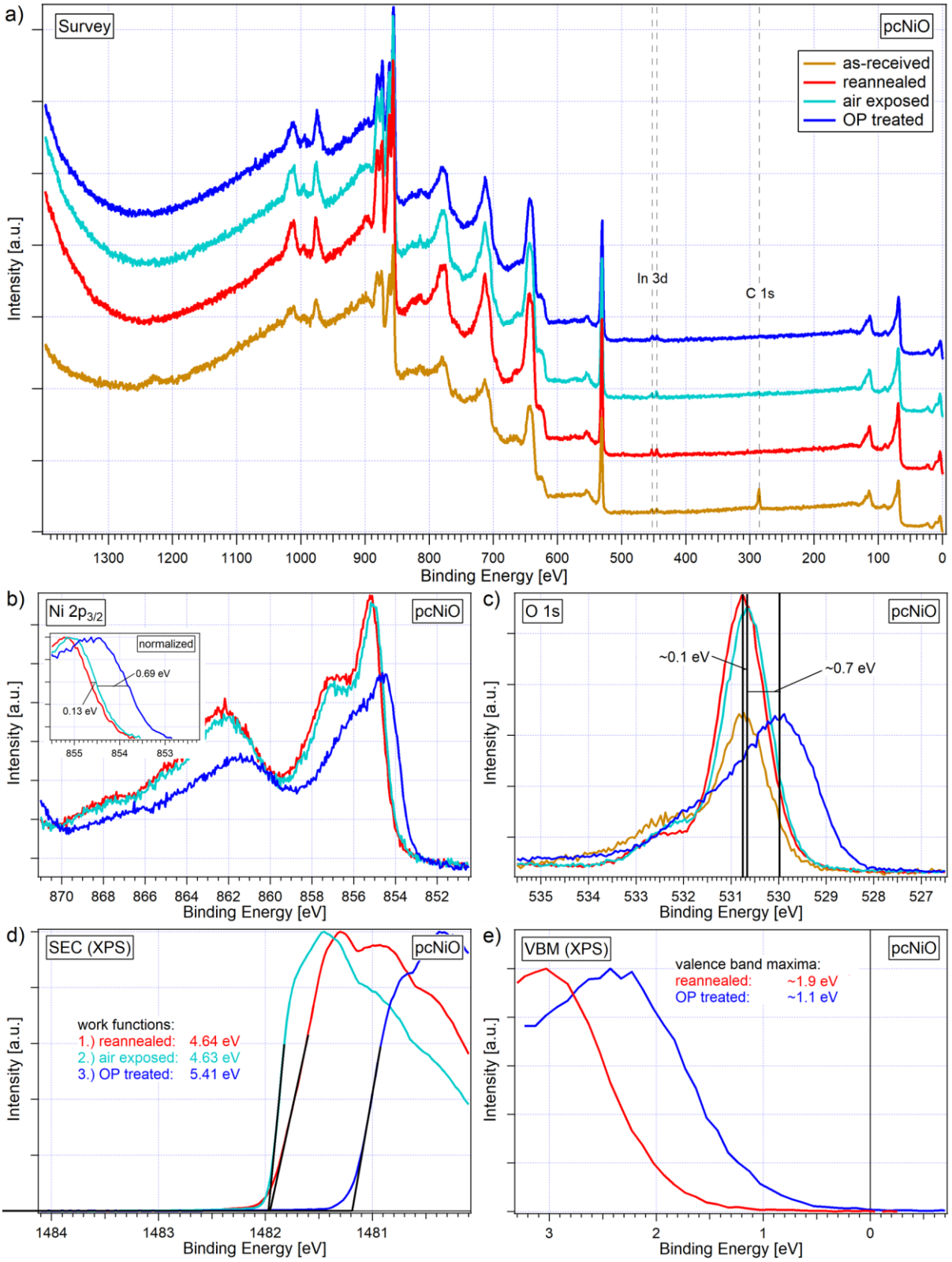

Figure 5.37: XP spectra of a polycrystalline NiO film oriented in (111) direction and grown at 300 °C on a GaN(0001) substrate by Melanie Budde at the Paul-Drude institute (PDI) in Berlin using plasma-assisted molecular beam epitaxy after different kinds of treatments: as-received, reannealing for 10 min at 400 °C in air, 5 min air exposure and finally OP treatment. The inset in (b) shows the Ni2 $p_{3/2}$ spectra normalized for better extraction of the spectral shifts.

In a final step, the sample was exposed to oxygen plasma. Qualitatively the same changes as reported earlier for solution-processed samples occur. In the case of the O 1s spectrum this implies a shifting of the whole spectrum to lower binding energies, increase and broadening of the side peak (in agreement

with the formation of NiOOH) and reduction of the main peak. Accordingly, also the Ni $2p_{3/2}$ feature experiences a shift in combination with a shrinking while the valley between main and side peak is filled (~856 eV, Figure 5.37b). The shifts of the core level spectra are about 0.7 eV (as indicated in Figure 5.37b and c) and thus rather high compared to the 0.3 eV noted for AD-sNiO-400 samples. Interestingly, all values before and after OP treatment are surprisingly high and so are the valence bands (Figure 5.37e). A VBM at almost 2 eV in the case of the reannealed sample indicates a Fermi level close to mid-gap and actually even a slight n-type behavior, given a band gap between 3.5 and 3.7 eV of vacuum-processed NiO (see Chapter 5.2.2). A Fermi level close to mid-gap generally is a sign for a low defect concentration, however, in the present case it seems more likely that the high Fermi level is influenced by the residual indium. Additionally, a charging effect could not be completely ruled out, although no clear signs like peak shifting were observed.
Also the work function behaves similarly to what was measured for the solution-processed samples (Figure 5.37d). Both after reannealing and after air exposure, it is quite low and only slightly higher than the average value of AD-sNiO-400 samples (4.6 compared to 4.4 eV). During OP exposure it raises to 5.4 eV and thus slightly below the 5.5 to 5.6 eV of solution-processed samples.

In summary, the changes upon OP treatment are at least qualitatively the same as the ones observed for solution-processed NiO. NiOOH seems to be formed at the surface, or at least is the formation of NiOOH compatible with the spectral changes (see also Figure 5.38). The NiOOH again leads to an upward shift of the bands at the surface and moreover pushes the work function to higher values with an additional surface dipole. The latter, however, is much less pronounced than what was expected based on the previous measurements on sNiO films. Reasons for this could be linked to a possibly different composition of the films in first few layers, the inhomogeneity of the surface (work function values at different spots had a standard deviation of ~0.2 eV instead of ~0.01 eV for sNiO films) and the indium contamination. The pinning of the VBM upon OP treatment at relatively high binding energies of about 1 eV is probably influenced by similar artifacts.
However, despite quantitative deviations, these measurements show the transferability of the results obtained from solution-processed samples to polycrystalline ones grown in vacuo. A further examination of quantitative discrepancies lies beyond the scope of this work.

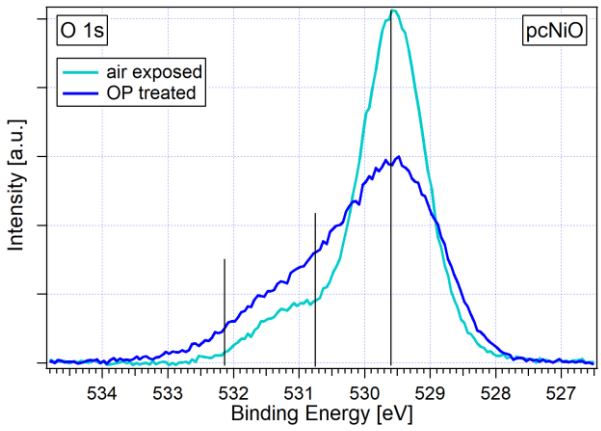

Figure 5.38: Replication of Figure 5.37c with main peaks referenced in binding energy to 529.6 eV to visualize the spectral changes of the side peak. The increase seems to be cause by two features with an energetic distance of ~1.4 eV.

5.6.2. Single crystalline NiO

Figure 5.39: Picture of the NiO single crystal on a sample holder.

The NiO single crystal was obtained from Dr. M. Fingerle[12] and originally purchased from MaTeck. It was oriented in (100) direction and had dimensions of 5x5x1 mm^3. For XPS measurements it was mounted onto a special sample holder (see Figure 5.39). The experiment was conducted similarly as for the pcNiO sample with the difference that the single crystal was given time to cool down after reannealing (before introduction into vacuum). Additionally, a heating step up to 420 °C in vacuo was added. According spectra are displayed in Figure 5.40.
Without any cleaning step the sample contained significant amounts of contamination, mainly in form of carbon (see yellow spectrum in Figure 5.40a at ~280 eV). To clean NiO crystals annealing at ~450 °C for ~5 min is suggested [209]. In a first step, a temperature of 400 °C was chosen, in accordance to previously described annealing steps. While carbon could be effectively removed by reannealing in air, strong signals of further contamination appeared, which turned out to be mostly molybdenum (binding energy of ~230 eV). It presumably originated from the two metal wires fixing the single crystal. Since molybdenum was still visible after two additional annealing steps to 400 °C both in air and in vacuo (black spectrum in Figure 5.40a), the sample was exposed to several short units of argon sputtering with increasing intensity (0.5 kV for ~4 min to 3 kV for ~40 s). With this measure it was possible to remove the Mo contamination to a large extent. Afterwards, the single crystal was annealed another time in air (5 min @ 400 °C) to cure potential damage and reoxidize emerged metallic nickel. As a combination of sputtering and subsequent oxidation by annealing is also suggested for the preparation of NiO(100) films [209], it is supposed that the damage induced by the necessary sputtering step was not profound, although the exact surface reconstruction was probably affected. The survey spectrum taken after the procedure (red spectrum in Figure 5.40a) shows no contamination except for small amounts of argon (binding energy of ~243 eV). To further check artifactual impact, Ni $2p_{3/2}$, O 1s and VBM spectra are compared before and after sputtering and reannealing in Figure 5.41 (black and red lines, respectively): both the main and the side peak in the O 1s region undergo a certain reduction. Interestingly, the reduction of the main peak is reversed upon heating in UHV (dark-red line in Figure 5.40b). In contrast, no clear impact of the sputtering process on the spectral shape in the Ni $2p_{3/2}$ region is noticeable.

In particular, the Ni $2p_{3/2}$ spectrum of the scNiO(100) sample after reannealing (red line in Figure 5.40b) has the typical shape of crystalline NiO (see Chapter 5.1) and is identical in shape to the pcNiO sample discussed in the last section. Nevertheless, the O 1s spectrum (Figure 5.40b) reveals a significant amount of hydroxide with a SP-to-MP ratio of 1:8.7, which is, however, still smaller than the SP-to-MP ratio of AD-sNiO-400 samples (~1:4). Obviously, heating in air cannot remove all OH from the scNiO(100) surface, or at least rehydroxylation takes place in a short amount of time after the heating step while still being exposed to air. With binding energies of 854.2 and 529.8 eV of the Ni $2p_{3/2}$ and O 1s main peaks, respectively, the spectra are located at slightly higher binding energies than recorded in literature for scNiO(100), but at slightly lower binding energies than recorded for NiO(100) grown on Ni(100) by oxidation (see Table A.1 and Table A.2). Compared to AD-sNiO-400 samples from this work, the VBM lies only slightly higher at 0.9 eV instead of 1.0 eV.
Upon heating in UHV, spectra shift further to higher binding energies while hydroxide is removed to a large extent (dark-red spectra in Figure 5.40): the SP-to-MP ratio now decreases to a very low value of 1:24. This confirms that the single crystal oriented in (100) direction indeed has a stronger tendency to release OH than polycrystalline NiO(111) or solution-processed NiO, although heating to 420 °C in vacuo is not enough to obtain an entirely clean surface. Interestingly, the Ni $2p_{3/2}$ spectral shape stays about the same. OH (or H) removal from the (100) surface does not seem to influence the Ni $2p_{3/2}$

[12] Dr. Matthias Fingerle, Materials Science Institute in Darmstadt.

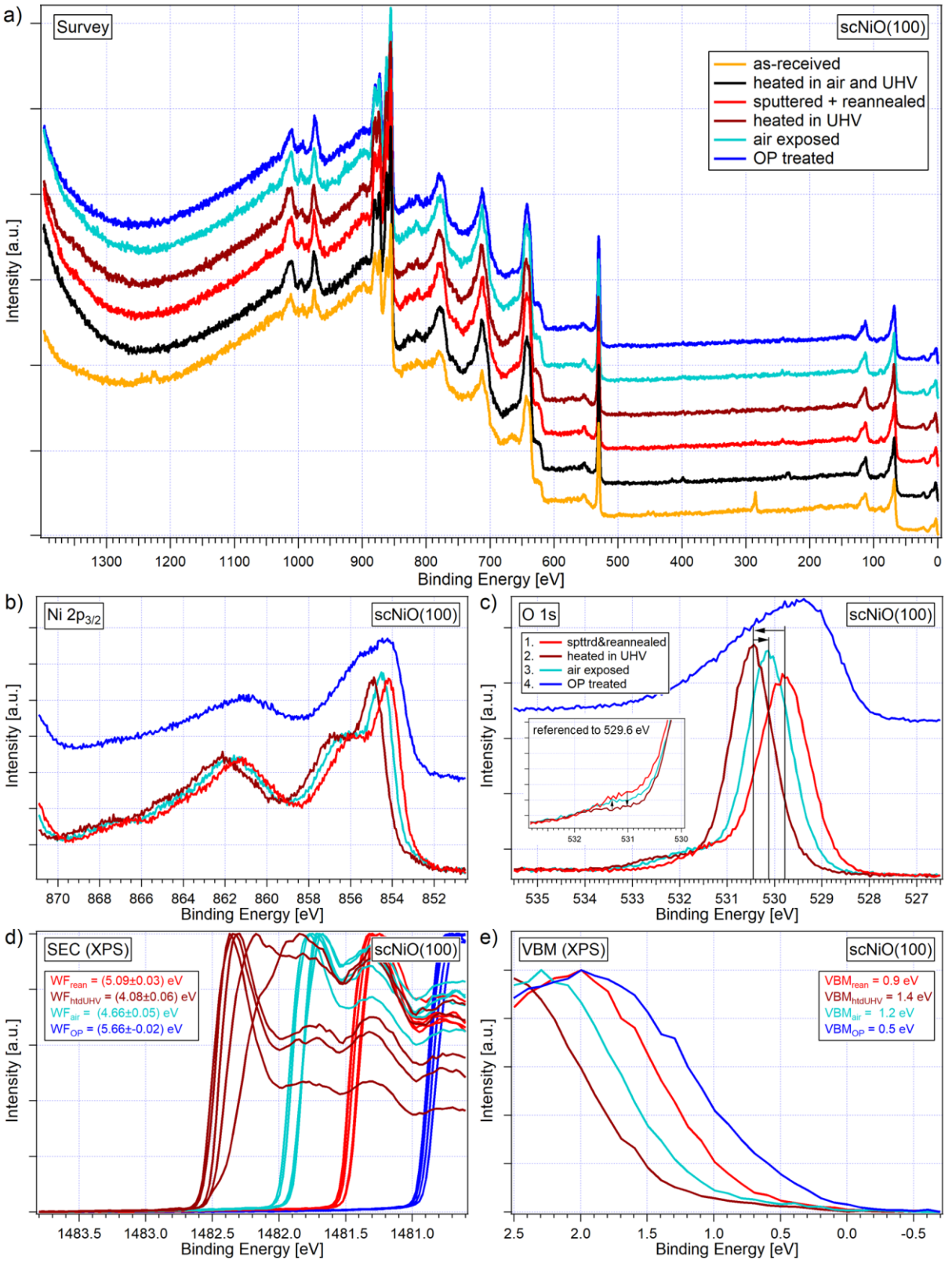

Figure 5.40: XP spectra of a single crystalline NiO after different kinds of treatment. In all cases the sample was at room temperature during the measurement.

spectrum significantly, which is similar to the observation made for the heated sNiO sample in Chapter 5.5.4. Also similar as for the sNiO sample, the core levels and the VBM of the single crystal shift toward higher binding energies (here by 0.6 to 0.7 eV instead of by more than 1 eV for the sNiO samples).

Air exposure (1 min) counteracts this shift by 0.3 to 0.4 eV while hydroxide is formed again (light-blue spectra in Figure 5.40). SP-to-MP ratio increases to 1:13, confirming the strong tendency of NiO surfaces to hydroxylate.
Similarly, the work function is affected by these both treatments (heating in vacuo and exposure to air). Qualitatively it follows exactly the trend of the CLs and the VBM, however, significantly more pronounced, which indicates that also the surface dipole is changed: Reducing OH during heating in vacuo leads to a reduction of the surface dipole (here -0.5 eV) and increasing the OH amount during air exposure increases the surface dipole again (here +0.4 eV). This results contrast the OH-dependence of the surface dipole of sNiO films (Chapter 5.5.4).

Upon OP treatment, VBM and CLs shift drastically upwards again by about 0.7 - 1 eV.[13] This shift is accompanied by huge spectral changes, which are qualitatively similar to what one would expect based on the experiments with sNiO and pcNiO, but more pronounced. While in the Ni $2p_{3/2}$ region the valley between main and side peak is filled and the satellite region between 861 and 870 eV is flattened (similar as for sNiO in Figure 5.15a), the side peak in the O 1s region is strongly enlarged such that only one single broad feature is present. Contributing components cannot be separated anymore. However, besides NiO, the hydroxidic species $Ni(OH)_2$ and NiOOH are the most probable candidates. This strong impact of OP treatment is a priori unexpected for a well ordered single crystal and may lead to the tentative conclusion that a (100) orientation of the surface is "softer" than a (111) surface in the sense that it is more prone to hydroxylation or oxidation by OP, although this might as well be influenced by the sputtering process in the present case. Further evaluation of this hypothesis lies beyond the scope of the work.
Interestingly, the work function of the single crystal after the OP treatment settles close to the 5.5 to 5.6 eV of solution-processed sNiO-400 samples at 5.66 eV, supporting the assumption of a NiOOH layer formation, although the VBM here is slightly closer to the Fermi level than in the case of solution-processed NiO.

In conclusion, single crystalline NiO(100) was detached to a very large extent from OH groups by heating in vacuo and the qualitative behavior upon treatments like OP is comparable to the one of solution-processed NiO.

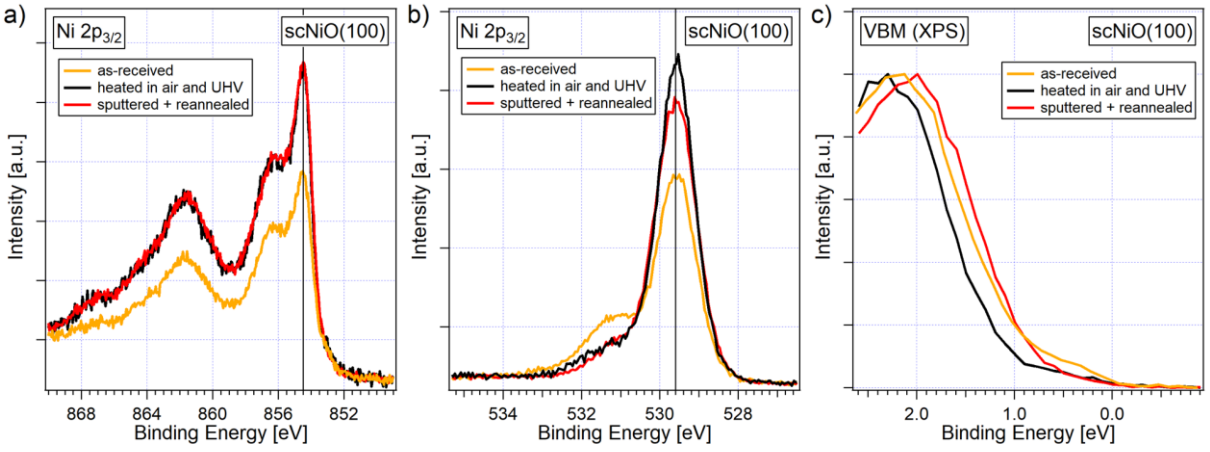

Figure 5.41: XP spectra of a nickel oxide single crystal (100), before (black) and after sputtering and reannealing (red). Additionally, spectra of the as-received sample are shown (yellow). Ni $2p_{3/2}$ spectra in (a) and (b) are referenced in binding energy to the indicated values (854.7 and 529.6 eV, respectively). Without referencing, the spectra show the same shifting as the VBMs.

[13] The value 1 eV is based on the lower binding energy edges of the normalized O 1s and Ni $2p_{3/2}$ spectra. Based on the extracted VBM values, the shift only amounts to 0.7 eV. The deviation may originate from the scope which exists for linearly approximating the leading edge of the valence band, especially in the case of the OP treated sample where the tail states are even more pronounced than in the other cases.

Stoichiometry and sensitivity factors

The discussion above has shown that spectra of this single crystalline sample come close to literature spectra of NiO(100) single crystals cleaved in vacuo, although a certain amount of non-lattice oxygen remains. Therefore, the O:Ni ratio extracted from XPS measurements should be close to unity. To test this assumption, background corrected spectra of the scNiO(100) sample after the cleaning procedure and after heating in UHV (brown lines in Figure 5.40b and c) were integrated and weighted with the respective sensitivity factors (see Chapter 4.1.1. for details). In the case of the nickel spectrum, only the Ni $2p_{3/2}$ part was considered, as recommended by Biesinger et al. [95]. In the case of the oxygen spectrum, the whole O 1s region was integrated. As explained in Chapter 4.1.1., relative sensitivity factors only account for the cross-section, i.e., the probability for a certain orbital of a certain atom to be ionized by an X-ray photon. Often, RSFs by Scofield are used [132]. However, as the sample has bulk character, the inelastic mean free path λ of electrons in the sample additionally influences the measured intensity. Furthermore, tabulated factors based on RSFs by Scofield exist, which account for matrix effects like the inelastic mean free path: so-called average matrix RSFs (AMRSFs) [210]. Finally, there are empirical values adjusted for the XPS setup of this work, which are referred to as atomic sensitivity factors (ASFs) [125].

To provide a comparison, the atomic O:Ni ratio of the scNiO(100) sample after heating in UHV was calculated for all three relevant factors, whereas also the non-relevant RSF was added for the sake of completeness (see Table 5.3). Unexpectedly, the resulting ratio is far off from unity in all cases and would indicate a strong oxygen deficiency. A probable explanation for this severe deviation is the apparent strong dependence of the sensitivity factor on the charge state in case of transition metals [211] such as nickel. For this reason, the present measurement itself was taken as reference. Although deviations from a perfect NiO(100) single crystal surface exist, the calibration is considered to be accurate within some percent (probably less than 10 %) and certainly better than values based on literature sensitivity factors for metallic nickel.

Table 5.3: O:Ni ratio calculated for the scNiO(100) sample after heating in UHV for different sensitivity factors. The inelastic mean free path λ is estimated via the TTP-2M formula [129] with kinetic energies of 957 and 627 eV for the O 1s and the Ni $2p_{3/2}$ region, respectively. Unexpectedly, all resulting ratios are far off from unity.

	RSF [132]	RSF * λ	AMRSF [210]	ASF(54.7°) [125]
O 1s	2.93	2.93 * 1.77	2.46	0.711
Ni $2p_{3/2}$	14.61	14.61 * 1.30	9.03	2.696
O:Ni ratio	0.87	0.64	0.64	0.66

With this calibration, the following O:Ni ratios for the scNiO(100) sample after the four treatments were calculated.

1.) Sputtered + reannealed: 1.03
2.) Heated in UHV: 1.00
3.) Exposed to air: 1.02
4.) OP treated: 1.46

Obviously, air contact leads to a slightly higher oxygen content at the surface, which is likely due to formation of hydroxyl groups in agreement with the slight increase of the side peak in the O 1s spectrum and with earlier observations for sNiO and pcNiO samples. OP treatment raises the ratio to 1.46, which is the same value as for OP treated sNiO-400 samples.

5.7. Summary

In this chapter, the impact of oxygen plasma treatment on the chemical and electronic properties of solution-processed NiO films annealed at different temperatures was examined. Prior to OP treatment, films had lower work functions for higher annealing temperatures, a phenomenon which was attributed to a decrease of the concentration of hydroxidic species. This decrease was accompanied by a larger amount of stoichiometric NiO both in the bulk and at the surface. Upon OP treatment the formation of a thin NiOOH surface layer on top of NiO grains was concluded and both a higher work function and conductivity was found. The commonly used four-component fit of the sNiO O 1s XP spectrum, in which NiOOH is considered with only one contribution, was shown to be questionable. Instead, evidence that NiOOH contributes with two components was provided and discussed.
Moreover, it was demonstrated that more NiOOH is created upon OP treatment for higher annealing temperatures, explaining the larger increase of the work function. After the treatment all samples exhibit similar overall amounts of NiOOH and similar electronic properties at the surface such as work function, Fermi level position and electrical conductivity. These findings led to the conclusion that the topmost layers of OP treated samples are chemically similar, despite the different chemical compositions of the as-deposited samples.

Additional heating of as-deposited sNiO samples in different atmospheres demonstrated that residual OH is mostly due to a surface hydroxylation of the annealed film and not an inherent part of the bulk due to incomplete conversion. The bulk itself was shown to be close to stoichiometric.

Experiments with vacuum-processed samples showed that changes induced by OP treatment are qualitatively similar to those induced at solution-processed NiO films. Furthermore, calibration factors for the determination of O:Ni ratios were obtained from single crystalline NiO.

6. Organic Solar Cells: The Interface between sNiO and F_4ZnPc

In the last chapter, important details on the impact of OP treatment on the chemical and electronic properties of sNiO thin films have been thoroughly examined. As described in the introduction, the importance of this treatment lies in the positive impact it has on the performance of NiO-based OPVs [12]. However, despite some research [13], many questions about the mechanism which leads to the improvement remain unclear. In particular, effects like band bending, charge transfer or chemical interaction at the very interface between NiO-HTLs and the adjacent donor have not been examined yet. It is not even clear if the chemically altered sNiO surface remains unchanged during evaporation of the donor material.

Therefore, in this chapter, the impact of the OP treatment on the interface of sNiO to F_4ZnPc, an important vaporizable organic donor material, is investigated and related to the performance of according OPV devices. Finally, the findings are compared to interface properties and characteristics of devices with similar stacks but with MoO_3 as hole transport material.

6.1. Performance of sNiO-based organic solar cells and the role of OP treatment

To confirm the positive impact of OP treatment on solar cell performance, OPV devices were built and characterized by Jakob Bombsch from the TU Braunschweig under the supervision of Dr. Sebastian Hietzschold [185]. Parts of the data have been published in [25]. The following layer stack was chosen: ITO/sNiO/F_4ZnPc:C_{60}/TPBi/Ag. All layers subsequent to sNiO were deposited by thermal evaporation in UHV. Further details may be found in [185] and [25]. As annealing of the sNiO layers at 325 °C led to better performances than annealing at 275 °C, this work focuses on cells based on sNiO-325. Higher temperatures were not possible due to the degradation of ITO, as known from literature [192] and confirmed by Dr. Sebastian Hietzschold [185]. Layer thicknesses of sNiO on ITO were about 20 nm, as estimated based on SEM images. Grains with diameters comparable to those of sNiO on silicon are visible via AFM imaging, now superimposed by the larger substructure of the ITO substrate (Figure 6.1). In the course of this work, both bulk heterojunction (BHJ) and flat heterojunction (FHJ) cells were fabricated. As expected, higher efficiencies could be achieved with the BHJ, however, the characteristics of FHJ cells provide better insight into the HTL/donor interface.

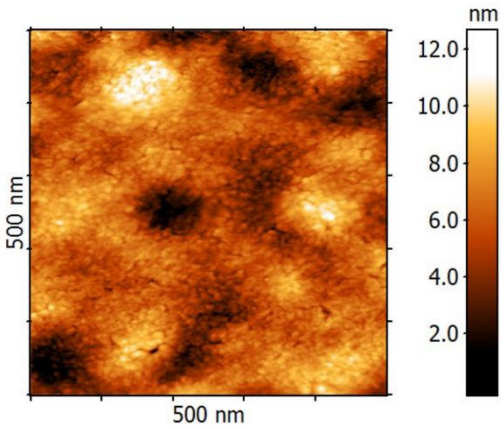

Figure 6.1: AFM image of AD-sNiO-325 on ITO.
Image taken by Dr. Sebastian Hietzschold [185].

In a first step, the functionality of AD-sNiO as HTL was confirmed. For this purpose, BHJ cells were built with and without HTL. Representative J-V characteristics are depicted in Figure 6.2. As expected, the usage of sNiO as HTL strongly enhances all device parameters compared to devices without HTL. The fill factor (FF) increases by a factor of 1.5, the short circuit current J_{SC} roughly doubles and the open-circuit voltage V_{OC} reaches a value which is about eight times higher (a table of averaged absolute values is provided in Figure A.11e in the Appendix). In fact, J-V curves of devices without HTL do not even show diode behavior: strong reverse currents due to a low shunt resistance R_{SH} witness poor charge blocking abilities. This is drastically changed by inserting sNiO between ITO and F_4ZnPc, which demonstrates the strong electron blocking abilities of sNiO. Reverse current is now very small and the shunt resistance R_{SH} large. Furthermore, a threshold voltage of about 0.6 V appears for non-illuminated devices (Figure A.11b and d). The series resistance R_S increases slightly, which is can be understood from the large sheet resistance of sNiO [185]. Finally, the power conversion efficiency (PCE) rises from (0.10 ± 0.07) % to (2.29 ± 0.19) %, underlining the necessity of an HTL for rectification (i.e., a large shunt resistance) and for suppression of charge carrier recombination at the anode. Upon OP treatment of the sNiO HTL, the efficiency is further increased to (2.71±0.12) %, mainly due to an enhanced fill factor (see table in Figure A.11e for further device parameters).
It should be noted that OP treatment of ITO also delivers huge improvements of devices without HTL (grey line in Figure 6.2 compared to the black line). However, the efficiency is still almost 30 % smaller than for devices with sNiO as HTL. The lack of blocking behavior in reverse direction is still striking.

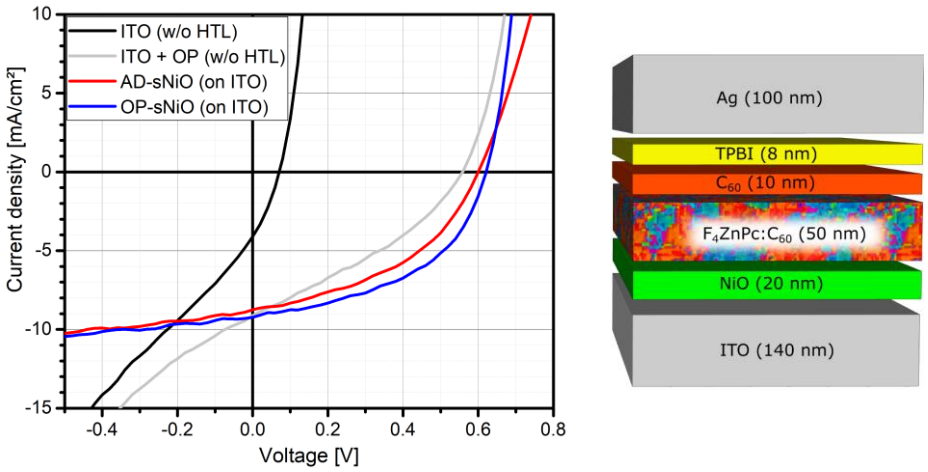

Figure 6.2: Representative J-V characteristics of BHJ solar cells (ITO/[sNiO]/F_4ZnPc:C_{60}/C_{60}/TPBi/Ag) with and without sNiO as HTL, measured under illumination of AM 1.5G. The layer stack on the right hand side was reprinted from [313].

To obtain cells with an HTL/donor interface similar to the interface in an according interface experiment, additionally FHJ cells were fabricated. Representative J-V curves are given in Figure 6.3 along with tabulated device parameters. It becomes clear that reverse currents almost stay the same, which indicates a similarly pronounced rectifying behavior of AD- and OP-sNiO. While also J_{SC} and V_{OC} appear to be unaffected, the fill factor increases significantly from 53 % to over 60 %. This is related to the severe drop of the series resistance of more than 50 %, which is manifested in a steeper incline in forward direction. One cause is certainly the chemical and electronic change of sNiO upon OP treatment, namely the formation of a conductive NiOOH layer, as concluded in Chapter 5.3. As result, the PCE improves by about 16 %.

However, also an improved energy level alignment and a different orientation of the F_4ZnPc molecules on top of the OP-sNiO interlayer may contribute. This will be examined in the following by analyzing the interface between the donor material F_4ZnPc and the HTL sNiO.
Note, that efficiencies achieved here are comparable to those obtained for similar stacks in former work at the same system [144] and in literature: the maximum efficiency achieved by Brendel et al. in 2015 with MoO_3 as HTL was 1.4 % with a V_{OC} of 0.65 V and a fill factor of 55 % [212].

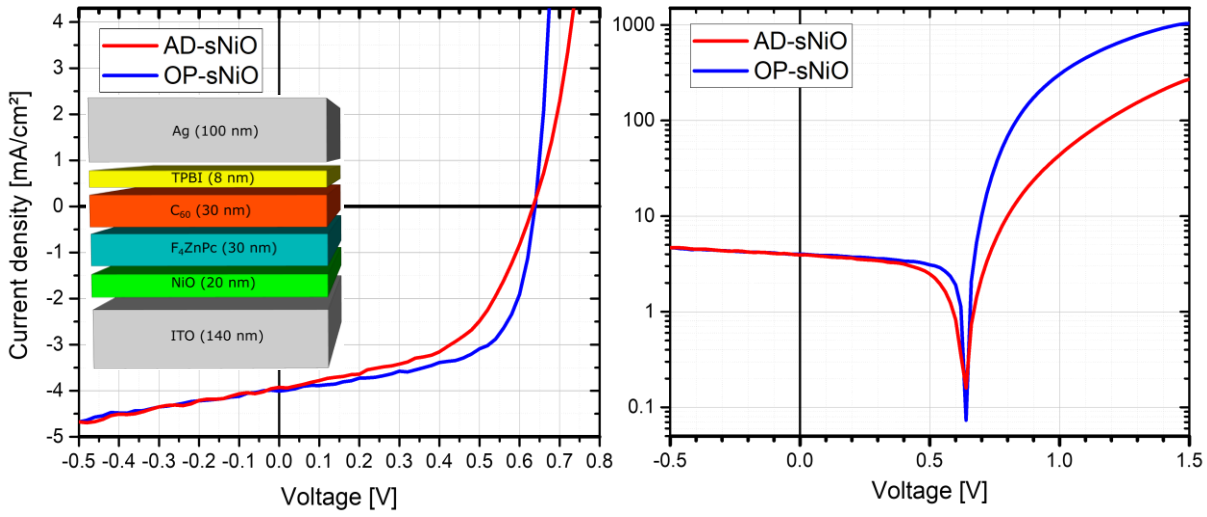

FHJ	J_{SC} [mA cm^{-2}]	V_{OC} [eV]	R_S [Ω cm^2]	R_{SH} [Ω cm^2]	*FF* [%]	*PCE* [%]
AD-sNiO	4.1 ± 0.1	0.64 ± 0.01	37 ± 2	772 ± 120	52.9 ± 0.8	1.37 ± 0 06
OP-sNiO	4.1 ± 0.1	0.64 ± 0.01	15 ± 2	840 ± 80	60.8 ± 0.9	1.59 ± 0.09

Figure 6.3: Representative device characteristics of FHJ OPVs with sNiO as HTL, with and without OP treatment with linear y-axis (left) and logarithmic y-axis (right). The table provides averaged device parameters of batches with 12 to 13 cells. The illustration of the stack was reprinted from [313].

6.2. Theoretical background: The organic/inorganic interface

To enable both a detailed understanding of the interface data and a comparison to literature, in this section a short review on existing theories on potential processes at interfaces between inorganic and organic materials is given.
A general, yet instructive, overview of possible interaction mechanisms of organic molecules with inorganic surfaces was provided by Ishii et al. [5] in 1999. The review focusses on organic/metal interfaces, while the concepts are not necessarily restricted to metallic substrates. Four different cases were distinguished for nonpolar molecules. First, a charge transfer between substrate and adsorbed molecule can occur, leading to the formation of anions or cations. Second, the interaction between the electron clouds of the molecule and the substrate may polarize the adsorbing molecule by the mirror charge formed in the metal. Another result of this interaction is known as "push-back" or "pillow" effect. Here, the metal's electron wave tailing into the vacuum (also called spill-out) is reduced and pushed back toward the substrate's surface, leading to a reduction of the substrate's work function. Third, a chemical reaction can take place and finally, interface states may exist or are formed, also influencing the energy alignment by providing an additional density of states (DOS) in the band gap. Moreover, polar molecules can create interface dipoles. In this case, also the orientation of the molecules plays a crucial role for the magnitude and direction of the potential step induced by the molecular layer.

In a large number of experiments by different groups the interface formation of nonpolar organic molecules and polymers on inorganic substrates has been studied with UPS [66,213–219]. In these experiments, the most important quantities are the work functions of the clean substrates Φ_{sub} and the work functions of the thin organic layers on the substrates $\Phi_{\mathrm{org/sub}}$. The overall findings can be summarized as follows: for the weakly interacting, in particular nonreacting interfaces between organic adsorbate (whether it is a small molecule or a polymer) and inorganic substrate, three different types of interface alignments are found. For both very high and low work functions (i.e., in the range of the molecule's HOMO and LUMO, respectively) a Fermi level pinning is observed such that the work function of the thin organic layer on top of the substrate is independent of the substrate's work function. For intermediate substrate work functions the alignment roughly follows a linear trend. The slope

$$S = \frac{d\Phi_{\mathrm{org/sub}}}{d\Phi_{\mathrm{sub}}}, \tag{6.1}$$

also called slope or screening parameter, depends on the type of the substrate and the specific fabrication process of the interface [220]. There has been a series of publications [6,215,216], in which thin conjugated polymer films were spin-coated onto different substrates, including metals with native oxide, gold and organic layers. Slope parameters close to unity were found. Thus, the Schottky-Mott rule, i.e., vacuum level alignment, applies. The authors concluded that in this regime no charge transfer between substrate and adsorbate takes place.
The pinning behavior, in contrast, was explained by a charge transfer from or into, respectively, so-called integer charge transfer (ICT) states of the adsorbing molecules. The ICT^+ (ICT^-) state is the energy level of a singly positive (negative) charged molecule and does not coincide with the LUMO (HOMO) of the respective molecule due to polaronic relaxation [6]. According to the model, a charge transfer takes place when the work function of the substrate is larger (smaller) than the energy with respect to to the vacuum level of the ICT^+ (ICT^-) states of the organic molecules. Thus an interface dipole is created, which aligns the Fermi level with the ICT states. This explains the pinning of the Fermi level several hundred meV below (above) the LUMO (HOMO). The ICT model was criticized for resulting in unrealistically large values of the polaronic relaxation energy [220,221] and for

relying on data measured at films with thicknesses in the range of 10 nm instead of measuring monolayers.
For molecules evaporated in vacuo on ultra-clean metal surfaces, much smaller slope parameters were observed [222]. Vazquez et al. applied the induced density of interface states (IDIS) model, originally developed for inorganic semiconductor interfaces, to interfaces between evaporated molecules and metal films and succeeded in predicting interface dipoles and hole injection barriers [222–224]. The model is based on the idea that the overlap of the electronic wavefunctions of (flat-lying) molecules with those of the metal results in a Lorentzian broadening of the discrete energy levels of single undisturbed molecules. Thus, a new, now continuous, DOS is created and can be obtained via DFT calculations. In a next step, the DOS is filled with electrons equal in number to electrons in the neutral molecule. The highest filled level is referred to as charge neutrality level (CNL) and can be seen as the Fermi level of the molecule. The difference between the energetic position E_{CNL} of this CNL of the adsorbed molecules and the Fermi level of the metal substrate, defined by the work function of the metal Φ_{m}, leads to a charge transfer across the interface and thus to an interface dipole reducing the distance between the Fermi level of the combined system and the CNL. The extent of this equalization depends on the slope (or screening) parameter

$$S = \frac{1}{1 + 4e^2 D(\mathrm{CNL}) d/A'} \tag{6.2}$$

where d is the distance between the molecule and the metal surface, A is the area associated with the molecule and $D(\mathrm{CNL})$ is the induced DOS around the CNL. The screening parameter influences the interface dipole

$$\Delta = (1 - S)(\Phi_{\mathrm{m}} - E_{\mathrm{CNL}}), \tag{6.3}$$

which pushes the Fermi level of the combined system

$$E_{\mathrm{F}} = E_{\mathrm{CNL}} + S(\Phi_{\mathrm{m}} - E_{\mathrm{CNL}}) \tag{6.4}$$

closer to E_{CNL}. For small values of S ($S \approx 0$) the screening is low, the induced DOS around the CNL is large, therefore the position of the highest occupied energy level of the molecule is little affected, even if much charge is transferred, such that an interface dipole is created until E_{F} is pinned to the E_{CNL}. For large values of S ($S \approx 1$), the screening is large, which means that only little charge has to be transferred to shift the position of the highest occupied energy level of the adsorbate toward to Fermi level of the substrate. Thus, the interface dipole is small, and the alignment roughly follows vacuum level alignment.
As can be seen in Equation (6.2), the slope parameter depends on the DOS around the CNL, which in turn is decisively determined by the interaction of the molecule with the substrate. If, for example, the distance of the molecule to the metal surface is increased from 2.8 to 3.5 Å, the calculated DOS decreases by a factor of three [214]. This is why S for contaminated metal surfaces [214] and also for organic/organic interfaces is larger [222]. The reduced interaction leads to a reduced density of states in the band gap and thus the alignment rather follows the Schottky-Mott rule.

For organic/metal oxide interfaces, it was a point of discussion whether also the Fermi level of the substrate dictates the alignment at the interface or rather the transport states, i.e., the valence and conduction band, respectively. In 2012, however, it was shown experimentally by Greiner et al. by investigating the interface of (nonpolar and nonreacting) organic molecules with a large variety of metal oxides that also in the case of the semiconducting metal oxide substrates the work function Φ and not the band structure is the decisive quantity for predicting the energy level alignment at the

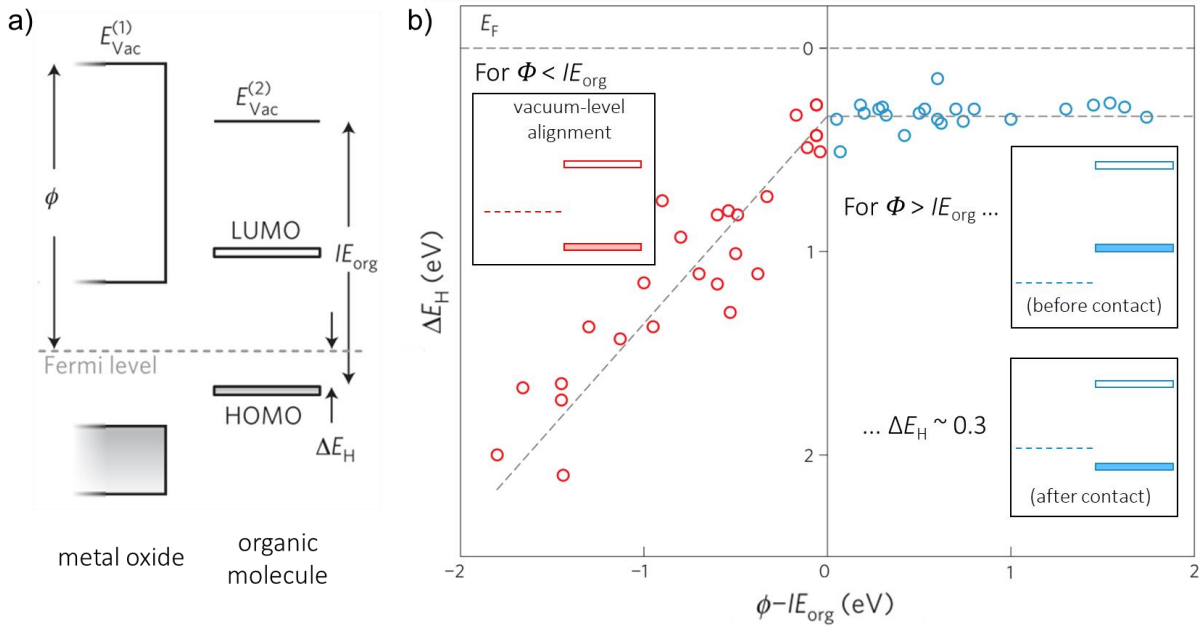

Figure 6.4: Illustration of the "universal energy-level alignment of molecules on metal oxides" accoring to Greiner et al. [225]. (a) Depicts the definition of the work function Φ of the metal oxide, the ionization energy IE_{org} of the organic molecules and the HOMO offset ΔE_H. (b) Experimentally determined HOMO offsets plotted against the difference of the substrates' work function and the ionization energy of the organic molecules. For the plot, three different organic molecules (CBP, α-NPD and 2T-NATA) were measured on various different metal oxide substrates. The insets depict the Fermi level of the metal oxide and the HOMO/LUMO positions of the organic adsorbate for the two cases $\Phi < IE_{org}$ and $\Phi > IE_{org}$ to illustrate the findings of Greiner et al. Reprinted and adapted from [225].

interface [225]. By interface experiments and taking UPS data of monolayers the authors found a very similar dependency as discussed above, whereas here the HOMO offset ΔE_H, i.e., the difference between the substrate's Fermi level and the adsorbate's HOMO onset at the interface was plotted against the difference between the substrate's work function Φ and the ionization energy of the adsorbing organic molecules IE_{org} (Figure 6.4). They concluded that only this difference Φ - IE_{org} determines the alignment and gave the following explanation: when the substrate's Fermi level lies above the HOMO onset ($\Phi < IE_{org}$), charge transfer is energetically not favorable and vacuum level alignment occurs (Figure 6.4b, red data points). In this regime, the HOMO offset ΔE_H roughly depends linearly on the difference Φ - IE_{org} before contact. However, when a substrate-molecule combination was chosen for which $\Phi > IE_{org}$ applied, a Fermi level pinning at about 0.3 eV above the ionization potential of the organic adsorbate was found and explained by a charge transfer from the adsorbate to the substrate (Figure 6.4b, blue data points). As the study comprised a large variety of different types of metal oxides, other influences like the valence band position could be excluded.
The experimental data was fitted by the authors by a model based on Fermi-Dirac statistics and basic electrostatic. Ley et al. [221] criticized the model for being physically unreasonable (it was necessary to model a thick adsorbate layer in order to explain the experimental data of one monolayer) and provided a refined model without any adjustable parameter. Still, only discrete energy levels were assumed. In 2014, Oehzelt et al. presented a versatile electro-static model [226] which also takes the finite width of the HOMO and LUMO level into account and is able to describe all regimes of energy level alignment for different types of interfaces. It also predicts non-integer values of S when the Lorentzian contribution is increased compared to the Gaussian contribution and underlines the importance of the DOS in the band gap for energy level alignment.

What is common to all these models and experimental data is the linear regime for substrate work functions between HOMO and LUMO of the organic adsorbate, whereas the slope depends on the

specific system, and Fermi level pinning for a Fermi level of the substrate in vicinity to the HOMO or LUMO level of the organic adsorbate, respectively.
In the current experiment, the validity of these relations will be tested for the interface of the organic molecule F_4ZnPc and solution-processed NiO.

6.3. Details on F_4ZnPc

This chapter provides basic information on F_4ZnPc. The molecule is a derivative of phthalocyanine, an organic molecule with the chemical formula $F_4(C_8H_4N_2)_4H_2$. Phthalocyanine has a flat structure with a fourfold rotational symmetry, as it is made of four identical isoindole units, which are connected via nitrogen atoms to form a macrocycle. It features high chemical and thermal stability. In the center of the molecule, a zinc ion is located, whereas also other metals like iron or copper can be used instead [227,228]. By replacing outer hydrogen atoms the morphological and electronic properties of the molecule can be altered [119,229,230]. In the case of F_4ZnPc, four of the outer hydrogen atoms are substituted by fluorine. Due to its strong electronegativity, fluorine possesses the ability to increase the ionization potential and thus the effective band gap in C_{60}-based solar cells [119,212,230,231], which in turn can lead to an increased V_{OC} and a gain of efficiency of 30 % [119]. In contrast, the band gap is barely influenced by the fluorination [232]. The molecular structure of F_4ZnPc is shown in Figure 6.5. According to literature, F_4ZnPc has an electron affinity of 3.9 eV, an ionization energy of 5.3 to 5.5 eV, and a work function of 4.4 eV [119,212]. The molecular mass is 649.88 g/mol, the density amounts to 1.6 g/cm³ [233]. The lateral dimensions are about 1.3 nm x 1.3 nm [234].
As described in Chapter 4.1.2, IR spectroscopy provides the possibility to obtain information about the orientation of molecules on a surface or in a sample through the detection of in-plane (ip) and out-of-plane (oop) modes. For F_4ZnPc this is nicely possible as both types are present with strong modes [143]. Figure 6.5 illustrates the two strongest modes which were used by Dr. Sabina Hillebrandt for the calculation of the molecular orientation.

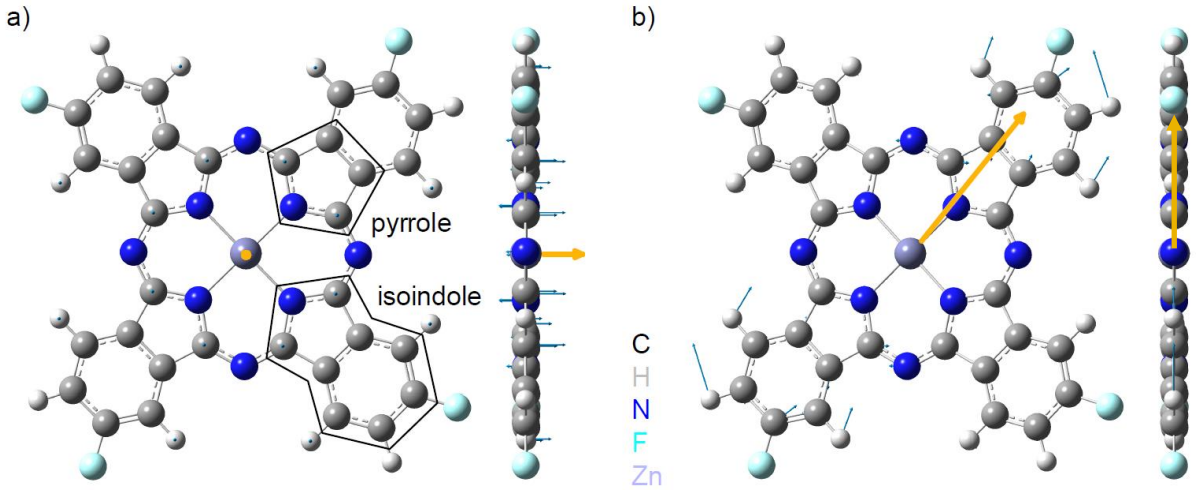

Figure 6.5: Structure of an F_4ZnPc molecule including visualizations of the strongest oop and ip modes in (a) and (b), respectively. The yellow arrows indicate the changes of the transition dipole moment, induced by the vibrational modes. Reprinted from [143].

6.4. The influence of OP treatment on the sNiO/F_4ZnPc interface

The interface experiment being presented in this chapter was performed at the clustertool of the InnovationLab in Heidelberg (see Chapter 4.2.1) in collaboration with Dr. Sabina Hillebrandt from the Kirchhoff-Institute for Physics in Heidelberg. F_4ZnPc was evaporated in UHV step-wise on top of two sNiO-325/ITO samples, whereas one of both samples was treated with OP. The substrate material sNiO was produced in the same way as before (see Chapter 4.3.2). To provide comparability to the device data discussed in Chapter 6.1, 325 °C was chosen as annealing temperature. Both sNiO films were produced at the same day to avoid batch-to-batch variations. During the whole experiment samples were kept in UHV.
F_4ZnPc was simultaneously evaporated on both samples with a deposition rate of 1.5 Å/min according to a calibrated quartz crystal microbalance (QCM). After 8, 18, 36 and 80 Å XPS and IR measurements were performed. For the thickness of 80 Å, spectra were almost identical, and the work functions were the same. Therefore, no significant differences between both samples were expected for thicknesses larger than these 80 Å. Also IR confirmed a range of interaction within the first nm and a constant molecular orientation for thicknesses above 150 Å. Two additional thicknesses (180 and 300 Å) were measured on the AD sample. The values obtained from the thickest layer (300 Å) were regarded as intrinsic values of F_4ZnPc and also referred to as bulk-F_4ZnPc in the following. Evaporation was conducted by Dr. Michael Scherer from the TU Braunschweig.

6.4.1. PE spectroscopy

Survey spectra depicted in Figure 6.7 for both AD- and OP-sNiO show clean sNiO substrates largely free of adsorbates or contaminations. All characteristic NiO lines are visible. Additionally, the spectra confirm that the sNiO layers are closed also on relatively rough ITO: no sign of indium ($BE_{\mathrm{In3d}} \approx 450$ eV) passing the sNiO layers is detected.
After the first evaporation step, all major lines which are expected from the atomic composition of F_4ZnPc appear and gain intensity as the evaporation continues. For 180 Å no lines from the AD-sNiO substrate are visible anymore. Based on the damping of the Ni 2p signal, and an IMFP of 18.7 Å (estimated by TTP-2M formula [129] for $E_{\mathrm{kin}} = 617$ eV) nominal layer thicknesses were calculated. As it can be seen in Figure 6.6, the curves indicate a "Volmer-Weber growth" in the beginning, which is assumed to be due to incomplete coverage for submonolayers (8 Å and below). A different sticking coefficient of the molecules on the NiO substrate than on themselves is also possible. For thicknesses above 8 Å, the growth appears to be rather uniform without large islands as the curves align approximately parallel with the measurements of the QCM. The deviation from fully parallel curves may also be related to an uncertainty in the estimated IMFP.

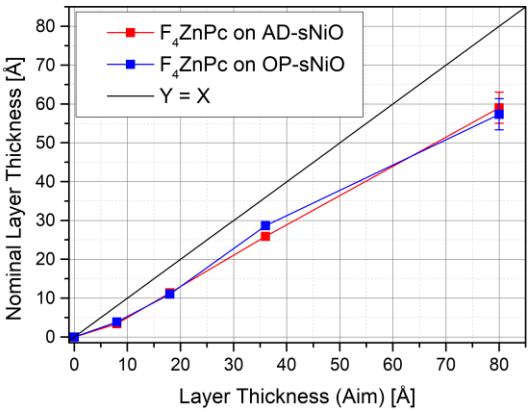

Figure 6.6: Nominal layer thicknesses of the evaporated F_4ZnPc films on both substrates (AD- and OP-sNiO) as a function of the thickness measured via a QCM.

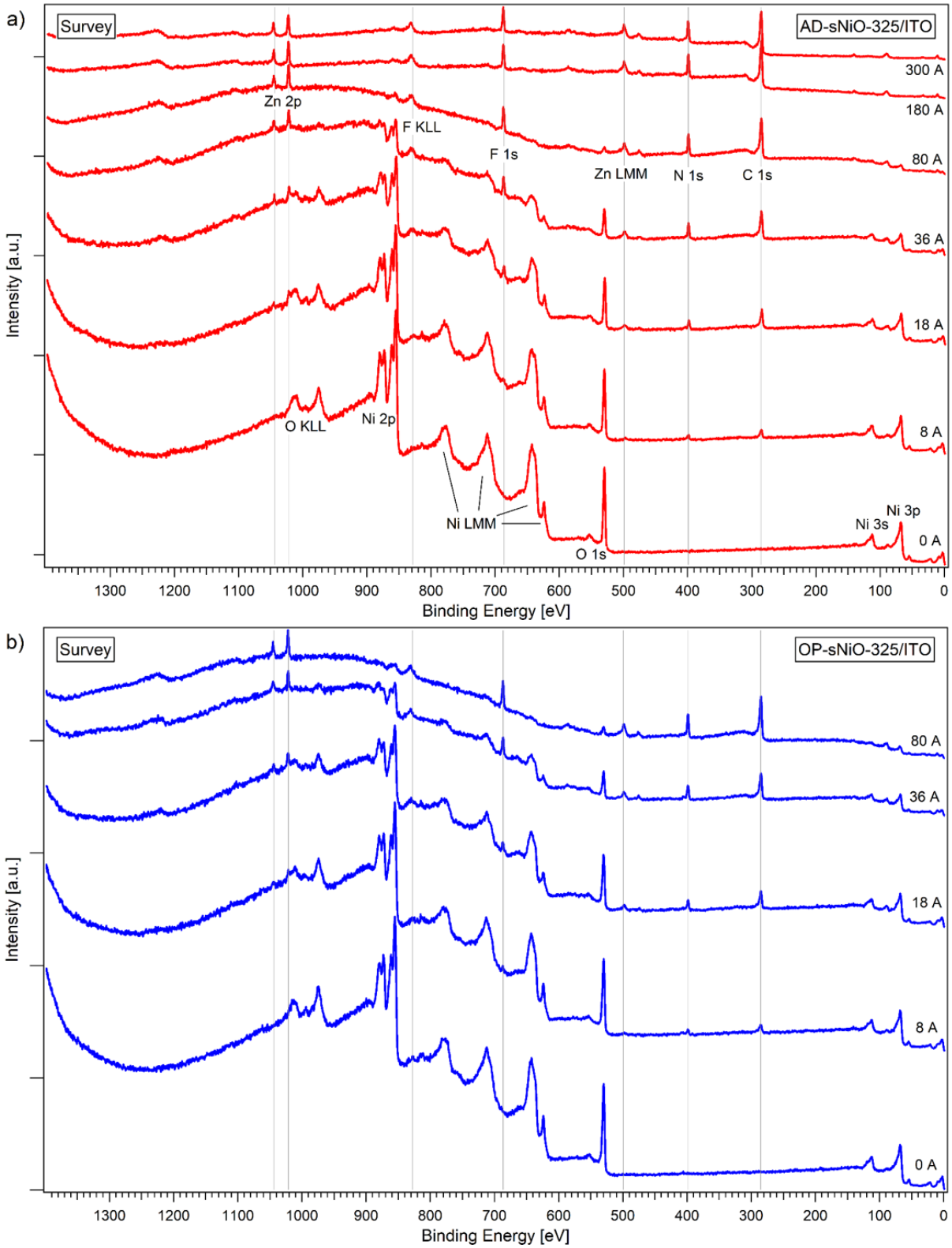

Figure 6.7: Survey spectra of AD- and OP-sNiO films with evaporated F_4ZnPC in different layer thicknesses.

Core level spectra of the substrates

Figure 6.8a and b show the evolution of the substrate's core level lines (Ni $2p_{3/2}$ and O 1s) during evaporation. The diagrams contain both spectra as-measured and those normalized in intensity to the uncovered substrate for a better visibility of minor changes. Additionally, secondary electron cutoff (SEC) and valence band maximum (VBM) spectra measured with XPS are displayed (Figure 6.8c and d). Since the cross-section for X-ray induced photoionization close to the Fermi level in organic compounds is small, the valence band signal can be assigned to the sNiO substrate. Spectra on the left-hand side were taken on the AD-sNiO sample (red), spectra on the right hand side from the OP-sNiO film (blue). In the Ni $2p_{3/2}$ region no strong changes are visible, neither regarding the Fermi level position nor regarding the spectral shape. In particular, the spectral differences between AD- and OP-sNiO are preserved. This is also true for the O 1s peaks (see Figure A.18 for a direct comparison). In particular the regions assigned to NiOOH formation stay the same. However, small but significant alterations in the side peaks occur after the first deposition step: for both substrates (AD- and OP-sNiO), the side peak increases and sharpens slightly (insets in Figure 6.8b). Tiny changes of the side peak still occur after the second step (18 Å), but afterwards it stays about the same. Obviously, OH groups are somehow affected by the first layers of the adsorbate. Still, evaporation of F_4ZnPc does not destroy the NiOOH layer created during the OP treament.
The scans of the valence band regions reveals tiny shifts in the range of 50 meV toward lower binding energies for the AD sample, whereas for OP no trend is visible.

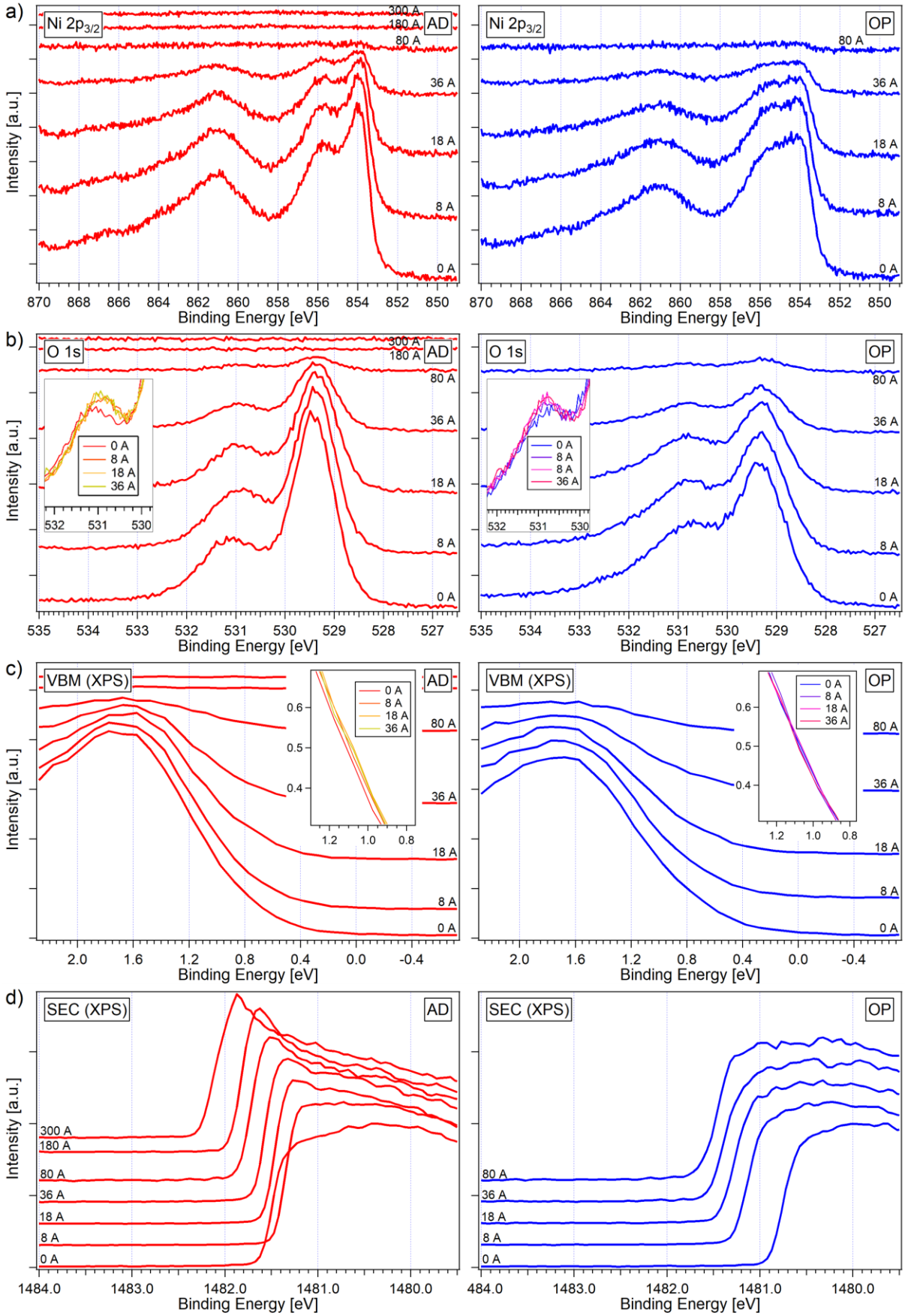

Figure 6.8: Core level lines, VBMs and SECs of the two sNiO samples after multiple evaporation steps. From bottom to top the layer thicknesses are 0, 8, 18, 36, 80, 180 and 300 Å. The insets show the same spectra but normalized.

Core level spectra of the adsorbate

The adsorbate lines and its evolution will be discussed in more detail. The C 1s regions of both samples are depicted in Figure 6.9a. Especially for thicker layers of F_4ZnPc the spectra are composed of basically three distinct features, whereas the middle one contains at least two different contributions. It is well known that the main peak at the lowest binding energy around 284.7 eV can be attributed to carbon which is only connected to other carbon or hydrogen atoms [125,228,232,234]. According to literature measurements on phthalocyanins, the component at the highest binding energy at ~288 eV can be assigned to a π-π* satellite [228,231,235]. In the case of ZnPc, the non-fluorinated derivate of F_4ZnPc, the middle structure around 286 eV contains only one main contribution, which was attributed to those carbon atoms being attached to nitrogen [232]. Therefore, the lower binding energy feature of the double peak structure in the case of the fluorinated derivative investigated here (~286 eV) is also assigned to CN, while the additional feature at slightly higher binding energies of about 287 eV can be explained by carbon bound to fluorine [232]. A similar assignment has also been found for F_4CuPc [228,235]. The shift of the CF component with respect to the CN component is related to the stronger electronegativity of flourine compared to nitrogen (3.98 vs. 3.04 on the pauling scale [236]). Additionally, a small π-π* satellite contributes to the middle feature around 286.5 eV [235]. All in all, the C 1s spectra are almost identical to spectra of F_4CuPc in literature. This shape is roughly preserved for all thicknesses in both cases (AD and OP). Only for the thinnest layers deviations are observed (see Figure 6.9b). Possible reasons will be discussed later.

F 1s core levels of both samples (Figure 6.9c,d) show a peculiarity: two clearly separated components are visible in the first nanometers of F_4ZnPc, while for an intact F_4ZnPc molecule only one component is expected [228]. The first peak, at higher binding energy, is located at about 687 eV, in good agreement with literature (687.2 eV measured by Peisert et al. for F_4CuPc on Au [235]). The additional feature is located at 3 to 4 eV lower binding energies and is similar for both samples. With increasing layer thickness, the component decreases and has vanished for a thickness of 80 Å.
A similar splitting of the F 1s peak has also been observed for F_4CuPc on ITO [228] and ascribed to a ITO-F-Pc bond. However, due to the octet rule, such a configuration appears to be unlikely and is excluded.
Another possible explanation is a transfer of a negative charge from the substrate to the adsorbate. However, the shift is rather large for transition of a neutral to a charged molecule [237–240]. Furthermore, a similar component would be expected also in the other core level spectra (C 1s, N 1s and Zn $2p_{3/2}$), since the LUMO is not limited on the fluorine atoms, as shown by various DFT calculations [231,240,241]. On the contrary, experiments in which negative charge was transferred on phthalocyanine molecules indicated that the additional charge will mostly be located in the inner part of the molecules. Therefore, a charge transfer is excluded as well as origin for the second low-binding energy peak.
A final possibility is a chemical shift. According to literature, the F 1s binding energy of metal fluoride is several eV lower than the one of carbon fluoride [125,242]. Thus, the spectra could be consistent with the formation of a Ni-F bonds at the surface of sNiO. However, the binding energy of F 1s in NiF_2 is measured at about 685 eV and thus almost 2 eV too low [125]. On the other hand, fluorine can have such low binding energies, e.g., in alkali metal fluorine compounds [125]. Furthermore, it has to be considered that the binding energy in NiF_2 was measured in a solid, which differs from the proposed Ni-F bond at the surface of a NiO_x layer. Therefore, the formation of a Ni-F bond is considered to be reconcilable with the binding energy of ~683 eV measured here.
For these reasons a chemical reaction, which separates the fluorine from the molecule and leads to the low-binding energy component, is assumed. Details on this reaction will be discussed later in Chapter 6.4.4.

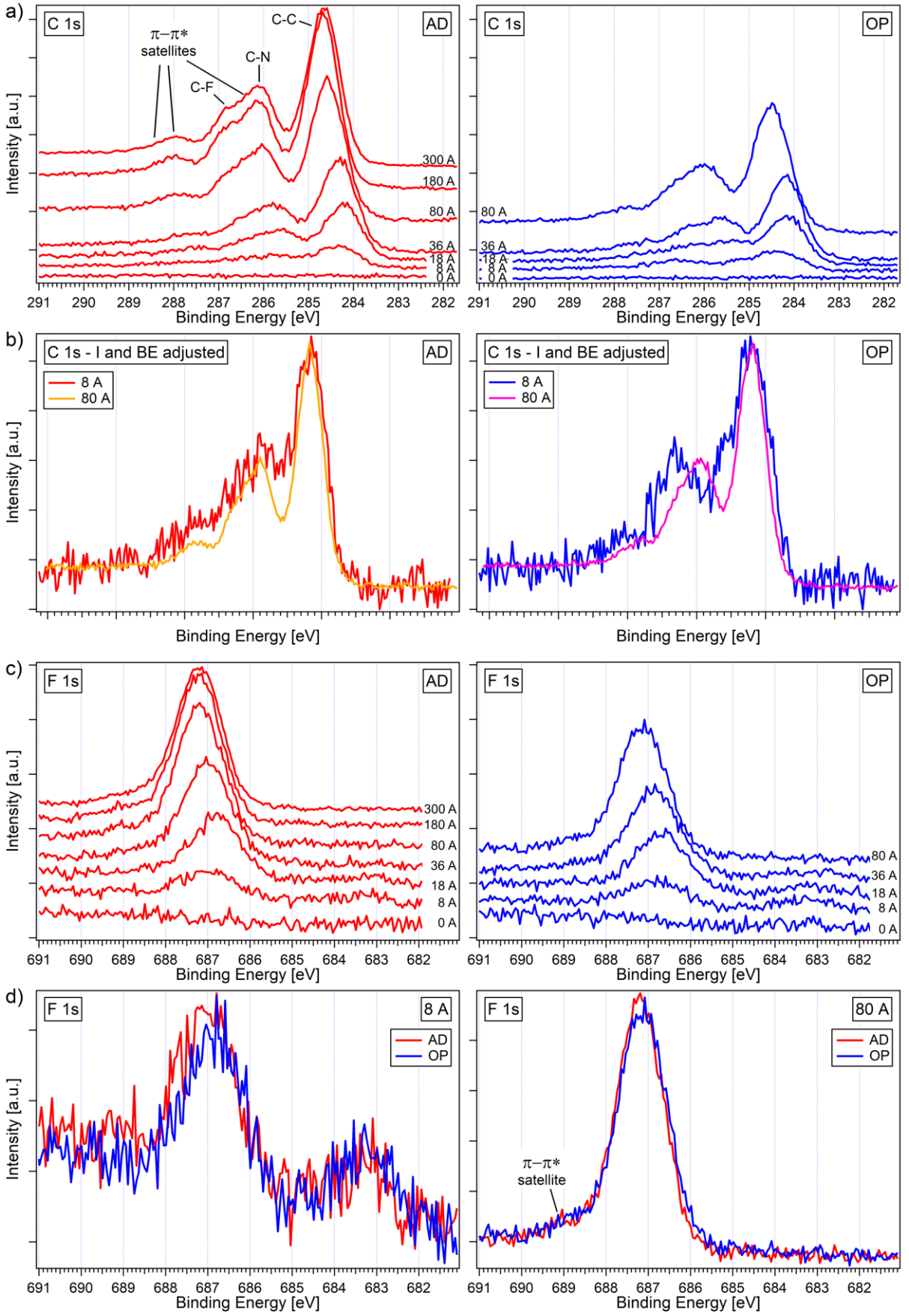

Figure 6.9: C 1s and F 1s detail spectra of the two sNiO samples (AD and OP) after multiple evaporation steps. From bottom to top the layer thicknesses are 0, 8, 18, 36, 80, 180 and 300 Å. The spectra in (b) were stretched in intensity and shifted in binding energy to enable a better comparison of the spectral features.

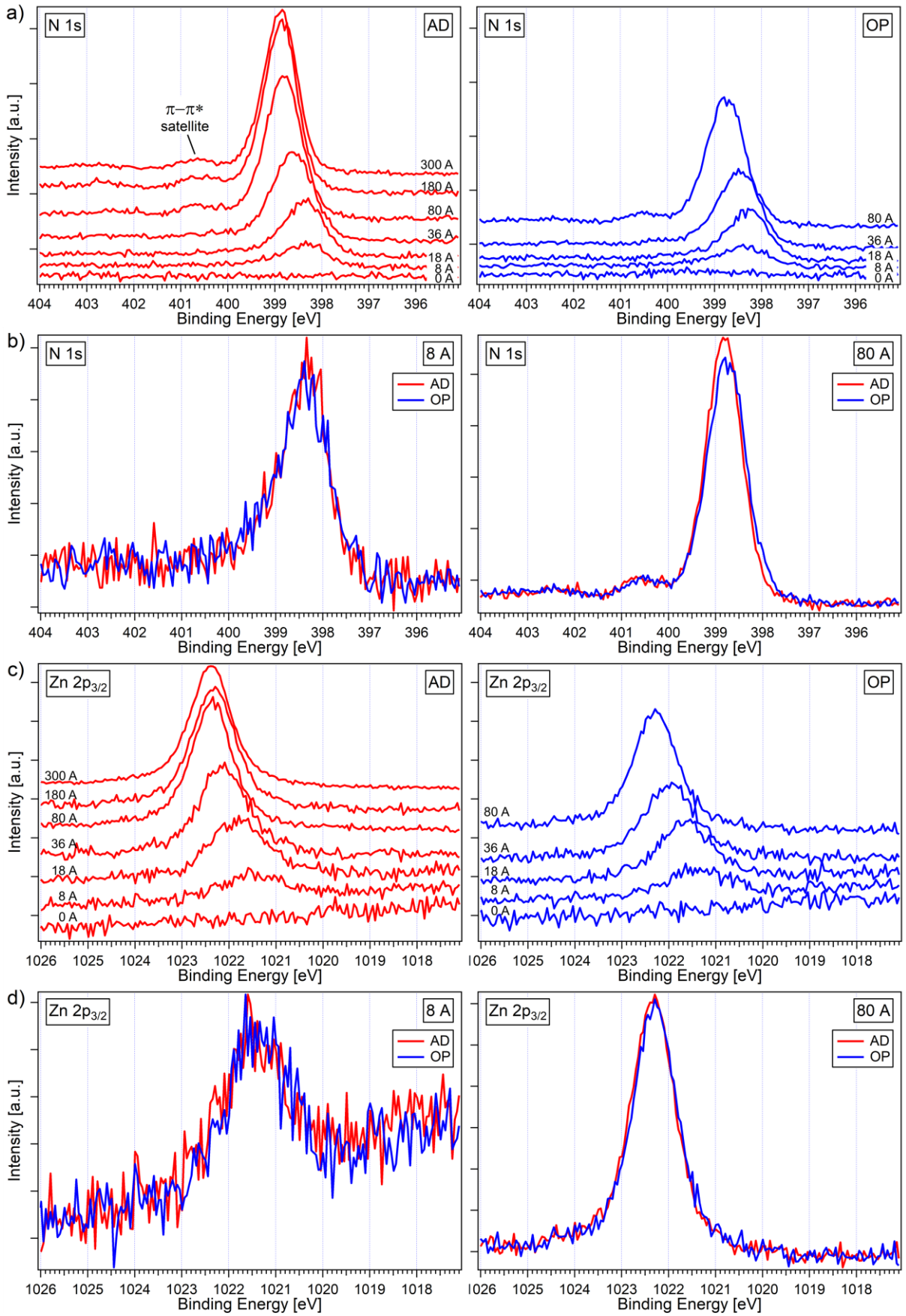

Figure 6.10: N 1s and Zn $2p_{3/2}$ detail spectra of the two sNiO samples (AD and OP) after multiple evaporation steps. From bottom to top the layer thicknesses are 0, 8, 18, 36, 80, 180 and 300 Å.

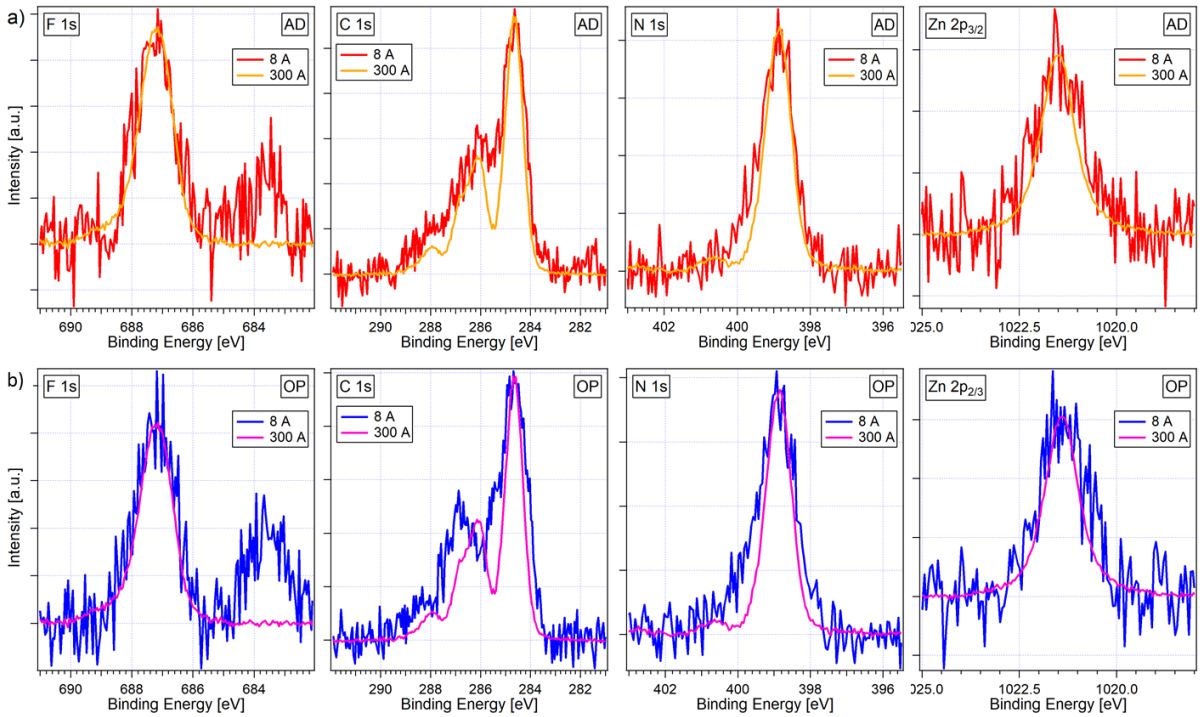

Figure 6.11: Comparison of core level spectra of 8 Å F_4ZnPc on AD-sNiO (a) and OP-sNiO (b), respectively, with respective spectra of 300 Å F_4ZnPc. The spectra of the thick layer were adjusted in both binding energy and intensity to fit to the spectra of the 8 Å film and enable a comparison of the shape.

In both regions, C 1s and F 1s, the spectral changes are accompanied by a clear ELS to higher binding energies in the range of about 0.5 eV during the course of the deposition. Similar observations regarding the Fermi level position also apply to the N 1s and Zn $2p_{3/2}$ detail spectra in Figure 6.10. Again, the spectra of both samples are very similar. The small side peak in the N 1s region (e.g., Figure 6.10b, right side) can be ascribed to the π-π* satellite [235]. This satellite is not clearly distinguishable in the spectrum of 8 Å F_4ZnPc (Figure 6.10b, left side). Instead, the peaks appear to be broader.

In fact, a slight broadening is visible for all four core level lines (F 1s, C 1s, N 1s and Zn $2p_{3/2}$) as a comparison between spectra taken at the thinnest F_4ZnPc layer with those taken at the thickest F_4ZnPc layer reveals (Figure 6.11). Such broadening can have different origins and will be discussed on p. 99.

UPS investigation

The valence band regions measured with UPS are displayed in Figure 6.12a and c. Figure 6.12b and d show magnifications of the HOMO onset regions of the same data together with the fits which were used for the determination of the onset values. For the saturated F_4ZnPc layer, reasonable values of 0.94 and 0.97 eV were obtained for measurements with He I and He II, respectively, in agreement with literature values of about 1 eV [119,212]. For the uncovered substrates, the determination of the valence band onset value is ambiguous. If the steepest incline of the first feature is taken as starting point for the tangent, quite large values are obtained (dashed lines). As thus a significant tail is neglected and the results differ from those obtained via XPS, fitting the tail instead is considered to be more appropriate.

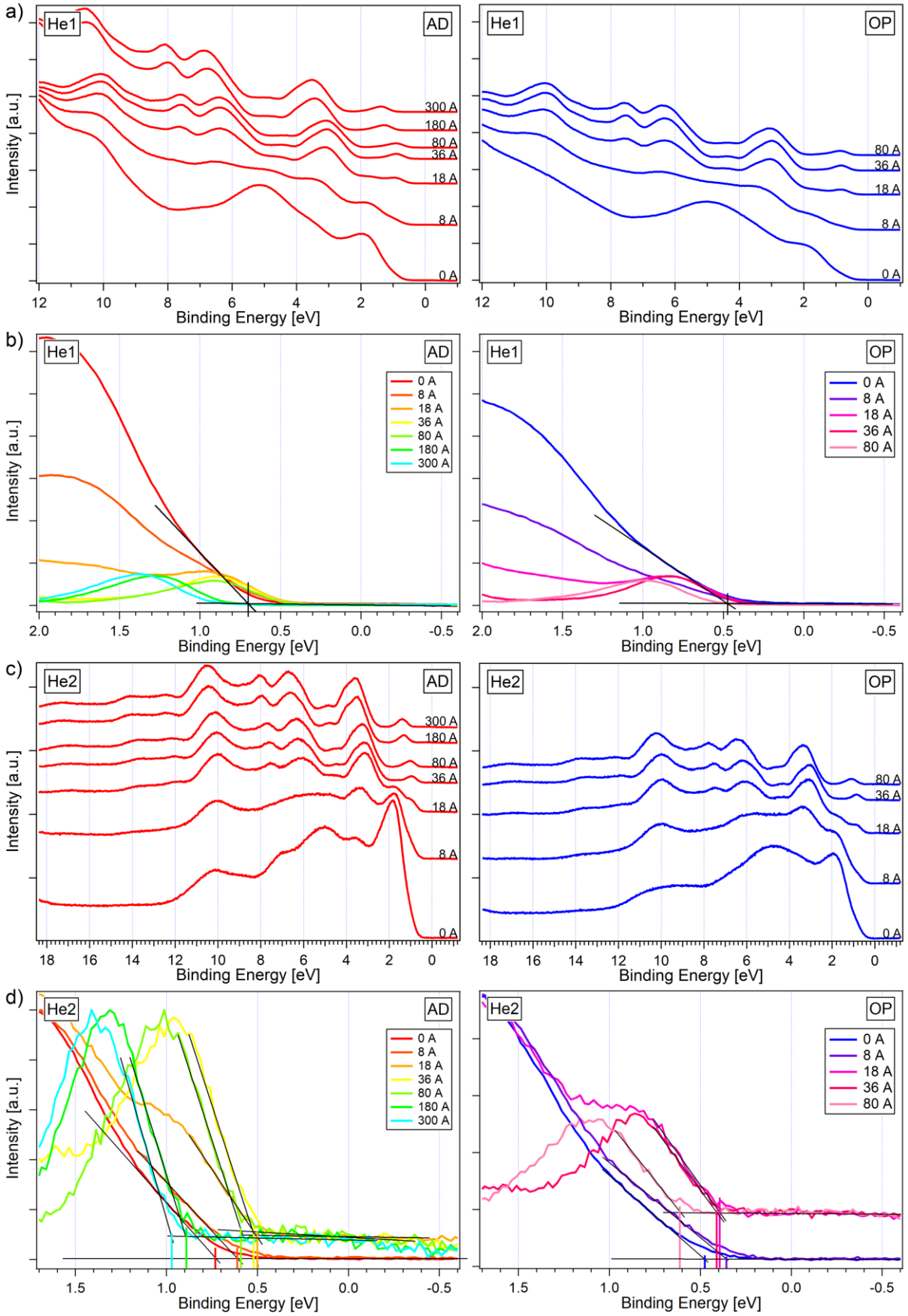

Figure 6.12: He I and He II spectra of the two sNiO sample after multiple evaporation steps. From bottom to top the layer thicknesses are 0, 8, 18, 36, 80, 180 and 300 Å. Spectra in (d) are scaled and shifted in intensity to enable a better visibility and comparability.

Quantitative analysis

To gain further quantitative insight into the situation at the interface, core level positions were determined with a simple gaussian fit function. For the F 1s line position, the main feature of the nonseparated fluorine atoms at higher binding energies was used. The changes of the substrate line positions with respect to the clean AD surface and the changes of the adsorbate line positions with respect to the final positions of bulk-F_4ZnPc are plotted against the estimated layer thickness in Figure 6.13a. Additionally, the work functions and the HOMO onset positions were extracted according to the description in Chapter 4.1.1 and added to the diagram. The error bars of the work function data points are the standard deviations of five measurements on different spots on each sample.

Both recorded core level lines (O 1s and Ni $2p_{3/2}$) of both sNiO substrates shift only slightly and for OP-sNiO no change at all can be observed. The VBM evolution (see Figure 6.8c for spectra) is qualitatively consistent with the shifts. The O 1s position is regarded as the most trustworthy, as it features the most distinct peak. This applies especially to the OP sample, where the Ni $2p_{3/2}$ main peak merges with the side peak and thus the position of the Ni^{2+} component cannot be unambigously extracted anymore, which is why the respective data points are missing in Figure 6.13a. Also the VBM data points were not added to the Figure, as fitting of the XPS-VBM of sNiO is always prone to some error due to the low intensity, especially for damped signals as it is the case here.

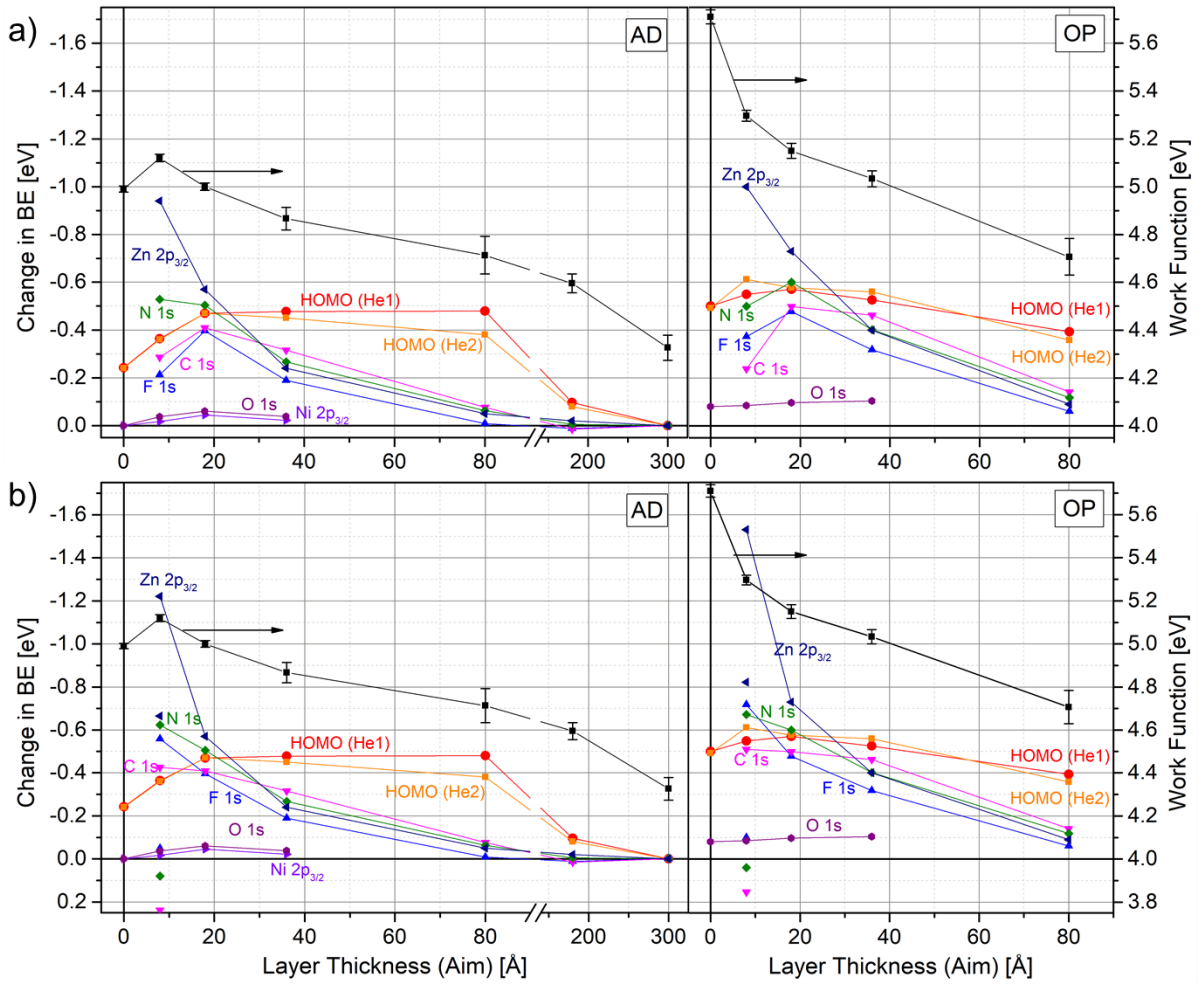

Figure 6.13: (a) Summary of changes of core level, VBM and HOMO onset positions during the deposition of F_4ZnPc on AD- and OP-sNiO, respectively. Core level positions were determined via fitting with a Gaussian function. In the case of the split F 1s peak, the peak at higher binding energies was used as it is attributed to undecomposed F_4ZnPc. (b) Shows the same data as in (a) except for the first layer thickness (8 A), where the binding energy positions of two-component fits are plotted (see Chapter 6.4.2). The data points connected with a line refer to neutral molecules, the unconnected points refer to supposedly positively charged molecules.

The work function of the AD-sNiO sample, again measured with XPS, slightly increases with the first deposition step. Thereafter, it roughly follows the trend of the adsorbate core levels for thicknesses until 180 Å. Consequently no strong changes of the ioniziation potential of F_4ZnPc occur in this range. Contrastingly, between 180 to 300 Å the ionization potential is suddenly reduced, although based on the evolution of the core levels it seems like the equilibirum bulk value has already been reached. A relation to changes in the molecular orientation is possible [243,244], also charge redistribution or polarization effects are thinkable. The work function of the final layer thickness of 300 Å is with (4.33±0.05) eV slightly below values in literature in the range of 4.4 eV [119,144,212]. In agreement with the observations from Chapter 5.3, the work function of the OP-sNiO sample starts at a higher value and is still increased for the first layer but similarly drops monotoneously to reach the same value at a thickness of 80 Å.

UPS measurements also deliver information on the potential distribution within the organic adsorbate, based on the HOMO position. While for the AD-sNiO sample the distance between the values for the first non-reacted layer (18 Å) and the final values agrees very well with the ones extracted from XPS corel level measurements, deviations exist in the distribution of the potential in between: for thicknesses of 36 and 80 Å the HOMO stays almost constant and only drops at higher thicknesses.
One tentative explanation might be the higher surface sensitivity of UPS compared to XPS in the range of only one or two monolayers. The different environment of molecules at the surface compared to molecules in the bulk may lead to the deviation. The sudden drop between 80 and 180 Å however, cannot be explained in this way. A change of molecular orientation is another possibility. The HOMO values measured on the OP-sNiO sample fit somehow better to the core levels, although the decline is still weaker than the one of the core levels.

The core levels behave very similarly for both samples for layer thicknesses of 18 Å and above: a monotoneous increase of all binding energies is observed. However, this is not the case for the first evaporation step. Here, only the Zn line follows the trend toward lower binding energies. All other core levels, which are the core levels from the macrocyle, deviate from the behaviour which is expected for a simple band bending. Of course the precision of peak fitting suffers from bad signal-to-noise ratio for such thin layers in the range of one monolayer, yet the effect has to be considered as significant.
At first glance, an explanation could be a charge transfer from the substrate to the adsorbate. If the charge was transferred to the central Zn atom, this would explain the low binding energies compared to the atoms of the macrocycle. Vice versa, a charge transfer from the macrocycle to the substrate may be a possibility. Such charge transfer can also be a reason for the broadening in the spectra of thin F_4ZnPc films and will be examined in the following.

6.4.2. Charge transfer – analysis and discussion

A charge transfer (CT) to a molecule leads to a change of the local potential due to the additional charge and thus a change of the electron's binding energies. Therefore, a compound consisting of a mixture of neutral and charged molecules exhibits spectra which are a superposition of the spectroscopic signature of neutral molecules and a shifted spectrum of the charged molecules. This has been demonstrated for example by S. Stolz [239]. Typically, an additional negative charge shifts spectra to lower binding energies, and an additional positive charge shifts spectra to higher binding energies. Shifts in the range of 1 to 2 eV have been measured [238,239]. If spectra are fitted and the two contributions can be separated, the ratio of charged to neutral molecules can be concluded based on the intensity ratio of both contributions. This idea is illustrated in Figure 6.14.

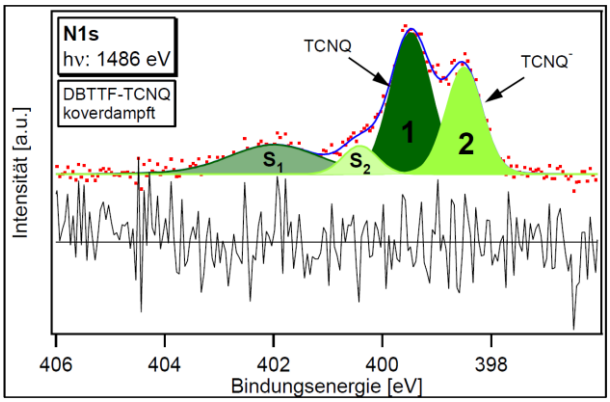

Figure 6.14: Exemplary fit of the N 1s region of a sample containing two differently charged TCNQ molecules. Each type is fitted with a main contribution and an additional peak accounting for a shake-up satellite. The contribution of molecules with an additional negative charge ($TCNQ^-$) is located at about 1 eV lower binding energies. Based on the integral intensity ratio, it was concluded that 37 % of the molecules are charged. Reprinted from [239].

In case of a charge transfer, the ratio of charged to neutral species should be found in all spectra of the respective molecule, while the energic shift depends on the probability of presence of the additional charge at the respective atomic site.
To examine the present spectra for the occurrence of a charge transfer, each spectrum of the atomic orbital AX of the first layer of F_4ZnPc was fitted with a superposition of two spectra $f_{\mathrm{AX}}^{300\mathrm{A}}(x)$ of bulk-F_4ZnPc (300 Å on AD-sNiO):

$$f_{\mathrm{fit}}(x) = h_1\, f_{\mathrm{AX}}^{300\mathrm{A}}(x - x_1) + h_2\, f_{\mathrm{AX}}^{300\mathrm{A}}(x - x_2) \tag{6.5}$$

The heights h_1 and h_2 and the shifts x_1 and x_2 were allowed to be optimized by the fit program to reduce the sum of squared residuals (SSR). The results are first shown and discussed for the AD-sNiO substrate and afterwards for the OP-sNiO substrate.

Analyzing XP spectra of F_4ZnPc on AD-sNiO

Figure 6.15 displays the fit results for the F_4ZnPc film on AD-sNiO. In all cases the fits converged and describe the data quite well. Only in the C 1s region some deviation of the fit from the data exists.
In all four regions, the component at lower binding energies (labelled with peak1) is more pronounced compared to the component at higher binding energies (labelled with peak2). According to the considerations of the last paragraph, peak1 can be attributed to neutral F_4ZnPc molecules and peak2 to F_4ZnPc molecules with an additional positive charge. In principle, the peaks could also be attributed to negatively charged molecules (peak1) and neutral molecules (peak2). In this case, however, the N 1s

binding energy of neutral F_4ZnPc would be even higher than when extracted from the nonfitted data, with the consequence that the "kink" between the first and the second layer (8 and 18 Å, respectively) in the diagram in Figure 6.13a would be even more pronounced. Therefore, in the following, it is focused on the former interpretation: peak1 corresponds to neutral and peak2 corresponds to positively charged molecules.

For N 1s, C 1s and Zn $2p_{3/2}$, the ratios $r = h_2/h_1$ between both components (peak1 and peak2) lie in a narrow range from 0.33 to 0.4. For the fit of the N 1s spectrum, the relative error of the ratio is given as 0.01, which results in $r_{N1s} = 0.33 \pm 0.03$. Thus, the ratio of $r_{Zn2p3} = 0.36$ from the Zn $2p_{3/2}$ region lies within the error bar. In contrast, this does not apply for $r_{C1s} = 0.42 \pm 0.03$.

For the F 1s region, the ratio $r_{F1s} = 0.79 \pm 0.21$ is significantly larger. However, here a second emission at lower binding energy is present. This component was attributed to a chemically different fluorine species and has about one third of the integrated intensity of the main line at higher binding energies. If one assumes that it completely stems from neutral molecules (peak1), the ratio between charged and neutral molecules would amount to $r_{F1s,corrected} = 0.50 \pm 0.14$ and thus still is hardly compatible with $r_{N1s} = 0.33 \pm 0.03$.

To test the validity of the fits, the same data has been fitted with different start parameters. The parameters were chosen such that the data is described sufficiently well while it was made sure that this time the high-binding energy component exceeds the low-binding energy component. Then again, the fit program minimized the SSR. The results are shown in Figure 6.16.

For the C 1s spectrum, the converged fit has a peak ratio r of 0.54 ± 0.04 instead of 0.42 ± 0.03, which illustrates that the fit result is not unique and does depend on the start parameters. The mean squared

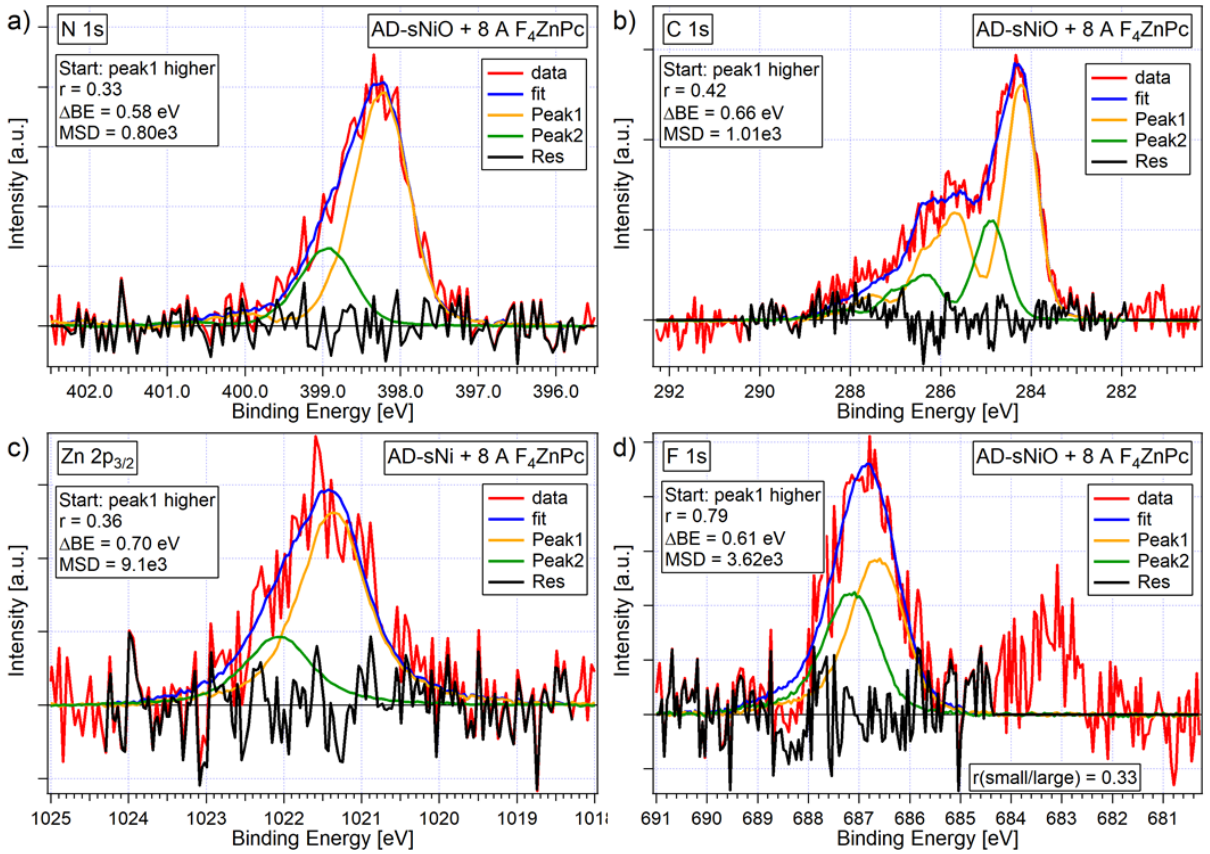

Figure 6.15: Two-component fits of core level spectra of 8 Å F_4ZnPc on AD-sNiO. In each case, the starting parameters were chosen such that the left peak (peak1) was smaller than the right peak (peak2). During the fit, the height and binding energy position were adjusted to minimize the sum of squared residuals (SSR). The residua are indicated in black. The insets show the intensity ratio r between peak2 and peak1, the difference in binding energy ΔBE between both peaks and the mean squared deviation (MSD) of the fit result, which is defined as the SSR divided by the number of data points. All data was corrected for Shirley background prior to fitting. See Figure A.12 for more details.

deviation (MSD, defined as SSR divided by the number of data points) is only 4 % larger than for the fit in Figure 6.15b and thus also possesses a certain validity, especially given further influences like uncertainties for background-subtraction. Therefore, it was tried to obtain a fit with r = 0.33, the unique ratio obtained from the fit of the N 1s region (Figure 6.15a). Indeed, as shown by the diagram in Figure 6.16b, a reasonable fit with a similar MSD as before is possible. Thus, considering the freedom in fitting the C 1s emission, an amount of 33 % charged molecules would also be consistent with the C 1s spectrum.
Also for the Zn $2p_{3/2}$ and the F 1s spectra (Figure 6.15c,d) different fit results are possible, when different start parameters are used. Here, the converged fits even exhibit an inverted intensity ratio r with similar or even smaller MSDs.
Therefore, one must conclude that a charge transfer of 0.33, which means that one third of the molecules at the interface is charged, as dictated by the fit of the N 1s line, might be found as well in the Zn $2p_{3/2}$ and C 1s lines, but hardly in the F 1s region. Furthermore, in none of these three spectra the confirmation of the ratio is unambiguous.
A further argument is found in the evolution of the work function. According to Poisson's equation a change in the charge density is accompanied by a change in the electric potential and vice versa. This is for example the reason why the push-back effect leads to a reduction of the work function of metal, as discussed in Chapter 6.2. However, as shown in Figure 6.13a, the work function of AD-sNiO is not reduced after the deposition of 8 Å F_4ZnPc as one would expect in case of positive charge transferred to the adsorbate, but even slightly increased instead.

Therefore, at this point, the occurrence of a charge transfer at the F_4ZnPc/AD-sNiO interface seems to be unlikely, although it is roughly compatible the spectra.

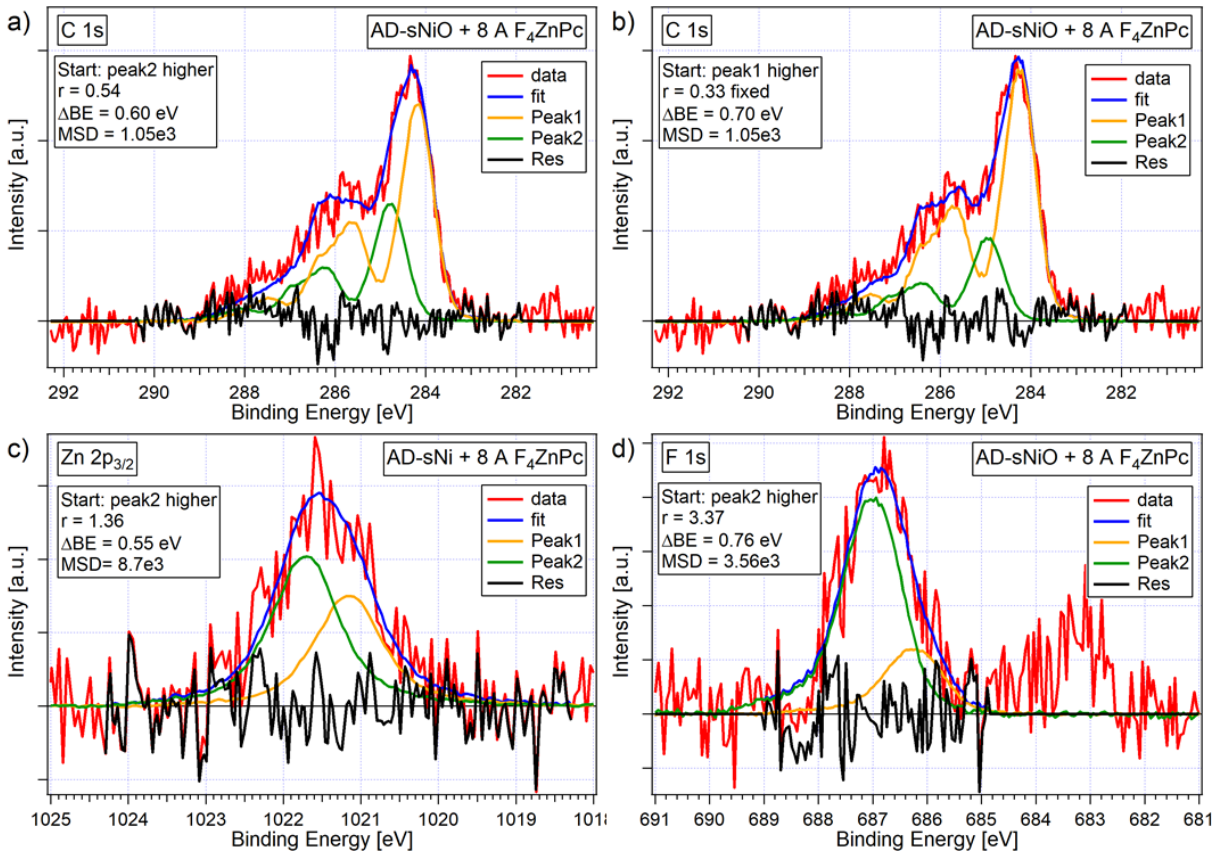

Figure 6.16: Two-component fits of core level spectra of F_4ZnPc similar to the fits in Figure 6.15, except for different start parameters: in (a), (c) and (d) peak2 was set significantly larger than peak1. In (b) the ratio between both contributions was set to a fixed value of 0.33.

Analyzing XP spectra of F_4ZnPc on OP-sNiO

For the F_4ZnPc/OP-sNiO interface the situation is different, insofar as a strong change of the work function at the interface indicates the formation an interface dipole and thus the exchange of charge. As the work function is reduced upon adsorption of F_4ZnPc (by about 0.4 eV, see Figure 6.13a), the transfer of positive charge on the adsorbate is expected. Therefore, in the following, also the interface between OP-sNiO and F_4ZnPc is examined for charge transfer.

As can be seen in Figure 6.17 also the spectra of 8 Å F_4ZnPc on OP-sNiO can be fitted with a supercomposition of two spectra of bulk-F_4ZnPc. Only for C 1s a deviation exists, which is even larger than for the according spectrum of F_4ZnPc on AD-sNiO. The ratio between the two components of the N 1s emission (Figure 6.17a) is here determined to $r_{N1s} = 0.51 \pm 0.04$. However, as demonstrated in Figure 6.18a, if the peak ratio of the start parameters is inverted ($h_1 < h_2$), also a ratio of $r_{N1s} = 0.61 \pm 0.04$ can be obtained with a similar MSD.

The fit of the C 1s spectrum converges uniquely with $r_{C1s} = 0.82 \pm 0.06$. Thus, it is clearly not compatible with the fit result of the N 1s spectrum. For Zn $2p_{3/2}$ the fit even does not converge with a ratio smaller than one. Independent of the start parameters, peak1 is finally larger than peak2 (Figure 6.17c and Figure 6.18c). Both ratios ($r_{Zn2p3} = 1.34 \pm 0.14$ and $r_{Zn2p3} = 2.1 \pm 0.4$) are neither compatible with r_{C1s} not with r_{N1s}.

Also, for the F 1s line the fit does not converge uniquely and ratios larger or smaller than one can be obtained depending on the start parameters (Figure 6.17d and Figure 6.18d). Even if the result with the ratio smaller than one is used to estimate the corrected ratio by counting the low-binding energy

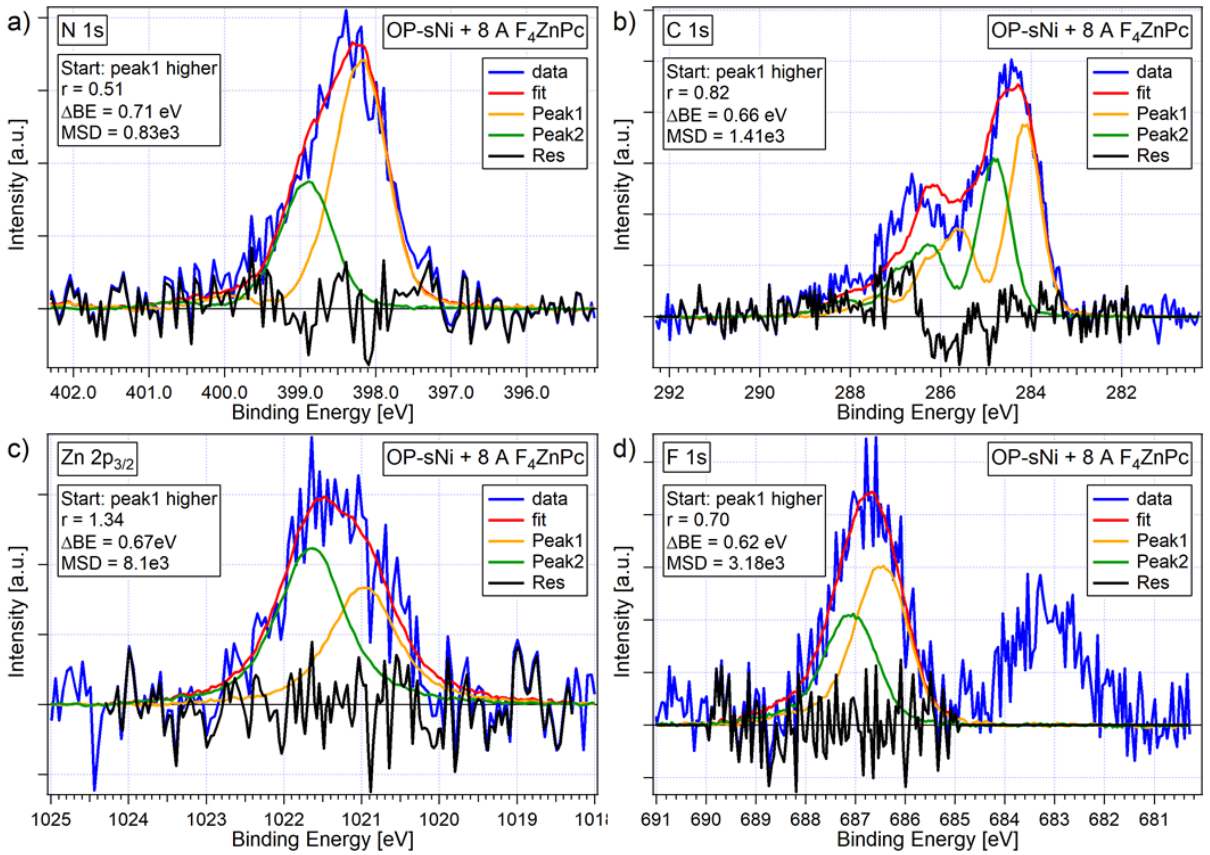

Figure 6.17: Two-component fits of core level spectra of 8 Å F_4ZnPc on OP-sNiO. In each case, the starting parameters were chosen such that the left peak (peak1) was smaller than the right peak (peak2). During the fit, the height and binding energy position were adjusted to minimize the sum of squared residuals (SSR) from the data. The insets show the intensity ratio r between peak2 and peak1, the difference in binding energy ΔBE between both peaks and the mean squared deviation (MSD) of the fit result, which is defined as the SSR divided by the number of data points. All data was corrected for Shirley-background prior to fitting. See Figure A.12 for more details.

component, which is about 50 % of the high-binding energy component, as part of the neutral molecules, a ratio of 0.37 ± 0.03 between peak2 and peak1 is obtained.
Consequently, even if the whole range of possible fit terminations is regarded, none of the computed component ratios is compatible with each other within the mutal margin of error. Thus, the occurrence of a charge transfer at the F_4ZnPc/OP-sNiO interface and the presence of two types of differently charged molecules in the first molecular layer cannot be supported by the spectral analysis. Considering the differences in interface dipoles between the F_4ZnPc/AD-sNiO and the F_4ZnPc/OP-sNiO interface (see Figure 6.13a), clear differences between the ratios of charged to neutral molecule must be expected. However, all computed ratios are in the same order of magnitude. For instance, for the N 1s and the C 1s the ratios for the AD- and OP-sNiO film differs by less than a factor of two. Thus, also the occurrence of a charge transfer at the F_4ZnPc/AD-sNiO interface is becoming less likely.
However, for the sake of completeness, the shifts in binding energy of the fit-components shown in Figure 6.15 and Figure 6.17 relative to the binding energies in bulk-F_4ZnPc were plotted in Figure 6.13b together with the data of Figure 6.13a. Now, in all cases, the "kink" at 8 Å has vanished such that for all core levels for both substrates the change in binding energy is a monotonuos function of the layer thickness in agreement with the expectations for a band bending. However, the evolutions of both Zn $2p_{3/2}$ lines still differ strongly from the other curves. This discrepency cannot be explained by the simple charge transfer model.
Another argument against this model is found in the evolution of the HOMO binding energy in the first layers of F_4ZnPc on AD-sNiO (Figure 6.13b). In case of a positive charge transfer to a part of the molecules in the first layer, the valence region is a superposition of the features of both the neutral and the positively charged molecules. As the HOMO of neutral molecules is located at lower binding energies than the HOMO of positively charged molecules, and for the determination of the HOMO onset always the feature with the lowest binding energy was fitted, one must expect to extract the

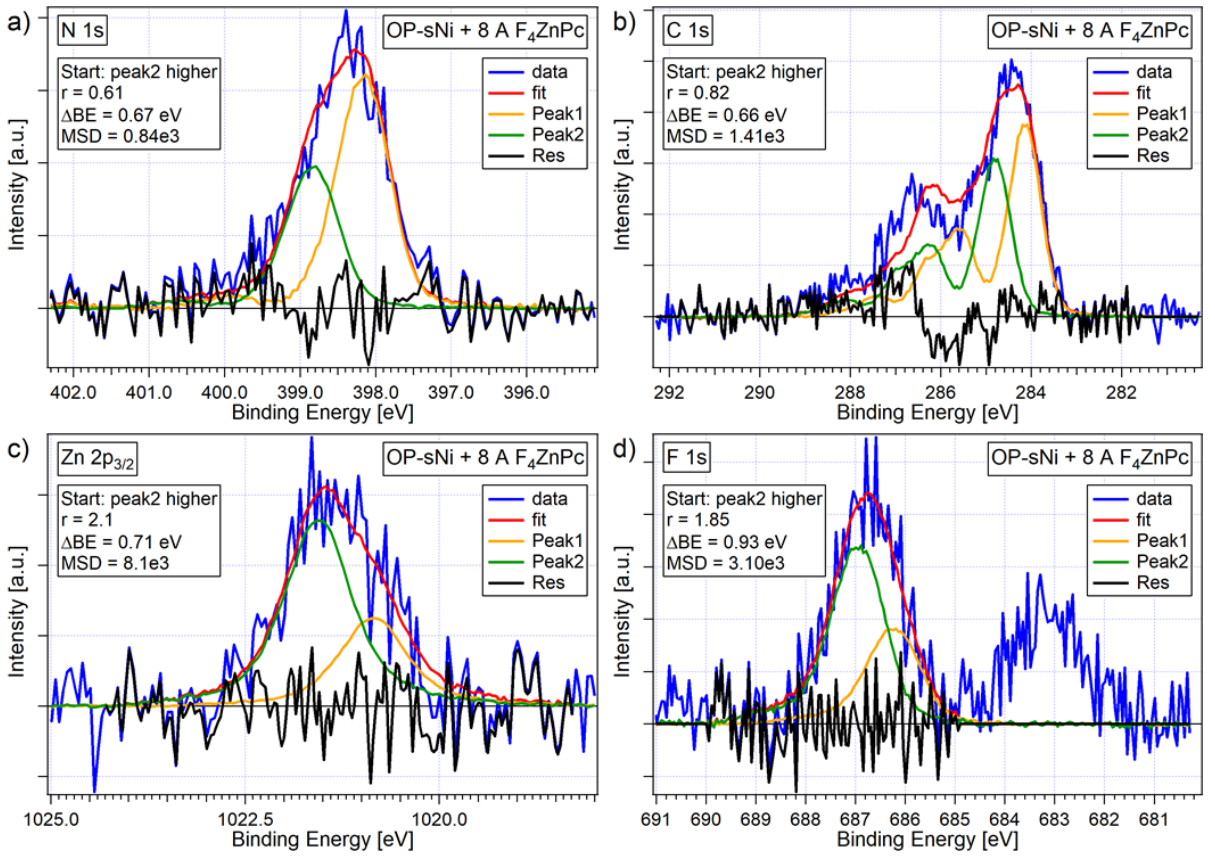

Figure 6.18: Two-component fits of core level spectra of F_4ZnPc on OP-sNiO similar to the fits in Figure 6.17, except for different start parameters: peak2 was set significantly larger than peak1.

HOMO onset of the neutral molecules even in a compound consisting of a mixture of neutral and positively charged molecules. Therefore, the apparent shift of the HOMO onset to higher binding energies in the first layer (8 Å) compared to the second layer (18 Å) cannot be explained.

For the reasons discussed above, it is concluded that the XP spectra of thin layers of F_4ZnPc on AD-sNiO and OP-sNiO do not proof the occurrence of a transfer of positive charge from the sNiO substrates to the F_4ZnPc adsorbate. For adsorption on OP-sNiO, spectra even contradict this interpretation, while for adsorption on AD-sNiO, the situation is less obvious. However, also in the latter case, the slight increase of the workfunction upon deposition of the first layer of F_4ZnPc and the HOMO onset position of F_4ZnPc at the interface does not support the charge transfer model. Therefore, an alternative approach is investigated in the following.

Alternative explanation for the broadening

It is possible that the spectral shape is explainable by a simple broadening of the according bulk-spectra. To test this, the spectrum of each line AX was fitted with a single-component fit, consisting of the spectrum of bulk-F_4ZnPc $f_{\mathrm{AX}}^{300\mathrm{A}}(x)$, which was allowed to be varied in position x_0, in height h and in width w.

$$f_{\mathrm{fit}}(x) = h\, f_{\mathrm{AX}}^{300\mathrm{A}}((x - x_0)/w) \tag{6.6}$$

The fits $f_{\mathrm{fit}}(x)$ are shown in Figure 6.19. Except for the C 1s region were the fits converge but do not describe the data very well, all emission lines can be fitted quite well with a stretching factor w (referred to as "str" in Figure 6.19) of 1.2 to 1.5 and MSD values which are very similar to the MSD values of the two-component fits dicussed previously. In most of the cases, the stretching factor is about 1.3. Only for the two F 1s spectra (Figure 6.19d and h) the stretching factors are about 1.2 and for the N 1s spectrum of F_4ZnPc on OP-sNiO the factor is about 1.5.
Obviously, a simple stretching of the bulk-spectra is suffient to describe the data in a similar accuracy as two-component fits (with the exception of the C 1s spectrum of 8 Å F_4ZnPc on AD-sNiO). For this reason and those discussed above, the occurrence of a charge transfer at the F_4ZnPc/sNiO interfaces cannot be proven. Even more, the analysis indicates that a charge transfer is unlikely.

To clarify whether charge has been transferred or not complementary IR spectroscopic measurements were performed. The results are discussed in the following.

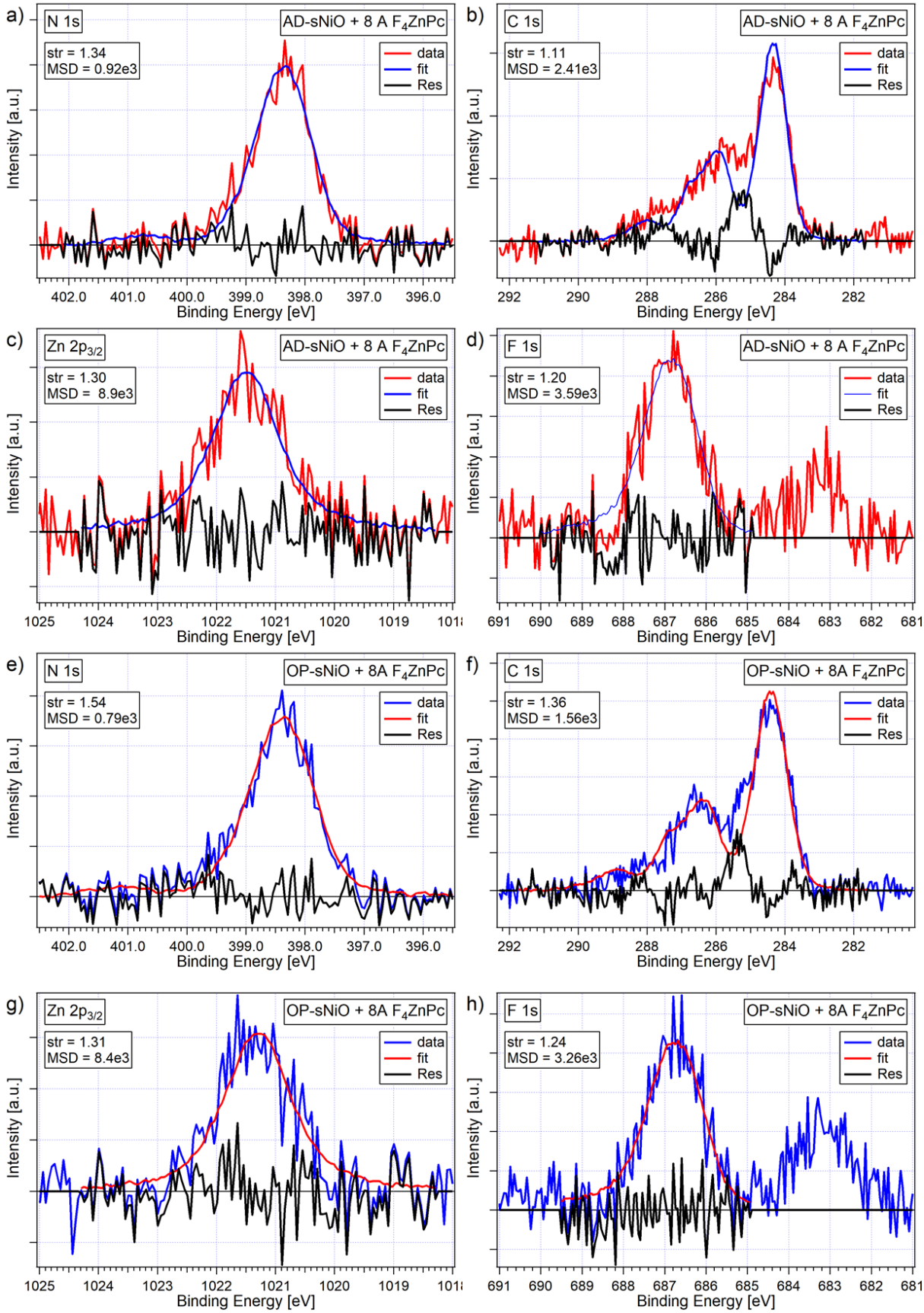

Figure 6.19: Single-component fits of XP spectra of 8 Å F_4ZnPc on AD-sNiO (a-d) and OP-sNiO (e-h). The spectra were fitted with the according spectra of bulk-F_4ZnPc, whereas the position, the height and the width of the component was optimized by the fit routine. The stretching factor str is indicated in each case in the upper left corner together with the MSD. The residua are shown in black.

6.4.3. IR spectroscopic analysis

IR spectroscopy can provide not only additional information on a possible charge transfer, but furthermore on molecular orientation and chemical processes. Among further measurements, also the very same samples which were investigated by XPS were crosschecked with IR spectroscopy. The measurements were performed, analyzed and interpreted by Dr. Sabina Hillebrandt. The results can be read in [143]. Here, only the most important findings will be reported and discussed in relation to XPS data.

Figure 6.20 shows IR measurements of 4, 10 and 60 Å F_4ZnPc on AD- and OP-sNiO. Clear differences between the interfaces on AD- and OP-sNiO, respectively, are not visible. For both substrates, small energetic shifts of the oop mode around 740 cm^{-1} and a shoulder at 1323 cm^{-1} in the ip mode at 1340 cm^{-1} are visible in the first evaporated layers (4 and 10 Å). These observations could result from a chemical interaction of the adsorbate with the substrate directly at the interfaces.

Additionally, indications for more flat-lying molecules in the vicinity of the substrate (i.e., < 60 Å) were found, although this conclusion has to be treated with caution due to the apparent interaction of the molecules with the substrate. Moreover, due to a bad signal-to-noise ratio induced by the ITO beneath the sNiO layer, only qualitative statements could be drawn.

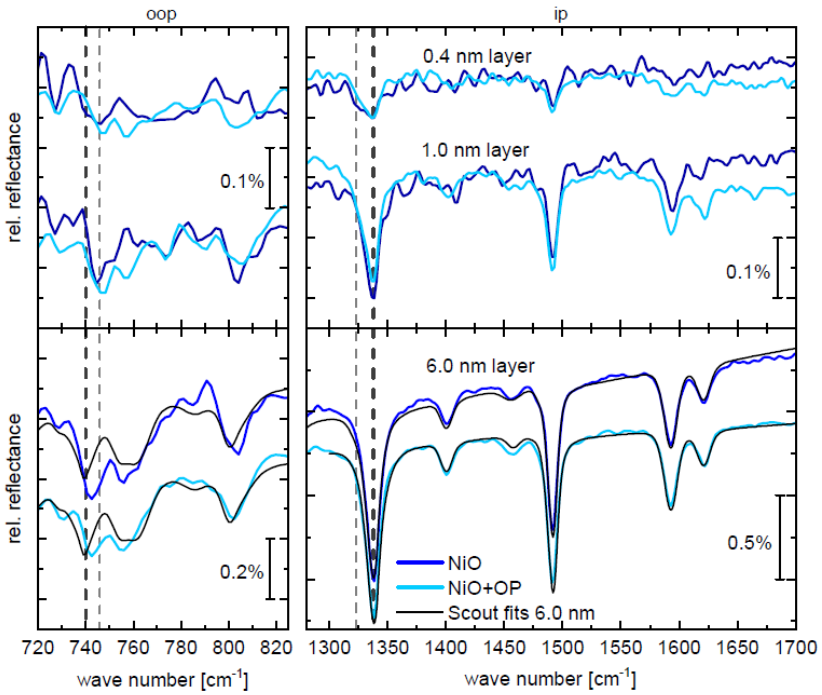

Figure 6.20: IR spectra of F4ZnPc on AD- (blue) and OP- (light blue) sNiO. Slight deviations of the spectral shape from the bulk-spectra (lower diagrams) can be observed in the thinnest layers (upper diagrams), as indicted by the grey lines. Reprinted from [143].

Therefore, an additional experiment was performed on an AD-sNiO film on gold instead of ITO (Figure 6.21c). Hence, it was possible to improve the signal-to-noise ratio and to extract quantitative results. For a layer thickness of 210 Å, a mean orientation of $(25 \pm 3)°$ and $(35 \pm 3)°$, respectively, was calculated for two different ip modes in comparison with an oop mode. As the angles are indicated with respect to the surface normal, the molecular orientation is quite upright. The results appear reasonable, as similar values were also found for (F_4)ZnPc on OP treated ITO and MoO_3 [245]. Similar to the measurement on AD-sNiO on ITO, deviations from this angle were observed for thinner layers, indicating a slightly more parallel orientation with respect to the surface. Again, a solid quantitative analysis of the orientation is not possible for such thin layers, but due to the existence of ip modes, entirely flat-lying molecules in the first molecular layer can be excluded. Furthermore, it can be stated

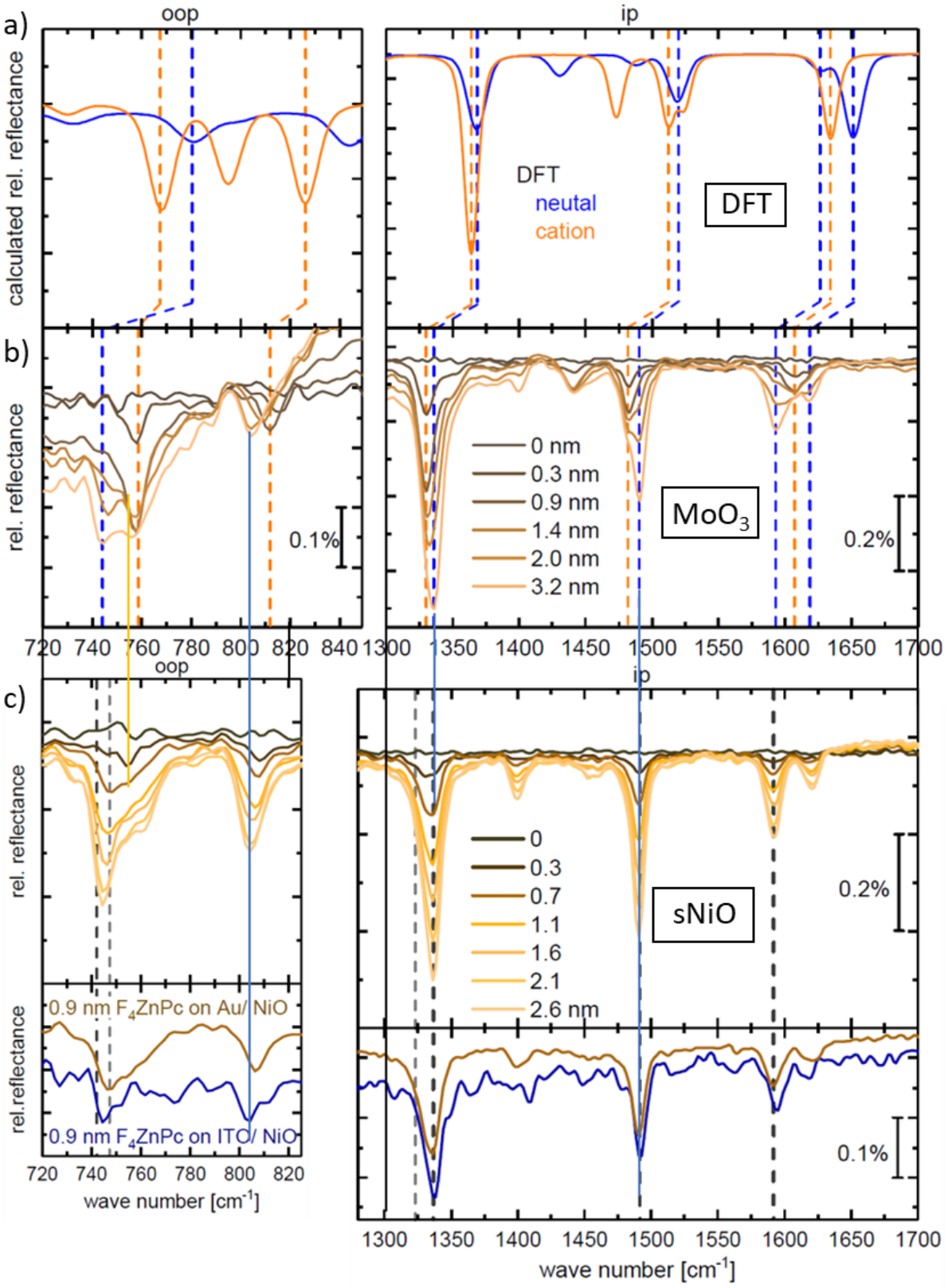

Figure 6.21: (a) DFT calculated IR spectra of neutral and cationic F_4ZnPc molecules. (b) and (c) Measured IR spectra of F_4ZnPc on MoO_3 (b) and on sNiO (c). Reprinted from [130].

that for thicknesses above 150 Å definitively no changes of the orientation occur anymore. Due to similar contact angles of AD- and OP-sNiO and the qualitatively similar results for both sNiO types on ITO, these results should also be transferable to F_4ZnPc on OP treated sNiO [143].

Moreover, an interaction of F_4ZnPc with OH groups on the sNiO substrate was found for thicknesses below 10 Å (see Figure A.15 in the appendix). The data set also confirms limited interaction distance as the OH mode does not change anymore for thicknesses above 10 Å. Assuming molecular orientations of 25° to 35°, respectively, results in a monolayer thickness of 11 to 12 Å. For potentially larger angles in the vicinity of the interface the value is accordingly smaller. Thus, the absence of direct interaction of the adsorbed molecules with the substrate for layers thicker than 10 Å is reasonable.

Finally, based on the measurements, Dr. Sabina Hillebrandt excluded a charge transfer for both interfaces as no signs for charged molecules appeared, even in direct vicinity of the interface [143]. The conclusion is justified as follows. In Figure 6.21b, IR measurements of F_4ZnPc on MoO_3 are depicted. For this interface, all modes undergo very clear changes for increasing layer thickness. These changes are in qualitative agreement with the differences between DFT calculations for IR spectra of neutral and cationic F_4ZnPc molecules (Figure 6.21a). It is concluded that at the interface between F_4ZnPc and MoO_3 a positive charge transfer from the substrate to the adsorbate occurs. This conclusion was further supported by spectral changes in modes of MoO_3 [143].
A comparison between the data of the F_4ZnPc/MoO_3 interface (Figure 6.21b) and the data of the F_4ZnPc/sNiO interface (Figure 6.21c) reveals much smaller spectral changes for F_4ZnPc/sNiO. In particular, the modes at 1490 and 1590 cm^{-1} exhibit no shift at all. The positions of these two modes are the same for all layer thicknesses. Small changes, however, are visible for the modes at 745 and 1330 cm^{-1}. Anyway, in case of a charge transfer, all modes would change, which is why a charge transfer (of a considerable number of charges) can be excluded. A direct comparison of spectra from both interfaces can be found in Figure A.17 in the appendix.
According to the DFT calculation, the two slightly changing modes (745 and 1330 cm^{-1}) stem from a collective mode of the phthalocyanine macrocycle and from a mode of the isoindole units, respectively. Thus, both modes are influenced by the fluorine atoms. Therefore, it is reasonable to assume that the separation of fluorine from F_4ZnPc molecules (as concluded based on the XP spectra) is responsible for the spectral changes in the IR spectra of thin layers of F_4ZnPc on sNiO. Note that also other modes of the isoindole unit exist. However, all of them are superposed by further modes, which explains why the defluorination is not visible there.

At this point, the reader shall be made aware of the fact that XP and IR spectra of samples in which a charge transfer has taken place are not always easily to interpret congruently. As was shown in Figure 6.21 and additionally in Figure A.16, the IR absorption modes of charged molecules exhibit a shift compared to neutral molecules. Already in the 1980th, it was shown that a partial charge transfer (e.g., in a charge transfer complex) results in a partial shift of the IR modes [246]. The relation between the fraction of transferred charge and shift of the modes was found to be linear (see Figure A.16). This contrasted XPS results, e.g., those of S. Stolz [239]. Instead of a single shifted component, Stolz found two separated peaks, as was shown in Figure 6.14. This discrepancy was explained by the difference in time constants of IR and XP measurements.
In the present case (F_4ZnPc on sNiO), however, in two modes no shift at all can be detected (1490 and 1590 cm^{-1}). In a similar system, in which definitively a charge transfer occurs (F_4ZnPc on MoO_3), in contrast, these modes clearly shift. Therefore, it can be stated that in case any charge is transferred at the F_4ZnPc/sNiO interface, only a very small fraction of molecules in the first molecular layer has a changed charge status. This fraction would lie below the detection limit of IR and likely also of XP spectroscopy.

As the results of IR measurements exclude the occurrence of a transfer of a significant number of charges at the F_4ZnPc/sNiO interface and XP spectra do not clearly support but rather contradict a charge transfer, it is concluded that no considerable number of charges is exchanged at the F_4ZnPc/sNiO interface, whether sNiO was OP treated or not, even though the work function of OP-sNiO is well above the ionization potential of F_4ZnPc.

In the following, different possible scenarios for the interaction of F_4ZnPc molecules with the sNiO substrates are presented and discussed under consideration of the findings from XP and IR analysis.

6.4.4. Discussion of the chemical reaction at the interface

One of the findings from the past sections was the partial defluorination of F_4ZnPc molecules at the surface of both sNiO substrates. This conclusion was drawn based on an additional peak in the F 1s spectra at lower binding energies (Figure 6.9d). This additional peak has about 1/4 of the total F 1s integrated intensity for F_4ZnPc on AD-sNiO and about 1/3 of the total integrated intensity of the F 1s emission for F_4ZnPc on OP-sNiO. Therefore, all models include the partial defluorination of F_4ZnPc molecules at the interface to sNiO. For simplicity, the considerations are limited to the separation of one fluorine atom per molecule, which would correspond to the average situation at the F_4ZnPc/AD-sNiO interface. However, the models can also be extended to the separation of more fluorine atoms per molecule. Three models are proposed in Figure 6.22.

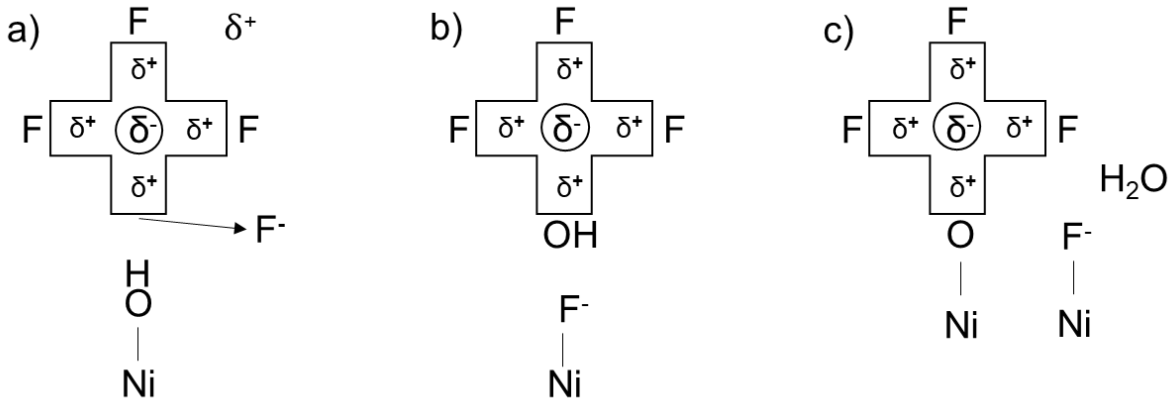

Figure 6.22: Models of the chemical interaction of F_4ZnPc molecules with the sNiO surface.

Model (a) is the simplest scenario. It depicts the situation that an F^- ion is separated from the molecule and leaves behind a singly positively charged molecule. The model is able to explain the lower-binding energy component in the F 1s spectrum by the F^- ion with an increased electron density. It may furthermore explain the "kink" in the binding energies of the atoms from the macrocycle in the first layer (Figure 6.13a). The defluorinated molecule is left behind with a positive charge. If this charge is rather located at the macrocycle than at the central Zn^{2+} ion, the binding energies of the atoms in the macrocycle would be increased. The effect could be furthermore amplified by a polarization, i.e., a charge redistribution between the macrocycle and the center.
Furthermore, the different shapes of the C 1s spectra in the first layer compared to following layers may be related to the partial defluorination as thus an asymmetry is imposed to the system. The spectral shape of the impacted isoindole unit will change due to the separation of F^- from the carbon atom. The C*F contribution (see Figure 6.9a) of this isoindole arm will vanish. Additionally, the Fermi level in unfluorinated ZnPc is about $0.4 - 0.5$ eV lower than in F_4ZnPc [232]. Thus, the C 1s spectra would be the superposition of two slightly different spectra with an energetic offset. The spectral differences between F_4ZnPc on AD- and OP-sNiO could be explained by the higher amount of separated F^- for the OP-sNiO sample. Note that also a reactive dissociation of the molecule beyond the defluorination could give rise to the spectral changes of the C 1s emissions. This has been observed by Gassenbauer et al. [234] for unfluorinated ZnPc on ITO which had been sputtered with a mixture of Ar and O_2. An additional high-binding energy peak in the C 1s region was interpreted as C-O and the breaking of C-C or C-N was concluded. This scenario, however, is not considered here as the disintegration of F_4ZnPc at the interface would induce much stronger changes in the IR spectra.

Model (a) is able to explain large part of the data, however, it is unlikely that the bond of the former fluorine site stays unsaturated.[14] Also, a reaction of the F^- ion is likely. For these reasons model (a) in this form is discarded.

Model (b) proposes the separation of F^- from the molecule (similar to model (a)) but accompanied by an exchange with an OH^- group stemming from the hydroxylated sNiO surface. F^-, in turn, occupies the place of the former surface OH group. The exchange of OH^- by F^- during a chemical reaction has been well known for decades in relation to the fluorination of hydroxyapatite ($Ca_5(PO_4)_3OH$), the main constituent of enamel, to fluorapatite ($Ca_5(PO_4)_3F$) [247,248]. A similar reaction has also been found by Kemnitz et al. for fluoroalkanes on hydroxylated metal/metal oxide surfaces [249] and by Petitto et al. for the adsorption of bromobenzene on NiO. In the latter case, bromide was found to separate from the benzene ring to form a Ni-Br complex. Thus, the defluorination of organic molecules in the vicinity of hydroxylated surfaces in combination with the exchange of surface OH with F^- ions is well known.
In the present case, such reaction would explain the reduction of surface OH modes as observed in IR spectra (Figure A.15). From an XPS perspective, the transition from Ni-OH to C-OH could explain the shifted side peak maximum (Figure 6.8b), however, the slight increase of the side peak relative to the main peak, contradicts model (b).
Furthermore, following this scenario, one would expect a change in the Ni $2p_{3/2}$ signal, since the spectrum of NiO clearly differs from a spectrum of NiF_2, as shown in Figure 6.23c. As shown in Figure 6.23a and b, this is not the case. However, two points have to be considered. On the one hand, in the present model no NiF_2 is created but only Ni-F bonds which replace Ni-OH bonds. The transferability of the NiF_2 reference spectrum to the present case, thus, is limited and the difference between the Ni $2p_{3/2}$ emission of Ni-F and Ni-OH may be small. On the other hand, the strength of the signal of nickel ions bound to fluorine compared to the total intensity has to be estimated. For this purpose, one reacted fluorine atom per F_4ZnPc molecule is supposed. F_4ZnPc has a length of 13 Å and an effective stacking distance of about 4 Å (interlayer distance of CuPc is 3.4 Å [250] and a tilt angle of F_4ZnPc molecules on sNiO of about 30° (25-35°) has been found by IR spectroscopy in Chapter 6.4.3). In case of a fully closed molecular monolayer, this would amount to one Ni-F bond per 52 Å². With a lattice constant of NiO of ~4 Å [49] this yields a percentage of 31 % fluorinated nickel sites at the surface. If additionally the information depth of λ_{Ni2p} = 20 Å (≙ 60 % of the total intensity) is considered, a contribution of 3.8 % to the total intensity is estimated. This corresponds to a maximum fraction of a 1/26 of fluorinated nickel to the Ni $2p_{3/2}$ signal. In the theoretical case of flat-lying molecules, the value would decrease to 1/87. Both considerations may contribute to the fact that no changes are visible in the Ni $2p_{3/2}$ spectra.
Similar to model (a), the "kink" could be explained by a partial positive charge on the macrocycle induced by the lower electronegativity of the hydroxide group compared to fluorine and a by charge

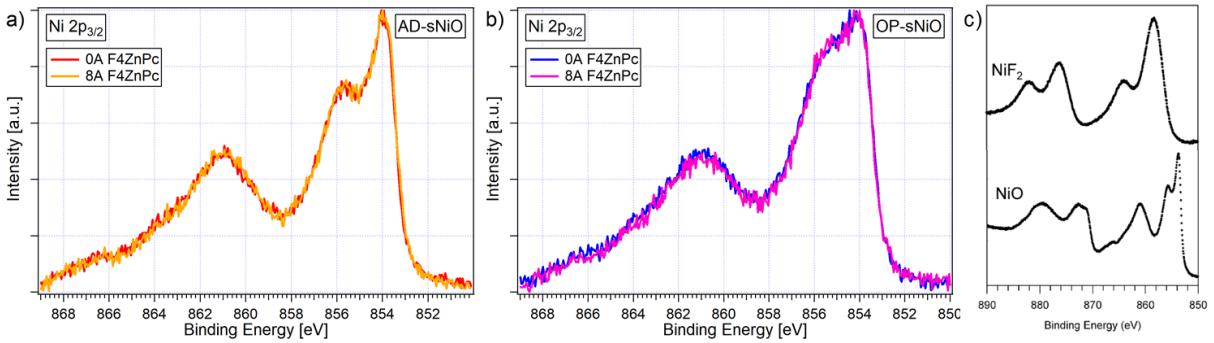

Figure 6.23: (a,b) Comparison of XP spectra of the Ni $2p_{3/2}$ region before and after deposition of 8 Å F_4ZnPc on AD- (a) and OP-sNiO (b). Changes are not visible. (c) Literature spectra of NiF_2 and NiO. Reprinted from [194].

[14] Personal communication with Frank Simon Benneckendorf from the Institute of Organic Chemistry in Heidelberg.

redistribution between the macrocycle and the center due to polarization. Also, the C 1s changes could be explained in the same way as in model (a).

In model (c), also Ni-F is formed, but the F_4ZnPc molecule is bound to the surface via an Ni-O-C bond. This mechanism has already been proposed by John and Liang for the reaction of an acyl fluoride with a clean iron surface [242]. Most of the consideration regarding model (b) can be transferred to model (c). However, based on the stoichiometry of the reaction partners, the formation of water is expected. This is neither seen in XP nor in IR spectroscopy and speaks against model (c).

The three models give ideas about the chemical processes at the F_4ZnPc/sNiO interface. While model (a) can be discarded, model (b) and (c) are able to describe large parts of the analytical observations, however, some discrepancies remain. Likely, the actual processes are more complex. Possible is as well a simultaneous occurrence of model (b) and (c).
Afterall, a chemical interaction of the adsorbed molecules with the sNiO substrate in form of a defluorination, likely in combination with charge redistribution between the macrocycle and the central zinc ion, can be stated. To obtain more detailed information, experiments wih synchotron radiation would help to obtain a better signal-to-noise ratio and a higher surface sensitivity. Thus, also near edge X-ray absorption fine structure measurements could be performed to get additional information on molecular orientations.

This final paragraph shall address again the broadening of the spectra in the first layer, which gave rise to the investigation via two-component fits in Chapter 6.4.2. First, it shall be mentioned that a spectral broadening has often been observed in literature on metal phthalocyanines [228,234,251], but evidenced explanations were not provided. In the following, several approaches are discussed whereas all of them are related to some kind of inhomogeneity.

An inhomogeneity can, e.g., be caused by clustering of the molecules in the first submonolayer such that at least two types of molecules exist: those which are surrounded by other molecules on both sides (illustrated in green in Figure 6.24), and those which are "at the sides" of the clusters (illustrated in blue in Figure 6.24). Additionally, molecules on top of the clusters are possible and molecules with different tilt angles. Such inhomogeneities could cause spectral broadening in several ways.
One idea is that molecules are differently polarized due to the different environment, which affects the binding energies. Additionally, a different potential of molecules in a cluster compared to molecules at the surface of a cluster could impact the binding energy.

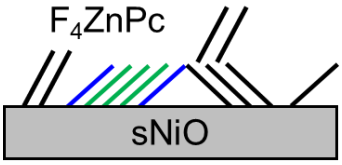

Figure 6.24: Illustration of the concluded disorder in the first layer of F_4ZnPc on sNiO.

Furthermore, such inhomogeneity could cause the existence of molecules with differences in “backbonding”, which “refers to delocalization of electron density from a transition metal to its ligand coordination sphere” [238], i.e., slightly different electron distributions between the coordinated Zn ion and the phthalocyanine ligand for the different “types” of molecules. This may also be related to the “kink” in the binding energy due to likely incomplete coverage in the first layer.
Finally, final state effects due to different polarizability of the environment of a molecule in the first submonolayer, compared to a molecule in the bulk can impact the binding energies by several hundred meV [252]. This could also lead to different binding energies of molecules “in” or at the side” of the clusters.
These effects, or a combination of them, is believed to be responsible for the observed broadening. The further analysis the processes lies beyond the scope of the work.

Independent of the exact mechanism, energy level diagrams of the two interfaces can be constructed and are presented in the following.

6.4.5. Energy level diagrams

Based on the core level binding energies shown in Figure 6.13, schematic energy level diagrams were built and depicted in Figure 6.25a and b for AD- and OP-sNiO as substrate, respectively. The left-hand side of each diagram gives information about the uncovered substrate. It depicts the situation at the very surface and does not contain any spatial information like possible surface band bending in the substrate. It is based on the values measured with XPS for 0 Å. However, as the first layer of F_4ZnPc reacts with the substrates, simple band bending theory based on the surface properties of the unperturbed substrate is not suffient to describe the processes. According to Braun, Salaneck and Fahlman [6], the substrate after the deposition of the first monolayer can be seen as the surface of a new, modified film, if the chemical interaction is limited to the first monolayer. The presented XPS data suggests that this is the case here. The following layers then adopt to this chemically passivated surface. Therefore, the measurements taken after the first evaporation step were used to extract the properties of the chemically modified surface, even though of course some deviation from a perfect monolayer may exist. Values of F_4ZnPc at the interface are based on measurements after the second evaporation step (18 Å). As it seems that the 300 Å film on AD-sNiO has reached bulk properties the values were used for both samples. Here, the HOMO position indicates the average of the onset values extracted from both the He I and He II valence band scans. The LUMO onset was estimated based on the absorption onset of optical spectra from literature [119,212,230]. To obtain a value for the potential drop within the organic adsorbate layer (i.e., "band bending"), the potential differences of all lines (core levels and HOMO values from both He I and He II) were averaged, as all of them should be affected similarly. The value of the HOMO onset at the interface is the sum of this averaged potential difference and the onset obtained from the bulk-F_4ZnPc. The indicated potential distribution within the F_4ZnPc layers qualitatively reflects the evolution of the core levels, which should be less affected by additional effects like potential polarization or orientation than the evolution of the HOMO levels.

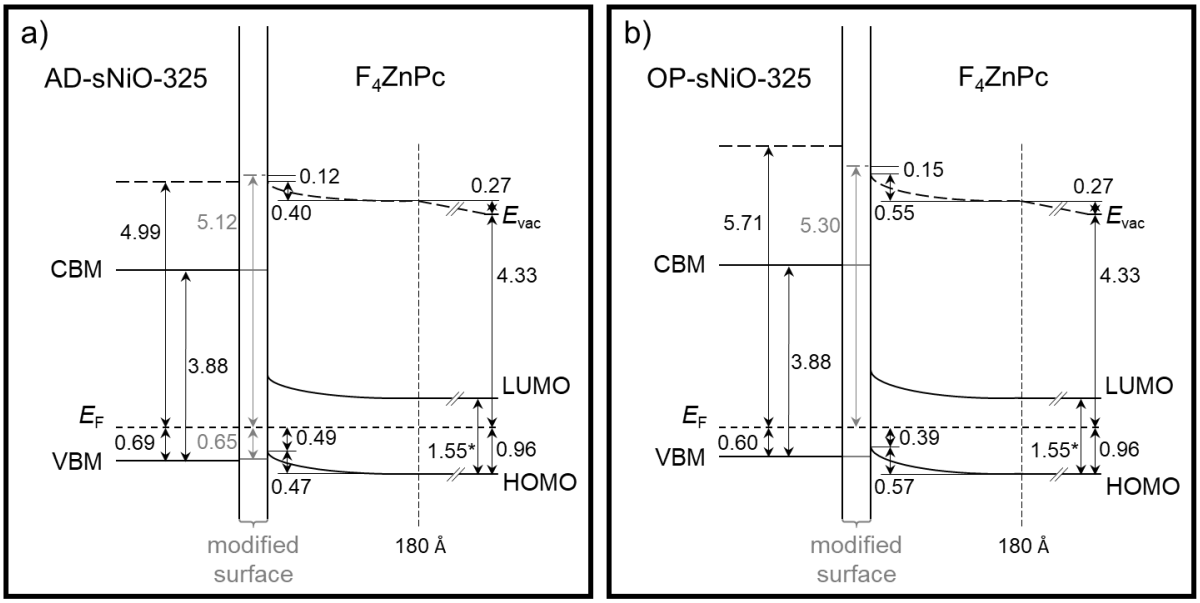

Figure 6.25: (a) and (b) show schematic energy level diagrams. The band gap of F_4ZnPc (*) was estimated based on the onset of optical absorption spectra from literature [119,212,230]. Note that these spectra show two maxima at ~1.8 and ~2.0 eV in agreement with the optical (excitonic) band gap determined by Mayer et al. [314] and with the π-π* satellite energies in XP spectra. All other values are directly extracted from the measurements presented in (a). Values of the substrates correspond to 0 Å and values of the modified surfaces correspond to 8 Å. The HOMO position is derived from He I and He II measurements and the potential drops in the organic layers are based on the average evolution of core levels and HOMOs. The dashed lines correspond to the work functions measured after the respective evaporation steps. See text for more details.

The diagrams thus constructed are quite similar for both samples: In both cases chemical reactions occur during the deposition of the first layer, resulting in a partial equalization of both the work functions and the VBM positions. The work functions of the modified substrates are smaller than or equal to the ionization energy of F_4ZnPc: 5.12 eV for AD-sNiO and 5.30 eV for OP-sNiO compared to an ionization energy of 5.29 eV of bulk-F_4ZnPc. This is in particular valid when the ionization energy of the molecules directly at the interfaces is considered, which is about 5.5 eV for both substrates. Therefore, as discussed in Chapter 6.2, no significant charge transfer is expected and thus vacuum level alignment – or at least in first approximation - takes place. This is indeed the case, as in both cases only small interface dipole of ~0.15 eV occur. Thus, the HOMO offset ΔE_H is smaller for the substrate with a higher work function: $\Delta E_{H,OP} = 0.39$ eV compared to $\Delta E_{H,AD} = 0.49$ eV. In agreement with the findings of Greiner et al. [225], both values lie above the observed pinning value of ~0.3 eV. The hole extraction barriers, i.e., the energetic distances between the VBM of the substrates and the HOMO onset of the adsorbates, are found to be $\Delta E_{h,AD} = 0.16$ eV for the AD-sNiO sample and $\Delta E_{h,OP} = 0.21$ eV for the OP-sNiO sample. The alignment at the interface is followed by a potential drop in the organic layers of 0.47 eV for the AD substrate and a slightly larger drop of 0.57 eV for the OP substrate.

It is still to be explained how such potential drop is caused if no charge is transferred at the interface, as concluded in the Chapters 6.4.2 and 6.4.3. One possibility is an artefact due to charging, which, however, can be excluded since the shift for UPS measurement would be much stronger than for XPS measurements due to the higher photon flux density and increased cross-sections in the case of UPS.
Another possibility is a change in the orientation of the molecules. It was shown that molecular orientation can impact the measured binding energies [243,244]. This can even lead to an evolution of the binding energies which is similar to a band bending [253,254]. However, here a gradual change of molecular orientation would be necessary. Moreover, the change in orientation of F_4ZnPc molecules with layer thickness in the present case is only small according to the IR measurements. Therefore, this possibility is considered to be unlikely.
Finally, a gradual charge transfer due to thermodynamic Fermi level alignment delivers a conclusive explanation. At the interface, there is a discrepancy between the CNL of F_4ZnPc, which is estimated from the Fermi level in the bulk, and the Fermi level of the sNiO substrate. Therefore, some negative charge is transferred to the substrate during the evaporation of the first layer of F_4ZnPc. Due to the low DOS in the molecular gap, a small number of charges is sufficient to equalize the Fermi levels and reach thermodynamic equilibrium. The alignment almost follows vacuum alignment in agreement with the IDIS model for a low DOS around E_F. Due to the non-metallic substrate, the rather upright orientation of the molecules in the first layer and an $E_{F,substrate}$ above from the band edges, this assumption is reasonable (see Chapter 6.2). The slope factor S in the IDIS model is large (close to one) and the interface dipole is small (see Equation (6.3)). The amount of transferred charge in the first layer is so small that it is not detectable by neither IR nor XP spectroscopy. This process is continued in each following layer until the Fermi level of the covered substrate reaches the CNL position of F_4ZnPc. Only then, the total amount of charges has been transferred. Still, due to the layer thickness, it is undetectable for IR.
This explanation is in agreement with the IDIS model by Vazquez et al. [222–224], but also with the distributed density of states model by Mankel et al. [255], as well as with the measurements of this work. However, it complements the statement of Greiner [225] and Braun, Salaneck and Fahlman [6] that no charge transfer takes place when $IE_{org} > \Phi_{sub}$ ($> EA_{org}$). Without any charge transfer, the band bending, i.e., potential distribution, cannot be explained. Therefore, it is concluded that some charge is transferred, driven by the discrepancy between the Fermi level of the substrate and the CNL of adsorbing molecules, but in a number which is below the detection limit of both IR and XP spectroscopy.
In the next chapter these findings on a microscopic scale will be related to macroscopic device data presented in Chapter 6.1.

6.5. Correlation between interface properties and device performance

It was shown that additional OP treatment of the sNiO interlayer significantly increases the fill factor of cells with FHJ architecture, while all other parameters like J_{SC} and V_{OC} stay the same. Therefore, the improvement was connected to a lower series resistance caused by the NiOOH layer which was formed upon OP treatment. The interface experiment showed that this chemically altered layer is preserved during the evaporation process, hence this conclusion can still be supported. Additionally, the experiment showed that the interface between OP treated sNiO and F_4ZnPc features three differences compared to the one without OP treatment:

1. A higher-lying VBM in OP-sNiO (by ~0.1 eV).
2. A slightly larger hole extraction barrier (0.21 instead of 0.16 eV).
3. A stronger band bending, or fields, respectively, in the F_4ZnPc adlayer (by ~0.1 eV).

While it can be assumed that the first point stands in connection with the decreased series resistance, the second point would actually be favorable for devices based on untreated sNiO. However, a positive impact on device performance of AD-sNiO-based OPVs cannot be found in the present data, which is likely related to the small magnitude of the difference in hole extraction barriers of only 0.05 eV. The third point, slightly stronger fields in the organic at the interface, can be beneficial to the charge carrier extraction from the poorly conductive F_4ZnPc. This would contribute to the enhanced PCE, most likely via the fill factor.

After all, both interfaces are very similar and the improvement upon OP treatment is mainly attributed to the enhanced conductivity with a further beneficial impact of the increased band bending.

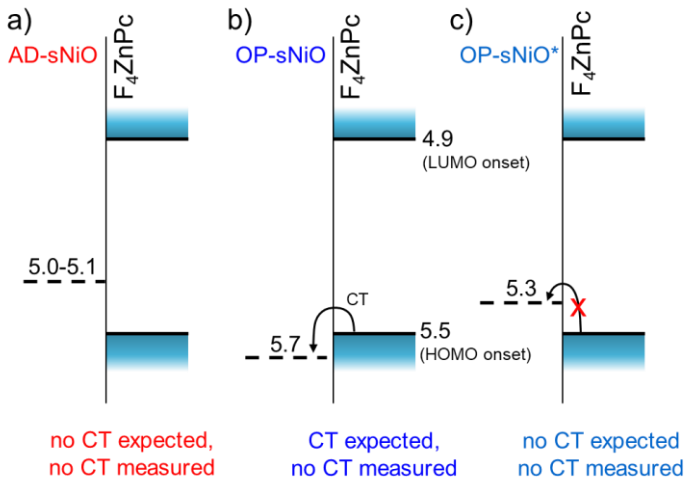

Figure 6.26: Vacuum level alignment of different sNiO surfaces with F_4ZnPc to illustrate the charge transfer (CT) prediction by Greiner et al. The surfaces are AD-sNiO (a), OP-sNiO (b) and chemically modified OP-sNiO with a layer of F_4ZnPc (OP-sNiO*), approximated by 8 Å F_4ZnPc (c). While for the OP-sNiO/ F_4ZnPc interface a CT is expected, but not measured, for the OP-sNiO*/F_4ZnPc interface, a CT is neither expected nor measured. The values are given in eV with respect to the vacuum level and are taken from Figure 6.25. Note that "no CT" actually means "below the detection limit", as explained in the text.

6.6. Summary

In summary, the performance of sNiO films as HTL in organic solar cells based on a F_4ZnPc/C_{60} active layers was confirmed and the efficiency improvement by OP treatment was examined by spectroscopic analysis of step-wise evaporated layers of the donor material on sNiO films.

XPS showed that at both interfaces between F_4ZnPc and sNiO (OP treated and non-treated sNiO), F_4ZnPc partially decomposes by defluorination. IR data agreed with this observation. A reaction of F_4ZnPc and sNiO, in which fluorine from the molecules replaces hydroxide at the substrate's surface, was concluded. Three models to describe the reaction in detail were discussed. A charge redistribution within the molecules from the macrocycle to the central zinc site due to the chemical reaction could explain the anomaly of binding energies observed for submonolayers. For thicker layers, the peak of the separated fluorine vanished. Here, only electronic changes in form of a potential drop (i.e., "band bending") of 0.47 eV for the AD sample and 0.57 eV for the OP sample occur. Molecular orientation was found to be slightly flatter in the vicinity of the substrate (<60 Å), but definitively stays constant in a rather upright position for layers thicker than 150 Å.
In-depth analysis of XP spectra of the first layer resulted in the conclusion that a charge transfer is unlikely for the AD-sNiO interface and can be excluded for the OP-sNiO interface. The absence of considerable charge transfer was confirmed by IR measurements for both interfaces. For the F_4ZnPc/OP-sNiO interface, this, however, contradicts the straightforward prediction for charge transfer at interfaces between organic molecules and transition-metal oxides (TMOs) according to the findings of Greiner et al. [225], which is solely based on the work function of the substrate (here: 5.7 eV for OP-sNiO) and the ionization energy of the adsorbate (here: 5.5 eV for F_4ZnPc at the interface). This contradiction was resolved by considering the chemical reaction in the first layer and treating the reacted surface (with a work function of 5.3 eV) as the clean surface of a fresh interface experiment. A charge transfer is now not expected anymore, although the number of transferred charges in the present case cannot be exactly zero due to the observed band bending in the organic adlayer. The processes are summarized in schematic band diagrams in Figure 6.26.

The data set complements current literature on F_4ZnPc, e.g., the work of Brendel et al. [212], in which only UPS was used and possible chemical effects were not regarded with XPS. Additionally, here for the first time the interface between F_4ZnPc and NiO_x was examined with XPS. The universal energy-level alignment found by Greiner et al. was confirmed for two interfaces with chemically modified TMO surfaces.

It was confirmed that the PCE of organic solar cells can be improved by OP treatment of the sNiO-HTL. The improved conductivity by formation of NiOOH, which was shown to be stable during evaporation of F_4ZnPc, was identified as the main factor for the enhancement. This result contradicts findings of Ratcliff et al. [13], who attributed the improvement of sNiO-based solar cells largely to an enhanced electron blocking behavior of the HTL, while increased conductivity of the HTL was considered to play a minor role only – without actually investigating the HTL/active-layer interface. The current results show that these conclusions cannot be transferred to the FHJ cells analyzed in this work.

Apart from OP treatment, the functionalization and passivation of the surface with self-assembled monolayers is another strategy for interface engineering and will be the topic of the next chapter.

7. Interface Engineering: Functionalization with Phosphonic Acids

Different organic donor material possess different ionization potentials, i.e., HOMO level positions versus vacuum level [256,257]. Improved energy level alignment for hole extraction can be achieved by adjusting the work function of the anode, or hole transport layer (HTL), respectively [121,258,259]. Therefore, for a certain well-working HTL like sNiO, tunability of the work function is desirable. One way to alter the work function is treatment with oxygen plasma (OP). However, it has been shown that the work function of NiO saturates to a fixed value after less than a minute of exposure [21], rendering a precise adjustment difficult. Moreover, a variability regarding the surface chemistry and, especially the surface energy γ is beneficial. The surface energy is important as it can influence the molecular orientation of subsequently deposited active materials in the vicinity of the HTL. Furthermore, it plays a crucial role for the wettability of solution-processed films in the course of low-cost solar cell fabrication via printing.

Both features can be realized by molecular functionalization of surfaces with self-assembled monolayers (SAMs) [39,184,260–262]. The molecules of such monolayers are chemisorbed onto a surface by an anchoring group. In a suitable system where the anchoring group fits to the type of substrate (e.g., thiols on gold) molecules form a highly ordered system due to van der Waals interaction between the molecules, which orients the backbones of the molecules parallel to each other. The backbones can be equipped with functional groups, which determine the surface properties of the functionalized material including both the work function and the surface energy [147,148,263,264]. Chemical engineering provides the possibility to exchange the functional group or to functionalize the backbone itself and thus alter the intrinsic dipole moment of the molecule [38,148,186]. Hence, the work function change can be adjusted. Especially on metal surfaces this concept has been thoroughly studied and it was proven that SAMs can vary the work function of a certain surface in a wide range of more than 1 eV [39]. Also, the functionalization of metal oxide surfaces like ITO [37,38,147,186,265] or ZnO [148,266] has been intensively investigated and it was shown that the performance of organic solar cells can be improved [41,42,264,267]. However, only few reports on the functionalization of nickel oxide [41,43–45] and even less on the impact on device performance [41] exist. Regarding the functionalization of solution-processed NiO only one short report is published so far [45].

To combine the benefits of nickel oxide thin films, such as its strong electron blocking ability in solar cells, with the versatility of SAMs, the primary goal of this chapter is to clarify whether a functionalization of solution-processed NiO is possible and, if this is the case, to study the binding mechanism in detail. A secondary goal is to achieve an enhancement of organic solar cell's photon conversion efficiency (PCE) due to functionalization of sNiO. For this purpose, a phosphonic acid (PA) molecule was chosen, since PAs can chemically bind to hydroxylated metal oxide surfaces and form well-ordered, oriented SAMs [263,268–271].

In the first part of this chapter, the chosen PA molecule is presented and characterized. Both a theoretical and an experimental background regarding the SAM functionalization is provided. In the second part, the influence of the solvent, which necessarily gets into contact with the film surface during the functionalization process, is studied in order to extract the net impact of the SAM thereafter. Then, the binding mechanism, i.e., the chemical and electronic interaction between the substrate and the SAM, is investigated, as well as the properties of the functionalized surface, such as work function change, coverage and potential molecular orientation. The dependence of these properties on the composition of the sNiO substrate based on the annealing temperature and OP treatment is examined. Subsequently, the electronic impact is quantified and discussed. Finally, the performance of functionalized sNiO films in OPVs is tested and evaluated.

Parts of the results presented in this chapter have been published in [25] in collaboration with Dr. Sebastian Hietzschold and Jakob Bombsch from the TU Braunschweig, who built and characterized the OPVs, and Dr. Sabina Hillebrandt and Valentina Rohnacher from the Kirchhoff-Institute for Physics in Heidelberg, who performed the IR measurements and their evaluation.

7.1. CYNOPPA: the SAM of choice

7.1.1. Why CYNOPPA?

The molecule chosen for the study is the organic molecule 4-cyanophenylphosphonic acid (CYNOPPA) with the molecular formula $C_7H_6NPO_3$, a molecular mass of 183 u and a total length of 0.81 nm [25]. The molecular structure is depicted in Figure 7.1. The phosphonic acid head group (left hand side) enables anchoring to the substrate and was chosen for the reasons stated in the last section. Details of the anchoring process will be discussed in Chapter 7.1.4. The middle part is a phenyl ring with a delocalized π-electron system to provide necessary conductivity. The molecule is functionalized with a cyano functional group, which possesses a negative partial charge due to the large electronegativity of nitrogen [236]. Thus, a strong total dipole moment μ of 3.6 D [147] is created, which was proven to increase the work function of ZnO by 0.71 eV [148] and the work function of ITO by 0.77 eV [147]. Such increase of the work function is supposed to be beneficial for the solar cell architecture of this work, since in the last chapter it was shown that the HTL with the larger work function (i.e., OP treated sNiO) delivers the larger PCE.

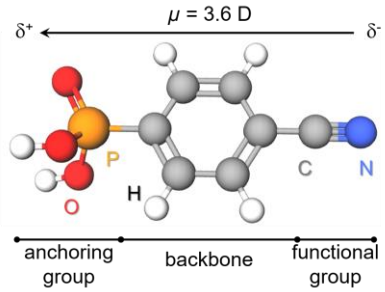

Figure 7.1: Molecular structure of 4-cyanophenylphosphonic acid (CYNOPPA). The molecular dipole points toward the anchoring group and increases the work function of a properly functionalized surface.

Furthermore, CYNOPPA appeared to be suitable due to the CN group. It provides the advantage that the nitrogen signal, which is not damped by further atoms when a proper SAM has formed, can be used as an indicator for the surface density of the molecules by XPS. As the CN group has a distinct absorption mode in IR spectra, statements about the amount can be crosschecked qualitatively. Moreover, using angle-resolved IR spectroscopy, conclusions on the molecular orientation should be possible based on the CN absorption line.

Finally, the CN group leads to a water contact angle of (42±3)° of CYNOPPA-functionalized surfaces [147], which is suitable for printing applications.

7.1.2. Characterization of bulk-CYNOPPA

To characterize the adsorbate before chemisorption, XPS measurements on supposedly randomly orientated CYNOPPA (bulk-CYNOPPA) were performed. The layers were deposited by drop-casting. Randomness was ensured by omitting the heating step which activates the bonding reaction when SAM formation is desired, as will be explained in Chapter 7.1.5. Only a mild annealing step at 80 °C was performed to ensure evaporation of the solvent, i.e., ethanol. However, a certain order or orientation of the molecules, e.g., due to polarization effects cannot be entirely excluded. To ensure reproducibility and to be able to estimate the influence of the substrate, the procedure was repeated on several surfaces: two differently doped silicon substrates (n and n^{++}) and an AD-sNiO-400 film (i.e., an as-deposited solution-processed NiO film which was annealed at 400 °C).[15]

Survey spectra (see Figure A.19 in the Appendix) show the expected peaks (C, N, P and O) without signs for contamination. Figure 7.2 displays the corresponding normalized, background corrected detail spectra. It is evident that the CYNOPPA layers are very similar, independent of the substrate. The different noise levels are due to the different layer thicknesses (see Table A.6 in the Appendix for values).

[15] See Table 4.1 for details on the silicon substrates. The n-type silicon used here was from another batch and had a slightly higher resistivity (10-20 Ωcm).

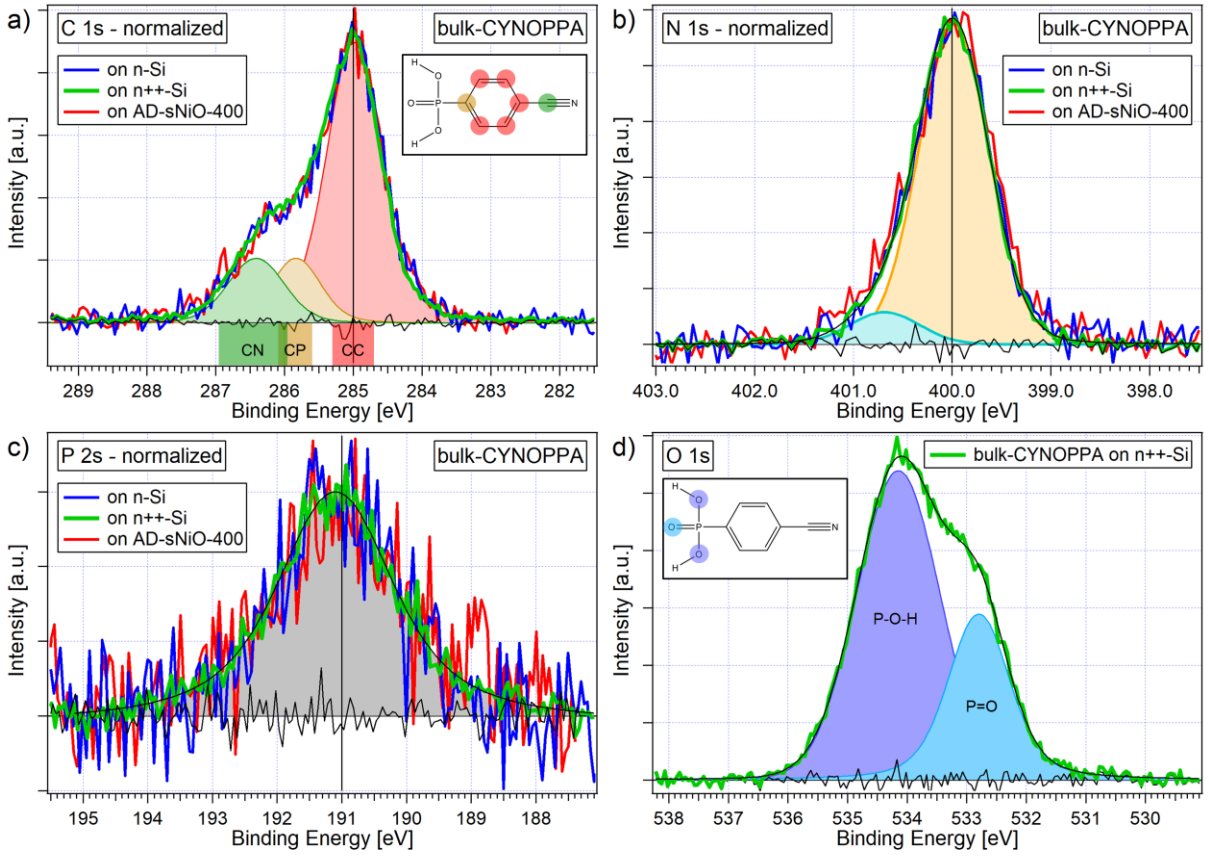

Figure 7.2: XP detail spectra of bulk-CYNOPPA on different substrates. All spectra are background corrected according to Shirley [5] and normalized in intensity. For better comparability the spectra in (a), (b) and (c) are referenced in binding energy to 285, 400 and 191 eV, respectively. Original data is provided in Figure A.20. For all fits, the data of bulk-CYNOPPA on n^{++}-Si was used for the best signal-to-noise ratio. The highlighted regions in (a) indicate ranges of line positions from literature [125,148,315,316]. These regions fit well to the binding energies of the three-component Voigt fit. The N 1s spectra in (b) exhibit a slight asymmetry, indicative for a second component (light blue). Due to the thickness of bulk-CYNOPPA on n^{++}-Si, the oxygen signal from the native oxide of the silicon substrate is not detected in the O 1s spectrum (d).

The C 1s spectra in Figure 7.2a are in agreement with spectra from literature [148] and contain at least two clear contributions, which stem from the differently bound carbon atoms in the molecule. A possible fit of the bulk-CYNOPPA spectrum on n^{++}-Si was added to the diagram. The three fit-components of the fit have a ratio of 1.1:1:5.2 in good agreement with the expected ratio of 1:1:5. This demonstrates that the spectra fit to the molecular structure of CYNOPPA, although possible additional contribution cannot be excluded for sure.[16]

The N 1s spectra in Figure 7.2b exhibit a certain asymmetry. A two-component fit shows that this could be caused by a second component of unclear origin. Possible is a separation of CN units from the molecule, in which case the shoulder of the C 1s spectra would be expected to be smaller, or an overlap of signals from different depth with different Fermi level positions, e.g., due to a band bending or different polarizations of the molecules and their surrounding in the bulk compared to the surface. The P 2s emission in Figure 7.2c show one feature, which can be properly described by a single Voigt function. The O 1s region in Figure 7.2d is only shown for the n^{++}-Si substrate as only for this sample the coverage was high enough to cover the O 1s signal from the substrate. As expected, the spectrum shows two contributions with an intensity ratio close to two (2.2). In accordance with literature spectra of powdered samples of PA molecules [263], the contribution at higher binding energies is assigned to P-O-H and the contribution at lower binding energies to P=O.

[16] See Figure A.21 and the description in the caption for background information on the fitting.

Based on the integral intensities of these spectra and average matrix relative sensitivity factors (AMRSFs) values [272] the following atomic ratios were calculated:

Table 7.1: Atomic ratios of bulk-CYNOPPA on different substrate based on the respective background-corrected core level spectra and AMRSFs.

Substrate	P 2s	C 1s	N 1s
n-Si	0.9	8.4	1.0
n^{++}-Si	1.1	8.1	1.0
AD-sNiO-400	1.0	7.8	1.0
expected	1	7	1

The experimental results agree very well with expectations, only the carbon amount is too high for all three samples. This could be caused either by residual carbon species or by systematic overestimation of the carbon signal by the sensitivity factors. Due to a large amount of different influences (background subtraction and bound of integration, especially in case of a bad signal-to-noise ratio like for the P 2s spectra, IMFP dependence on compound, etc.) the experimental results are compatible with the theoretical values expected from the composition of CYNOPPA molecules.

For one sample (bulk-CYNOPPA on sNiO), potential bond formation to the substrate was tested by ultrasonication of the sample in ethanol for 20 min and subsequent dry-blowing with nitrogen. Afterwards, survey spectra show that phosphor and nitrogen peaks have vanished and only a small carbon signal is left (Figure A.19). N 1s and P 2s regions show barely more than noise. This is seen as proof for the absence of chemisorption, since chemisorbed layers stay attached to the surface even during sonication, as will be shown later.

7.1.3. Theoretical relation between coverage, orientation, and work function change

A relevant question is which work function change can be expected for a functionalized surface depending on the properties of the adsorbed molecules and the details of adsorption bonding. There is agreement that for a certain SAM molecule with a certain dipole three main factors determine the resulting change in work function: the type of bonding, coverage and orientation. In a simplified picture and neglecting the bonding mechanism for a moment, the SAM can be approximated as a parallel-plate capacitor [48]. The surface potential difference across the SAM $\Delta\Phi_{\mathrm{SAM}}$ is then estimated according to

$$\Delta\Phi_{\mathrm{SAM}} = \rho_{\mathrm{A}} \frac{\mu \cos\Theta}{\epsilon_0 \epsilon_{\mathrm{r}}} \quad . \tag{7.1}$$

Here, ρ_{A} is the coverage (or surface density, respectively) of the SAM molecules, μ is the molecular dipole moment and Θ is the tilt angle of the molecules with respect to the surface normal. ϵ_0 is the vacuum permittivity and ϵ_r is the relative permittivity of the molecular layer. Thus, the coverage contributes linearly to the resulting change in work function. The same holds for the projection of the dipole moment perpendicular to the surface $\mu_{\mathrm{z}} = \mu \cos\Theta$. An illustration of this approximation is given in Figure 7.3. A real SAM layer certainly deviates from this idealized model, for example by depolarization at high coverages [273] or disorder like simultaneous presence of different tilt angles and inhomogeneities in the coverage. Still, a linear relation between the dipole moment μ of the molecule and the resulting work function change of the modified film has been experimentally demonstrated multiple times [38,263,274–276], whereas also coverage dependent molecular dipole moments have been found by DFT calculation [273].

Moreover, the binding process creates an additional shift of the surface potential $\Delta\Phi_{\mathrm{bond}}$ due to charge rearrangement during the binding process [38,48,274,277,278]. $\Delta\Phi_{\mathrm{bond}}$ can have several different contributions. One contribution is the dipole of the chemical bond itself, whereas the size and sign of this dipole was shown to depend decisively on the combination of substrate and anchoring group [277], but not on the functional head group for sufficiently high coverage. Additionally, the "push-back" effect can contribute in case of metal surfaces [278]. In both cases, the potential step is located around the interface between substrate and SAM and is therefore often referred to as bond dipole. Additionally, in the case of a semiconductor as substrate, a change of the band bending due to charge transfer can occur [274]. Here, obviously, the bond dipole is not limited to the area between substrate surface and molecular anchoring group. Moreover, the charge rearrangement during the binding process can even change the charge distribution between anchoring group and backbone, as found e.g. by Romaner et al. by DFT calculations [273]. In this case the splitting of the contributions into bond dipole and dipole of the SAM is related to the calculation and not to the spatial distribution. Here, $\Delta\Phi_{\mathrm{SAM}}$ is the potential distribution which results from the isolated monolayer in the identical arrangement as calculated for the substrate-SAM system. $\Delta\Phi_{\mathrm{bond}}$ includes all other effects of charge rearrangement which go along with the binding process. The resulting work function change of the modified surface compared to the unmodified surface sums up to

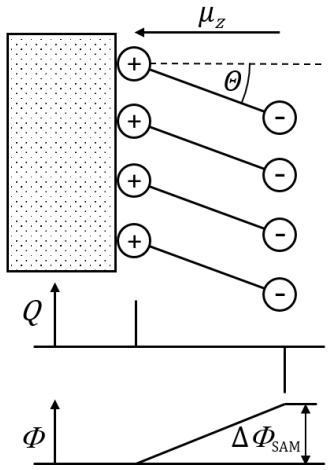

Figure 7.3: Simplification of a SAM as plate capacitor. μ_z is the projection of the molecular dipole moment on the surface normal. In this example the work function is increased.

$$\Delta\Phi_{\mathrm{tot}} = \Delta\Phi_{\mathrm{bond}} + \Delta\Phi_{\mathrm{SAM}}. \tag{7.2}$$

7.1.4. Theoretical predictions for the adsorption process

Phosphonic acids in general are known to exhibit several possible binding modes to hydroxylated metal oxide surfaces [263,279,280]. Besides a physisorption, three types of chemisorption are possible: monodentate, bidentate and tridentate, which denote chemical bonding of the molecules via up to three metal-oxygen-phosphorous (M-O-P) bonds, as is illustrated in Figure 7.4. Chemically, formation of these bonds is accompanied by creation of water molecules (i.e., a dehydration), which are formed by deprotonation of the PA molecule and decoupling of OH^- from the hydroxylated metal oxide surface. Such kind of reaction is called heterocondensation reaction.

These different binding modes were optimized for the adsorption of CYNOPPA on differently reconstructed nickel oxide surfaces via density function theory (DFT) calculations by Dr. S. Ma[17] and Dr. W. Liu[18]. Figure 7.4 displays the results for an ideal fully hydroxylated NiO(111) surface. While the tridentate configuration is fixed in a rather upright position, molecules with a mono- or bidentate binding possess more degrees of freedom and are tilted toward the surface.

To estimate the probability and stability of each binding mode, adsorption energies have been calculated. It was found that for all investigated surface reconstructions, both mono- and bidentate binding modes are energetically possible as well as physisorption, while the formation of tridentate bindings is mostly not accessible. Only on a perfect non-hydroxylated NiO(100) surface a constructed tridentate binding is stable. Additionally, it was shown that under consideration of thermal fluctuation binding modes can change: for example initial bidentate bonds can transfer into monodentate bonds.

[17] Dr. Shuangying Ma, Institute of Theoretical Chemistry in Stuttgart and InnovationLab in Heidelberg.
[18] Dr. Wenlan Liu, Institute of Theoretical Chemistry in Stuttgart and InnovationLab in Heidelberg.

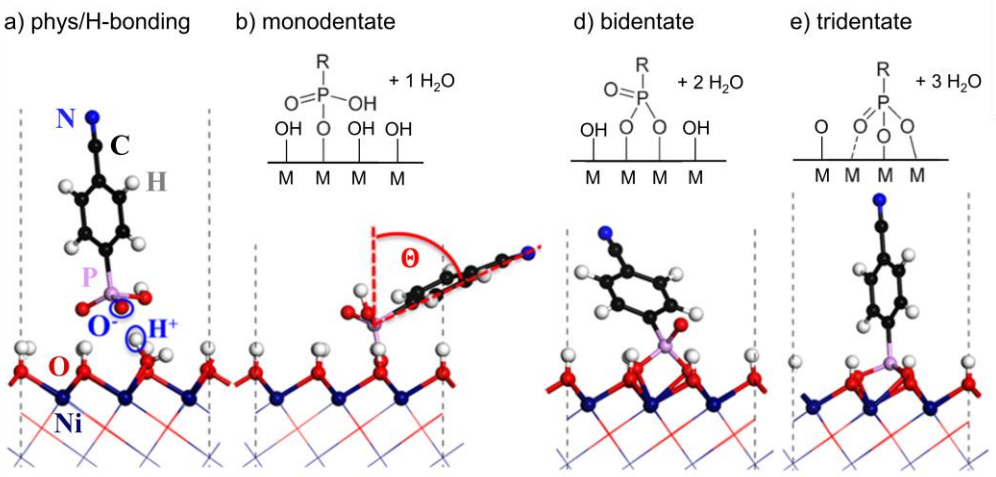

Figure 7.4: Survey of different theoretically possible binding modes of CYNOPPA to an ideal hydroxylated NiO(111) surface after optimization of the structures via DFT calculations. Besides physisorption, three chemisorption modes may exist: mono-, bi- and tridentate. The bonds are formed by heterocondensation reactions, during which an OH^- group reacts with an H^+ to a water molecule. Molecules bond via tridentate mode are oriented almost upright, while mono- and bidentate binding modes lead to larger tilt angles θ. Simulation performed by Dr. S. Ma.

Therefore, particularly on less defined surfaces consisting of a mixture of different surface orientations and reconstructions, it is highly likely that both mono- and bidentate configurations coexist whereas the ratio of monodentate is expected to be larger.[19]
This is a priori unfavorable, as in order to use the dipole moment of the backbone optimally, a preferably upright position (as in the case of a tridentate mode) is desired. However, according to the calculation, all binding configurations increase the work function compared to the non-functionalized NiO surfaces. Therefore, also a functionalization consisting of a mixture of binding modes is expected to increase the work function of the NiO substrate.

Moreover, the DFT calculations provide the possibility to differentiate between different contributions to total work function change

$$\begin{aligned}\Delta\Phi_{\mathrm{tot}} &= \Delta\Phi_{\mathrm{bond}} + \Delta\Phi_{\mathrm{SAM}} \\ &= \Delta\Phi_{\mathrm{sub-reco}} + \Delta\Phi_{\mathrm{charge-redis}} + \Delta\Phi_{\mathrm{SAM}}.\end{aligned} \tag{7.3}$$

Here, $\Delta\Phi_{\mathrm{SAM}}$ is the work function change induced by the isolated CYNOPPA layer in the geometry of the optimized NiO-CYNOPPA system, $\Delta\Phi_{\mathrm{sub-reco}}$ is the work function change due to the reconstruction of the NiO substrate during the simulation of the chemisorption and $\Delta\Phi_{\mathrm{charge-redis}}$ is the work function change due to the charge redistribution upon chemisorption. The latter is calculated as the difference between $\Delta\Phi_{\mathrm{sub-reco}} + \Delta\Phi_{\mathrm{SAM}}$ and $\Delta\Phi_{\mathrm{tot}}$ (see Figure 7.5a for further explanation). The results are displayed in Figure 7.5b. The diagram shows that for all examined surfaces and binding modes $\Delta\Phi_{\mathrm{charge-redis}} > 0$, which means that chemisorption is accompanied by a net charge redistribution of negative charge from the substrate to the adsorbate (red symbols). The magnitude of this contribution depends on the respective combination of surface and binding mode.
A similar observation is made for $\Delta\Phi_{\mathrm{SAM}}$ (green symbols). The contribution of the isolated CYNOPPA layers strongly depends on both the surface reconstruction and the binding mode but is mostly positive (i.e., work function increasing), as expected from the dipole moment of the isolated molecule.

[19] Note that also physisorption occurs in the theoretical system. However, it is unlikely that physisorbed molecules withstand the experimental adsorption procedure including elevated temperatures and ultrasonication (see Chapter 7.1.5).

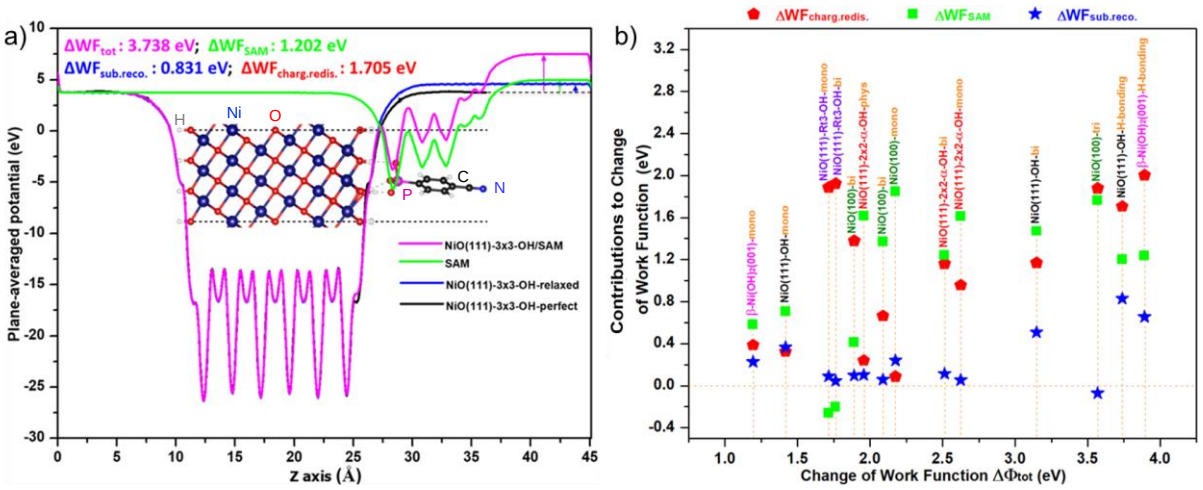

Figure 7.5: (a) DFT-calculated plane-averaged potential distribution of a CYNOPPA functionalized NiO(111) slab (purple). Additionally, the potential distribution of a perfect NiO(111) slab is plotted (black). By splitting the optimized NiO+SAM structure into SAM and relaxed NiO lattice, the contributions of the SAM (green) and of the relaxation of the NiO(111) due to the adsorption of CYNOPPA (blue) can be calculated. The difference of the sum of these two contributions to the total change of work function is attributed to charge redistribution. (b) Shows the contributions for several different NiO surface reconstructions and adsorption modes as a function of the total work function change induced by each SAM. Simulation performed by Dr. S. Ma.

7.1.5. How to prepare a SAM

Experimentally, the accumulation process is realized via immersion of the substrate into a solution of SAM molecules and subsequent annealing to initiate bonding. In the present work, the whole procedure comprised the following four steps:

1. Immersion of sNiO films in 1 mM ethanolic solution of purified CYNOPPA overnight for about 16 h at 50 °C (in nitrogen atmosphere).
2. Annealing at 140 °C for 3 h (in nitrogen atmosphere) to induce the transition from physisorption to chemisorption.
3. Exposure to ultrasonic bath in ethanol for 20 min (in air) to remove potential multilayers.
4. Dry blowing with nitrogen and removal of residual ethanol by annealing at 120 °C for about 10 min (in air).

After this procedure, samples were analyzed by XP and IR spectroscopy. However, to discriminate the impact of SAM molecules, the interaction of the solvent on the surface properties of sNiO films has to be known.

7.2. Influence of ethanol on the properties of sNiO surfaces

For the purpose of extracting the changes of sNiO film properties induced by interaction with ethanol, the immersion process was simulated with the following steps:

1. Immersion of samples in pure ethanol for 30-45 min at 50 °C (in nitrogen atmosphere).
2. Annealing at 140 °C for 15-30 min (in nitrogen atmosphere).

The influence will be discussed for sNiO films annealed at 400 °C, since these films are the best-defined ones as discussed in Chapter 5. One sample was treated with oxygen plasma (OP) prior to immersion, the other one was used as-deposited (AD). The very same samples were measured before and after immersion. XP spectra for 325 and 275 °C annealing temperature are given in the Appendix (Figure A.22). The focus of this chapter is on the chemical changes, while the electronic impact is only qualitatively discussed. The quantitative examination of the electronic impact is the topic of Chapter 7.4.

7.2.1. XPS analysis

The impact of immersion in ethanol on XP spectra of sNiO-400 films is depicted in Figure 7.6. One sample was OP treated, the other one was used as-deposited (AD). Obviously, all core level spectra as well as the VBMs shift to higher binding energies. The final positions in each spectral range are similar for both samples independent of the OP treatment (Figure 7.6b,c and e). In each spectral range, the whole emission lines shift (particularly the Ni^{2+} and O^{2-} components) and for each sample these shifts are similar in magnitude. Therefore, the shifts are related to a Fermi level shift in the probed surface regions. Hereafter, these electronic shifts will be referred to as energy level shifts (ELS).
Also the work functions are reduced in both cases, whereas the reduction is much stronger for OP treated samples (Figure 7.6d). In the case of the AD sample, the reduction of the work function has a similar magnitude as the ELS, which implies that the surface dipole stays about the same and is not influenced by the immersion in ethanol. In contrast, for the OP treated sample, the reduction of the work function is clearly larger than the ELS: the surface dipole is reduced by the ethanol treatment.
Ni $2p_{3/2}$ and O 1s spectra of AD-sNiO-400 hardly change their shape, as can be seen more clearly in Figure 7.7. However, the total intensities are reduced. This damping is attributed to the remaining carbon signal around 280 eV (see Figure 7.6 a), which evidently is due to a residue from ethanol. The latter is as well seen as the reason for the slightly increased side peak in the O 1s spectrum. A slightly increased $Ni(OH)_2$ contribution is also possible, although IR spectra rather indicate a reduction of hydroxidic species, as will be show in Chapter 7.2.2.
In contrast, the core level spectra of the OP treated sample show clear changes. This applies especially to the O 1s region (see Figure 7.7b). In the two regions which have previously been attributed to NiOOH (indicated by arrows) the intensity is reduced. The side peak visibly sharpens and approaches the shape of the side peak of AD samples, whereas the peak intensities still differ: the larger side peak in the case of the ethanol treated OP-sNiO is attributed to an increased amount of $Ni(OH)_2$ compared to the AD films. As this hydroxide was formed by the interaction with ethanol, it can be assumed to be located at or on the surface, which also explains the lower intensity of the O 1s main peak and the Ni $2p_{3/2}$ spectrum compared to AD films. Note, that the amount of residual carbon is similar on both ethanol treated samples according to Figure 7.6a (and also Figure 7.21), which is why corresponding oxygen can be excluded as reason for the higher side peak of the OP-sNiO film after ethanol treatment.

In summary, ethanol seems to have only a small effect on AD-sNiO-400 samples, whereas it largely reverses the impact of OP treatment without exactly reaching the situation of a sample prior to the treatment (i.e., AD). After ethanol treatment both AD and OP samples are similar but not identical and show equal amounts of residual carbon. The sample with OP treatment prior to immersion in ethanol exhibits an increased signal in the hydroxide region (~531.5 eV). sNiO films annealed at 275 and 325 °C behave similarly, as shown in Figure A.22.

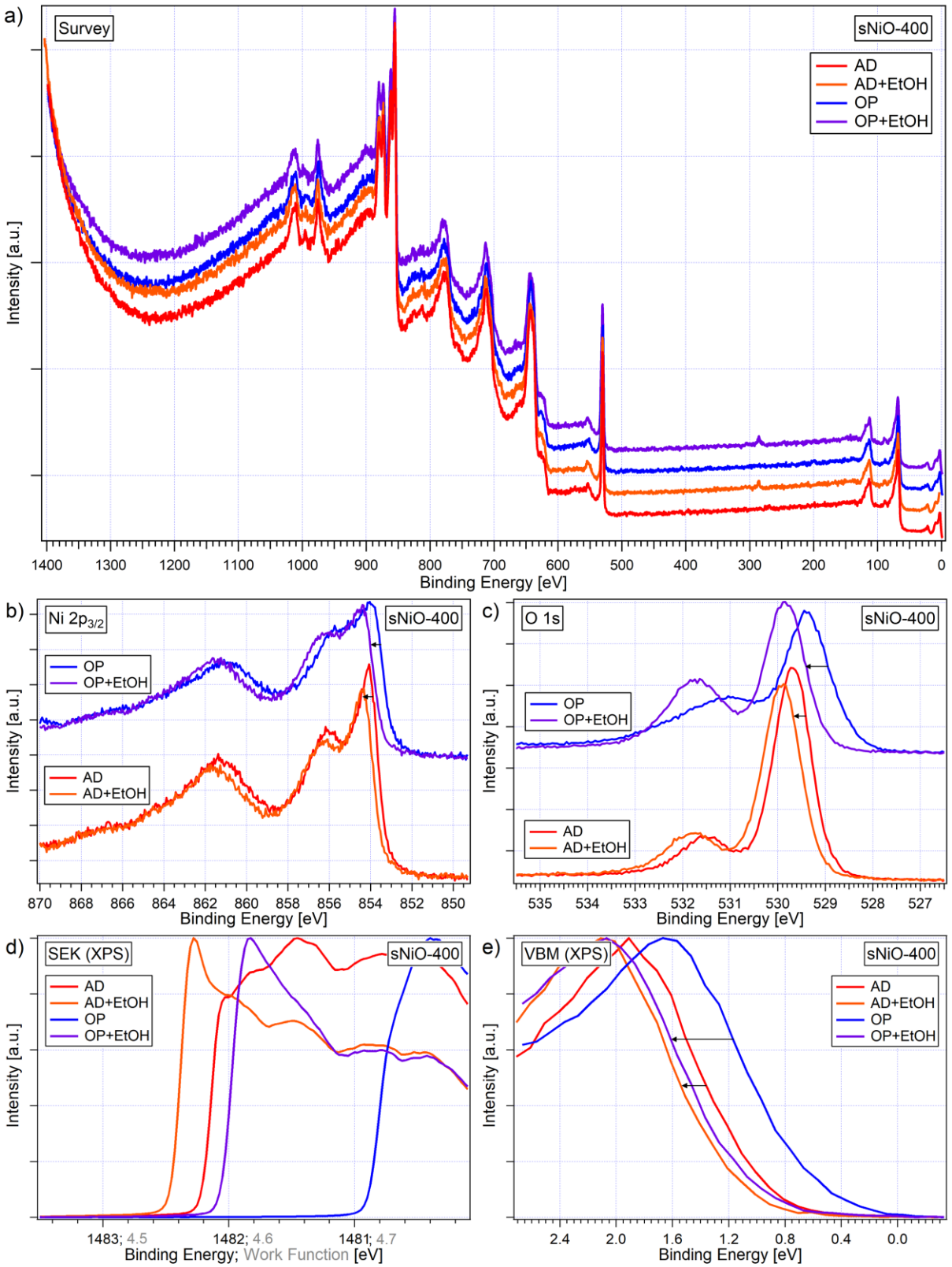

Figure 7.6: XP spectra of AD- and OP-sNiO-400 films before and after immersion in ethanol (EtOH). The spectra exhibit energy level shifts (ELS) toward higher binding energies and the impact induced by OP treatment is reversed to a large extent.

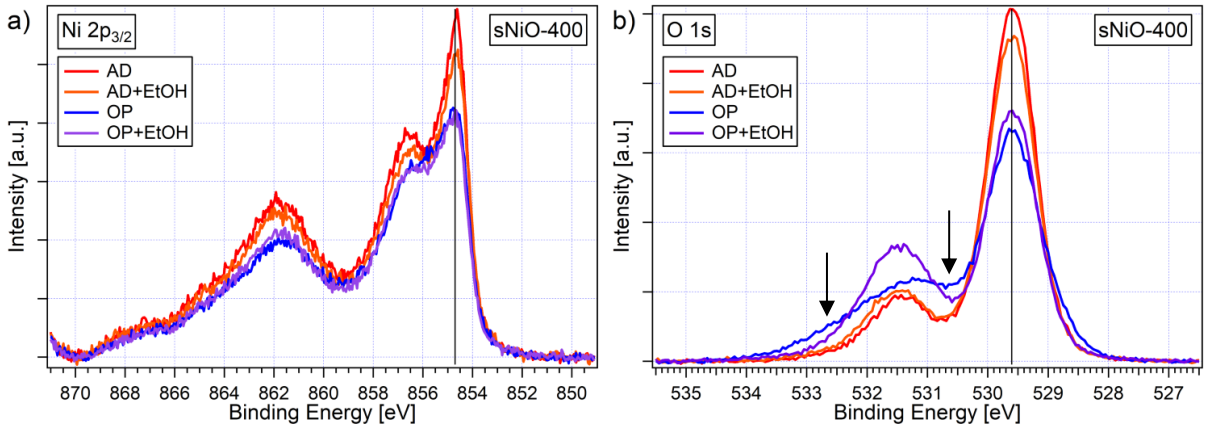

Figure 7.7: Ni $2p_{3/2}$ and O 1s detail spectra of AD- and OP-sNiO-400 films before and after immersion in ethanol (EtOH). The diagrams show the same spectra as in Figure 1.4 but corrected for Shirley background [16] and referenced in binding energy to the indicated positions. Both areas which were previously attributed to NiOOH undergo a reduction, as indicated by the arrows.

7.2.2. IR spectroscopic analysis

Similar samples have been examined with IR spectroscopy. Under the assumption that ethanol does not penetrate into the sNiO films, similar observations as made with XPS are expected. According spectra are displayed in Figure 7.9. The upper part shows spectra of an AD-sNiO-400 film before and after immersion in ethanol (red and yellow line, respectively). Prior to ethanol treatment, the spectrum exhibits the features typical for AD-sNiO-400 as discussed in Chapter 5.2. After the treatment, the main features are preserved, however, the surface component of β-$Ni(OH)_2$ is slightly reduced and the α-$Ni(OH)_2$ signature is altered. Additionally, two C-H modes appear around 2900 cm^{-1} [281].
In the spectrum of the OP treated sample displayed in blue in the middle part of Figure 7.9, the surface mode of β-$Ni(OH)_2$ has vanished, while the mode which has been attributed to β-NiOOH has appeared. Also bulk β-$Ni(OH)_2$ is visible now. As discussed in Chapter 5.3, these changes are typical for OP treatment of sNiO. Interestingly, the NiOOH mode completely disappears during immersion in ethanol (purple spectrum), as well as the signal of bulk β-$Ni(OH)_2$. At the same time, the surface mode of β-$Ni(OH)_2$ reappears. Thus, IR measurements confirm that immersion of OP treated sNiO films in ethanol reverses the effects of OP treatment.
Finally, both ethanol treated samples are compared in the lower part of Figure 7.9 (black line) by dividing the spectrum of the EtOH treated OP-sNiO film by the spectrum of the EtOH treated AD-sNiO film. Negative modes (pointing downwards) indicate species which are present in the OP treated sample, but not or less present in the AD sample. In the range between 2700 and 3800 cm^{-1} only one broad feature is visible, indicating a slight surplus of α-$Ni(OH)_2$ in the ethanol treated OP-sNiO film. This observation agrees with the increased side peak in the O 1s region of the corresponding XP spectrum. Regarding the CH amount, no difference is noticed, again in agreement with XPS measurements.
Note that additional modes around 1500 cm^{-1} appear, which, however, were not representative. All other changes regarding the $Ni(OH)_2$ and NiOOH modes were observed in all similar experiments.

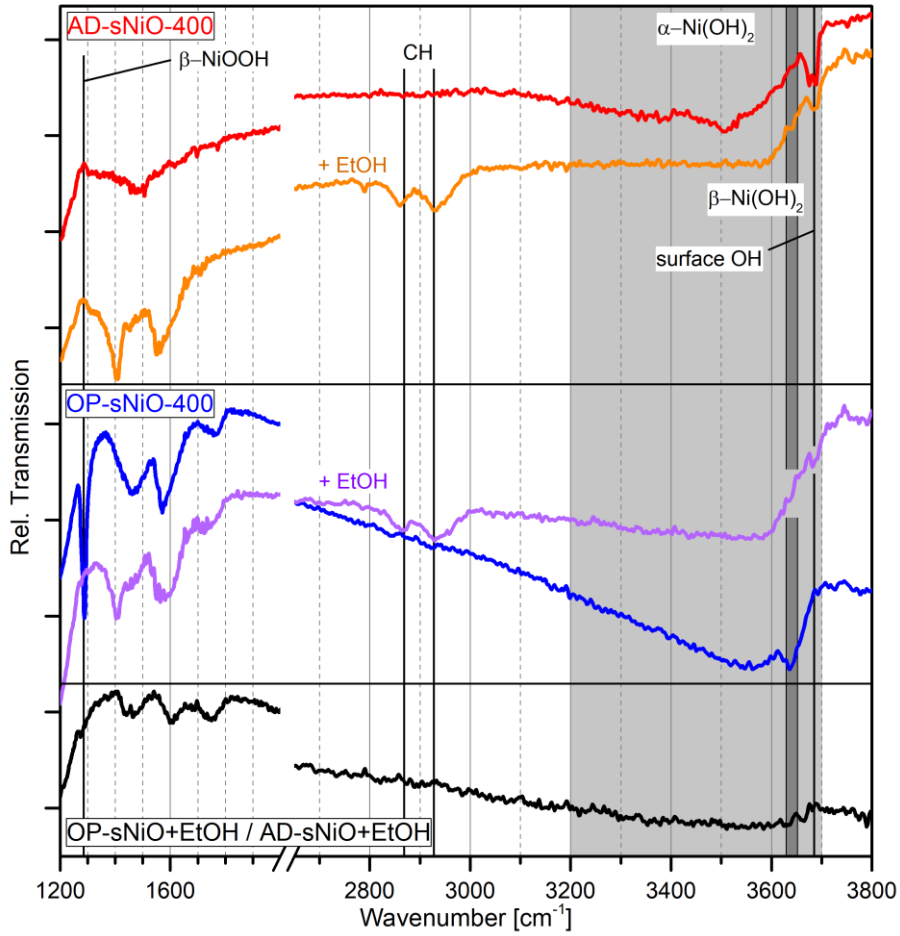

Figure 7.9: IR transmission spectra of AD-sNiO-400 and OP-sNiO-400 films before and after immersion in ethanol. The black line indicates differences between both samples after ethanol treatment. In the region between 2700 and 3800 cm^{-1} no differences are visible except for a broad absorption between 3200 and 3700 cm^{-1}, which is attributed to a higher α-$Ni(OH)_2$ content in the OP treated sample after immersion in ethanol. The negative peaks between 1400 and 1800 cm^{-1} arose during OP treatment and are not typical. Measurements performed by Dr. Sabina Hillebrandt, Kirchhoff-Institute for Physics in Heidelberg.

7.2.3. Conclusion

It was shown that immersion in ethanol and subsequent annealing does influence the surface properties of solution-processed NiO films. Core levels are shifted toward higher binding energies and work functions are decreased. Both observations are significantly more pronounced for those samples which were treated with OP prior to immersion in ethanol. The effect of OP treatment is almost completely reversed: the intensity in the two regions of the O 1s spectra which have been attributed to NiOOH drops while the NiOOH line in IR spectra disappears. Thus, the surface dipole is reduced. However, after immersion, both types of samples (AD and OP) are not exactly identical. The findings are summarized in an illustration in Figure 7.8.

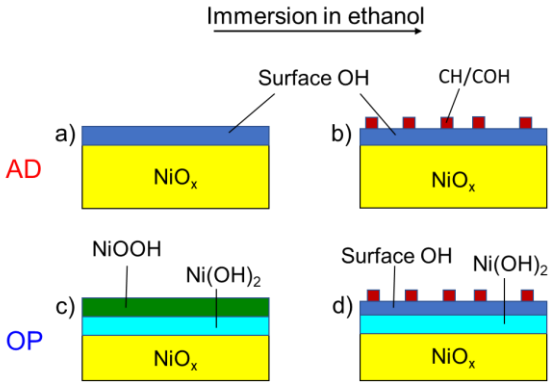

Figure 7.8: Illustration of the impact of ethanol treatment on the surface chemistry of AD- and OP-sNiO films. NiOOH which is produced during OP treatment vanishes during ethanol treatment. Instead, surface OH appears. The surface OH on AD-sNiO is only slightly reduced. On both samples similar amounts of carbon residues were found.

7.3. Functionalization of sNiO – chemical considerations

As the impact of the solvent has been clarified, now the changes of sNiO films upon functionalization with CYNOPPA can be investigated in dependency on the preparation parameters of the sNiO substrates and the question if and how the molecules bind to the sNiO surfaces. The focus of this chapter is on chemical changes, while the electronic impact will be quantified in the next chapter.

7.3.1. Investigation of the adsorbate

A first and quick indication for a successful surface functionalization is the measurement of the water contact angle. Hydrophobic surfaces (like teflon) are water-repellent and have a large water contact angle, while hydrophilic surfaces have smaller ones (see, e.g., [282] for more details). Functionalized surfaces exhibit specific contact angles, which depend on the functional group of the SAM molecules. In the present case, the contact angle of sNiO was increased by CYNOPPA functionalization from about 15-20° to 42-49°, as measured by V. Rohnacher[20] which agrees well with literature values ((42 ± 3)° [147]) and is a clear indication for successful functionalization. Another indicator is the change of the work function. As the SECs in Figure 7.10f clearly show, an increase of the work function compared to the ethanol treated references is observed for all substrates, in agreement with expectations based on the negative dipole moment of CYNOPPA. Further quantitative evaluation can be found in Chapter 7.4.1.

A deeper investigation of the functionalized samples was performed with XP core level spectroscopy. Core level spectra of all six differently prepared sNiO films (three annealing temperatures, each with and without OP treatment) are presented in Figure 7.10 after SAM functionalization in comparison to ethanol treated reference films. C 1s, N 1s and P 2s core level spectra (Figure 7.10a-c) confirm the presence of CYNOPPA on all samples. This fact is a strong indication for chemisorption, since physisorbed molecules disappear after ultrasonication, as was discussed in Chapter 7.1.2. The adsorption process will be discussed in Chapter 7.3.2 in more detail. First, spectral differences between the samples are investigated.
For this purpose, the detail spectra of the adsorbate's core levels were corrected for Shirley background, normalized in intensity and binding energy and plotted in Figure 7.11. Within the given signal-to-noise ratio no clear differences can be found for the spectra of none of the core levels. One exception exists: in the C 1s spectrum of the CYNOPPA functionalized OP-sNiO-275 film, and to a less extent also for the AD-sNiO-275 film, the shoulder between 286 and 287 eV is more pronounced. Compared to the reference spectra of randomly oriented bulk-CYNOPPA (black lines), the spectra of the functionalized films are very similar in shape, but broadened, whereas the magnitude of the broadening varies between 1.1 and 1.6 and depends on the core level investigated. N 1s spectra exhibit the strongest broadening (1.5 and 1.6, respectively), while P 2s and C 1s spectra are broadened by factors between 1.1 and 1.3. Such broadening is a sign for inhomogeneity. In case of the C 1s spectra, the shoulder between 286 and 287 eV is less pronounced for the functionalized samples compared to the broadened bulk-CYNOPPA reference and could be related to a lower carbon contamination in the functionalized films due to the annealing step at 140 °C (see Chapter 7.1.5) or to loss of nitrogen from some adsorbed molecules.

Composition of CYNOPPA layers - atomic ratios

Atomic ratios were calculated based on the integral intensities of the detail spectra in Figure 7.10a-c after correction for Shirley background and on RSFs provided by Scofield [132] (see Figure A.23 for more details on the background correction). Table 7.2 shows the atomic ratios normalized to the nitrogen integral. The uncertainties are due to low signal-to-noise ratios for P 2s and N 1s and were estimated based on the scope for subtracting the background properly. A general agreement with the

[20] Valentina Rohnacher, Kirchhoff-Institute for Physics in Heidelberg.

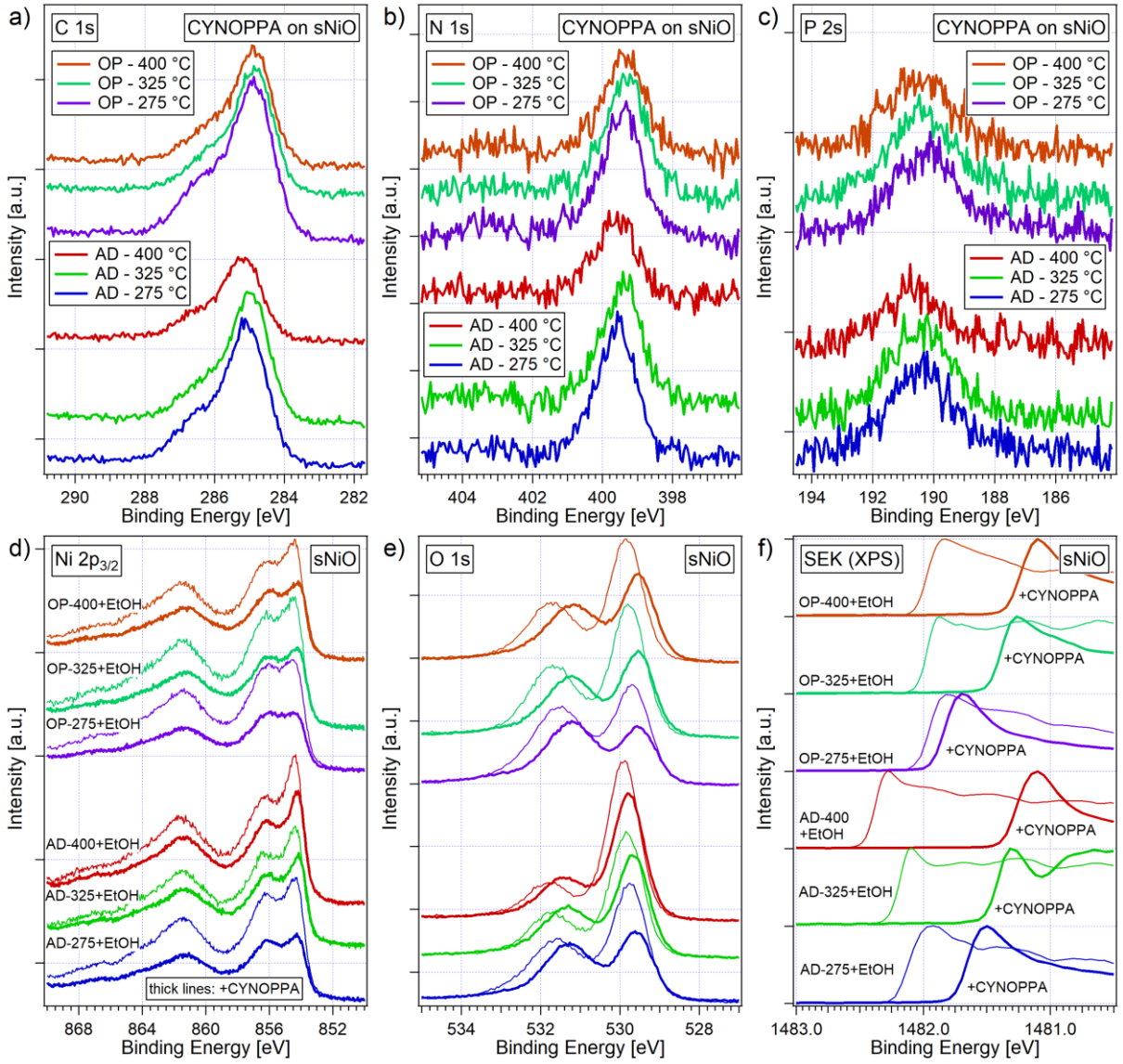

Figure 7.10: XP spectra of CYNOPPA-functionalized sNiO samples. (a-c) Core levels of the adsorbates. (d,e) Core levels of the according sNiO substrates in comparison to the spectra of samples treated with pure ethanol. All spectra were corrected in intensity using the Ag $3d_{5/2}$ emission intensity of a sputter-cleaned Ag film as reference. (f) SEC spectra before and after functionalization.

Table 7.2: Atomic ratios of CYNOPPA SAMs on sNiO films relative to the integrated N 1s intensity based on RSF values provided by Scofield [132]. The error of the P/N ratio is based on the estimated relative uncertainties of the N 1s and P 2s integrals of 5 %. The relative error of the C/N ratio is 5 % as the error of the C 1s integral is negligible. The values in brackets indicate the respective ratio when the additional feature in the N 1s spectra around 403 eV is included.

Substrate	P 2s	C 1s	N 1s (reference)
AD-sNiO-275	1.12 ± 0.08 (1.02 ± 0.07)	9.0 ± 0.4 (8.2 ± 0.04)	1
AD-sNiO-325	1.22 ± 0.09 (1.13 ± 0.08)	8.4 ± 0.4 (7.8 ± 0.04)	1
AD-sNiO-400	1.28 ± 0.09 (1.24 ± 0.09)	8.2 ± 0.4 (7.5 ± 0.04)	1
OP-sNiO-275	1.11 ± 0.08 (1.05 ± 0.07)	9.5 ± 0.5 (9.0 ± 0.05)	1
OP-sNiO-325	1.17 ± 0.08 (1.17 ± 0.08)	8.5 ± 0.4 (8.5 ± 0.04)	1
OP-sNiO-400	1.17 ± 0.08 (1.06 ± 0.07)	8.0 ± 0.4 (7.3 ± 0.04)	1
Theory	1	7	1

expectations based on the molecular structure is found. Within the error, all values are actually very similar. However, even under consideration of the uncertainties, the nitrogen amount seems to be underestimated compared to phosphorous and carbon.
A possible reason could be a separation of N or CN groups. This could be the origin of a faint additional feature at higher binding energies around 403 eV which is found in most of the N 1s spectra in Figure 7.10b. The size of the feature is estimated to be less than 10 % of the respective main peak. When this feature is considered in the N 1s integration, the P/N ratio gets closer to one for most of the samples but stays about the same in some cases where no feature exists (see values in brackets in Table 7.2). The latter is the case for OP-sNiO-325 and AD-sNiO-400. This neither reveals any systematics nor are these the films with a particularly pronounced shoulder in the C 1s spectra in Figure 7.11e, which would be expected in case of nitrogen loss from CYNOPPA molecules. Thus, also a relation between the lowered shoulder in the C 1s spectra of functionalized sNiO films compared to bulk-CYNOPPA and separation of nitrogen from CYNOPPA molecules can be excluded.
Also the C/N ratios are larger than expected, even when the high binding energy feature in the N 1s region is considered. It is striking that both 275-sNiO samples have considerably higher C/N ratios, which fits to the increased side peaks in the respective C 1s spectra and is attributed to contamination by hydrocarbon.

For the reasons mentioned, the conclusion that the CYNOPPA layer is completely clean and undecomposed cannot be drawn. However, as atomic ratios are close to expectation, it is found that most of the layer consists of stoichiometric CYNOPPA molecules with a minor contribution from contamination or decomposed molecules.

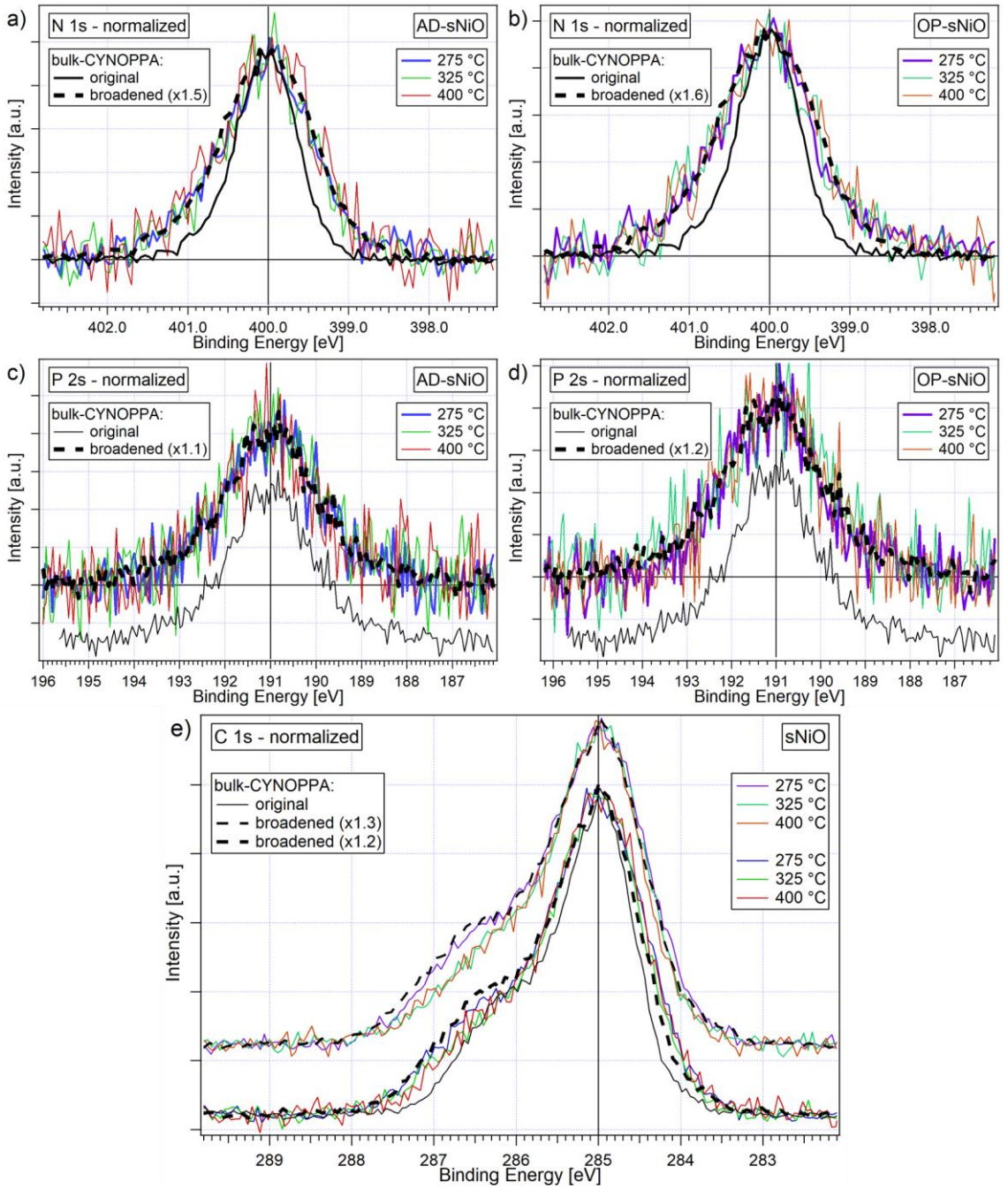

Figure 7.11: Comparison of normalized XP core level spectra of CYNOPPA functionalized sNiO films with spectra of bulk-CYNOPPA (on n++-Si). The spectra were shifted to the indicated values to enable comparison. All spectra of the functionalized sNiO films are broadened compared to spectra of bulk-CYNOPPA. In case of the C 1s spectra, the shoulder is reduced compared to the reference, especially for CYNOPPA on sNiO-275 and sNiO-325.

CYNOPPA amount on the differently prepared sNiO films

The Ni $2p_{3/2}$ and O 1s core level lines of the CYNOPPA functionalized sNiO films (Figure 7.10d,e) exhibit a small but systematic shift toward lower binding energies compared to those treated with pure ethanol. These shifts will be discussed in Chapter 7.4 in more detail. Additionally, the intensities are reduced due to the damping by the CYNOPPA layer. According to Equation (4.6), the nominal layer thicknesses can be calculated based on the ratio between the intensity of the Ni $2p_{3/2}$ signal before and after functionalization. However, when ethanol treated samples are taken as references for the situation before the functionalization, the detected intensity is disturbed by residual carbon, as was shown in Figure 7.6. Therefore, nominal layer thicknesses were additionally estimated based on the respective AD samples Ni $2p_{3/2}$ intensity (without ethanol treatment). Note that OP treated samples do not provide a reliable reference either due to the damping NiOOH layer, which is erased by ethanol during the immersion. Since both ways to extract the CYNOPPA layer thickness have inherent weaknesses, the respective results were averaged and plotted in Figure 7.12.

The values are in reasonable agreement with those reported in literature. For instance, Kedem et al. determined a nominal layer thickness of CYNOPPA on ZnO pillars of 1 nm [148], whereas parts of the damping was ascribed to additional carbon, explaining a nominal layer thickness exceeding the molecular length of 0.81 nm. Another uncertainty arises from the inelastic mean free path λ, which was estimated via the TTP-2M formula [129] for bulk-CYNOPPA and can depended on the packing density itself. Additionally, the difficulty to find reliable reference samples, as explained before, contributes to the uncertainty. Finally, nominal layer thicknesses for submonolayers have to be handled with care and cannot be directly related to average layer thicknesses. These considerations render it difficult to give a meaningful estimation of an error. Nevertheless, a clear dependency on the preparation conditions of the sNiO substrate is visible. The nominal layer thickness decreases with increasing annealing temperature and increases upon OP treatment for each annealing temperature.

Another possibility to estimate the amount of a thin adsorbate layer is the analysis of the core level lines of the adsorbate itself. For submonolayers, integral intensities of core levels should scale linearly

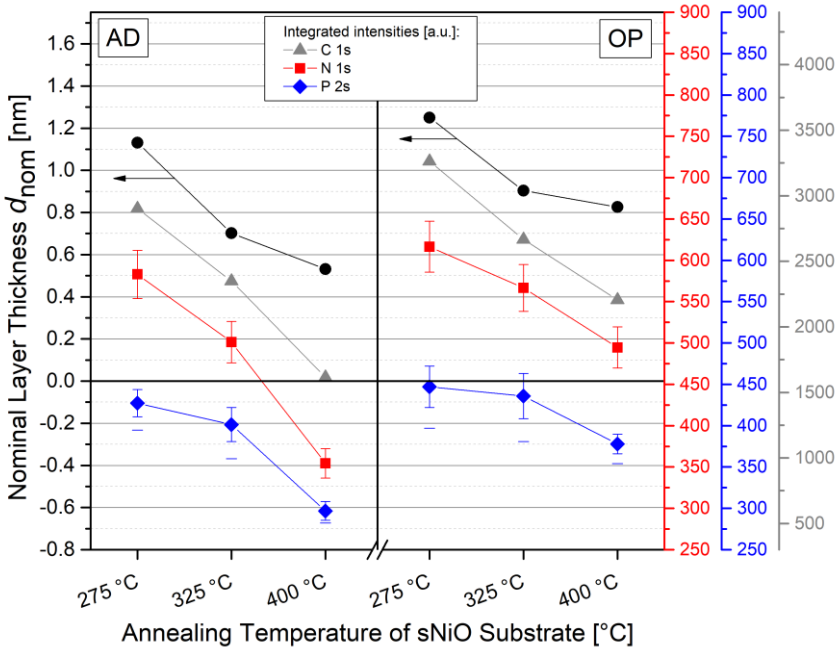

Figure 7.12: Nominal layer thicknesses and integrated XPS core level intensities of CYNOPPA layers on the differently prepared sNiO films. Nominal layer thicknesses are represented with black dots and refer to the scale on the left-hand side. They were estimated via the damping of the Ni $2p_{3/2}$ emission lines and IMFPs of 1.86 nm, as estimated using TPP-2M formula. All other data points indicate integrated core level intensities and refer to the scales on the right-hand side. The error bars of the N 1s and P 2s intensities are estimated based on the impact of reasonable variation of the details of the background subtraction and are in the range of 5 %.

with the coverage or the molecular surface density, respectively. Therefore, the integral intensities of the N 1s, C 1s and P 2s spectra from which the atomic ratios in Table 7.2 have been determined were added to Figure 7.12. Qualitatively, the same dependencies as for the nominal layer thickness are found for all three core levels. However, the evolution of each line slightly differs from the evolution of the nominal layer thickness, whereas the annealing temperature dependency of the integrated core level intensities is very similar for all three core levels. Thus, the trustworthiness in the accuracy of the nominal layer thickness values is further reduced.

In order to relate the amount of CYNOPPA on the differently prepared samples to a physical quantity rather than only to the annealing temperature, the OH content of each differently prepared sNiO was estimated. Due to the binding mechanism of phosphonic acids to hydroxylated metal oxide surfaces (see Chapter 7.1.4) it is reasonable to assume that the amount of OH on the surface of the samples, or Ni-OH, respectively, influences the amount chemisorbed molecules. In Chapter 5, it has already been demonstrated that the OH amount of sNiO films is reduced when the precursor films are annealed at higher temperatures. However, it has not been quantified yet. Additionally, the influence of ethanol has to be considered to approximate the surface composition which the CYNOPPA molecules actually see. Therefore, the O 1s spectra of ethanol treated sNiO films (discussed in Chapter 7.2) were fitted with Voigt functions, whereas as few as possible components were used, and plotted in Figure 7.13. In most of the cases, two components were sufficient. Only for the two films annealed at 275 °C, a small third component was necessary to describe the data appropriately.
While the main components undoubtedly can be ascribed to O^{2-} from NiO, the second component (light-blue) can contain contributions from different hydroxide species, in particular Ni-OH at the surface and α-/β-$Ni(OH)_2$ (which are located at similar binding energies as discussed in Chapter 5), and additionally from OH from residual ethanol. However, simply the possibility to properly describe the side peak with only one component demonstrates that these different contributions to this component lie at very similar binding energies and are hard to distinguish. Therefore, the integrated intensities of the light-blue peaks were determined and collectively referred to as "OH amount". This OH amount then is used as new abscissa for the data from Figure 7.12 and plotted in Figure 7.14.
For both the AD and OP films, the dependency of the CYNOPPA amount on the annealing temperature translates into a dependency on the OH amount in the surface region of the films: the more hydroxide, the more CYNOPPA is chemisorbed. Additionally, if the data points at an OH amount of 6356 are treated as outliers, the integrated peak intensities show a global behavior with a steep incline for lower OH amounts and a saturation behavior for higher OH amounts, as indicated by the

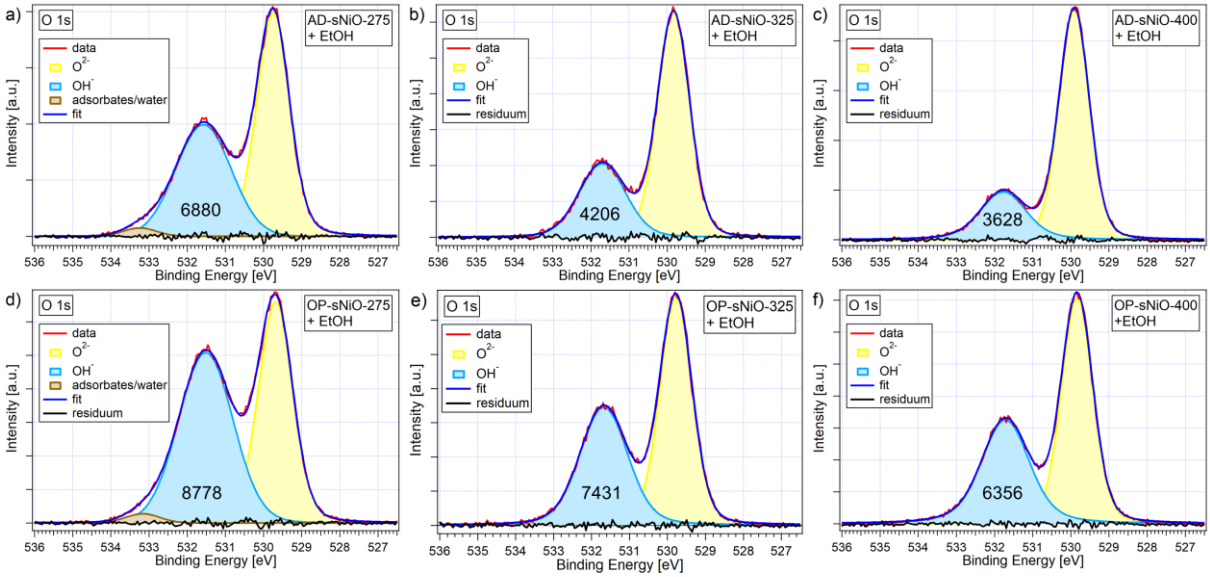

Figure 7.13: Normalized O 1s spectra of ethanol treated sNiO films. The spectra were fitted with as few as possible components. The light-blue component is attributed to hydroxide. In each case the integrated intensity is indicated in arbitrary units.

red-shaded area. This meets the expectations as each monolayer has a maximum layer thickness, which seems to have almost been reached.
In first order approximation, the OH amount can be interpreted as nickel hydroxide, whereas the actual manifestation (α-/β-$Ni(OH)_2$ or surface OH) as well as the contribution from ethanol is neglected. The latter, should add only an offset in x-direction to the data, since the amount of residual ethanol is similar on all ethanol treated sNiO films (see Figure 7.21), and therefore also the contribution to the "OH amount" is estimated to be similar for all films. Thus, the found trend should be transferrable to nickel hydroxide: The more nickel hydroxide is present in the surface region of sNiO films, the more CYNOPPA is chemisorbed.
It remains unclear, however, why the OH amounts which exceed a monolayer should influence the CYNOPPA coverage. This question arises as the surface of AD-sNiO-400 – which has the lowest OH amount - has been found to be already covered with OH groups in the range of one monolayer (see Chapter 5). A possibility is that bond formation of CYNOPPA to $Ni(OH)_2$ is preferred compared to bond formation to surface OH on NiO.

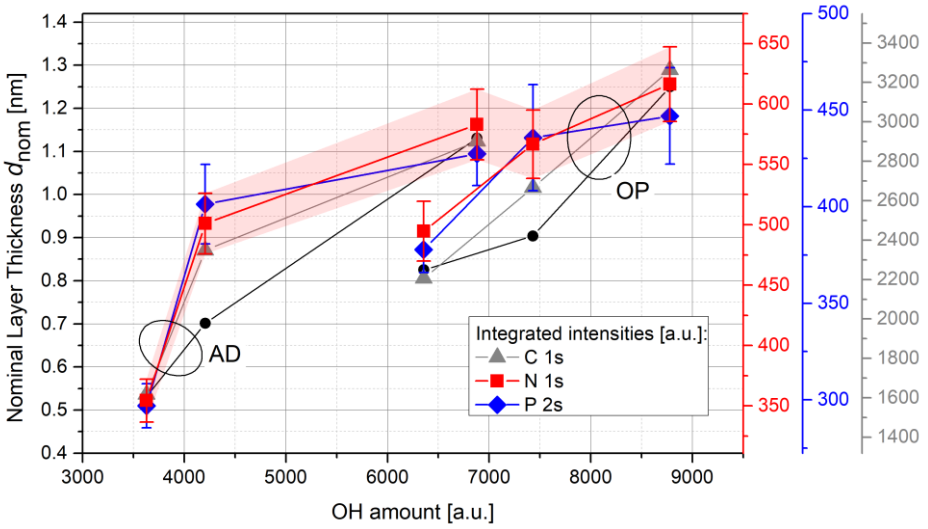

Figure 7.14: Nominal layer thickness and integrated core level intensities as a function of the OH amount in the surface regions of the sNiO films. For both sNiO types, AD and OP, a clear trend is seen: the higher the OH amount, the higher the coverage of CYNOPPA molecules. If the data points at an OH amount of 6356 are treated as outliers, the integrated peak intensities show a clear global behavior with a steep incline for lower OH amounts and a saturation for higher OH amounts. This is indicated by the red-shaded area.

Estimating the relation between the integrated N 1s intensity and the molecular surface density

From the core levels (N 1s, C 1s and P 2s) nitrogen is considered to be the most reliable indicator for the density of CYNOPPA molecules on the surface as nitrogen is the least prone to damping (the P 2s signal, e.g., is likely damped by the molecule's backbone, see Figure 7.4 for visualization). However, the factor to relate the integrated N 1s intensity, to the atomic (or molecular) surface density is unknown. Here, this factor was obtained from a common project, in which four similar molecules with different dipolar moments were synthesized by Dr. Frank Simon Benneckendorf from the Institute of Organic Chemistry in Heidelberg. This project and the determination of the relation between integral intensity and surface density will be briefly described in the following excursus. Details on the project were published in [186].

The goal of the project was to synthesize and characterize a set of SAM molecules with varying dipole moments but similar functional groups to enable controlled work function tuning while leaving the surface energy unchanged. The functional group chosen was dimethylamine, which contains one nitrogen atom (see Figure A.24 for molecular structures). The molecules were used to fabricate SAMs on ITO. Beside the work function change $\Delta\Phi_{\mathrm{tot,i}}$ induced by each type of SAM i, also the average orientation of the molecules Θ_{i} in each SAM was determined via angular-resolved IR spectroscopy (see Chapter 4.1.2). Additionally, the integrated N 1s signal N_{i} from the functional groups was measured with XPS and the dipole moments μ_{i} of each free molecule was calculated based on DFT. Thus, in the equation

$$\Delta\Phi_{\mathrm{tot,i}} = \Delta\Phi_{\mathrm{bond}} + \rho_{\mathrm{A,i}} \frac{\mu_{\mathrm{i}} \cos\Theta_{\mathrm{i}}}{\epsilon_0 \epsilon_{\mathrm{r}}} \quad , \tag{7.4}$$

which results from Equation (7.1) and (7.2), only the bond dipole $\Delta\Phi_{\mathrm{bond}}$ and the molecular surface densities $\rho_{\mathrm{A,i}}$ are unknown. As $\rho_{\mathrm{A,i}}$ is expected to scale linearly with the integrated N 1s signal N_{i} it can be rewritten as

$$\rho_{\mathrm{A,i}} = \rho_{\mathrm{A,0}} \frac{N_{\mathrm{i}}}{N_0} \quad . \tag{7.5}$$

Here, $\rho_{\mathrm{A,0}}$ and N_0 are the molecular surface density and the integrated N 1s signal of a certain SAM, respectively. Combining Equation (7.4) with Equation (7.5) yields

$$\Delta\Phi_{\mathrm{tot,i}} = \Delta\Phi_{\mathrm{bond}} + \frac{\rho_{\mathrm{A,0}}}{N_0} \frac{N_{\mathrm{i}}\, \mu_{\mathrm{i}} \cos\Theta_{\mathrm{i}}}{\epsilon_0 \epsilon_{\mathrm{r}}} \quad . \tag{7.6}$$

With the existing data set, $\Delta\Phi_{\mathrm{bond}}$ and the quotient $\frac{\rho_{\mathrm{A,0}}}{N_0}$ can now be obtained by plotting $\Delta\Phi_{\mathrm{tot,i}}$ against $\frac{N_{\mathrm{i}}\, \mu_{\mathrm{i}} \cos\Theta_{\mathrm{i}}}{\epsilon_0 \epsilon_{\mathrm{r}}} := x$ and perform a linear regression (see Figure A.24 in the appendix). The result is a bond dipole $\Delta\Phi_{\mathrm{bond}}$ of (0.19 ± 0.07) eV in good agreement with literature on PA SAMs on ITO [38,265,283]. The conversion factor $\frac{\rho_{\mathrm{A,0}}}{N_0}$ = (0.0034 ± 0.0004) nm^{-2} is then used to estimate the molecular surface coverage by multiplication with the integral N 1s intensities of the CYNOPPA layers plotted in Figure 7.12.[21] The results are given in Table 7.3. Note that the values contain an additional systematic uncertainty of about 12 % due to the fit. Additionally, they rather indicate an upper limit, since the nitrogen signal in the reference system may be damped to a certain degree by the methyl groups of the dimethylamine functional head. For a SAM with the same coverage but without damping the estimated coverage would therefore be too high.

[21] Note that daily fluctuations of the intensity of the XPS system were recorded using Ag reference films and taken into account.

Nevertheless, the values can give an estimate of the surface density of CYNOPPA molecules on the different sNiO surfaces. The values lie in the same order of magnitude as a theoretical maximum surface density of 4 nm^{-2} based on the size of the phosphonic acid anchoring group [284], without taking into account steric effects. Compared to an estimation of Koh et al. for the surface density of a CYNOPPA layer on ITO (2.5 nm^{-2}) the layers on sNiO seem to be somewhat less densely packed. However, they reasonably agree to the highest packing densities chosen for the theoretical calculations discussed in Chapter 7.1.4 (between 1.1 and 1.9 nm^{-2}).

Table 7.3: Estimated molecular surface coverages of the six different CYNOPPA functionalized sNiO films. The errors given are based on the errors of the N 1s integral intensities. Values contain an additional systematic uncertainty of about 12 % due to the conversion factor and rather indicate an upper limit.

Surface density of CYNOPPA molecules on sNiO [nm^{-2}]	275 °C	325 °C	400 °C
AD	1.73 ± 0.09	1.48 ± 0.07	1.05 ± 0.05
OP	1.82 ± 0.09	1.68 ± 0.08	1.46 ± 0.07

The results of this section show that solution-processed NiO can be functionalized with the phosphonic acid CYNOPPA and that the nominal layer thicknesses and molecular coverages are in the range of one monolayer. Both methods to estimate the amount of CYNOPPA on top of the sNiO films show the same dependency: the CYNOPPA amount is smaller on sNiO films annealed at higher temperatures with less hydroxide and is increased upon OP treatment of the films prior to the functionalization. Overall, a correlation between the hydroxide amount in the sNiO film and the CYNOPPA coverage was found. For all substrates, work functions are successfully increased compared to ethanol treated films.
In the next section, the binding mechanism of CYNOPPA molecules to sNiO film surfaces is investigated.

7.3.2. The adsorption process

As already mentioned, simply the fact that CYNOPPA is found on the samples' surfaces after ultrasonication is a strong hint for chemisorption. In the following, the adsorption process is examined in more detail.
For this purpose, the changes of O 1s and Ni $2p_{3/2}$ detail spectra of CYNOPPA functionalized sNiO films compared to EtOH treated films are investigated. The spectra were normalized and displayed in Figure 7.15. Ni $2p_{3/2}$ spectra in Figure 7.10a, show only minor changes in the side peak around 856 eV, which can be caused by chemisorption.
Additional information can be gained by the O 1s spectra in Figure 7.15b. To extract the spectral changes upon CYNOPPA functionalization, difference spectra were calculated. For this purpose, spectra of EtOH treated samples were adjusted such that the main peak fits to the spectra of CYNOPPA functionalized films. Interestingly, all six difference spectra can be described quite well by a single Voigt component, whereas OP difference spectra show small additional contributions at higher binding energies. This is in contrast to the O 1s peak shape of randomly oriented bulk-CYNOPPA as shown in Chapter 1.1.2 and is seen as further evidence for chemisorption. The classification of this additional component, however, is more complex.

A priori, the following scenario is reasonable. Surface OH, i.e., Ni-O-H, which contributes to peak 1 (light-blue), is transformed into Ni-O-P during the heterocondensation reaction. As H and P exhibit very similar electronegativities (2.20 and 2.19, respectively, on the Pauling scale [236]) it is reasonable to assume that the O 1s binding energy is little affected, although of course P is bond to further partners in contrast to H. In this case, the difference components at ~0.5 eV lower binding energies would be due to P=O. As no further components are visible (except for the small high binding energy features for the OP samples), this would favor a bidentate binding (two times P-O-Ni and once P=O

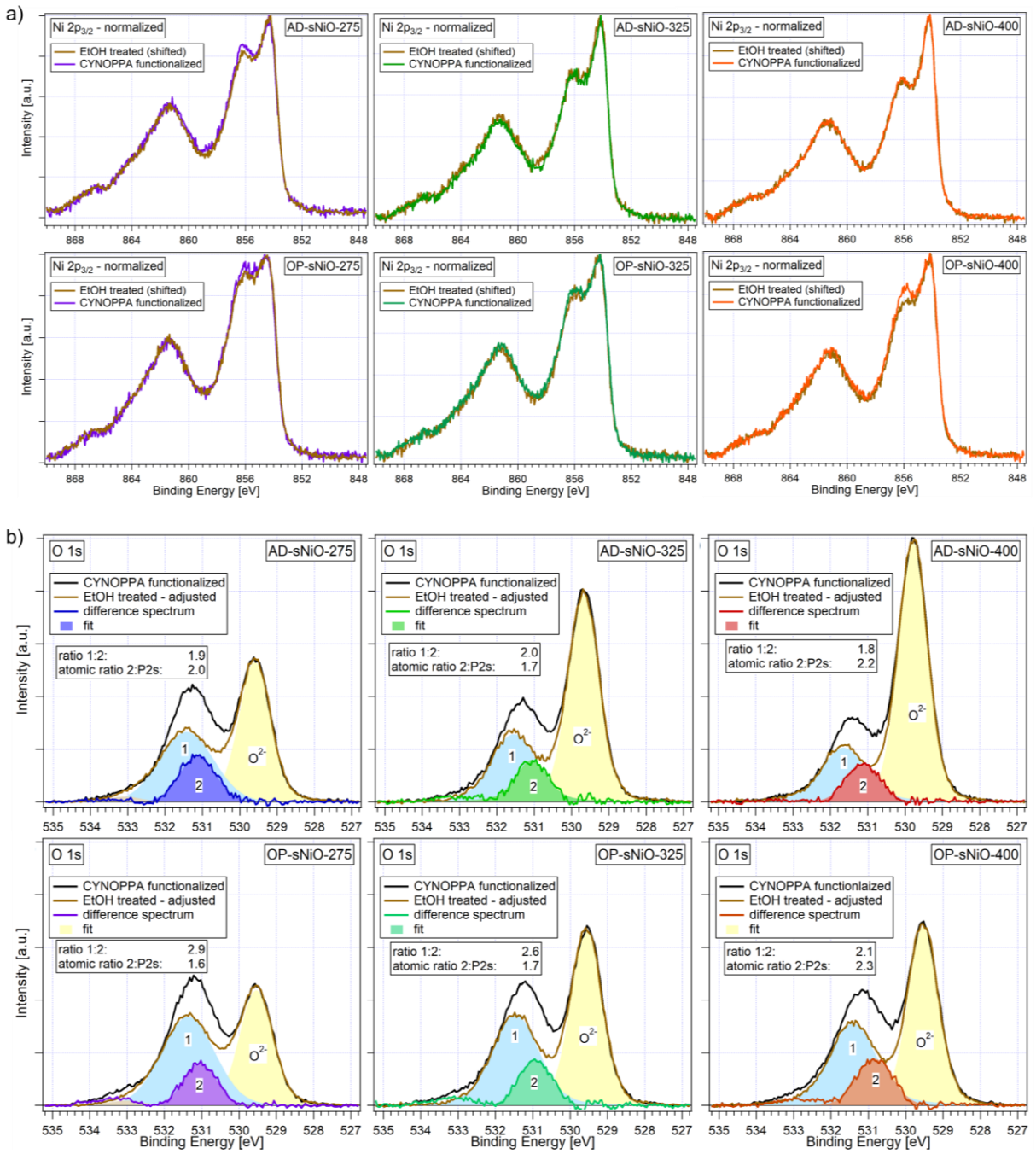

Figure 7.15: (a) Normalized and shifted Ni $2p_{3/2}$ spectra of CYNOPPA functionalized sNiO films compared to EtOH treated sNiO films. (b) Difference spectra of the O 1s regions of CYNOPPA functionalized sNiO films and EtOH treated films. The spectra of ethanol treated films (brown) were adjusted in height and x-position such that the main peaks at about 529.5 eV match with those of the CYNOPPA functionalized films (black). The difference spectra were fitted with Voigt functions. The yellow and light-blue peaks are the same as in Figure 1.13. Additionally, the ratio between the integrated areas of the side peaks of the EtOH spectra ("1", light-blue) and the difference spectra ("2") are indicated, as well as the RSF-based atomic ratios between atoms contributing to peak 2 and phosphorous atoms.

for each phosphorous atom). In this case, the ratio between peak 1 and the difference peak (colored, "peak 2") should not be smaller than two. Larger than two would be reconcilable, as further species like α-and β-$Ni(OH)_2$ contribute to peak 1. The peak ratios for all six cases are indicated in the insets in Figure 7.15b and generally agree with this constrain.

However, the atomic ratio between P and doubly bond O should be unity. This is obviously not the case, as the RSF-based values in the insets in Figure 7.15b indicate. Thus, it has to be concluded that the difference peaks cannot be solely be due to oxygen in P=O bonds.

Alternatively, the difference peaks could be attributed to the "bonding" oxygen in Ni-O-P. In this case, the atomic ratios between peak 2 and phosphorous (all about 2) would indicate bidentate modes. The missing contribution of surface OH, which is involved in the heterocondensation reaction, could be compensated e.g. by P=O.
After all, due to the complex overlapping of many different oxygen species (e.g., $Ni(OH)_2$, surface OH, P=O, P-O-H, and P-O-Ni) a clear assignment is not feasible. Nevertheless, the formation of chemical bonds can be concluded.

To obtain additional information about the bonding mechanism, IR measurements were performed and analyzed by Valentina Rohnacher [207]. Relative IR absorption spectra of functionalized AD-sNiO films are displayed in Figure 7.16b. The spectra show changes upon functionalization with CYNOPPA with respect to to AD-sNiO samples. Peaks pointing downwards indicate new or increased absorption modes, peaks pointing upwards indicate a reduction of the respective mode. For the assignment of the modes, the spectrum was compared to a calculated absorption spectrum of a single molecule in gas phase (Figure 7.16a). In this spectrum, at lower wavenumbers in the range between 800 and 1500 cm^{-1}, modes of the phenylene and the anchoring group are visible. Most important for the following considerations is the double structure with peaks at 840 and 882 cm^{-1}, which results from a stretching vibration of hydrogen against oxygen in the PA anchoring group (PO-H, marked in green). In the experimental spectra in Figure 7.16b, this mode appears at slightly lower wavenumbers and is strongly reduced in intensity compared to other modes of the anchoring group and of the phenyl ring (marked in blue). This is interpreted as an indication for chemical bonding of the CYNOPPA molecules to the sNiO surface in agreement with a heterocondensation reaction, in which a hydrogen atom of the PA anchoring group reacts with a hydroxide unit from the sNiO surface to form a water molecule and a Ni-O-P bond. Thus, PO-H modes are reduced. Further support for this interpretation

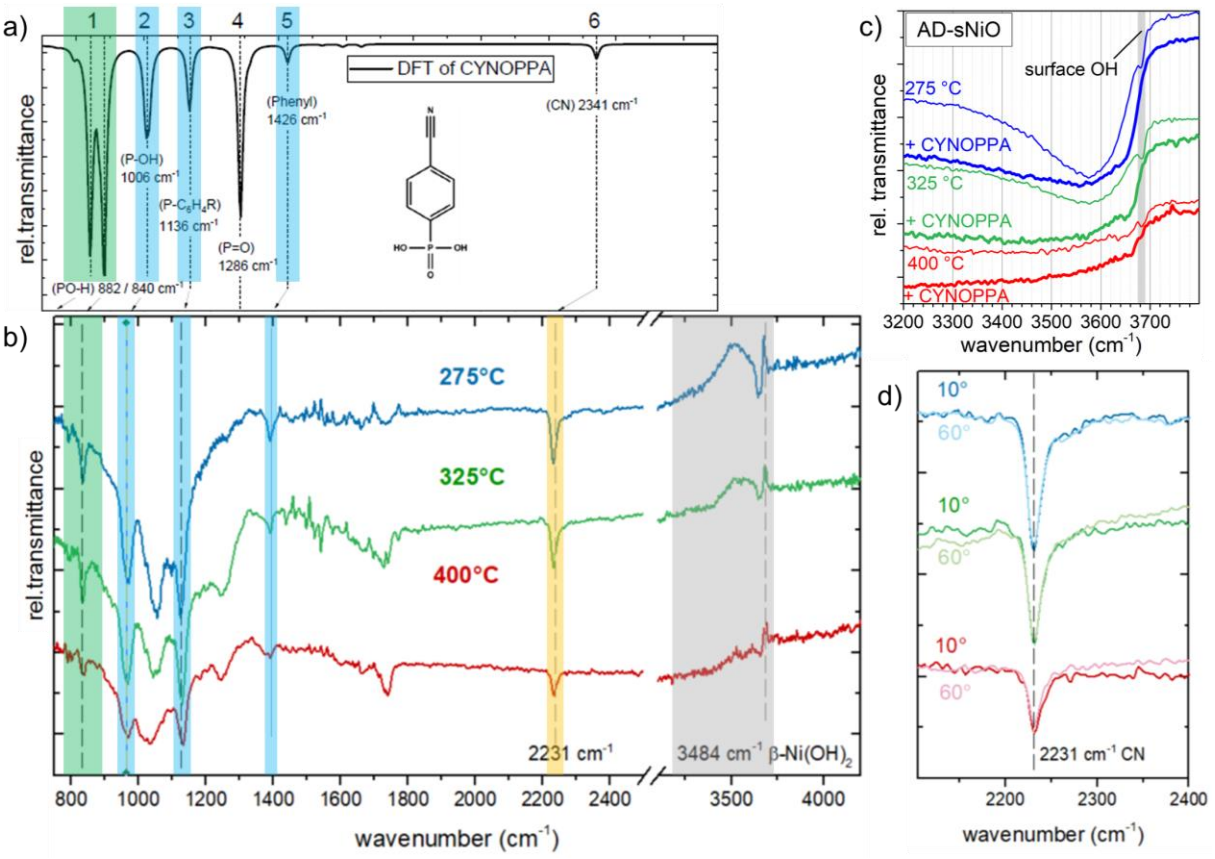

Figure 7.16: (a) Calculated IR spectra of a single CYNOPPA molecule in gas phase, based on DFT. Further details can be found in [207] (b) Measured relative IR spectra of AD-sNiO samples functionalized with CYNOPPA. (c) IR spectra of AD-sNiO samples before and after functionalization with CYNOPPA. (d) Angle-resolved measurements of the CN modes from (b). Data taken and evaluated by Valentina Rohnacher.

is delivered by the $Ni(OH)_2$ modes between 3200 and 3700 cm^{-1}, which show a clear reduction (marked in grey) in agreement with the release of OH groups from the adsorbate during the heterocondensation reaction. After the functionalization, the surface mode of β-$Ni(OH)_2$ around 3685 cm^{-1} has vanished completely (see Figure 7.16c, grey mark). In contrast, after ethanol treatment large parts of this mode are retained, as was shown in Figure 7.9 (orange line). Therefore, it can be concluded that not only ethanol but in particular CYNOPPA interacts with the hydroxide at the surface of the sNiO thin films.

Comparison of the measured spectra with the calculated one additionally enabled the identification of the CN mode at 2231 cm^{-1} (marked in yellow). This mode shows a clear dependence on the temperature: the higher the annealing temperature the smaller is the signal. As also other modes of the molecule show the same dependence (see blue marks), the previously described observation with XPS is confirmed by IR: the functionalization of sNiO films annealed at lower temperatures (with more hydroxide) leads to more densely packed layers of CYNOPPA. Note that in contrast to XPS results, IR spectra did not show clearly larger amounts of CYNOPPA molecules on OP treated surfaces. However, due to the higher surface sensitivity of XPS compared to IR spectroscopy and the unambiguous data discussed in the last section, the reliability of XPS results is considered to be higher. The CN mode was furthermore used to obtain information about a possible orientation of the CYNOPPA molecules. As this mode possesses a dipole moment in the direction of the backbone, it should not be visible for measurement angles close to zero (i.e., incoming IR beam parallel the surface normal) in case the molecules stand upright on the surface. In this case, for larger measurement angles the projection of the CN group's dipole moment on the electric field vector of the incoming IR beam should increase. For molecules lying on the surface, the situation is reversed. In the present case, the measurement angle close to zero is 10° and the larger angle is 60°. As shown in Figure 7.16d, for no temperature a significant difference between both measurement angles is found. Therefore, it is concluded that the CYNOPPA molecules are not homogeneously oriented but exhibit a broad distribution of different tilting angles.

7.3.3. Conclusion

In this chapter, sNiO films were successfully functionalized with a phosphonic acid. It was shown that CYNOPPA forms chemisorbed layers with thicknesses in the range of one monolayer. The layers consist of largely undecomposed molecules and increase the work function of sNiO substrates with respect to ethanol treated reference samples. Still, due to the absence of a homogeneous molecular orientation, the layers cannot be considered as self-assembled monolayers in the actual sense. Instead, a mixture of different tilt angles was concluded. This agrees with the presence of theoretically proposed mono- and bidentate bond formations, which provide enough degrees of freedom for tilting. Tridentate binding modes are not only energetically unfavorable for air-exposed surfaces, but also would contradict the missing uniform orientation. The latter is also an explanation for the observed broadening of CYNOPPA core level spectra. The formation of mono- and bidentate bonding by a heterocondensation reaction is additionally strongly supported by IR spectra by the reduction of respective modes of both the PA anchoring group and $Ni(OH)_2$ of the substrate. This reaction explains the observed dependence of the molecular surface density on the OH amount at the sNiO film surfaces: with more hydroxide present on the surface due to a lower annealing temperature, the probability for CYNOPPA to find a reaction partner and bond to the surface is increased. OP treatment further increases the coverage, as NiOOH created during OP treatment increases the $Ni(OH)_2$ amount during ethanol treatment in comparison to AD films.

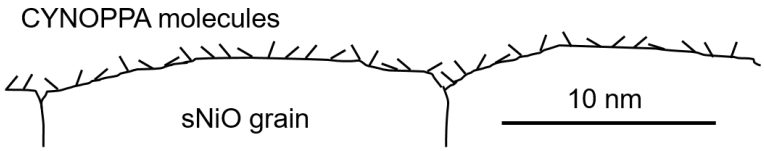

Figure 7.17: Scaled schematic model of CYNOPPA molecules on an AD-sNiO-400 surface. The topography is based on AFM measurements (see Chapter 5). The distance between CYNOPPA molecules is about 1 nm, which is the distance of nearest neighbors in an array with a surface density of 1 nm^{-2}. This value corresponds to the density of CYNOPPA molecules on an AD-sNiO-400 surface. At the surface with the highest density (OP-sNiO-275) the coverage is almost twice as high.

7.4. Functionalization of sNiO – electronic considerations

In the last chapter, a chemical bond formation of the CYNOPPA molecules to the sNiO surfaces was concluded. Now the electronic impact of the chemisorption is investigated. Based on DFT calculations, a net transfer of negative charge from the substrate to the adsorbate was predicted in Chapter 7.1.4. According to Poisson equation, this induces a change of the potential distribution and in case of a semiconductor a band bending upwards. The band bending can be seen by electronic shifts of all energy levels of the substrate including core levels and valence band. These shifts are referred to as energy level shift (ELS) in the following.
Additionally, the work function is affected by the functionalization. The total change of the work function

$$\Delta WF = ELS + \Delta\delta \tag{7.7}$$

is determined by the ELS (which reflects changes of the potential at the surface of the substrate) and the change of the surface dipole $\Delta\delta$. This relation is illustrated in Figure 7.18.

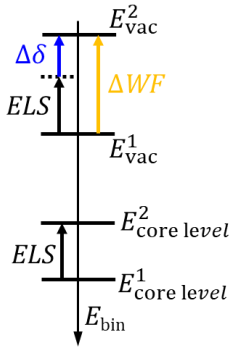

Figure 7.18: Illustration of Equation (7.6). A change of the potential at the surface of a sample similarly affects both the core level binding energies $E_{\text{corelevel}}$ and the vacuum level E_{vac}. The shift is indicated with *ELS*. Additionally, a surface dipole $\Delta\delta$ can contribute to the change of the work function ΔWF.

In the last chapter, it was shown that CYNOPPA increases the work function of sNiO samples compared to ethanol treated reference samples. This increase is now quantified and the two contributions (ELS and $\Delta\delta$) are extracted to test the theoretical prediction and understand the mechanism which leads to the increase in work function.

7.4.1. The impact of CYNOPPA on sNiO surface properties

To analyze the electronic impact of the CYNOPPA functionalization, work function values of functionalized sNiO films and of ethanol treated reference films were extracted from the SECs shown in Figure 7.10 and plotted in Figure 7.19a as a function of the respective type of sNiO substrate (defined by the annealing temperature and whether or not it was treated with OP). Additionally, the work functions of the not further treated AD- and OP-sNiO substrates were added (red squares). A similar behavior as seen in Chapter 5, where a larger number of samples was averaged, is reproduced: the work function decreases with increasing annealing temperature and is similarly high at around 5.6 eV for OP treated samples. In all cases, it is drastically reduced by immersion in ethanol (black diamonds). The pattern is preserved, although the differences between the samples are reduced. With respect to these reference samples, the work functions are increased again upon functionalization with CYNOPPA (brown dots). OP treatment prior to functionalization shows only a small impact. Instead, a new correlation appears: independent whether samples were treated with OP or not, the work function is higher for higher annealing temperatures. However, only in two cases (AD-325 and AD-400) an increase compared to the initial work function was achieved. For OP samples, this can largely be ascribed to the reduction of NiOOH upon immersion in ethanol.
For the tracking of ELSs, three data sources exist: O 1s spectra, Ni $2p_{3/2}$ spectra and spectra of the VBM. Analogous to the work functions in Figure 7.19a, the VBMs as well as the binding energies of the Ni $2p_{3/2}$ and the O 1s main features were determined and displayed in Figure 7.19b, c and d.

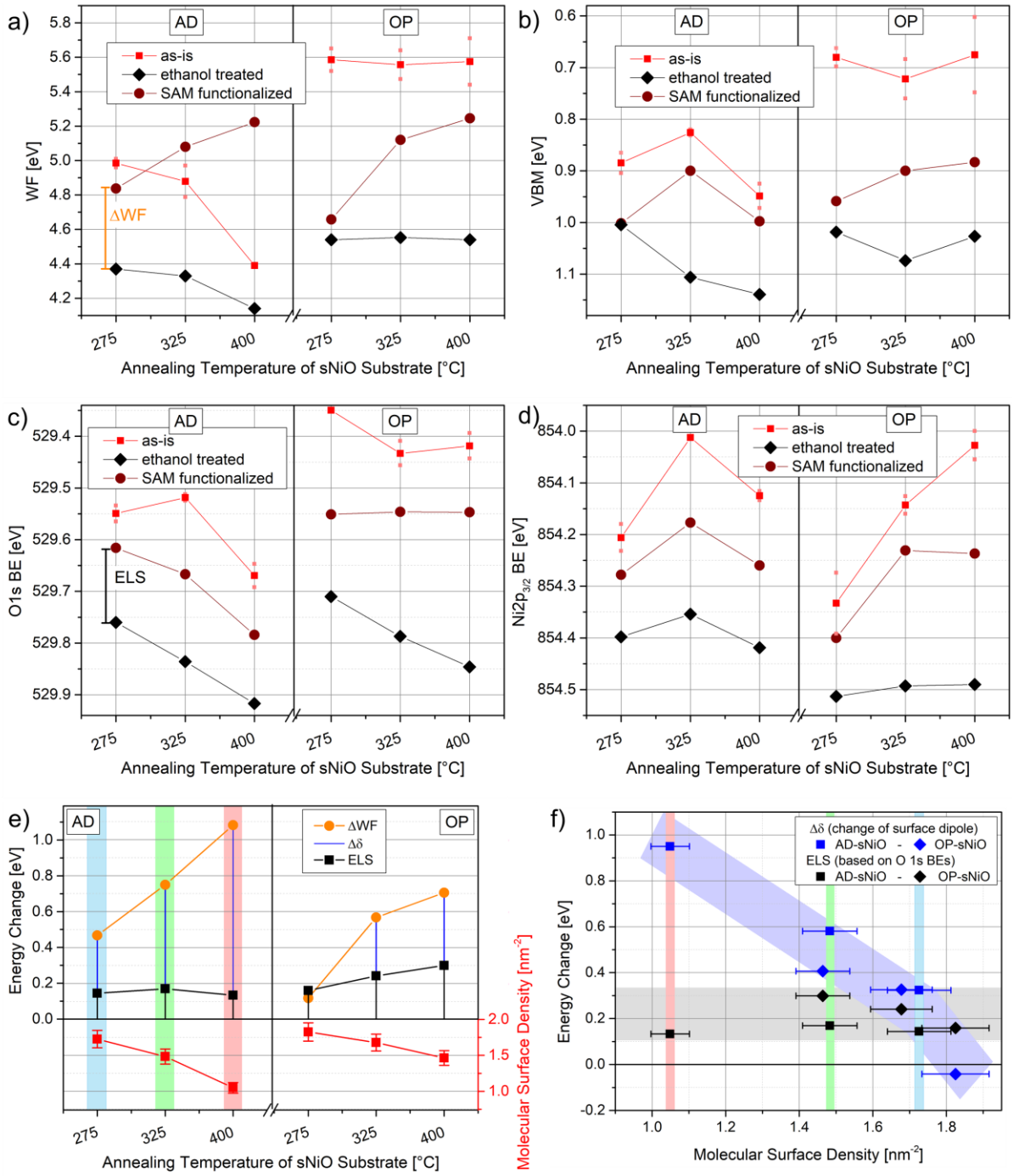

Figure 7.19: (a) Work function (WF) values of CYNOPPA functionalized sNiO films (brown dots) and of ethanol treated reference films (black diamonds) extracted from the SECs shown in Figure 7.10 as a function of the respective type of sNiO substrate defined by the annealing temperature and whether or not it was treated with OP. Additionally, the work functions of the not further treated AD- and OP-sNiO substrates are shown ('as-is', red squares). For each sNiO type, the value indicated with a red square is averaged over two AD-sNiO films from different batches (light red squares). In each case, one film was measured before immersion in ethanol and the other one before functionalization with CYNOPPA. (b) Shows the according valence band maxima. The binding energy (BE) positions of O 1s main peaks (c) were determined by fitting with a Gaussian function. The data points in diagram (d) indicate the Ni $2p_{3/2}$ peak positions, which were determined by fitting the maximum of each main feature with a Gaussian function. The shape of each Gaussian function was determined by defining the upper boundary at the lower parts of the right-hand edges (~853.5 eV). Each lower boundary was set to binding energies slightly above each maximum. (e) Displays the changes of the work function (ΔWF) and of the O 1s binding energy (ELS) upon CYNOPPA functionalization with respect to the ethanol treated reference samples, again as a function of the substrate type. Furthermore, the change of the surface dipole Δδ is indicated in blue. Additionally, the molecular surface density of CYNOPPA is plotted in red. (f) Shows the ELSs and the change of the surface dipole Δδ as a function of the molecular surface density. While ELS shows only little variation, Δδ shows a clear trend

From these three data sets, the values extracted from O 1s spectra are considered to be the most trustworthy for the following reasons. The VBM determination via the leading-edge is prone to uncertainty due to the linear extrapolation. This is especially true for valence bands measured with XPS as here the signal-to-noise ratio is rather low. Furthermore, the influence of chemical changes on the VBM is hard to evaluate and can lead to disturbed values. Finally, VBM has the highest information depth. Thus, in case of a potential band bending, the recorded signal is averaged over a larger depth and is less sensitive to the maximum potential change in direct vicinity to the surface. This argument would favor the Ni $2p_{3/2}$ emission line (highest binding energy, thus lowest kinetic energy) as indicator for changes of the potential. However, its shape is strongly influenced by OP treatment, which is why the position of the Ni^{2+} line cannot be tracked unambiguously (see e.g. Figure 5.15a). All O 1s emission lines, in contrast, feature a clearly distinguishable main peak, which is attributed to O^{2-}. This enables the extraction of electronic shifts, mostly independent from chemical influences.

As can be seen in Figure 7.19c, for all samples, O 1s core levels are shifted toward higher binding energies upon immersion of the samples in ethanol (as already discussed in Chapter 7.2) and are raised again upon functionalization, whereas in none of the cases the starting value is reached again. For each annealing temperature, samples with OP treatment exhibit higher-lying core levels (i.e., lower binding energies), even after immersion in ethanol and after functionalization. This emphasizes again that OP treatment leaves durable traces, which are still visible after immersion of sNiO films in ethanol, during which large parts of the OP influence is reversed (see Chapter 7.2).
In a next step, ELSs were quantified as the difference between the O 1s binding energies of functionalized sNiO films and those of ethanol treated reference films and plotted in Figure 7.19e (black squares). For all six types of sNiO films, the ELSs amount to 0.1 – 0.3 eV toward lower binding energies, whereas a slight dependence on the annealing temperature is visible for OP treated substrates.
Similarly, also the work function change upon functionalization is plotted in Figure 7.19e (orange dots). According to Equation (7.7), the difference between the total work function change ΔWF and the ELS is attributed to a change of the surface dipole $\Delta\delta$, which is indicated by blue lines. As expected from the direction of the molecular dipole moment of CYNOPPA (see Chapter 7.1), in almost all cases a positive change of the surface dipole is measured. For both types, AD and OP, $\Delta\delta$ is larger for higher annealing temperatures and for each annealing temperature, $\Delta\delta$ is reduced when the substrate was treated with OP. To find reasons for these dependencies, additionally, the estimated molecular surface densities extracted in Chapter 7.3.1 were added (red squares, scale on the right-hand side). A correlation between the surface density and $\Delta\delta$ becomes apparent.
For a closer investigation of this correlation, $\Delta\delta$ and ELS were plotted against the estimated molecular surface coverage (Figure 7.19f). Two trends appear. While the ELS upon CYNOPPA functionalization with respect to to the respective ethanol treated reference film is rather independent of the molecular surface density, the change of the surface dipole $\Delta\delta$ is reduced for higher coverages of CYNOPPA. These two trends become particularly obvious when only AD-sNiO samples (highlighted in red, green and blue) are considered.

7.4.2. Interpretation

The ELSs are interpreted as a change of the band bending ΔE_{BB} in the n-Si/sNiO substrate, which - according to the sign of ELS - is a change in upward direction in all cases. This supports the assumption that negative charge is transferred from the substrate to the CYNOPPA layer. Regarding the magnitude of the ΔE_{BB}, its independence on the molecular surface density (Figure 7.19f) appears contra intuitive. For a higher number of bonded molecules, one might be tempted to expect proportionally more transferred charges and thus a stronger ΔE_{BB}, in case the charge redistribution is only due to the chemical bonding itself. However, it was shown by DFT calculations that the magnitude of the charge rearrangement (at each bonding site) can depend on the coverage [273]. Thus, a conclusion on charge

distribution is more complex. Furthermore, the number of transferred charge carriers not only depends on the magnitude of the band bending, but also on the density of states N_V in the valence band and the distance of the Fermi level from the valence band maximum according to Equation (3.1) which differs for the differently prepared sNiO films. Therefore, different amounts of transferred charges are possible in spite of the equal ΔE_{BB}.

The second observation, that the change of the surface dipole $\Delta\delta$ is strongly reduced for higher coverages, drastically contradicts the expectations based on the dipole moment of CYNOPPA molecules in gas phase (see Chapter 7.1), as, according to Equation (7.1), the increase of work function induced by functionalization is in theory proportional to the molecular surface density ρ_A. This suggests the conclusion that the molecular dipole moment of the CYNOPPA molecules is inverted during the adsorption process, despite the overall increase of the surface dipole. A speculative, though possible explanation could be given by the following model.

The first assumption of this model is a strong rearrangement of charges leading to a strong bond dipole $\Delta\Phi_{bond}$ (see sketch in Figure 7.20a). One contribution is the formation of the dipole of the chemical bond itself. The bonding process also includes charge transfer from the substrate to the adsorbate and is manifested in the band bending. The total increase of the potential induced by the charge transfer is supposed to be significantly larger than ΔE_{BB}. The second assumption is that the dipole moment of the chemisorbed CYNOPPA layer is inverted compared to the dipole moment of the isolated molecule. As $\Delta\Phi_{SAM}$ should be proportional to the surface density ρ_A of CYNOPPA molecules, and ρ_A increases with increasing annealing temperature of sNiO, the absolute value of $\Delta\Phi_{SAM}$ also increases and leads to a stronger potential drop (see Figure 7.20b). Additionally, $\Delta\Phi_{SAM}$ is proportional to the cosine of the molecules' tilt angle. In literature, it was observed that a higher coverage favors a more upright orientation of the molecules (i.e., a smaller tilt angle) [285]. Therefore, it is likely that in the present case the net orientation of molecules on sNiO-275 films is larger (i.e., more perpendicular) than for molecules on sNiO-400 films, which additionally contributes to the larger $\Delta\Phi_{SAM}$ of sNiO-275 films.

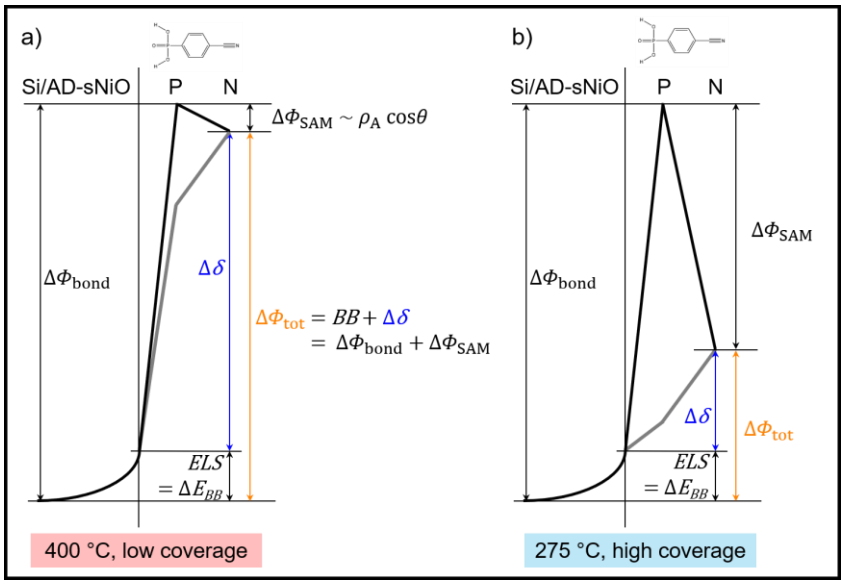

Figure 7.20: Illustration of a proposed model to explain the observed potential changes upon CYNOPPA functionalization. The smaller change of the surface dipole for higher coverages of CYNOPPA is explained by a negative dipole across the backbone of CYNOPPA molecules in the SAM layer reducing the potential by $\Delta\Phi_{SAM}$ (black lines). An alternative explanation is added in grey. Here, the dipole of the bond varies and the dipole of the SAM stays fixed.

7.4.3. Discussion

The discussion first focusses on the validity of the data and afterwards on the validity of the model. For the evaluation of the validity of the data, especially the trend of $\Delta\delta$ (see Figure 7.19c), several aspects have to be considered.

First, data points of ethanol treated and CYNOPPA functionalized samples result from only one sample each and as-is films show that certain sample-to-sample variations exist. While these variations are well below 0.1 eV for core levels (Figure 7.19), the work function values typically vary by ~0.2 eV. However, considering a difference between $\Delta\delta$ of a sNiO-275 substrate and $\Delta\delta$ of a sNiO-400 substrate of more than 0.6 eV, it is unlikely that this uncertainty is responsible for the observed dependency of $\Delta\delta$. Therefore, it is concluded that the observed dependency of $\Delta\delta$ is not due to the uncertainty of the measurement but an actual effect.

Another influence which must be taken into account is the residual carbon on ethanol treated samples, whose impact is not easy to estimate. However, since the amount of carbon on the present samples is comparable, as can be seen from the C 1s detail spectra in Figure 7.21, also the impact on the work function is considered to be similar in all cases. Only on the OP-sNiO-275 film the carbon amount is clearly lower. however, due to magnitude of the trend of $\Delta\delta$, it is unrealistic that it is caused by differences in the carbon contamination. Similarly, a possible influence of the residual carbon on the core level binding energies has to be considered. For these reasons, the observed dependency of $\Delta\delta$ are related to the actual functionalization process.

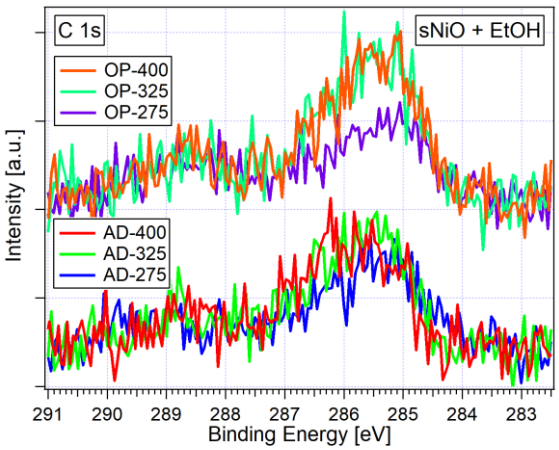

Figure 7.21: C 1s core level spectra of sNiO samples after ethanol treatment.

The plausibility of the model described in Chapter 7.4.2 is supported by DFT calculations by Dr. S. Ma and Dr. W. Liu. For (idealized) CYNOPPA adsorption on several NiO surfaces as presented in Chapter 7.1.4, a large contribution of a charge transfer to the total work function increase of up to 2 eV was found (Figure 7.5b). Although the absolute values of the calculation are quite large, they clearly support the formation of a strong bond dipole, i.e., the total work function shift induced by the charge rearrangement during chemisorption. Also in literature, bond dipoles of more than 1 eV have been calculated [273].

Additionally, for the NiO(111)-Rt3-OH surface reconstruction a negative contribution of the isolated CYNOPPA layer $\Delta\Phi_{SAM}$ was found by DFT calculations, as also shown in Figure 7.5b. This demonstrates that also in theory a scenario in which the CYNOPPA SAM layer itself reduces the work function exists. Additionally, charge rearrangement occurs. While usually charge rearrangement is supposed to be strongly confined to the region of the chemical bonds at the interface, Romaner et al. have found by DFT calculations [273] that it can also extent to the backbones of the SAM molecules: in their simulation, charge rearrangement also occurred between the phenyl ring of a molecule similar to CYNOPPA and the anchor group. While such scenario might support the inversion of the molecular dipole of CYNOPPA during adsorption, scientific proofs are missing at this point. In particular, it remains questionable if such strong dipole moments can be inverted upon chemisorption.

An alternative explanation is a charge rearrangement being restricted to a region close to the interface, which leaves the dipole moment of the molecules unaffected. As demonstrated by the DFT calculations (Figure 7.5b), the resulting dipole $\Delta\Phi_{charge-redis}$ depends on both the surface reconstruction and the binding mode. Thus, $\Delta\Phi_{charge-redis}$ might be smaller for 275-sNiO than for 400-sNiO due to the

different surface compositions and different binding modes. This explanation is visualized in Figure 7.20 in grey.

Unfortunately, the system is highly disordered and far away from the theoretical, idealized plate capacitor model, rendering the understanding and visualization of the system difficult. Due to the complexity of the system, a combination of both models is likely.

7.4.4. Conclusion

In summary, the quantitative analysis of electronic changes revealed a strong band bending downwards for all sNiO film types for treatment with ethanol and a somewhat smaller but still significant band bending upwards upon CYNOPPA functionalization. While the size of the latter is only little dependent on the sNiO film type, the change of the surface dipole is much smaller for sNiO films annealed at lower temperatures where the CYNOPPA coverage is larger. A possible explanation is a strong work function increase induced by a net transfer of negative charges from the substrate toward the adsorbate during the chemisorption. The effect of this bond dipole is reduced by the molecular dipole of the CYNOPPA layer, which has been inverted upon chemisorption. This reduction is more pronounced for closer packed CYNOPPA layers, i.e., on sNiO films annealed at lower temperatures. Arguments for and against this interpretation were discussed, while direct proofs could not be provided. Thus, at the present stage the model is a tentative attempt for the description of the experimental data.
Alternatively, the observation could be explained by a variable charge redistribution, which depends on the annealing temperature of the sNiO substrate while the dipole of the SAM is fixed in regular direction. For the purpose of clarification, a more defined system with a measurable orientation of the SAM molecules is required. Then direct comparisons between the measured binding energies, the plate capacitor model and DFT calculations could be drawn.

7.5. Performance of CYNOPPA functionalized sNiO in organic solar cells

Finally, the influence of functionalization of sNiO with CYNOPPA on solar cell performance was investigated for the same FHJ OPV stack as in Chapter 6: ITO/sNiO-325/[CYN]/ F_4ZnPc/C_{60}/TPBi/Ag. sNiO films were used both with and without OP treatment and functionalized with CYNOPPA. As was shown in Figure 7.19a, functionalization leads to a work function of about 5.1 eV for both types, AD and OP, which is slightly larger than the work function of AD-sNiO-325 and clearly lower than the work function of OP-sNiO-325.

Figure 7.22a shows representative J-V curves of OPVs with the four different modifications of sNiO HTLs, i.e., AD, OP, AD+CYN and OP+CYN. The curves of AD- and OP-sNiO-based OPVs have been discussed in Chapter 6 and show decent solar cell characteristics. Contrastingly, a second photodiode behavior, often also referred to as s-kink or s-shape, is observed for devices with CYNOPPA functionalized sNiO layers. The fill factors are strongly reduced und the current in forward direction significantly suppressed while V_{OC} stays about the same and J_{SC} is only slightly reduced.
Such behavior is known in literature and usually related to a hindered charge transport at interfaces [286–288], which can have different reasons. A common explanation is energy level mismatch between transport and active layer, which can create energetic barriers for charge extraction or injection [289–291]. The mechanism is explained by pile-up of charge carriers at the interface between transport and active layer, which leads to a field in the transport layer [290]. Thus, the field in the active layer is reduced for a certain voltage and so is the charge carrier extraction efficiency.
Furthermore, it was shown that strong interface dipoles [292] or low conductivity of an interface or an interlayer can lead to an s-kink [291]. Finally, charge transport properties of the active layer can also cause an s-shaped J-V curve [293]. The latter, however, can be excluded as reason here, since devices with the same active layer did not show an s-kink when used with non-functionalized sNiO and the influence of a change in molecular orientation has been excluded by fabrication of solar cells

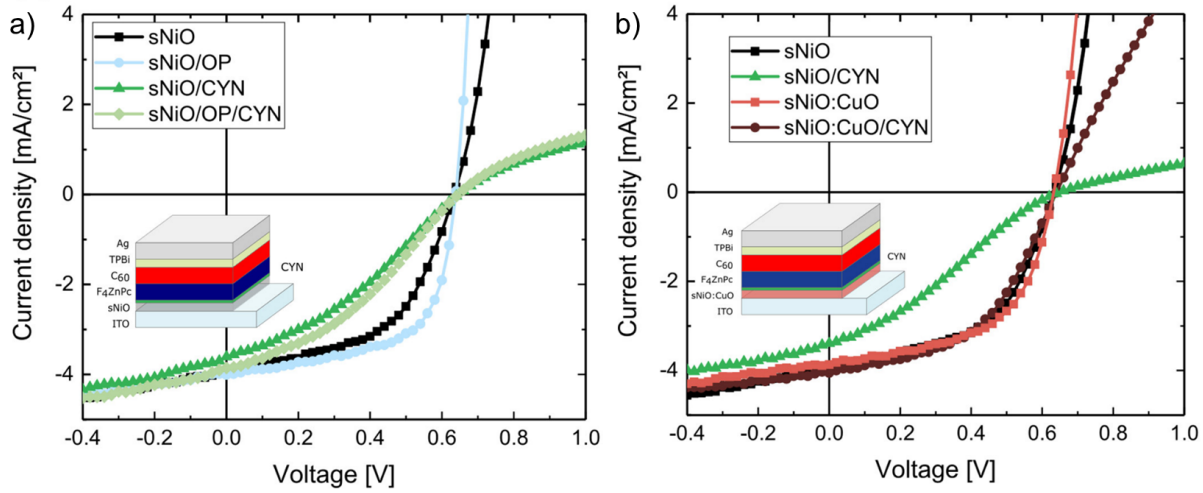

c)

HTL (325°C)	V_{oc} [V]	J_{sc} [mA cm^{-2}]	R_s [Ω cm^2]	FF [%]	PCE [%]
sNiO	0.64 ± 0.01	4.0 ± 0.1	37 ± 3	52.9 ± 0.8	1.31 ± 0.04
sNiO/OP	0.64 ± 0.01	4.1 ± 0.1	15 ± 2	60.8 ± 0.9	1.59 ± 0.09
sNiO/CYN	0.64 ± 0.02	3.7 ± 0.1	118 ± 39	38.9 ± 5.1	0.95 ± 0.17
sNiO/OP/CYN	0.65 ± 0.02	3.9 ± 0.2	133 ± 56	40.3 ± 4.9	1.05 ± 0.16
sNiO:CuO	0.65 ± 0.02	3.7 ± 0.2	27 ± 5	54.7 ± 1.4	1.34 ± 0.07
sNiO:CuO/CYN	0.64 ± 0.01	3.9 ± 0.2	63 ± 23	47.1 ± 7.8	1.25 ± 0.21

Figure 7.22: Representative J-V characteristics of sNiO-based FHJ OPVs. (a) Influence of CYNOPPA functionalization of AD- and OP-sNiO HTLs and (b) influence of Cu doping. (c) Device performance parameters, each averaged over 6-10 devices. Reprinted from [25].

with the hydrophobic SAM molecule 1H,1H,2H,2H-perfluorooctane-phosphonic acid (FHOPA). Due to hydrophobicity of FHOPA functionalized surfaces [185] compared to the hydrophilic character of CYNOPPA functionalized surfaces, a different orientation of F_4ZnPc molecules in vicinity of the interface is expected. Still, a strong s-kink is observed in according OPVs [25].

To get more information of the nature of the barrier, J-V curves were measured under various illumination intensities as proposed by Tress et al. [291], who showed that the two types of barriers, injection and extraction, lead to distinctly different intensity dependent behaviors of the J-V curves, based on which extraction and injection barrier can be distinguished. As can be seen in Figure A.25, the data clearly indicate the presence of an extraction barrier instead of an injection barrier. This barrier can be identified as hole extraction barrier in the present case, since the s-kink only occurred after introduction of the SAM at the anode side.

A hint that conductivity is a bottleneck in the present case is the drastically increased series resistance of cells based on CYNOPPA functionalized sNiO compared to devices without CYNOPPA (16-40 Ω cm² compared to 120-130 Ω cm², see table in Figure 7.22c). To verify this assumption, the conductivity of the sNiO layer was intentionally increased by blending the NiAc precursor with CuAc (10 wt.%) prior to spin-coating and annealing [294–296]. As a consequence, the specific resistance of films spin-coated on glass and measured with four-point probe drops from >30 Ω m to 6.6 Ω m [185].

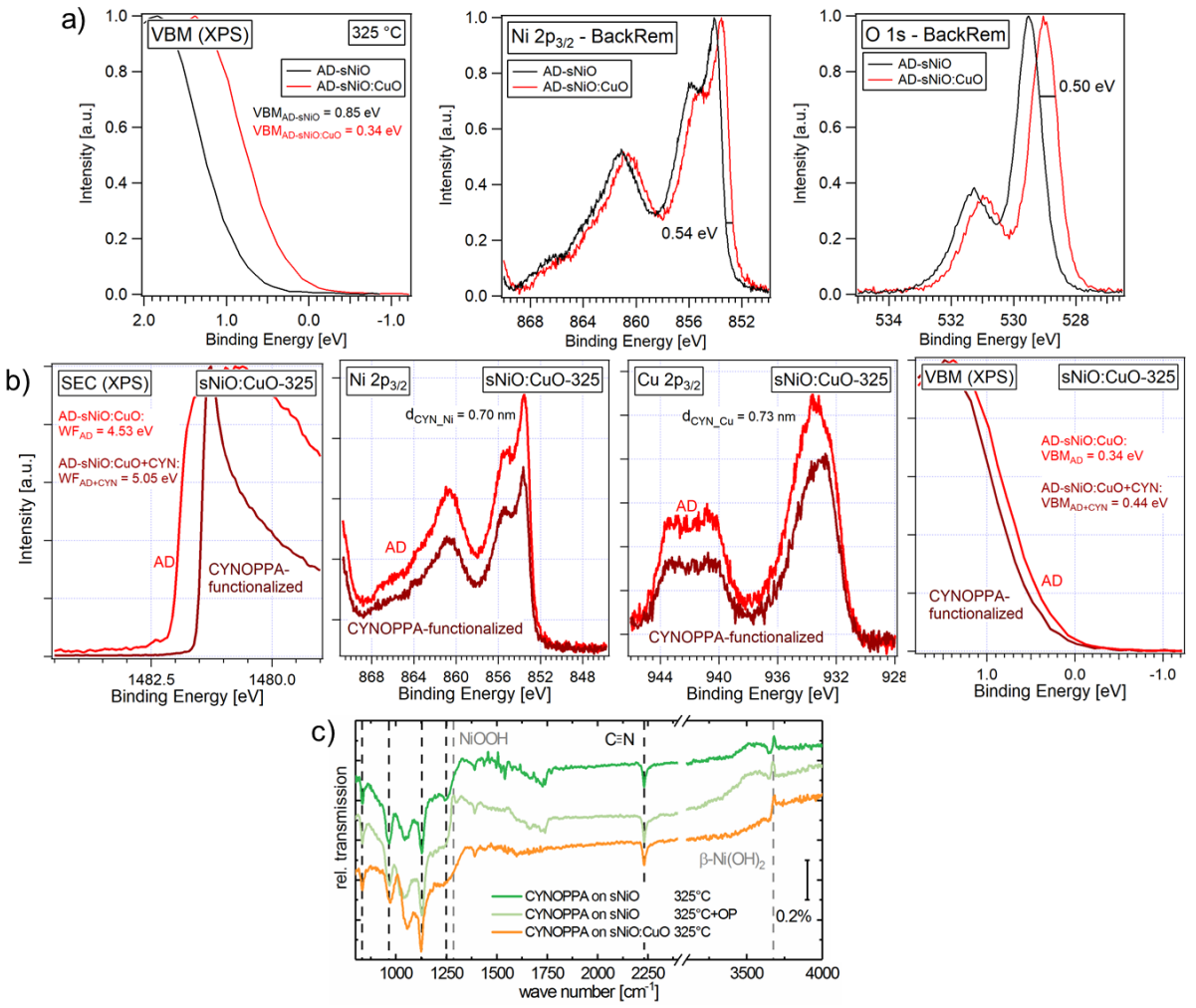

Figure 7.23: XP spectra of a doped sNiO film (sNiO:CuO) in comparison to an undoped film. A Fermi level shift of about 0.5 eV toward the VBM is visible. (b) XP spectra of CYNOPPA-functionalized doped sNiO films in comparison to non-functionalized doped films. The damping of both metal lines, Ni $2p_{3/2}$ and Cu $2p_{3/2}$ results in nominal CYNOPPA layer thicknesses of ~0.7 nm, which is similar to the nominal layer thickness determined for undoped films in Chapter 7.3 (0.70 nm). (c) IR spectra of CYNOPPA-functionalized sNiO films, with and without doping. The similarity of the spectra confirms similar amounts of CYNOPPA and indicates similar adsorption processes. The data has been published in [25].

Additionally, the Fermi levels shifts by about 0.5 eV closer to the valence band (see Figure 7.23a), indicating a higher charge carrier density if the density of states does not change much. Although this behavior reminds on a typical inorganic p-doping process (like, e.g., known for Li-doped NiO [297]), the replacement of a nickel atom in the lattice by a copper atom cannot be the cause for the Fermi level shift here, since copper has one valence electron more than nickel and thus would lead to n-doping. Instead, a charge transfer from NiO to CuO due to Fermi level alignment is a more reasonable explanation. Still, due to convenience and the common use in literature, the blending process is referred to as "doping" in the following. When Cu-doped sNiO films are used in F_4ZnPc-based FHJ, the higher conductivity is confirmed by a slight but significant reduction of R_s accompanied by only a small increase of the fill factor and the PCE (see table in Figure 7.22c).

For these reasons, Cu-doping of sNiO films is considered a viable mean to test the dependence of the s-kink on the HTL's conductivity. Therefore, sNiO:CuO films were functionalized with CYNOPPA and implemented in OPVs. To exclude an impact on device characteristics by differences in the CYNOPPA layer, both IR and XPS measurements have been performed. The results in Figure 7.23b and c confirm a similar amount of CYNOPPA on the doped films as on the undoped film (based on the nominal layer thickness calculated from both the Ni $2p_{3/2}$ and the Cu $2p_{3/2}$ signal (~0.7 nm) and on the intensity of the C-N mode) and similar binding mechanisms based on the absorption modes in the wavenumber range between 750 and 1250 cm^{-1}. Also the work function of functionalized NiO:CuO films is similar to the one of functionalized undoped sNiO films (~5.1 eV). Only the VBM is different. While the VBM of functionalized undoped sNiO was measured with ~0.9 eV (Figure 7.19b) the doped film has a VBM of 0.45 eV after functionalization (Figure 7.23b, diagram on the right).

As shown in Figure 7.22b, the s-kink of OPVs with functionalized doped sNiO films is significantly reduced compared to devices with functionalized sNiO films without doping. The fill factor is almost completely recovered for devices with doped sNiO. While V_{OC} is basically unaffected, J_{SC} is slightly increased. The biggest change, however, is seen in the series resistance, which almost doubles from (63±23) Ω cm^2 to (118±39) Ω cm^2. This indicates that the conductivity of the sNiO HTL plays a major role for the formation and vanishing of the s-kink. However, as the improvement upon doping of sNiO is accompanied by a shift of the valence band toward the Fermi level (~0.45 eV), also the distance between VBM of sNiO and the HOMO of F_4ZnPc at the interface is expected to change (see Figure 7.24 for visualization). The former extraction barrier of 0.9 eV in the case of the interface with undoped sNiO (Figure 7.24b) has vanished when doped sNiO is used as HTL (Figure 7.24c). It is likely that this change of the energetic extraction barrier also contributes to occurrence of the s-kink. The pileup of holes at the AD-sNiO+CYN/F_4ZnPc interface in Figure 7.24b is amplified by the low conductivity of the functionalized sNiO HTL.
Note that the low conductivity of the functionalized sNiO film is likely connected to the lowering of the valence band by the solvent, ethanol. Even though the bonding process shifts the valence bands up again, the original level is not restored. This holds in particular for the OP treated films, where the conductive NiOOH layer is erased by ethanol and therefore the downward shift of the VBM upon contact with ethanol is more pronounced. Thus, the beneficial effect of OP treatment of sNiO films on device performance is lost upon functionalization.

Finally, strong dipoles have been shown to be created by CYNOPPA functionalization (Figure 7.19), but as the CYNOPPA layers are similar for both the undoped and the doped sNiO, and in the latter case no s-kink occurs, it is concluded that dipoles play a minor role only.

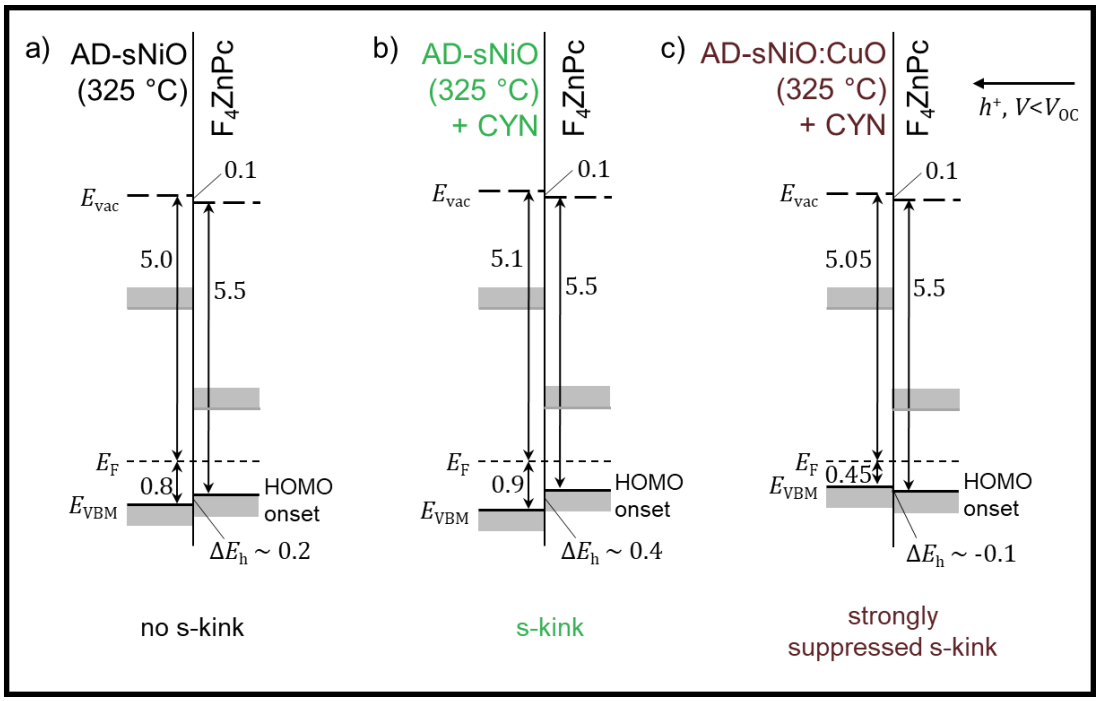

Figure 7.24: Estimated energy level alignment at the very interfaces between F_4ZnPc and AD-sNiO-325 (a), CYNOPPA-functionalized AD-sNiO-325 (b) and CuO-doped CYNOPPA functionalized AD-sNiO-325 (c) based on the interface dipole measured for the AD-sNiO/F_4ZnPc interface in Chapter 6 (0.1 eV) and the ionization potential of F_4ZnPc at the interface (5.5 eV). The data of the three films results from Figure 7.19 and Figure 7.19. As the films were measured on Si substrates, a deviation of the VBM and the WF values by ~0.1 eV from those extracted in the interface experiment in Chapter 6 (Figure 6.12) exists. Although the interfaces displayed here have not been measured directly, the diagrams should possess a certain validity. This applies especially to the comparison between (b) and (c) as both surfaces are chemically and electronically basically identical, expect for the higher-lying valence band in the case of doped sNiO (c). Therefore, a reduced hole extraction barrier in the latter case (c) can be expected.

7.6. Summary

The first goal of this chapter was to clarify whether SAM functionalization of solution-processed NiO with the phosphonic acid CYNOPPA is possible and to study the absorption in detail. In this regard, the chemisorption of PA molecules onto the film surface was shown and specified as a heterocondensation reaction via mono- and bidentate bonds in agreement with results of DFT calculations. XPS measurements proved the existence of about one monolayer of CYNOPPA on all sNiO film types. A tilt angle could not be determined by IR spectroscopy, which is why a low order of the monolayer was concluded. The density of the adlayer and the impact on electronic properties, like the change of the work function, was found to decisively depend on the film's surface composition and thus on its processing history. The amount of chemisorbed CYNOPPA correlated with the OH amount at the surfaces of the sNiO films, which is reasonable under consideration of the identified heterocondensation reaction. This led to the conclusion that the amount of CYNOPPA, and moreover generally the amount of phosphonic acids chemisorbing to an sNiO surface can be controlled via the annealing temperature and OP treatment. The effect of OP treatment on the sNiO film surfaces was largely reduced by treatment of the films with pure ethanol, whereas as result the amount of OH was increased compared to a similarly ethanol treated film which has not been exposed to oxygen plasma. Against the expectations, a lower CYNOPPA adsorption leads to a larger change of the surface dipole. Further, it was demonstrated that the solvent ethanol causes a strong core level shift downwards. It was emphasized that the impact of the solvent on the films' surface properties cannot be neglected but has to be considered in order to estimate the actual impact of the SAM functionalization.

The second goal was to increase the work function of sNiO films by means of SAM functionalization and thus to achieve an enhancement of the PCE of organic solar cells. While the work function was successfully increased compared to ethanol treated reference films, OPVs based on functionalized sNiO HTLs suffered from a pronounced double-diode behavior (s-kink). Light intensity dependent J-V measurements identified the existence of a hole *extraction* barrier. It was possible to overcome this barrier and the s-kink by increasing the conductivity of sNiO HTLs by doping. Therefore, it was concluded that the low conductivity of the functionalized sNiO films plays a major role for the formation of the s-kink. As also the distance of the valence band maximum to the Fermi level in sNiO is changed by the doping, it is assumed that additionally a reduced extraction barrier height supports the suppressed s-kink.
It is concluded that the occurrence of an energetic hole extraction barrier due to a deep-lying VBM in combination with a low conductivity of functionalized sNiO is responsible for the double-diode behavior. Even OP treated sNiO films do not provide enough conductivity as the conductive NiOOH surface layer formed during OP treatment is erased by immersion in ethanol.

8. Summary and Outlook

The present work aims at an understanding of chemical and electronic properties of solution-processed nickel oxide (sNiO) and its surface modification by oxygen plasma (OP) and functionalization with self-assembled monolayers (SAMs) with regard to application in organic solar cells (OPVSs). The main analytical tool was photoelectron spectroscopy, which was complemented by IR spectroscopy to obtain additional information on chemical composition and molecular orientation.

In a first step, the bulk and surface properties of sNiO thin films depending on the annealing temperature of the precursor film were studied. The films consisted of smooth, pinhole-free and electronically homogeneous layers of grains with lateral dimensions of 10-20 nm and thicknesses in the range of 20 nm. Additionally detected hydroxidic species like NiOOH, $Ni(OH)_2$ and surface OH surround these grains, which were shown to consist of close-to-stoichiometric NiO. In the case of the highest annealing temperature (400 °C) the OH concentration covering the surface was only in the range of one monolayer. Work functions were measured between 4.4 and 4.9 eV and decreased with increasing annealing temperature. This is attributed to the decreasing content of hydroxidic species. The Fermi level position showed only little variation.
Based on this knowledge, the impact of the common OP treatment was investigated in detail. It was found that OP treatment converts non-conductive NiO and β-$Ni(OH)_2$ into a thin conductive surface layer of a NiOOH-like phase, which possesses a pinning character and pulls both the Fermi level and the work function to same values, largely independent of differences in the chemical composition and the Fermi level position prior to the treatment. The qualitative transferability of the processes to vacuum-processed NiO was shown. In the case of sNiO, the increase of the surface dipole upon OP treatment was larger for higher annealing temperatures, where films had a lower NiOOH content, and correlated with the amount of created NiOOH. Based on the XPS measurements, energy level diagrams were extracted, and a layer model was conceived for the purest sNiO film (i.e., 400 °C) before and after OP treatment.
In addition, strong indications were found that NiOOH in XP spectra must actually be taken into account with two components, which result from the two different oxygen species instead of only with one, although the latter is a common assignment in literature.
The spectroscopic study contributes to a deeper understanding of the correlations between the fabrication parameters, chemical composition and electronic properties of solution-processed NiO.

In a next step, the positive impact of OP treatment on sNiO-based OPVs was examined by means of two interface experiments and correlation of the obtained energy level diagrams to OPV performance. In the experiments, interfaces of AD- and OP-sNiO with F_4ZnPc were studied by XPS and UPS and complemented by IR data. Generally similar properties were found for both interfaces. F_4ZnPc defluorinates in both cases at the interfaces. Three models to describe the process in detail were discussed. Charge transfer was investigated by fits of XP spectra and compared to IR results. A charge transfer could be excluded for both interfaces despite the expectation of a charge transfer based on energetic considerations in the case of the OP treated sNiO substrate. This apparent contradiction was solved by considering the lowering of the work function due to the chemical reaction at the interface. Moreover, for the first time, it was demonstrated that the NiOOH formed upon OP treatment is not only stable under UHV conditions but also during the evaporation of F_4ZnPc. The NiOOH led to elevated energy levels at the interface, which can be assumed to be related to the enhanced conductivity found by both lateral electrical measurements and OPV characterization. The improvement of OPVs upon OP treatment was mainly attributed to the enhanced conductivity with a further beneficial impact of increased band bending in the F_4ZnPc adlayer.

In the final part, another way to enhance the surface properties of sNiO was investigated, namely the functionalization with SAMs, which provides superior tunability of the work function and the surface

energy compared to OP treatment. A comprehensive study of SAM formation on sNiO has not been performed so far. Thus, it was of interest whether functionalization of sNiO was possible, how the SAM binds to the surface and how the properties of the SAM depend on the processing parameters of sNiO.
For the evaluation, a phosphonic acid, CYNOPPA, was chosen. It was able to demonstrate chemisorption and the formation of layers with a coverage in the range of one monolayer. However, due to the absence of uniform molecular orientation, the layer cannot be referred to as a SAM in the common sense. The exact coverage correlated with the processing-dependent hydroxide content of sNiO films prior to functionalization, which can be understood based on the identified heterocondensation reaction. Thus, annealing temperature of the sNiO films and OP treatment provide a mean to manipulate the coverage. The work function could be increased as expected, whereas most of the increase was caused by a change of the surface dipole with a smaller contribution of a band bending upwards in the substrate, indicative for a transfer of negative charge from the substrate to the adsorbate. Surprisingly, the increase of the surface dipole correlated inversely with the CYNOPPA coverage, which is why the inversion of the molecular dipole moment upon chemisorption was proposed in a model. A second alternative model explained the observation with a variable bond dipole at the interface and a fixed dipole of the SAM.
Important for the analysis was the examination and consideration of the impact of the solvent, ethanol, on chemical and electronic properties of the sNiO substrates. After immersion of sNiO films in pure ethanol, energy levels at the surface were shifted downwards by some hundred meV and for OP treated films, the NiOOH surface layer disappeared and was converted to surface OH and $Ni(OH)_2$. Thus, the OH content of sNiO films which were OP treated prior to immersion in ethanol was higher than in according films without OP treatment.
Despite the promising increase of work function upon functionalization with CYNOPPA, OPVs based on CYNOPPA functionalized sNiO exhibited a strong double-diode behavior, which was attributed to the occurrence of an energetic hole extraction barrier due to a deep-lying VBM in combination with a low conductivity of SAM functionalized sNiO. Even OP treated sNiO films do not provide enough conductivity as the conductive NiOOH surface layer formed during OP treatment is erased by immersion in ethanol.

For these reasons, future experiments with other solvents must be conducted. If it was possible to avoid the strong band bending downwards upon contact of sNiO films with ethanol, both a higher conductivity and a lower energetic hole extraction barrier could be achieved. To clearly distinguish between these both impacts, solid knowledge about the energy level alignment at the interface is needed. This knowledge can be obtained by interface experiments of F_4ZnPc on CYNOPPA functionalized sNiO films, with and without doping. Thus, also a potential influence of band bending at the donor side of the interface on the s-shaped J-V curve can be illuminated. Another conclusion is that a SAM-binding group which works well for the modification of a certain HTL, e.g., PA on ITO in OPVs [263], does not necessarily work on another HTL. This can be due to different interaction mechanisms of the molecules and the solvents with the substrate.
For a solid confirmation of the potentially inverted dipole of the backbone of CYNOPPA films, a more defined system is essential, since the interpretation of the results (like the band bending in the substrate) is complicated by the change of sNiO film properties with different annealing temperatures. This renders the understanding of charge redistribution during chemisorption, especially between substrate and SAM difficult. Finding a way to vary the surface OH amount independently from the film properties will provide a decisive benefit. This might, e.g., be realized by UHV-annealed sNiO (or better single crystalline NiO) in UHV and the leaking of oxygen or water into the system, although then ideally a way to deposit PAs in UHV would have to be developed. The disadvantage of such procedure, however, is the loss of direct comparability to applications in OPVs. Furthermore, the use of different molecules will be interesting. A comparison between molecules with and without phenyl ring could shine light on the influence of the delocalized π-electron system on the reversibility of the

dipole moment. Moreover, variation of substrate properties (p/n-type and work function) could give further evidence. In any case, a system of highly ordered molecules, which enabled the comparison between experimental data, simple physical approaches like the plate-capacitor model and DFT calculations, would be crucial. In such a system, the molecular orientation could be determined by angular-resolved IR spectroscopy and crosschecked by NEXAFS. Finally, synchrotron radiation would deliver a higher spectral intensity and thus enhanced signal-to-noise ratio.

The fundamental importance and extraordinary properties of sNiO produced from a NiAc precursor investigated in this work were demonstrated in state-of-the-art Perovskite solar cells (PVSCs) in cooperation with Dr. Nakita Noel from Princeton University. As shown in Figure 8.1, PVSCs with (AD-)sNiO as HTL reached 20 % stabilized PCE, which is among the highest reported values for PVSCs based on undoped sNiO.

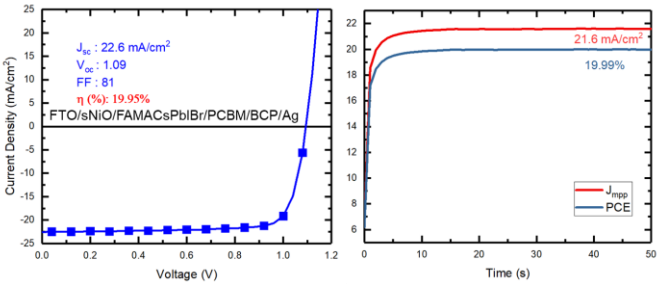

Figure 8.1: Example for successful application of sNiO in state-of-the art PVSCs. Solar cells fabricated and data recorded by Dr. Nakita Noel.

It would be interesting to analyze the interface between the perovskite and sNiO to understand the origin of the obviously excellent alignment. This, however, is difficult as the Perovskite is deposited from solution. A solution could be a new way to access interfaces in complete devices stacks, which has been developed in the group of Prof. Jaegermann at TU Darmstadt. First experiments in this direction have already been performed.

Furthermore, tandem solar cells provide a promising possibility for drastic increase of efficiency by combining well-known silicon solar cell technology with the more tunable perovskites. In such architecture, an interface between silicon and sNiO can occur, which is essential for the performance of the tandem cell. In this work, first steps have been done by investigating the properties of sNiO thin films on different silicon substrates. To gain more knowledge for the application in tandem solar cells, an intensification of this effort will be necessary.

In summary, this work contributes to the understanding and controlling of surface properties of solution-processed nickel oxide. These properties are crucial for optimized application of functional sNiO films in electronic devices like organic photovoltaic cells, but also in non-fullerene, perovskite and tandem solar cells as well as in batteries and for water splitting.

A. Appendix

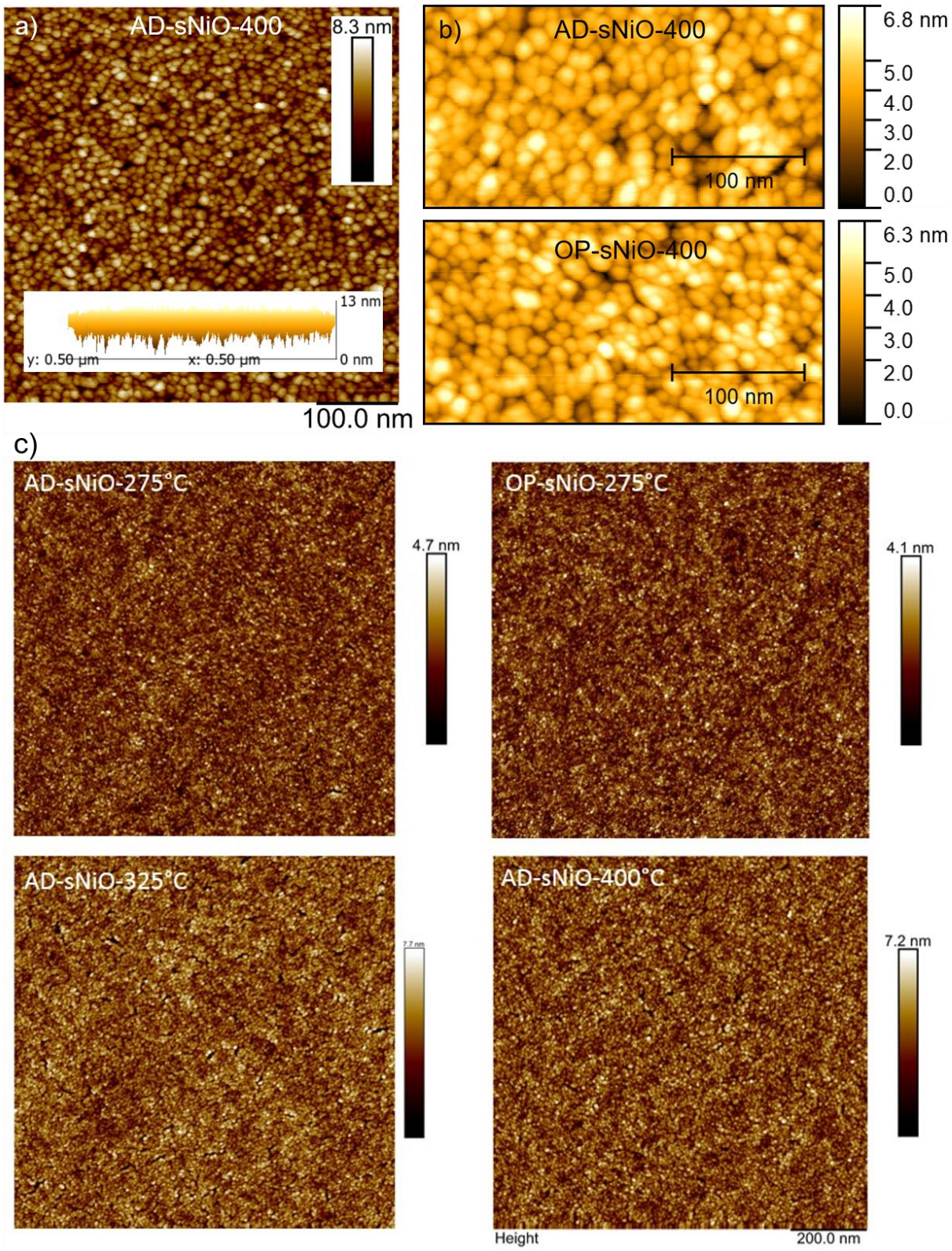

Figure A.1: Peak-force AFM images of an AD-sNiO-400 film (a), an AD-sNiO-400 film compared to an OP-sNiO-film (b) and sNiO films annealed at different temperatures. Films annealed at lower temperatures exhibit slightly smaller grain sizes. OP treatment does not have a significant impact on the topography.

Table A.1: Literature values of O 1s binding energies. The values in brackets are referenced in BE to the position of the main peak measured by Ratcliff et al. (529.6 eV [13]) to provide better comparison.

Material	Ni oxide (O^{2-}) [eV]	Ni hydroxide (OH^-) [eV]	H_2O [eV]	Source
scNiO(100)	529.4	-	-	Kuhlenbeck et al. (1991) [298]
scNiO(100)	~529.3	-	-	Uhlenbrock et al. (1992) [63]
scNiO(100)	529.4[22]	-	-	Alders et al. (1996) [49]
NiO(100)/Ni(100)	530.2	-	-	Kuhlenbeck et al. (1991) [298]
NiO(100)/Ni(100)	530.3	532.2 (531.5; 1.9)	-	Cappus et al. (1993) [61]
NiO(111)/Ni(111)	529.9	531.4 (531.1; 1.5)	-	Cappus et al. (1993) [61]
NiO(111)/Ni(100)	529.4[22]	531.2 (531.4; 1.8)	-	Langell et al. (1994/1995) [103,158]
Oxidized Ni (O_2)	529.9	531.7 (531.4; 1.8)	533.5 (533.2; 3.6)	Kim et al. (1974) [67]
Oxidized Ni (O_2)	529.6	531.3 (1.7)	533.1 (3.5)	Ratcliff et al. (2011) [13]
Oxidized Ni (air)	529.1	-	-	Kim et al. (1972) [68]
Oxidized Ni (air)	529.9	-	-	Kim et al. (1974) [67]
Oxidized Ni (air)	529.2	531.4 (531.8; 2.2)	-	Robert et al. (1972) [299]
pcNiO powder	529.5	531.4 (531.5; 1.9)	-	Gaskell et al. (2007) [157]
pcNiO powder	529.3	531.1 (531.4; 1.8)	532.8 (533.1; 3.5)	Biesinger et al. (2009) [95]
pcNiO powder	529.3	531.0 (531.3; 1.7)	-	Payne et al. (2009) [154]
$Ni(OH)_2$ (β?)	-	530.9	-	Biesinger et al. (2009) [95]
$Ni(OH)_2$ (β?)	-	531.1	-	Payne et al. (2009) [154]
β-$Ni(OH)_2$	-	530.9	-	Payne et al. (2012) [180]
NiOOH	529.8	531.6 (531.4; 1.8)	532.8 (532.6; 3.0)	Hoppe et al. (1989) [50]
β-NiOOH (150/220°C)	529.7	531.4 (531.3; 1.7)	533 (529.9; 3.3)	Moroney et al. (1983) [179]
β-NiOOH	529.3	530.8 (531.1; 1.5)	?	Payne et al. (2009) [154]
γ-NiOOH	529.5	531.1 (531.2; 1.6)	~533?	Payne et al. (2009) [154]
γ-NiOOH	529.5	531.2 (531.3; 1.7)	~533?	Payne et al. (2012) [180]

[22] Assumed to be corrected for charging

Table A.2: Literature values of Ni $2p_{3/2}$ binding energies. Values indicate the maximum intensity of the respective peak.

Material	NiO main [eV]	NiO intersite [eV]	$Ni(OH)_2$ [eV]	NiOOH [eV]	Source
scNiO(100)	854.1	855.6 (1.5)	-	-	Kuhlenbeck et al. (1991) [298]
scNiO(100)	854.0	855.8 (1.8)	-	-	Uhlenbrock et al. (1992) [63]
scNiO(100)	853.2	854.9 (1.7)	-	-	Alders et al. (1996) [49]
NiO(100)/Ni(100)	854.4	856.2 (1.8)	-	-	Kuhlenbeck et al. (1991) [298]
NiO(100)/Ni(100)	-	-	-	-	Cappus et al. (1993) [61]
NiO(111)/Ni(111)	-	-	-	-	Cappus et al. (1993) [61]
NiO(111)/Ni(100)	854.0	855.7 (1.7)	-	-	Langell et al. (1994/1995) [103,158]
Oxidized Ni (O_2)	854.5	855.8 (1.3)	-	-	Kim et al. (1974) [67]
Oxidized Ni (O_2)	853.1	854.7 (1.6)	-	-	Ratcliff et al. (2011) [13]
Oxidized Ni (air)	854.0	855.8 (1.8)	-	-	Kim et al. (1972) [68]
Oxidized Ni (air)	854.5	856.3 (1.8)	-	-	Kim et al. (1974) [67]
Oxidized Ni (air)	-	-	-	-	Robert et al. (1972) [299]
pcNiO powder	~854	~856 (1.8)	-	-	Gaskell et al. (2007) [157]
pcNiO powder	854.0	856.0 (2.0)	-	-	Biesinger et al. (2009) [95]
pcNiO powder	853.8	855.7 (1.9)	-	-	Payne et al. (2009) [154]
$Ni(OH)_2$ (β?)	-	-	855.4	-	Biesinger et al. (2009) [95]
$Ni(OH)_2$ (β?)	-	-	855.6	-	Payne et al. (2009) [154]
β-$Ni(OH)_2$	-	-	855.4	-	Payne et al. (2012) [180]
β-NiOOH (150/220°C)	-	-	-	855.6/856.0	Moroney et al. (1983) [179]
β-NiOOH	-	-	-	856.1	Payne et al. (2009) [154]
γ-NiOOH	-	-	-	856.4	Payne et al. (2009) [154]
γ-NiOOH	-	-	-	856.5	Payne et al. (2012) [180]

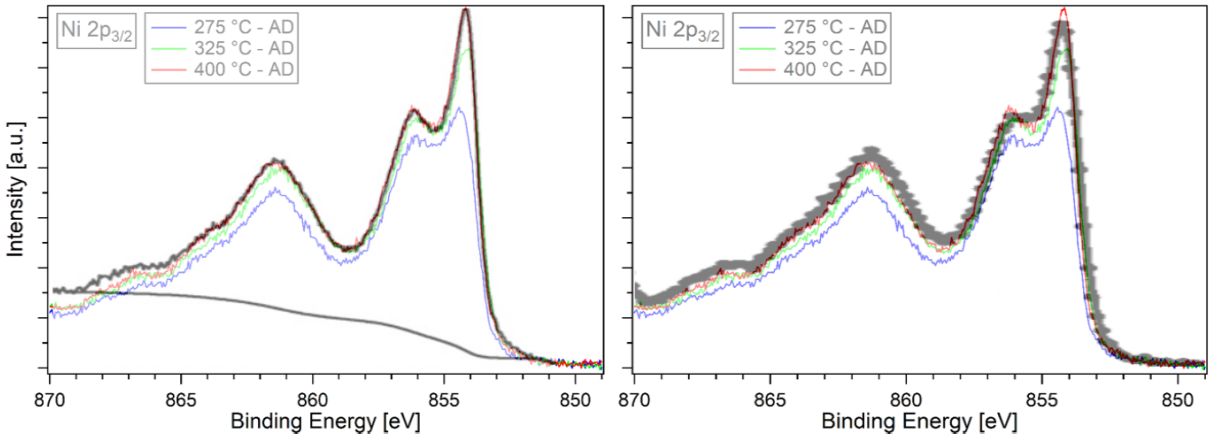

Figure A.2: Comparisons of the Ni 2p2/3 spectrum of an AD-sNiO-400°C sample with reference spectra taken on polycrystalline powder without air contact [154] (left) and on an epitaxially grown NiO(100) [49] (right). The side peak around 856.5 eV is part of the Ni $2p_{3/2}$ spectra of all NiO containing samples, regardless whether they are single- [49,63,317] or polycrystalline [152,153,180,317] or oxidized nickel metal [50,67,69]. Thus, it cannot simply be fitted as Ni^{3+}, even though this is very common in recent literature.

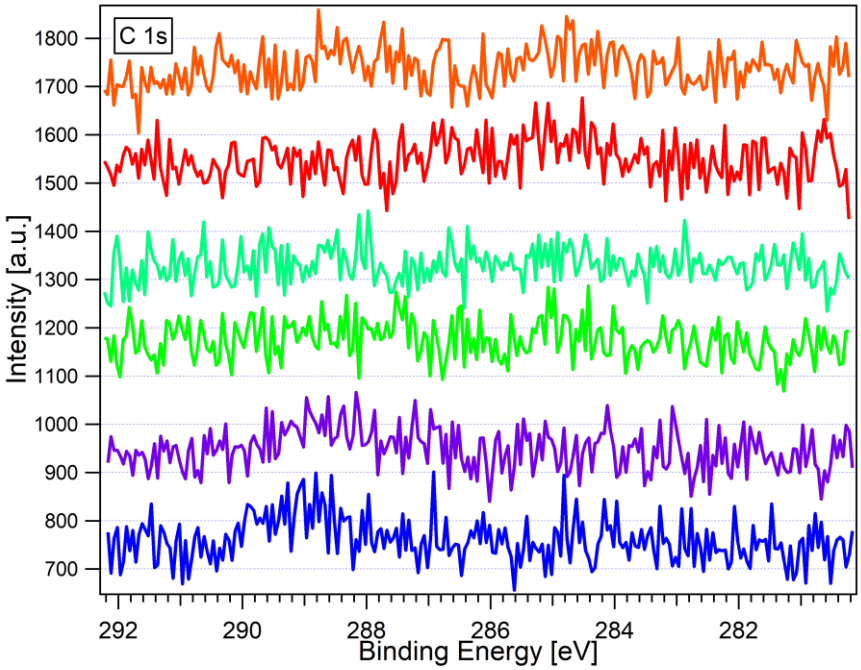

Figure A.3: C 1s spectra of sNiO samples. From bottom to top: AD&OP-sNiO-275, AD&OP-sNiO-325, AD&OP-sNiO-400.

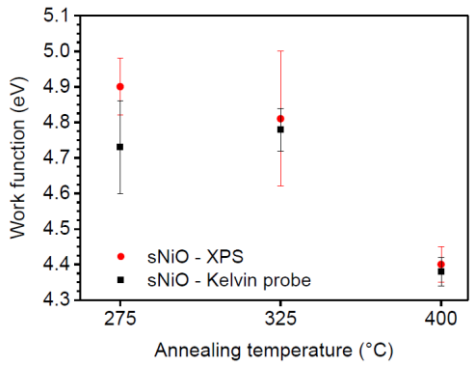

Figure A.4: Work function measurements of XPS compared to those measured with ambient KP.

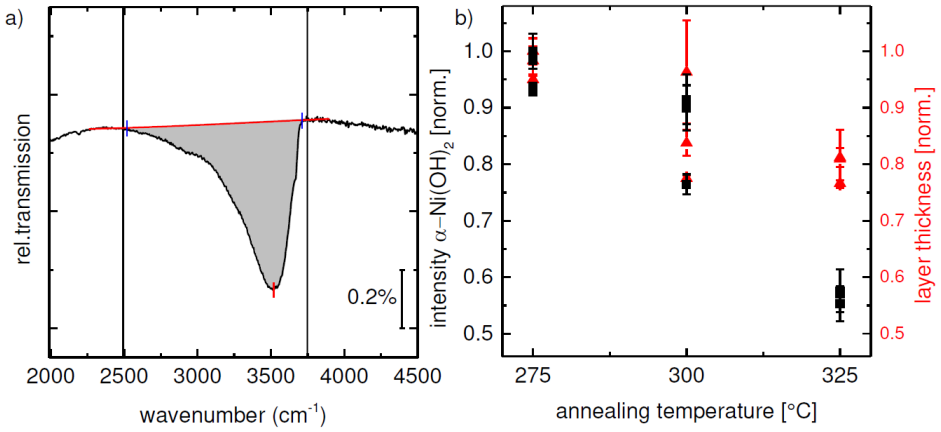

Figure A.5: (a) Gives an example for the determination of the intensity of the $Ni(OH)_2$ mode. (b) Correlation between NiO layer thicknesses and the intensities of the $Ni(OH)_2$ modes. Reprinted from [149].

Table A.3: Reaction enthalpies at 298.15 K (Δ_rH^0) of possible reactions of NiO with oxygen species present in oxygen plasma [137]. The standard enthalpies of formation (Δ_fH^0) of the negative ionic oxygen species were calculated by adding the respective electron affinity [300,301] to Δ_fH^0 of atomic and molecular oxygen, respectively. Δ_fH^0 of the positive ionic oxygen species were calculated by adding the respective ionization energies [302,303]. As a result, all reactions are exothermic, however with significantly differing values. While Δ_rH^0 for the reaction with molecular O is only slightly negative, it is more than an order of magnitude larger for atomic oxygen. The highest values are obtained for the reactions with the anionic oxygen species (O^+ and O_2^+). Thus, these reactions are the energetically most favorable ones.

Oxygen species	Δ_fH^0 [kJ/mol]	$2*\Delta_fH^0$(NiO) [kJ/mol] [304]	$\Delta_fH^0(H_2O)$ [kJ/mol] [305]	$2*\Delta_fH^0$(NiOOH) [kJ/mol] [305]	Δ_rH^0 [kJ/mol]
O	249 [306]	-482	-286	-782	-263
O^-	388	-482	-286	-782	-402
O^+	1559	-482	-286	-782	-1573
½ O_2	0	-482	-286	-782	-14
½ O_2^-	206	-482	-286	-782	-220
½ O_2^+	1419	-482	-286	-782	-1433
O_3	143 [307]	-482	-286	-782	-157

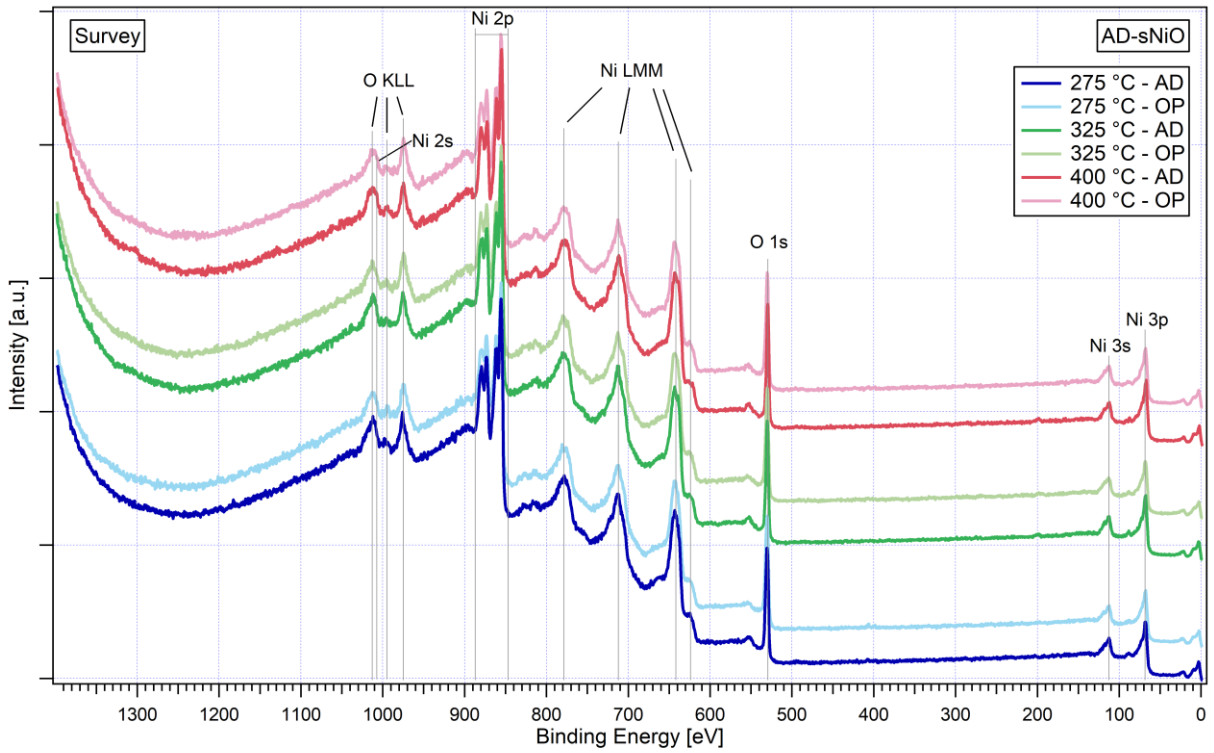

Figure A.6: XP survey spectra of AD- and OP-sNiO sampels, respectively.

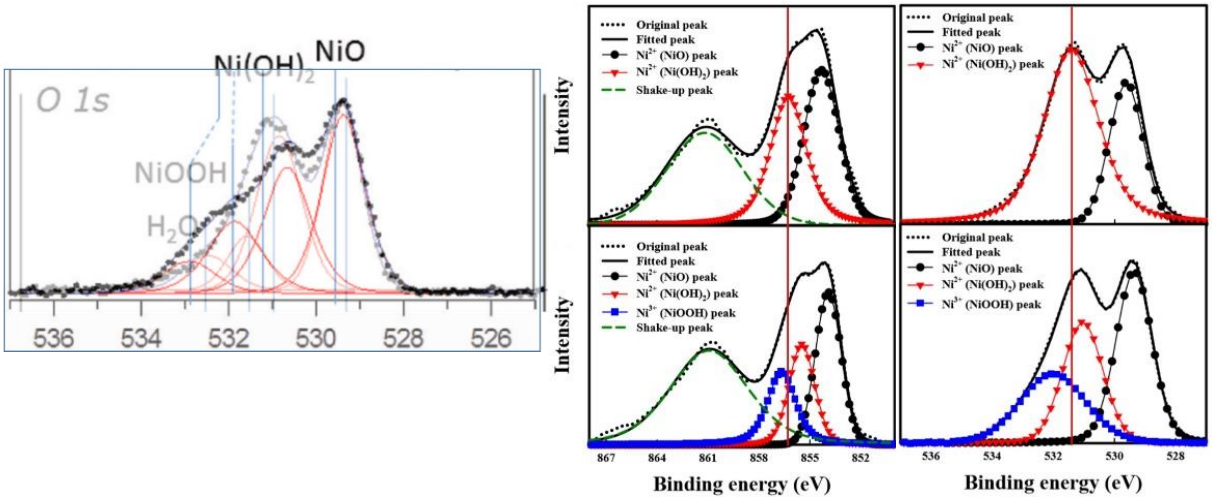

Figure A.7: Literature examples for inconsistencies due to the four-component fit. (Left) O 1s spectra before and after OP treatment, reprinted from [13]. (Right) Example for inconsistencies arising from the three-component fitting, reprinted from [18].

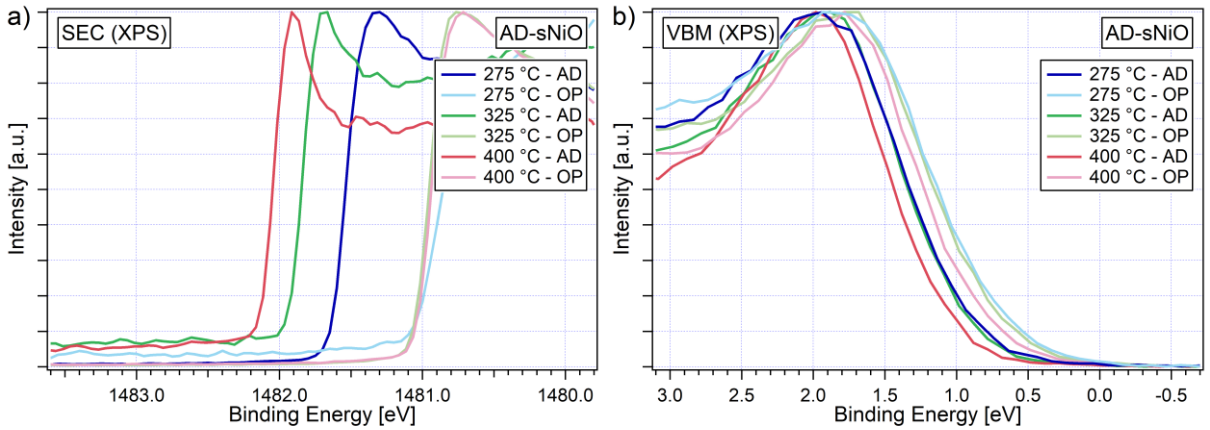

Figure A.8: Representative SEC and VBM spectra of differently prepared sNiO samples. OP treated films are marked with lighter colors.

Table A.4: Values of the data presented in Figure 5.21. The errors indicate the standard deviation.

		WF [eV]	VBM [eV]
275 °C	AD	4.90±0.08	0.89±0.08
	OP	5.53±0.03	0.76±0.09
325 °C	AD	4.81±0.19	0.87±0.06
	OP	5.55±0.08	0.73±0.06
400 °C	AD	4.40±0.05	0.98±0.04
	OP	5.63±0.13	0.71±0.08

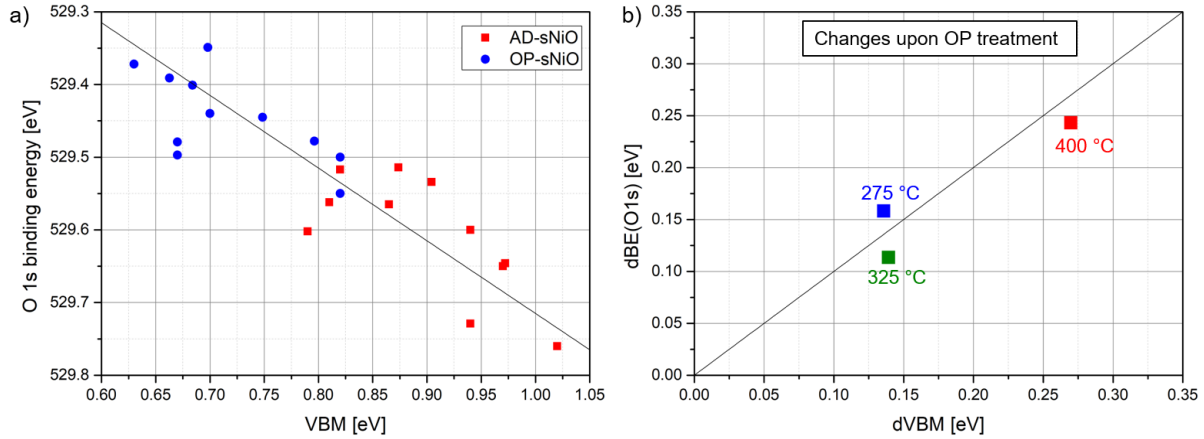

Figure A.9: (a) Binding energy of the O 1s main feature of sNiO samples annealed at 275, 325 and 400 °C with and without OP treatment versus the respective VBM position. The dependence can be described quite well by a linear function with a slope of one, which indicates that the VBM position roughly follows the Fermi level despite the different compositions of the samples at the very surface. (b) Shows that the same holds for the shift induced by the OP treatment, whereas the O 1s binding energies and VBM values of each annealing temperature were averaged before and after OP treatment. For each temperature the Fermi level shift measured via the binding energy position of the O 1s main peak (dBE(O1s)) matches well to the shift of the respetive VBM (dVBM). Afterall, there is no doubt that large part of the observed work function increase upon OP treatment is due to an increased surface dipole $\Delta\delta$ for all three annealing temperatures and not due to a Fermi level shift. Furthermore, $\Delta\delta$ is definitively larger at 400 °C than for the other both annealing temperatures.

Table A.5: Resistances for all three annealing temperatures before and after OP treatment evaluated according to the description in Figure A.10Figure A.10: Exemplary J-V measurement for an AD-sNiO-275°C film (blue) and linear fit (black) are shown on the left side. The inverse slope is the resistance R. For comparison two J-V measurements of an AD-sNiO-325 (green) and 400 (red) are depicted on the right side with a differing scaling of the ordinate (by one order of magnitude).

		R [MΩ]
275 °C	AD	14±3
	OP	9±2
325 °C	AD	208±70
	OP	18±3
400 °C	AD	200±10
	OP	9±2

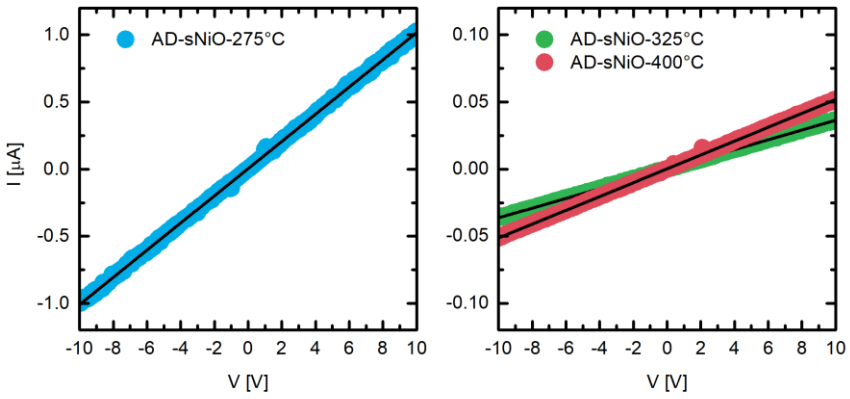

Figure A.10: Exemplary J-V measurement for an AD-sNiO-275°C film (blue) and linear fit (black) are shown on the left side. The inverse slope is the resistance R. For comparison two J-V measurements of an AD-sNiO-325 (green) and 400 (red) are depicted on the right side with a differing scaling of the ordinate (by one order of magnitude).

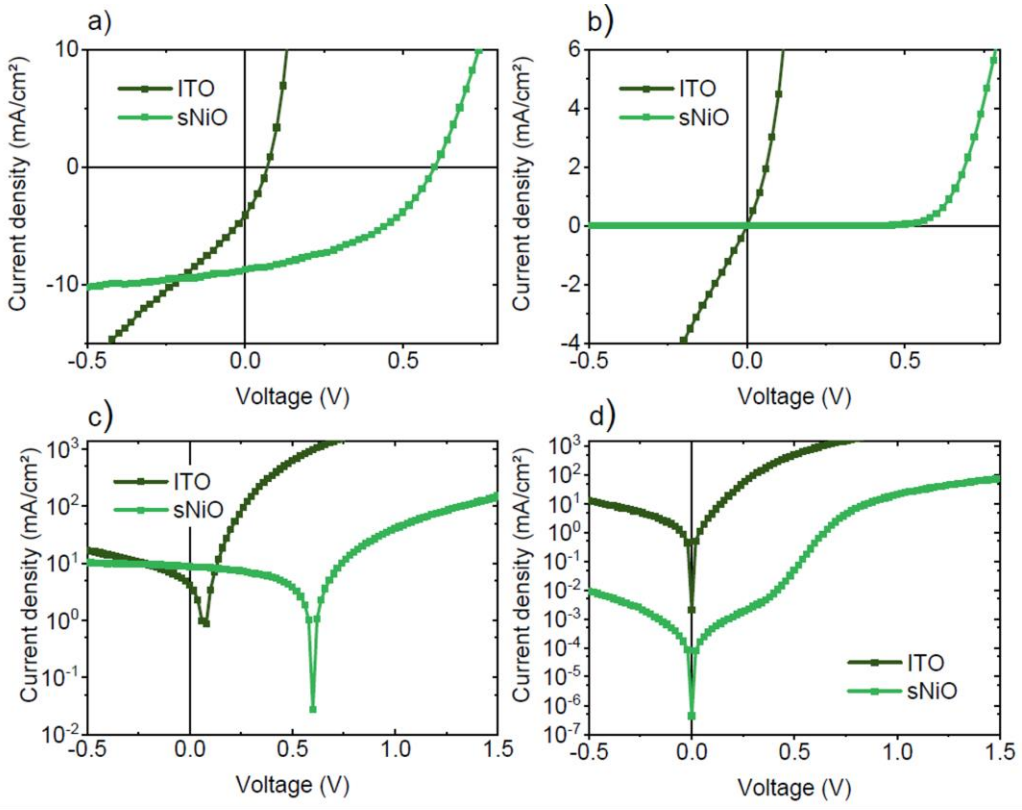

e)

BHJ	J_{SC} [mA cm^{-2}]	V_{OC} [eV]	R_S [Ω cm^{-2}]	R_{SH} [Ω cm^{-2}]	*FF* [%]	*PCE* [%]
ITO	4.0 ± 0.6	0.07 ± 0.03	10 ± 2	20 ± 13	31 ± 8	0.10 ± 0.07
ITO/AD-sNiO	8.5 ± 0.3	0.59 ± 0.01	16 ± 7	250 ± 40	45.8 ± 3.4	2.29 ± 0.19
ITO/OP-sNiO	8.8 ± 0.4	0.62 ± 0.01	12 ± 1	326 ± 47	49.1 ± 0.8	2.71 ± 0.12

Figure A.11: J-V curves of OPV devices in BHJ architecture both with and without sNiO as hole extraction layer. Reprinted from [19]. Data in (a) and (c) was taken under illumination, data in (b) and (d) was taken in the dark. The tabular in (e) provides averaged values from 12 to 14 cells each.

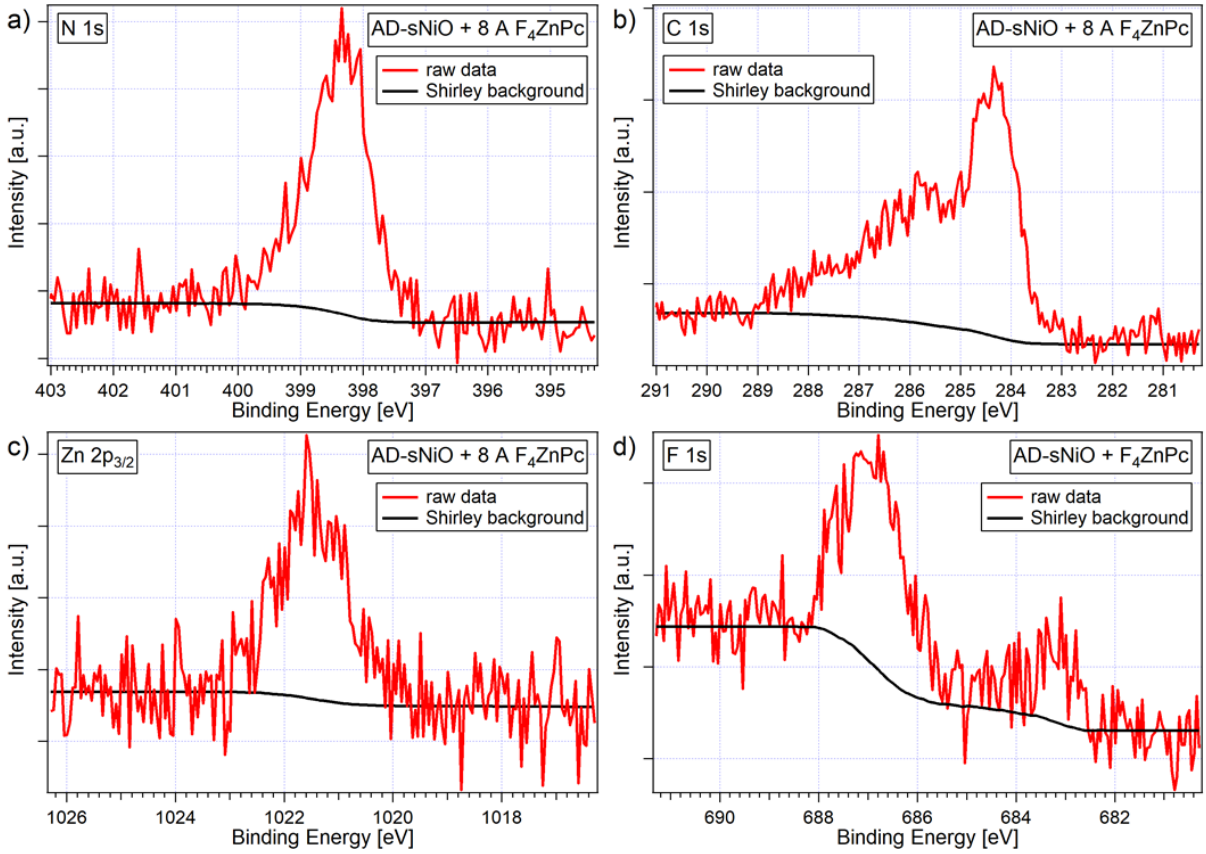

Figure A.12: XP spectra of 8 Å F_4ZnPc on AD-sNiO together with the Shirley background the spectra were corrected for. The background of the Zn 2p3/2 spectrum had to be corrected prior to correction for Shirley background, see Figure A.14.

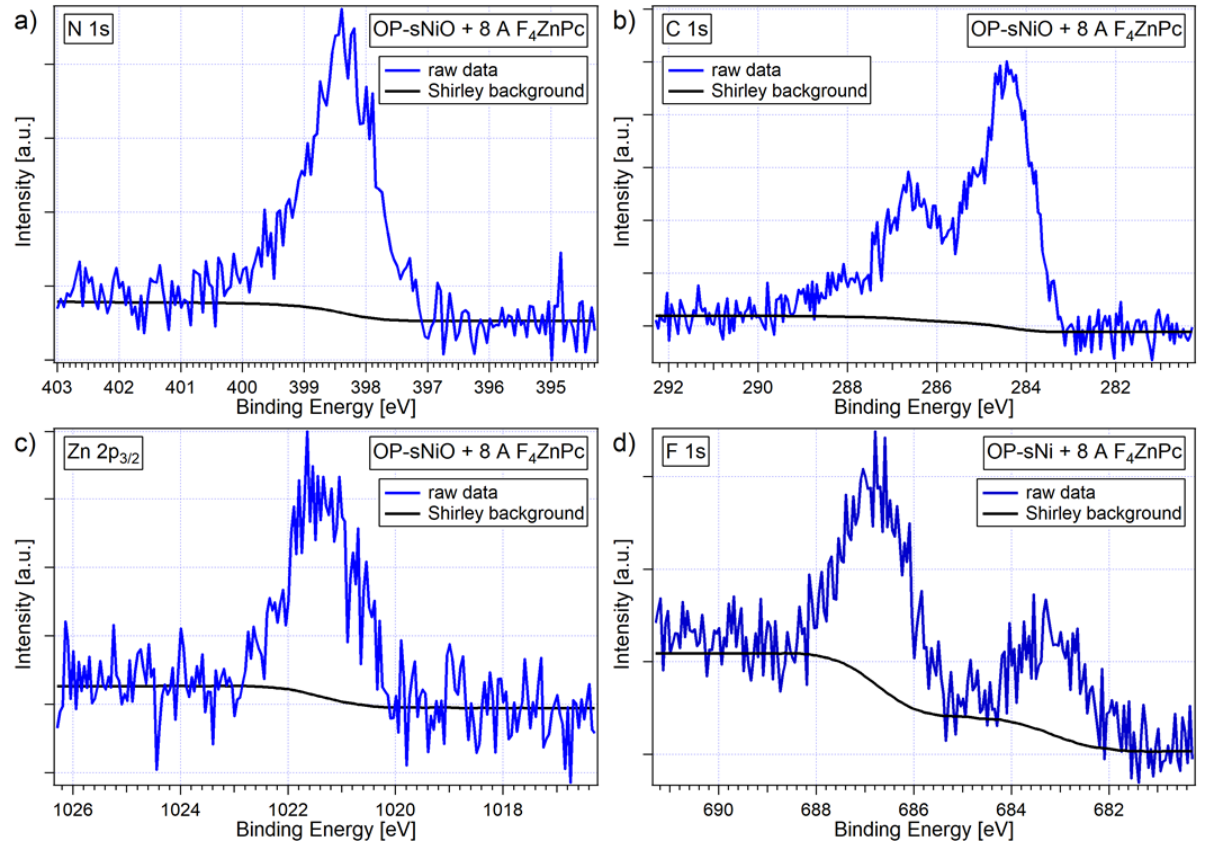

Figure A.13: XP spectra of 8 Å F_4ZnPc on AD-sNiO together with the Shirley background the spectra were corrected for. The background of the Zn $2p_{3/2}$ spectrum had to be corrected prior to correction for Shirley background, see Figure A.14.

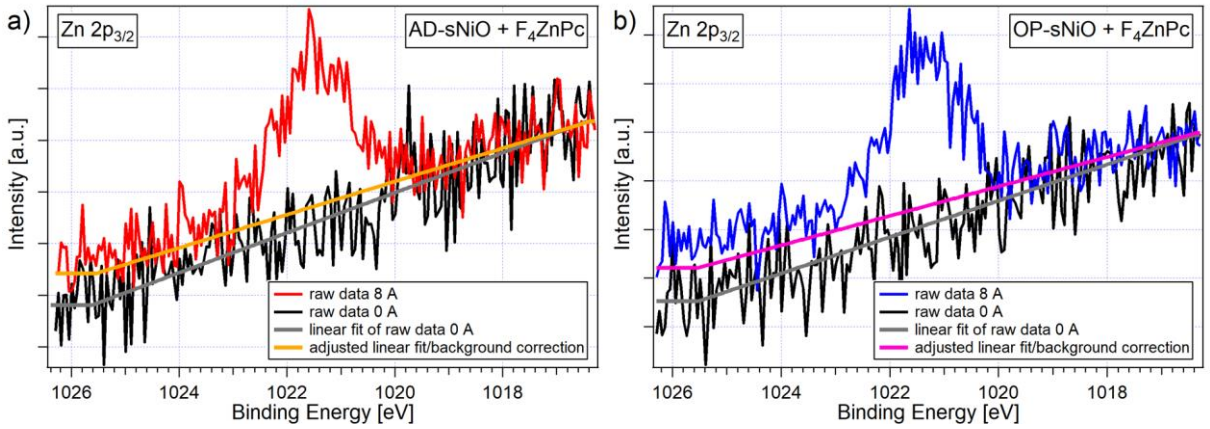

Figure A.14: XP spectra of the Zn $2p_{3/2}$ region of 8 A F_4ZnPc on AD- (a) an OP- (b) sNiO. The diagrams illustrate the background correction prior to the Shirley correction, which is necessary in this particular case, since the Zn $2p_{3/2}$ emission is superposed with a broad feature from the sNiO substrate. The produre to account for the atypical background was the following: first, the background of the clean sNiO substrates (black lines) was linearly fitted (grey lines). Each linear fit was then multiplied with a factor given by the damping of substrate lines due to the first layer of F_4ZnPc (yellow and pink lines). The factors were determined by the reduction of the Ni $2p_{3/2}$ spectra and were 0.83 (AD) and 0.81 (OP), respectively. Finally, these adjusted linear functions were corrected for offset and subtracted from the raw data (red and blue lines).

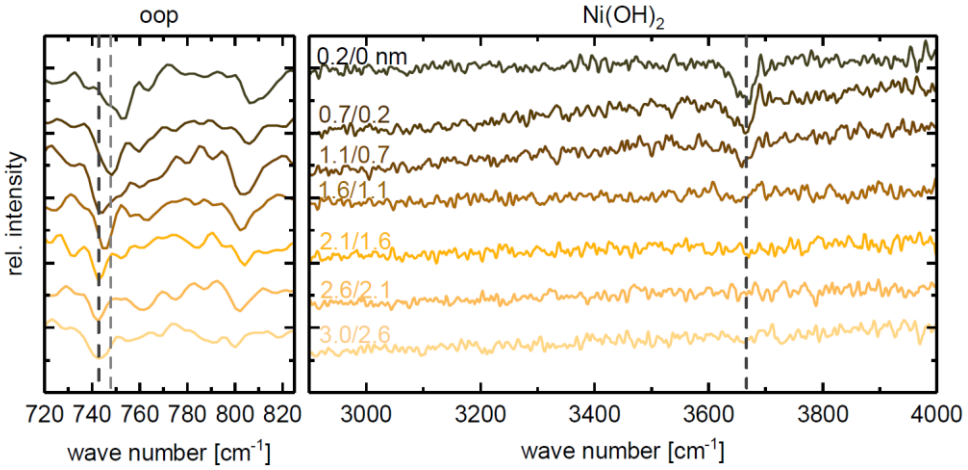

Figure A.15: Relative changes of IR spectra during adsorption of F_4ZnPc on sNiO/Au. Until a thickness of about 1 nm the mode at ~3685 cm^{-1}, attributed to surface OH, changes. Reprinted from [143].

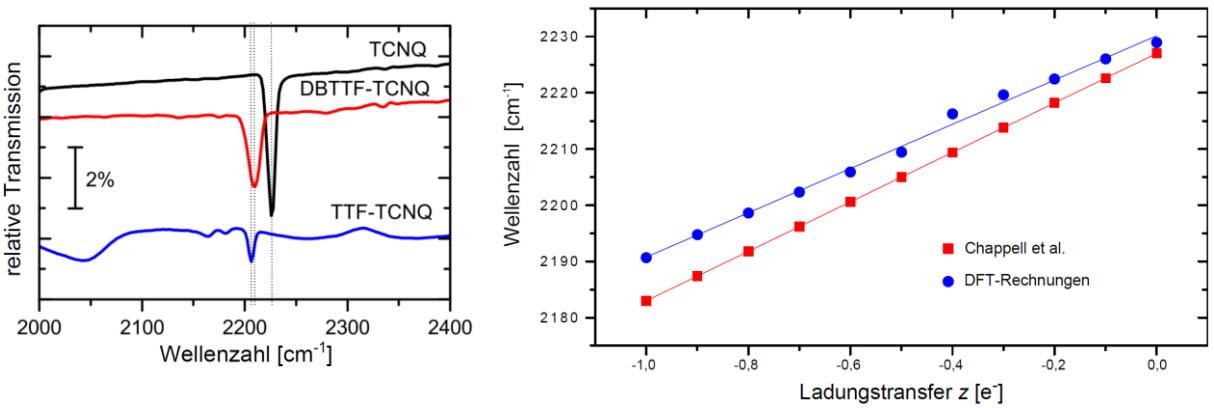

Figure A.16: (a) Example of IR spectra for the shift in wavenumber of absorption modes of charged molecules compared to neutral molecules, here for the CN vibration of TCNQ (black: neutral; red and blue: charged). Reprinted from [318]. (b) Dependency of the wavenumber of the CN absorption mode of TCNQ on the fraction of transferred charge. Data form [246], diagram reprinted from [319].

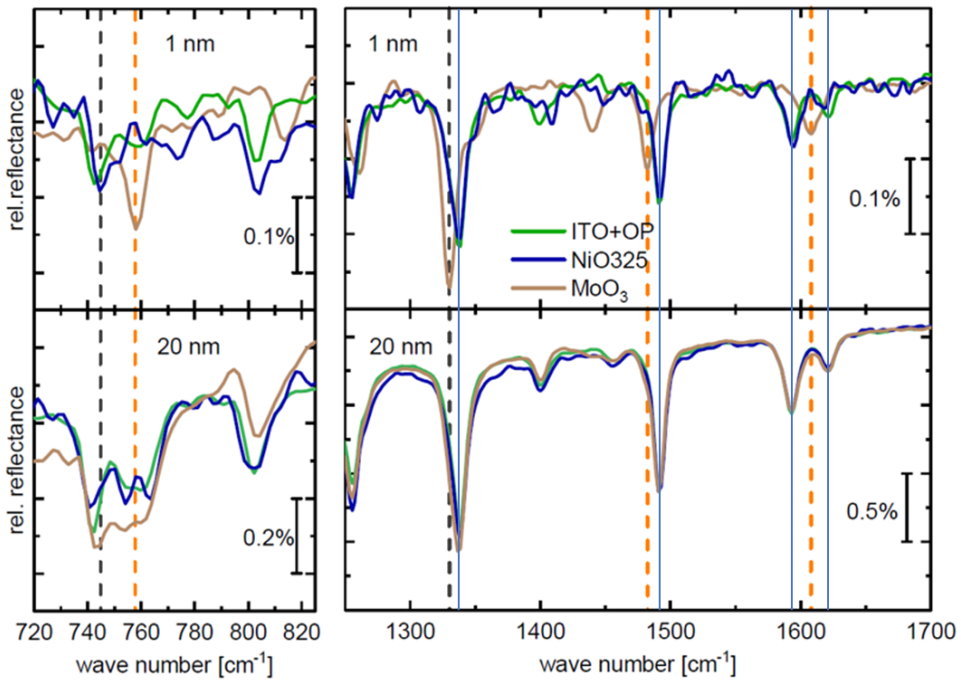

Figure A.17: Comparison of IR spectra of thin (1 nm) and thick (20 nm) F_4ZnPc layers on sNiO and MoO_3.Reprinted from [143]. Almost no deviations exist for the thick layer, while clear shifts are visible for the thin layers of F_4ZnPc on MoO_3.

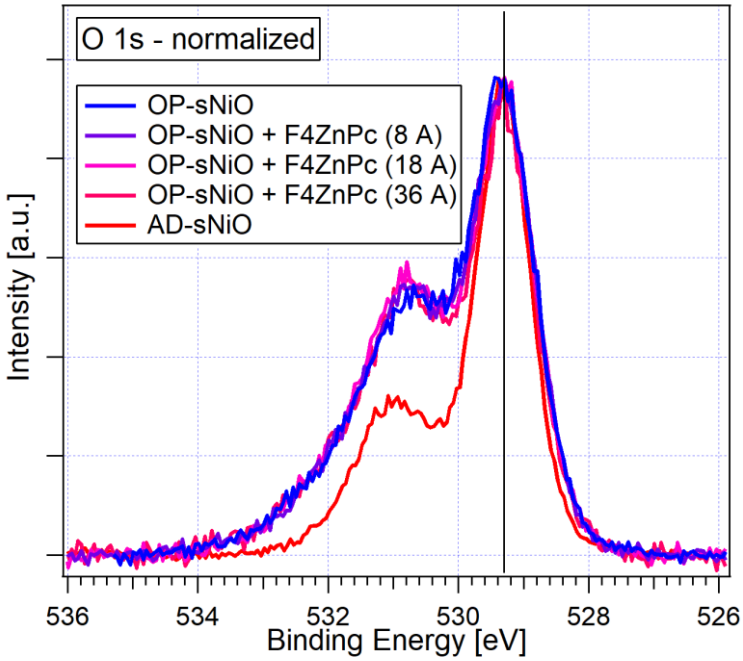

Figure A.18: O 1s detail spectra of an OP-sNiO evaporated with F_4ZnPc in comparison with a spectrum of an untreated AD-sNiO film (normalized). Evidently, the "OP-effect" is not reversed by the evaporation, which speaks against the existence of volatile and reactive oxygen species.

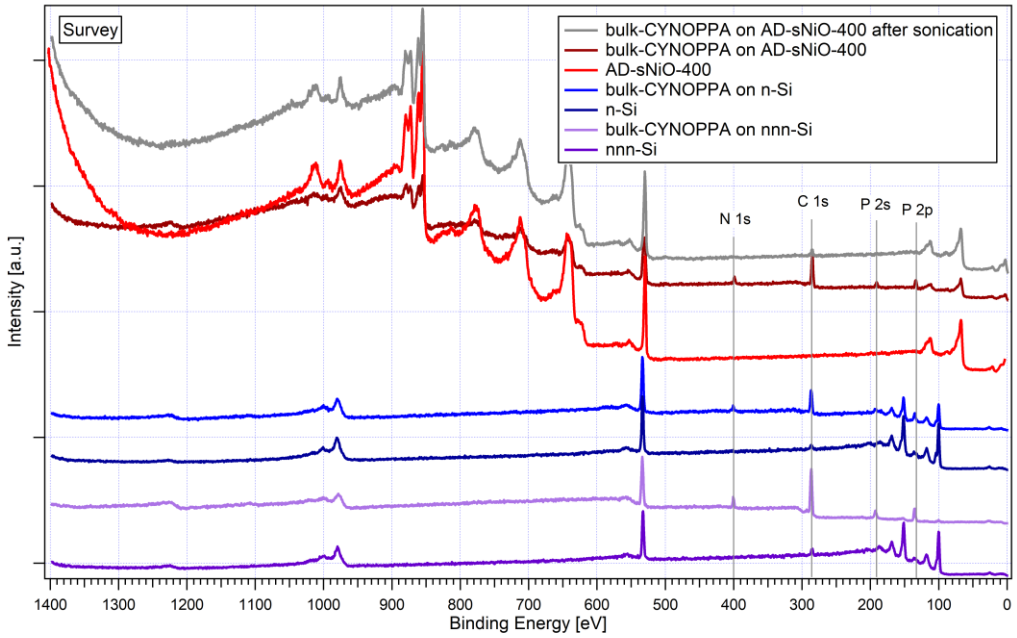

Figure A.19: SP survey spectra of bulk-CYNOPPA on different substrates.

Table A.6: Nominal layer thicknesses of bulk-CYNOPPA on different substrates. Calculated based on the damping of the Si 2s and the Ni $2p_{3/2}$ peaks, respectively. IMFP was estimated based on TPP-2M formula.

Substrate	Peak	IMFP	Nominal layer thickness
n-Si	Si 2s	3.38	2.1
n^{++}-Si	Si 2s	3.38	10.2
AD-sNiO-400	Ni $2p_{3/2}$	1.86	2.45

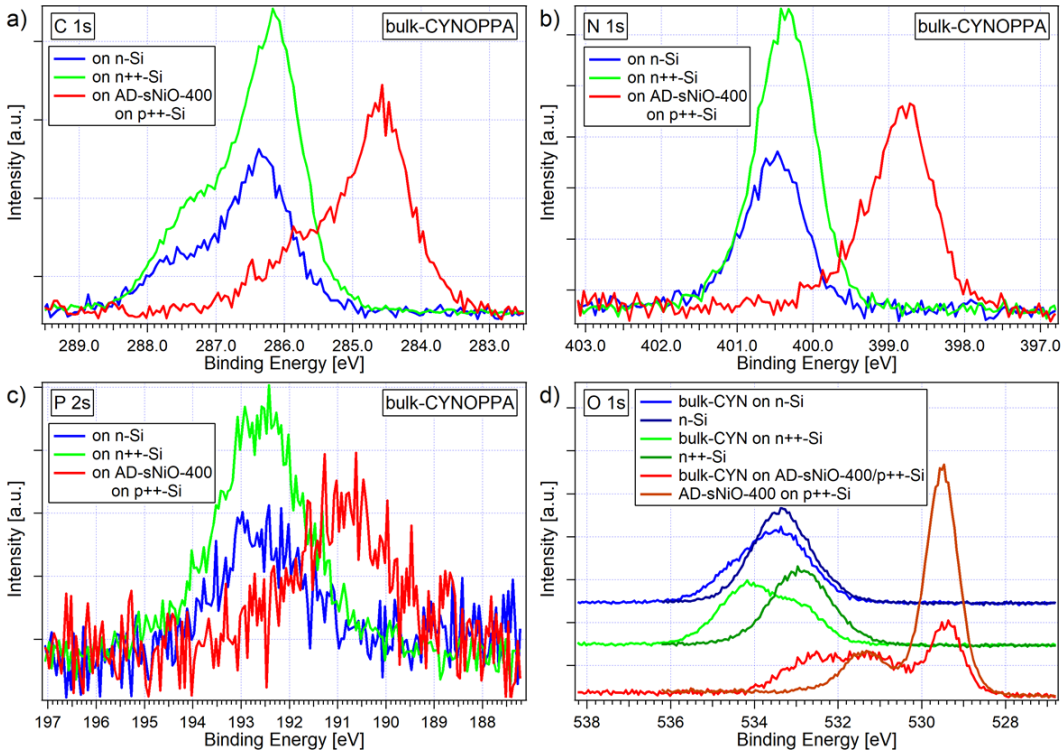

Figure A.20: XP as-measured detail spectra of bulk-CYNOPPA on different substrates. The huge difference in binding energy positions between the core levels of bulk-CYNOPPA on the two Si substrates compared to those on AD-sNiO-400 of almost 2 eV is striking. Charging can be excluded as reason, since all spectra were measured under illumination with a 365 nm LED to enhance photoconductivity. The phenomenon was not further investigated. Therefore, in this work, spectra of bulk-CYNOPPA were only used as reference for spectral shapes.

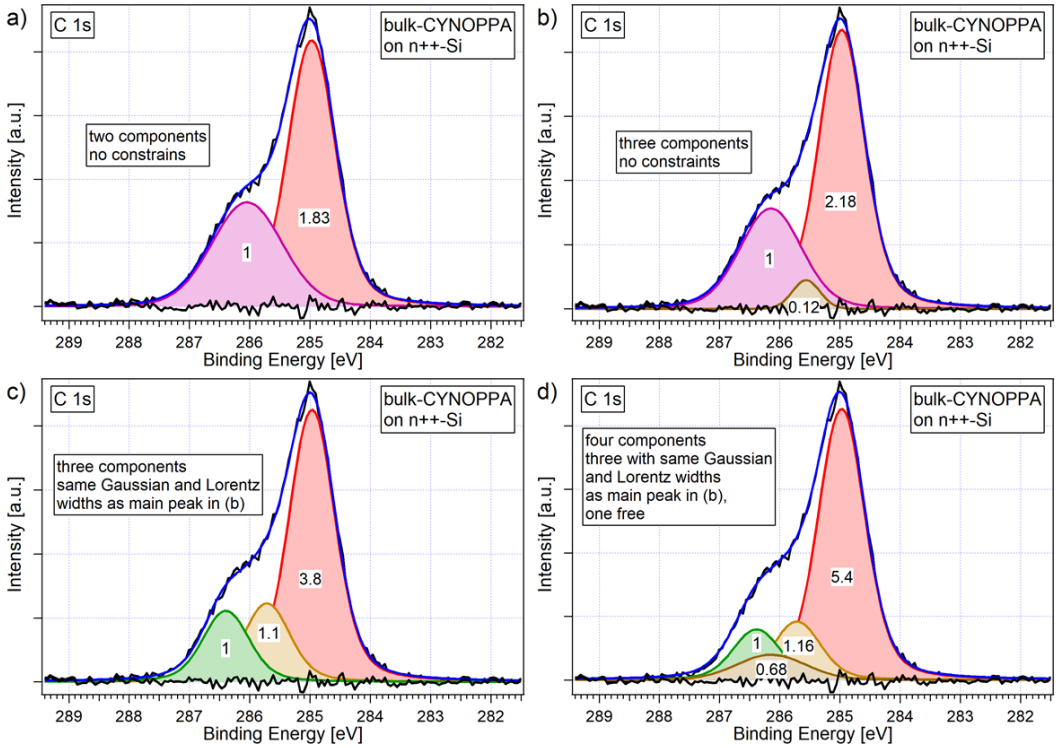

Figure A.21: Additional information on the fitting of the C 1s spectrum of bulk-CYNOPPA. Difficulties to fit the C 1s spectrum appropriately arise from the fact that already two Voigt components are enough to fit the spectrum very well (a). However, the side peak is much broader than expected for a component stemming from a single type of carbon atoms (0.55 eV Gaussian width instead of 0.32 eV for the main component). This is a hint for the existence of an additional contribution. Therefore, the spectrum was fitted with three components (b). Still, the widths vary strongly for the different peaks (0.22 - 0.46 eV). Consequently, another fit was performed (c), in which both the Gaussian and the Lorentz widths of all peaks were held constant at 0.32 eV and 0.14 eV, respectively, which are the values of the main component in the fit in (b). Now, two equally large side peaks appear, which can be attributed to CN (green) and CP (yellow). However, the main peak is smaller than expected (3.8 instead of 5). This feeds the suspicion that the spectrum contains a further component not stemming from CYNOPPA. A four-component fit, for which three components were constrained in width similar to the fit in (c) and one component was left without constraints, is shown in (d). The ratio of the integrated peak areas between the three peaks with constraints is close to expectations for CYNOPPA (1:1.2:5.4 instead of 1:1:5). The additional feature in brown can be ascribed to contamination. It makes 8 % of the total intensity of the C 1s feature. Unfortunately, the resulting height parameter have uncertainties of 100 % and more, which limits the validity of the fit result. Therefore, to test whether the recorded spectra are compatible with the molecular structure of CYNOPPA, a further fit was performed for which the ratio of the heights of the two side peaks was fixed to 1:1 and the height of the main peak was kept above a certain value. The result is the fit in Figure 7.2a with a ratio of 1.1:1:5.2 and a decent residuum. This demonstrates that the spectra are compatible with the molecular structure, although the correct ratio cannot be extracted from the spectra simply by fitting without constraints to the heights.

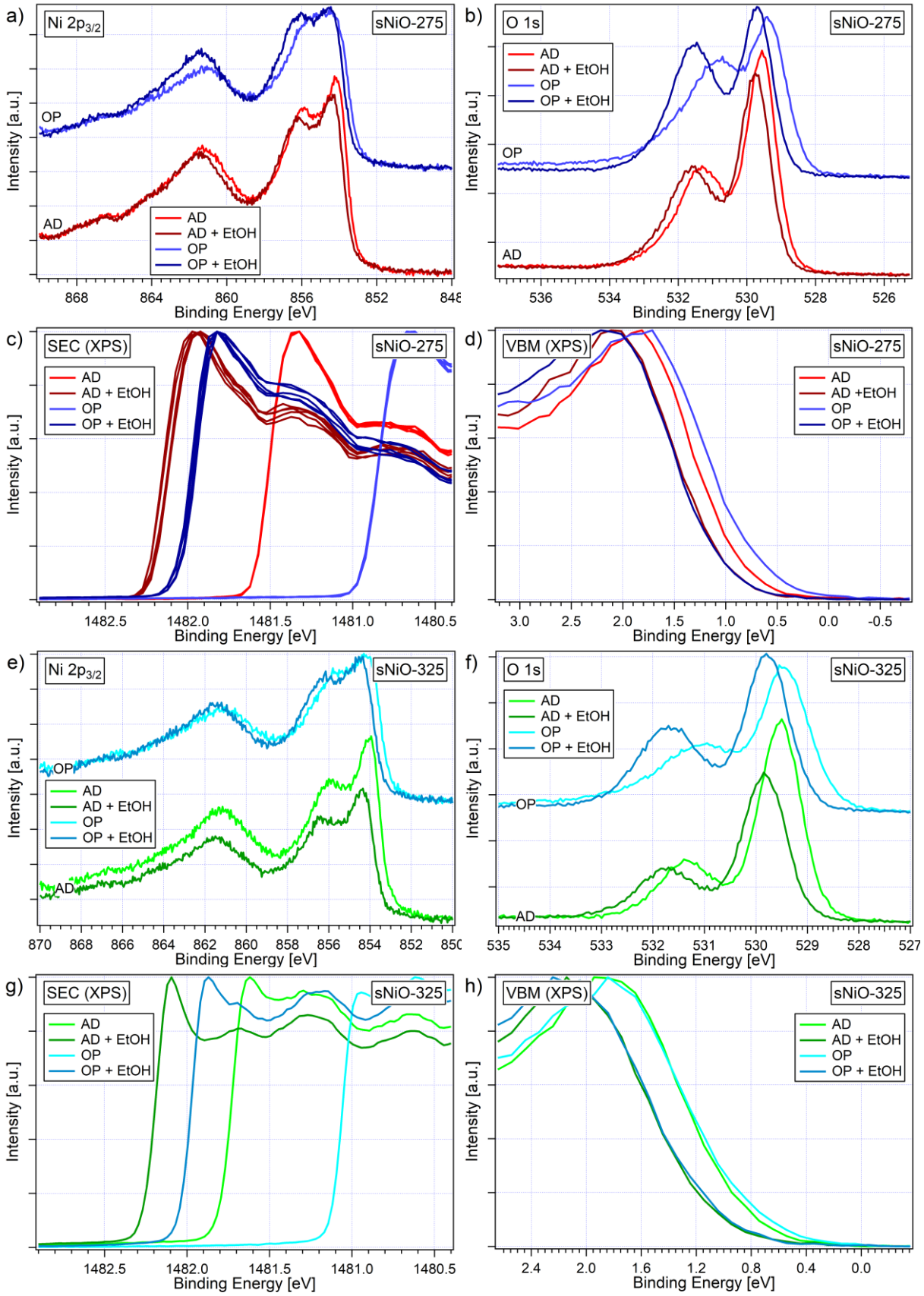

Figure A.22: XP spectra of sNiO samples annealed at 275 °C (a-d) and at 325 °C (e-h) before and after immersion in ethanol.

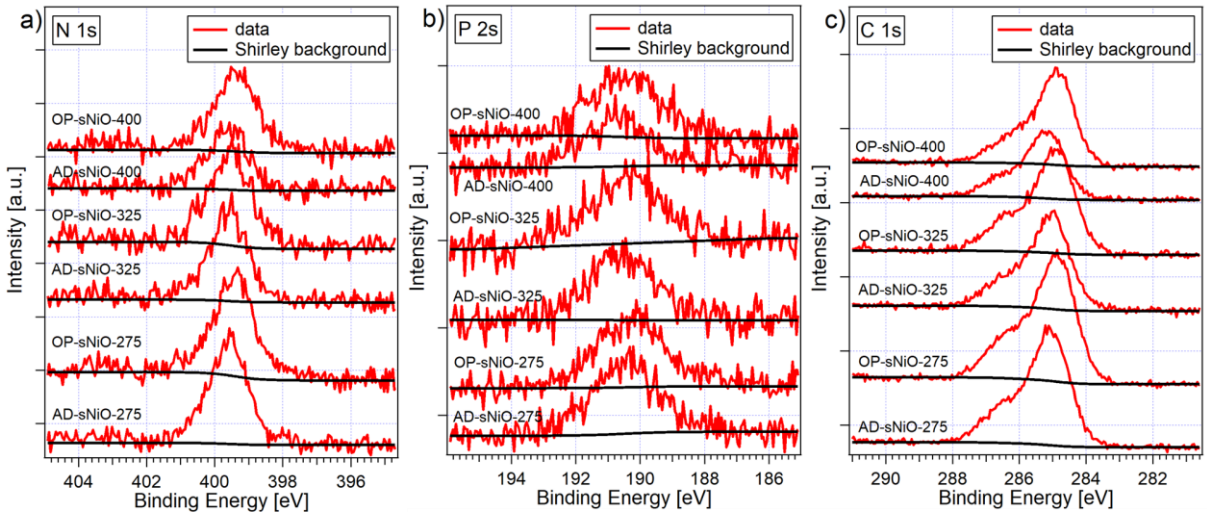

Figure A.23: XP spectra of CYNOPPA functionalized sNiO films and the respective Shirley backgrounds.

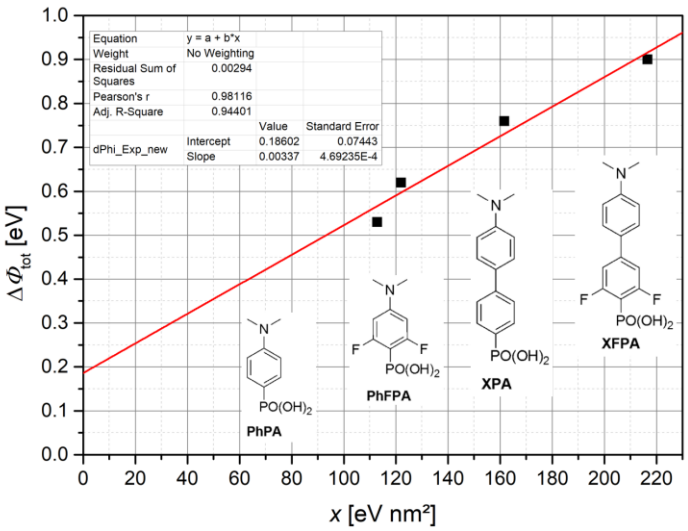

Figure A.24: Linear regression based on four PA molecules to extract a relation between the integrated N 1s XPS signal and the molecular surface density, see text for details. Details on the synthesis and analysis can be found in [186].

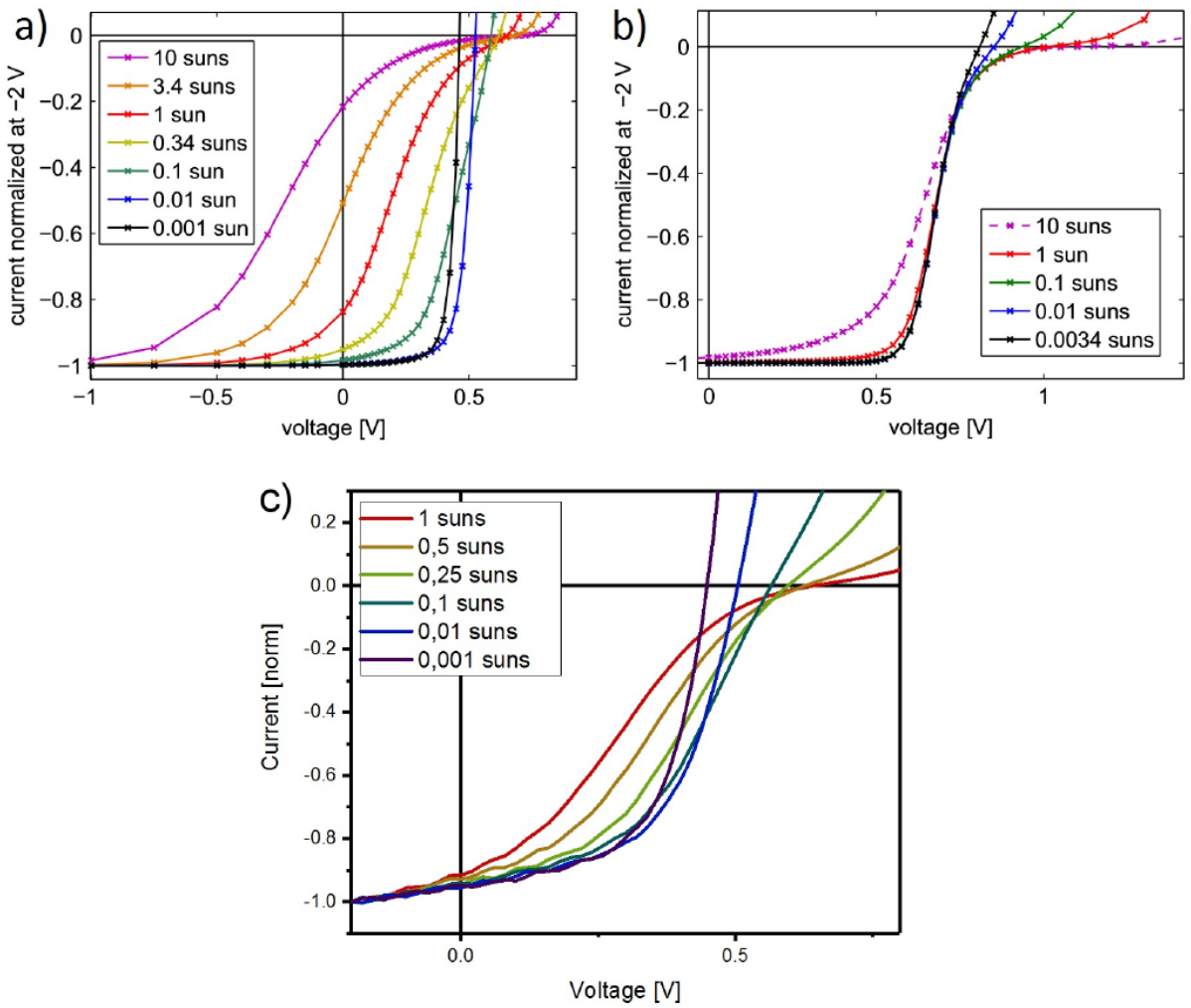

Figure A.25: (a,b) Simulated J-V curves to demonstrate the dependency of the s-kink on the illumination intensity, reprinted from [291]. (a) Simulation of an extraction barrier and (b) simulation of an injection barrier. (c) Experimental data of an FHJ F_4ZnPc/C_{60} OPV based on CYNOPPA-functionalized sNiO HTL. The intensity dependence evidences the presence of an extraction barrier. This conclusion has further been supported by variation of the sNiO HTL thickness, see [25] and [185].

Bibliography

[1] *The Nobel Prize in Chemistry*, (2000). https://www.nobelprize.org/prizes/chemistry/2000/summary/ (accessed May 1, 2019).

[2] A. Jeffries, J. Beach, *Invisible Solar Cells That Could Power Skyscrapers*, Bloomberg. (2015). https://www.youtube.com/watch?v=IZ__PjmC6Fg (accessed May 1, 2019).

[3] R.F. Service, *Skyscrapers could soon generate their own power, thanks to see-through solar cells*, Sci. Mag. (2018). https://www.sciencemag.org/news/2018/06/skyscrapers-could-soon-generate-their-own-power-thanks-see-through-solar-cells (accessed May 1, 2019).

[4] H. Bässler, *Charge Transport in Disordered Organic Photoconductors a Monte Carlo Simulation Study*, Phys. Status Solidi. 175 (1993) 15.

[5] H. Ishii, K. Sugiyama, E. Ito, K. Seki, *Energy level alignment and interfacial electronic structures at organic metal and organic organic interfaces*, Adv. Mater. 11 (1999) 605.

[6] S. Braun, W.R. Salaneck, M. Fahlman, *Energy-level alignment at organic/metal and organic/organic interfaces*, Adv. Mater. 21 (2009) 1450.

[7] NREL, *Best Research-Cell Efficiency Chart*, (n.d.). https://www.nrel.gov/pv/cell-efficiency.html (accessed May 1, 2019).

[8] G.A. Chamberlain, *Organic solar cells: A review*, Sol. Cells. 8 (1983) 47.

[9] C.W. Tang, *Two-layer organic photovoltaic cell*, Appl. Phys. Lett. 48 (1986) 183.

[10] M.T. Greiner, Z.-H. Lu, *Thin-film metal oxides in organic semiconductor devices: their electronic structures, work functions and interfaces*, NPG Asia Mater. 5 (2013) e55.

[11] P. Schulz, S.R. Cowan, Z.L. Guan, A. Garcia, D.C. Olson, A. Kahn, *NiOX/MoO3 Bi-layers as efficient hole extraction contacts in organic solar cells*, Adv. Funct. Mater. 24 (2014) 701.

[12] J.J. Berry, N.E. Widjonarko, B.A. Bailey, A.K. Sigdel, D.S. Ginley, D.C. Olson, *Surface treatment of NiO hole transport layers for organic solar cells*, IEEE J. Sel. Top. Quantum Electron. 16 (2010) 1649.

[13] E.L. Ratcliff, J. Meyer, K.X. Steirer, A. Garcia, J.J. Berry, D.S. Ginley, D.C. Olson, A. Kahn, N.R. Armstrong, *Evidence for near-Surface NiOOH Species in Solution-Processed NiO*, Chem. Mater. 23 (2011) 4988.

[14] M.P. de Jong, L.J. van IJzendoorn, M.J.A. de Voigt, *Stability of the interface between indium-tin-oxide and poly(3,4-ethylenedioxythiophene)/poly(styrenesulfonate) in polymer light-emitting diodes*, Appl. Phys. Lett. 77 (2000) 2255.

[15] M.T. Lloyd, C.H. Peters, A. Garcia, I. V. Kauvar, J.J. Berry, M.O. Reese, M.D. McGehee, D.S. Ginley, D.C. Olson, *Influence of the hole-transport layer on the initial behavior and lifetime of inverted organic photovoltaics*, Sol. Energy Mater. Sol. Cells. 95 (2011) 1382.

[16] A. Garcia, G.C. Welch, E.L. Ratcliff, D.S. Ginley, G.C. Bazan, D.C. Olson, *Improvement of Interfacial Contacts for New Small- Molecule Bulk-Heterojunction Organic Photovoltaics*, Adv. Mater. 24 (2012) 5368–5373.

[17] S. Liu, R. Liu, Y. Chen, S. Ho, J.H. Kim, F. So, *Nickel oxide hole injection/transport layers for efficient solution-processed organic light-emitting diodes*, Chem. Mater. 26 (2014) 4528.

[18] J. Kim, H.J. Park, C.P. Grigoropoulos, D. Lee, J. Jang, *Solution-processed nickel oxide nanoparticles with NiOOH for hole injection layers of high-efficiency organic light-emitting diodes*, Nanoscale. 8 (2016) 17608.

[19] M.D. Irwin, D.B. Buchholz, A.W. Hains, R.P.H. Chang, T.J. Marks, *p-Type semiconducting nickel oxide as an efficiency-enhancing anode interfacial layer in polymer bulk-heterojunction solar cells*, Proc. Natl. Acad. Sci. 105 (2008) 2783.

[20] A. Nattestad, A.J. Mozer, M.K.R. Fischer, Y.B. Cheng, A. Mishra, P. Bäuerle, U. Bach, *Highly efficient photocathodes for dye-sensitized tandem solar cells*, Nat. Mater. 9 (2010) 31.

[21] K.X. Steirer, J.P. Chesin, N.E. Widjonarko, J.J. Berry, A. Miedaner, D.S. Ginley, D.C. Olson, *Solution deposited NiO thin-films as hole transport layers in organic photovoltaics*, Org. Electron. 11 (2010) 1414.

[22] K.X. Steirer, P.F. Ndione, N.E. Widjonarko, M.T. Lloyd, J. Meyer, E.L. Ratcliff, A. Kahn, N.R. Armstrong, C.J. Curtis, D.S. Ginley, J.J. Berry, D.C. Olson, *Enhanced Efficiency in Plastic Solar Cells via Energy Matched Solution Processed NiOx Interlayers*, Adv. Energy Mater. 1 (2011) 813.

[23] J.R. Manders, S.-W. Tsang, M.J. Hartel, T.-H. Lai, S. Chen, C.M. Amb, J.R. Reynolds, F. So, *Solution-Processed Nickel Oxide Hole Transport Layers in High Efficiency Polymer Photovoltaic Cells*,

Adv. Funct. Mater. 23 (2013) 2993.
[24] B. Mustafa, J. Griffin, A.S. Alsulami, D.G. Lidzey, A.R. Buckley, *Solution processed nickel oxide anodes for organic photovoltaic devices*, Appl. Phys. Lett. 104 (2014) 063302.
[25] S. Hietzschold, S. Hillebrandt, F. Ullrich, J. Bombsch, V. Rohnacher, S. Ma, W. Liu, A. Köhn, W. Jaegermann, A. Pucci, W. Kowalsky, E. Mankel, S. Beck, R. Lovrincic, *Functionalized Nickel Oxide Hole Contact Layers: Work Function versus Conductivity*, ACS Appl. Mater. Interfaces. 9 (2017) 39821.
[26] M.B. Islam, M. Yanagida, Y. Shirai, Y. Nabetani, K. Miyano, *NiO_x Hole Transport Layer for Perovskite Solar Cells with Improved Stability and Reproducibility*, ACS Omega. 2 (2017) 2291.
[27] J. Ciro, D. Ramírez, M.A. Mejía Escobar, J.F. Montoya, S. Mesa, R. Betancur, F. Jaramillo, *Self-Functionalization Behind a Solution-Processed NiO_x Film Used As Hole Transporting Layer for Efficient Perovskite Solar Cells*, ACS Appl. Mater. Interfaces. 9 (2017) 12348.
[28] J. You, L. Meng, T.-B. Song, T.-F. Guo, Y.M. Yang, W.-H. Chang, Z. Hong, H. Chen, H. Zhou, Q. Chen, Y. Liu, N. De Marco, Y. Yang, *Improved air stability of perovskite solar cells via solution-processed metal oxide transport layers*, Nat. Nanotechnol. 11 (2016) 75.
[29] J.Y. Jeng, K.C. Chen, T.Y. Chiang, P.Y. Lin, T. Da Tsai, Y.C. Chang, T.F. Guo, P. Chen, T.C. Wen, Y.J. Hsu, *Nickel oxide electrode interlayer in CH3NH3PbI 3 perovskite/PCBM planar-heterojunction hybrid solar cells*, Adv. Mater. 26 (2014) 4107.
[30] U. Kwon, B.-G. Kim, D.C. Nguyen, J.-H. Park, N.Y. Ha, S.-J. Kim, S.H. Ko, S. Lee, D. Lee, H.J. Park, *Solution-Processible Crystalline NiO Nanoparticles for High-Performance Planar Perovskite Photovoltaic Cells*, Sci. Rep. 6 (2016) 30759.
[31] X. Yin, P. Chen, M. Que, Y. Xing, W. Que, C. Niu, J. Shao, *Highly Efficient Flexible Perovskite Solar Cells Using Solution-Derived NiO x Hole Contacts*, ACS Nano. 10 (2016) 3630.
[32] C. Chueh, C. Li, A.K. Jen, *Recent progress and perspective in solution-processed Interfacial materials for efficient and stable polymer and organometal perovskite solar cells*, Energy Environ. Sci. 8 (2015) 1160.
[33] W. Chen, Y. Wu, Y. Yue, J. Liu, W. Zhang, X. Yang, H. Chen, E. Bi, I. Ashraful, M. Grätzel, L. Han, *Efficient and stable large-area perovskite solar cells with inorganic charge extraction layers*, Science (80-.). 350 (2015) 944.
[34] K.C. Wang, P.S. Shen, M.H. Li, S. Chen, M.W. Lin, P. Chen, T.F. Guo, *Low-temperature sputtered nickel oxide compact thin film as effective electron blocking layer for mesoscopic NiO/CH3NH3PbI 3 perovskite heterojunction solar cells*, ACS Appl. Mater. Interfaces. 6 (2014) 11851.
[35] K.X. Steirer, R.E. Richards, A.K. Sigdel, A. Garcia, P.F. Ndione, S. Hammond, D. Baker, E.L. Ratcliff, C. Curtis, T. Furtak, D.S. Ginley, D.C. Olson, N.R. Armstrong, J.J. Berry, *Nickel oxide interlayer films from nickel formate–ethylenediamine precursor: influence of annealing on thin film properties and photovoltaic device performance*, J. Mater. Chem. A. 3 (2015) 10949.
[36] Z. Zhai, X. Huang, M. Xu, J. Yuan, J. Peng, W. Ma, *Greatly Reduced Processing Temperature for a Solution-Processed NiOx Buffer Layer in Polymer Solar Cells*, Adv. Energy Mater. 3 (2013) 1614.
[37] A. Sharma, P.J. Hotchkiss, S.R. Marder, B. Kippelen, *Tailoring the work function of indium tin oxide electrodes in electrophosphorescent organic light-emitting diodes*, J. Appl. Phys. 105 (2009) 084507.
[38] B.P.J. Hotchkiss, H. Li, P.B. Paramonov, S.A. Paniagua, S.R. Marder, S.C. Jones, N.R. Armstrong, J. Bre, *Modification of the Surface Properties of Indium Tin Oxide with Benzylphosphonic Acids : A Joint Experimental and Theoretical Study*, (2009) 4496.
[39] C. Vericat, M.E. Vela, G. Benitez, P. Carro, R.C. Salvarezza, *Self-assembled monolayers of thiols and dithiols on gold: new challenges for a well-known system*, Chem. Soc. Rev. 39 (2010) 1805.
[40] S.F.J. Appleyard, S.R. Day, R.D. Pickford, M.R. Willis, *Organic electroluminescent devices: enhanced carrier injection using SAM derivatized ITO electrodes*, J. Mater. Chem. 10 (2000) 169.
[41] J.D. Zimmerman, B. Song, O. Griffith, S.R. Forrest, *Exciton-blocking phosphonic acid-treated anode buffer layers for organic photovoltaics*, Appl. Phys. Lett. 103 (2013) 243905.
[42] K.M. Knesting, H. Ju, C.W. Schlenker, A.J. Giordano, A. Garcia, O.L. Smith, D.C. Olson, S.R. Marder, D.S. Ginger, *ITO Interface Modifiers Can Improve V_{oc} in Polymer Solar Cells and Suppress Surface Recombination*, J. Phys. Chem. Lett. 4 (2013) 4038.
[43] R. Quinones, A. Raman, E.S. Gawalt, *Functionalization of nickel oxide using alkylphosphonic acid self-assembled monolayers*, Thin Solid Films. 516 (2008) 8774.
[44] A. Raman, R. Quiñones, L. Barriger, R. Eastman, A. Parsi, E.S. Gawalt, *Understanding organic*

film behavior on alloy and metal oxides, Langmuir. 26 (2010) 1747.
[45] A. Bulusu, S.A. Paniagua, B.A. Macleod, A.K. Sigdel, J.J. Berry, D.C. Olson, S.R. Marder, S. Graham, *Efficient modification of metal oxide surfaces with phosphonic acids by spray coating*, Langmuir. 29 (2013) 3935.
[46] S.M. Sze, K.K. Ng, Physics of Semiconductor Devices: Third Edition, John Wiley & Sons, Inc., Hoboken, New Jersey, 2007.
[47] S. Hunklinger, Festkörperphysik, in: Festkörperphysik, Oldenburg Wissenschaftsverlag GmbH, München, 2009.
[48] L. Kronik, Y. Shapira, *Surface photovoltage phenomena: Theory, experiment, and applications*, Surf. Sci. Rep. 37 (1999) 1.
[49] D. Alders, F. Voogt, T. Hibma, G.A. Sawatzky, *Nonlocal screening effects in 2p x-ray photoemission spectroscopy of NiO (100)*, Phys. Rev. B. 54 (1996) 7716.
[50] H.-W. Hoppe, H.-H. Strehblow, *XPS and UPS examinations of the formation of passive layers on Ni in 1M sodium hydroxide and 0.5M sulphuric acid*, Surf. Interface Anal. 14 (1989) 121.
[51] N.N. Greenwood, A. Earnshaw, Chemistry of the elements, Pergamon Press, 1984.
[52] R. Newman, R.M. Chrenko, *Optical Properties of Nickel Oxide*, Phys. Rev. 114 (1959) 1507.
[53] R.J. Powell, W.E. Spicer, *Optical Properties of Nio and CoO&*, Phys. Rev. B. 2 (1970) 2182.
[54] G.A. Sawatzky, J.W. Allen, *Magnitude and Origin of the Band-Gap in Nio*, Phys. Rev. Lett. 53 (1984) 2339.
[55] A. Fujimori, F. Minami, *Valence-band photoemission and optical absorption in nickel compounds*, Phys. Rev. B. 30 (1984) 957.
[56] J. Zaanen, G.A. Sawatzky, J.W. Allen, *Band gaps and electronic structure of transition- metal compounds*, Phys. Rev. Lett. 55 (1985) 419.
[57] S. Hüfner, J. Osterwalder, T. Riesterer, F. Hulliger, *Photoemission and inverse Photoemission spectroscopy of NiO*, Solid State Commun. 52 (1984) 793.
[58] S. Hüfner, P. Steiner, I. Sander, F. Reinert, H. Schmitt, *The optical gap of NiO*, Zeitschrift Für Phys. B Condens. Matter. 86 (1992) 207.
[59] S. Hüfner, *Electronic structure of NiO and related 3d-transition-metal compounds*, Adv. Phys. 43 (1994) 183.
[60] J. Zhang, J. Wang, Y. Fu, B. Zhang, Z. Xie, *Efficient and stable polymer solar cells with annealing-free solution-processible NiO nanoparticles as anode buffer layers*, J. Mater. Chem. C. 2 (2014) 8295.
[61] D. Cappus, C. Xu, D. Ehrlich, B. Dillmann, C.A. Ventrice, K. Al Shamery, H. Kuhlenbeck, H.-J. Freund, *Hydroxyl groups on oxide surfaces: NiO(100), NiO(111) and Cr2O3(111)*, Chem. Phys. 177 (1993) 533.
[62] D. Wolf, *Reconstruction of NaCl surfaces from a dipolar solution to the Madelung problem*, Phys. Rev. Lett. 68 (1992) 3315.
[63] S. Uhlenbrock, C. Scharfschwerdt, M. Neumann, G. Illing, H.-J. Freund, *The influence of defects on the Ni 2p and O 1s XPS of NiO*, J. Phys. Condens. Matter. 4 (1992) 7973.
[64] N.N. Greenwood, A. Earnshaw, Chemistry of the elements, Butterworth-Heinemann, 1997.
[65] A.F. Holleman, E. Wiberg, N. Wiberg, Lehrbuch der anorganischen Chemie, De Gruyter, 2007.
[66] M.T. Greiner, M.G. Helander, Z.-B. Wang, W.-M. Tang, Z.-H. Lu, *Effects of Processing Conditions on the Work Function and Energy-Level Alignment of NiO Thin Films*, J. Phys. Chem. C. 114 (2010) 19777.
[67] K.S. Kim, N. Winograd, *X-ray photoelectron spectroscopic studies of nickel-oxygen surfaces using oxygen and argon ion-bombardment*, Surf. Sci. 43 (1974) 625.
[68] K.S. Kim, R.E. Davis, *Electron spectroscopy of the nickel-oxygen system*, J. Electron Spectros. Relat. Phenomena. 1 (1972) 251.
[69] P.R. Norton, R.L. Tapping, J.W. Goodale, *A photoemission study of the interaction of Ni(100), (110) and (111) surfaces with oxygen*, Surf. Sci. 65 (1977) 13.
[70] N. Wagner, O. Brümmer, V. V. Khodasevich, *XPS investigations of the interaction of oxygen with damaged (100) nickel surfaces*, Phys. Status Solidi. 62 (1980) 275.
[71] A.J. Tkalych, K. Yu, E.A. Carter, *Structural and Electronic Features of β-Ni(OH)₂ and β-NiOOH from First Principles*, J. Phys. Chem. C. 119 (2015) 24315.
[72] H. Bode, K. Dehmelt, K.D.J. Witte, *Zur Kenntnis der Nickelhydroxidelektrode - I. Über das Nickel (II)-Hydroxidhydrat*, 11 (1966) 1079.
[73] A. Szytula, A. Murasik, M. Balanda, *Neutron Diffraction Study of Ni(OH)2*, Phys. Status Solidi.

43 (1971) 125.
[74] C. Greaves, M.A. Thomas, *Refinement of the structure of deuterated nickel hydroxide, Ni(OD)2, by powder neutron diffraction and evidence for structural disorder in samples with high surface area*, Acta Crystallogr. Sect. B Struct. Sci. 42 (1986) 51.
[75] D.S. Hall, D.J. Lockwood, C. Bock, B.R. MacDougall, *Nickel hydroxides and related materials: a review of their structures, synthesis and properties.*, Proc. R. Soc. London, Ser. A. 471 (2015) 20140792.
[76] M. Wehrens-Dijksma, P.H.L. Notten, *Electrochemical Quartz Microbalance characterization of Ni(OH)2-based thin film electrodes*, Electrochim. Acta. 51 (2006) 3609.
[77] R.S. McEwen, *Crystallographic studies on nickel hydroxide and the higher nickel oxides*, J. Phys. Chem. 75 (1971) 1782.
[78] H. Yang, G. Gao, F. Teng, W. Liu, S. Chen, Z. Ge, *Nickel Hydroxide Nanoflowers for a Nonenzymatic Electrochemical Glucose Sensor*, J. Electrochem. Soc. 161 (2014) B216.
[79] R. Barnard, C. Randell, F. Tye, Studies concerning the ageing of α and β-Ni(OH)2 in relation to nickel–cadmium cells, in: Proc. 12th Int. Power Sources Symp. Bright. Sept. 1980, London, UK, 1981: pp. 401–425.
[80] W. Dennstedt, W. Löser, *Zur kenntnis der nickelhydroxid-elektrode—III. Thermogravimetrische untersuchungen an Nickel(II)-hydroxiden*, Electrochim. Acta. 16 (1971) 429.
[81] A. Audemer, A. Delahaye, R. Farhi, N. Sac-Epée, J. -M. Tarascon, *Electrochemical and Raman Studies of Beta-Type Nickel Hydroxides Ni(1−x)Co(x)(OH) Electrode Materials*, J. Electrochem. Soc. 144 (1997) 2614.
[82] M.B.J.G. Freitas, *Nickel hydroxide powder for NiO·OH/Ni(OH)2 electrodes of the alkaline batteries*, J. Power Sources. 93 (2001) 163.
[83] P. Jeevanandam, Y. Koltypin, A. Gedanken, *Synthesis of Nanosized α-Nickel Hydroxide by a Sonochemical Method*, Nano Lett. 1 (2001) 263.
[84] F.P. Kober, On the structure of electrochemically active hydrated nickel-oxide electrodes, in: Power Sources, Elsevier, 1967: pp. 257–268.
[85] M.C. Bernard, P. Bernard, M. Keddam, S. Senyarich, H. Takenouti, *Characterisation of new nickel hydroxides during the transformation of α Ni(OH)2 to β Ni(OH)2 by ageing*, Electrochim. Acta. 41 (1996) 91.
[86] D.S. Hall, D.J. Lockwood, S. Poirier, C. Bock, B.R. MacDougall, *Raman and infrared spectroscopy of α and β phases of thin nickel hydroxide films electrochemically formed on nickel*, J. Phys. Chem. A. 116 (2012) 6771.
[87] S.L. Medway, C.A. Lucas, A. Kowal, R.J. Nichols, D. Johnson, *In situ studies of the oxidation of nickel electrodes in alkaline solution*, J. Electroanal. Chem. 587 (2006) 172.
[88] W. Visscher, E. Barendrecht, *Anodic oxide films of nickel in alkaline electrolyte*, Surf. Sci. 135 (1983) 436.
[89] N. Kitakatsu, V. Maurice, C. Hinnen, P. Marcus, *Surface hydroxylation and local structure of NiO thin films formed on Ni(111)*, Surf. Sci. 407 (1998) 36.
[90] P. Oliva, J. Leonardi, J.F. Laurent, C. Delmas, J.J. Braconnier, M. Figlarz, F. Fievet, A. de Guibert, R. De Nosay, *Review of the structure and the electrochemistry of nickel hydroxides and oxy-hydroxides*, J. Power Sources. 8 (1982) 229.
[91] R.A. Huggins, H. Prinz, M. Wohlfahrt-Mehrens, L. Jörissen, W. Witschel, *Proton insertion reactions in layered transition metal oxides*, Solid State Ionics. 70–71 (1994) 417.
[92] A. Delahaye-Vidal, B. Beaudoin, N. Sac-Epée, K. Tekaia-Elhsissen, A. Audemer, M. Figlarz, *Structural and textural investigations of the nickel hydroxide electrode*, Solid State Ionics. 84 (1996) 239.
[93] Q. Song, Z. Tang, H. Guo, S.L.. Chan, *Structural characteristics of nickel hydroxide synthesized by a chemical precipitation route under different pH values*, J. Power Sources. 112 (2002) 428.
[94] M.C. Bernard, R. Cortes, M. Keddam, H. Takenouti, P. Bernard, S. Senyarich, *Structural defects and electrochemical reactivity of β-Ni(OH)2*, J. Power Sources. 63 (1996) 247.
[95] M.C. Biesinger, B.P. Payne, L.W.M. Lau, A. Gerson, R.S.C. Smart, *X-ray photoelectron spectroscopic chemical state Quantification of mixed nickel metal, oxide and hydroxide systems*, Surf. Interface Anal. 41 (2009) 324.
[96] Y.-F. Li, A. Selloni, *Mosaic Texture and Double* c *-Axis Periodicity of β-NiOOH: Insights from First-Principles and Genetic Algorithm Calculations*, J. Phys. Chem. Lett. 5 (2014) 3981.

[97] M. Gao, W. Sheng, Z. Zhuang, Q. Fang, S. Gu, J. Jiang, Y. Yan, *Efficient Water Oxidation Using Nanostructured α-Nickel-Hydroxide as an Electrocatalyst*, J. Am. Chem. Soc. 136 (2014) 7077.
[98] D.K. Bediako, B. Lassalle-Kaiser, Y. Surendranath, J. Yano, V.K. Yachandra, D.G. Nocera, *Structure–Activity Correlations in a Nickel–Borate Oxygen Evolution Catalyst*, J. Am. Chem. Soc. 134 (2012) 6801.
[99] B. Beverskog, *Revised Pourbaix Dialogs for Nickel at 25-300 °C*, Corros. Sci. 39 (1997) 969.
[100] H.M. Gu, W. Wang, Y.C. Zhai, *Study on Preparation and Properties of β-NiOOH*, Adv. Mater. Res. 239–242 (2011) 646.
[101] A.G. Marrani, V. Novelli, S. Sheehan, D.P. Dowling, D. Dini, *Probing the redox states at the surface of electroactive nanoporous nio thin films*, ACS Appl. Mater. Interfaces. 6 (2014) 143.
[102] L. Eriksson, U. Palmqvist, H. Rundlöf, U. Thuresson, R. Sjövall, *Structural aspects on the charged positive Ni electrode*, J. Power Sources. 107 (2002) 34.
[103] M.A. Langell, C.L. Berrie, M.H. Nassir, K.W. Wulser, *Adsorption of acetic acid on hydroxylated NiO(111) thin films*, Surf. Sci. 320 (1994) 25.
[104] M. Fingerle, S. Tengeler, W. Calvet, T. Mayer, W. Jaegermann, *Water Interaction with Sputter-Deposited Nickel Oxide on an n-Si Photoanode - Cryo Photoelectron Spectroscopy on Adsorbed Water in the Frozen Electrolyte Approach*, J. Electrochem. Soc. 165 (2018) 3148.
[105] S. Tengeler, M. Fingerle, W. Calvet, C. Steinert, B. Kaiser, T. Mayer, W. Jaegermann, *The Impact of Different Si Surface Terminations in the (001) n-Si/NiOx Heterojunction on the Oxygen Evolution Reaction (OER) by XPS and Electrochemical Methods*, J. Electrochem. Soc. 165 (2018) H3122.
[106] A.M. Reddy, A.S. Reddy, K.-S. Lee, P.S. Reddy, *Growth and characterization of NiO thin films prepared by dc reactive magnetron sputtering*, Solid State Sci. 13 (2011) 314.
[107] N.E. Widjonarko, P. Schulz, P.A. Parilla, C.L. Perkins, P.F. Ndione, A.K. Sigdel, D.C. Olson, D.S. Ginley, A. Kahn, M.F. Toney, J.J. Berry, *Impact of hole transport layer surface properties on the morphology of a polymer-fullerene bulk heterojunction*, Adv. Energy Mater. 4 (2014) 1301879.
[108] N.E. Widjonarko, E.L. Ratcliff, C.L. Perkins, A.K. Sigdel, A. Zakutayev, P.F. Ndione, D.T. Gillaspie, D.S. Ginley, D.C. Olson, J.J. Berry, *Sputtered nickel oxide thin fi lm for ef fi cient hole transport layer in polymer – fullerene bulk-heterojunction organic solar cell*, Thin Solid Films. 520 (2012) 3813.
[109] M.D. Irwin, J.D. Servaites, D.B. Buchholz, B.J. Leever, J. Liu, J.D. Emery, M. Zhang, J.H. Song, M.F. Durstock, A.J. Freeman, M.J. Bedzyk, M.C. Hersam, R.P.H. Chang, M.A. Ratner, T.J. Marks, *Structural and electrical functionality of NiO interfacial films in bulk heterojunction organic solar cells*, Chem. Mater. 23 (2011) 2218.
[110] T. Abzieher, S. Moghadamzadeh, F. Schackmar, H. Eggers, F. Sutterlüti, A. Farooq, D. Kojda, K. Habicht, R. Schmager, A. Mertens, R. Azmi, L. Klohr, J.A. Schwenzer, M. Hetterich, U. Lemmer, B.S. Richards, M. Powalla, U.W. Paetzold, *Electron-Beam-Evaporated Nickel Oxide Hole Transport Layers for Perovskite-Based Photovoltaics*, 1802995 (2019) 1.
[111] M. Budde, C. Tschammer, P. Franz, J. Feldl, M. Ramsteiner, R. Goldhahn, M. Feneberg, N. Barsan, A. Oprea, O. Bierwagen, *Structural, optical, and electrical properties of unintentionally doped NiO layers grown on MgO by plasma-assisted molecular beam epitaxy*, J. Appl. Phys. 123 (2018) 195301.
[112] W. Chen, Y. Zhou, L. Wang, Y. Wu, B. Tu, B. Yu, F. Liu, H.-W. Tam, G. Wang, A.B. Djurišić, L. Huang, Z. He, *Molecule-Doped Nickel Oxide: Verified Charge Transfer and Planar Inverted Mixed Cation Perovskite Solar Cell*, Adv. Mater. 1800515 (2018) 1800515.
[113] E.A. Slinish, Organic Molecular Crystals - Their Electronic States, Springer, Heidelberg, 1980.
[114] I.G. Hill, A. Kahn, Z.G. Soos, R.A. Pascal, Jr, *Charge-separation energy in films of π-conjugated organic molecules*, Chem. Phys. Lett. 327 (2000) 181.
[115] T.U. Kampen, *Electronic structure of organic interfaces - A case study on perylene derivatives*, Appl. Phys. A Mater. Sci. Process. 82 (2006) 457.
[116] C.J. Brabec, N.S. Sariciftci, J.C. Hummelen, *Plastic Solar Cells*, Adv. Funct. Mater. 11 (2001) 15.
[117] Z.D. Popovic, A. Hor, R.O. Loutfy, *A study of carrier generation mechanism in benzimidazole perylene/tetraphenyldiamine thin film structures*, Chem. Phys. 127 (1988) 451.
[118] B.A. Gregg, M.C. Hanna, *Comparing organic to inorganic photovoltaic cells: Theory, experiment, and simulation*, J. Appl. Phys. 93 (2003) 3605.
[119] J. Meiss, A. Merten, M. Hein, C. Schuenemann, S. Schäfer, M. Tietze, C. Uhrich, M. Pfeiffer, K.

Leo, M. Riede, *Fluorinated Zinc Phthalocyanine as Donor for Efficient Vacuum-Deposited Organic Solar Cells*, Adv. Funct. Mater. 22 (2012) 405.
[120] E. Siebert-Henze, V.G. Lyssenko, J. Fischer, M. Tietze, R. Brueckner, T. Menke, K. Leo, M. Riede, *Electroabsorption studies of organic p-i-n solar cells: Increase of the built-in voltage by higher doping concentration in the hole transport layer*, Org. Electron. 15 (2014) 563.
[121] E.L. Ratcliff, A. Garcia, S.A. Paniagua, S.R. Cowan, A.J. Giordano, D.S. Ginley, S.R. Marder, J.J. Berry, D.C. Olson, *Investigating the influence of interfacial contact properties on open circuit voltages in organic photovoltaic performance: Work function versus selectivity*, Adv. Energy Mater. 3 (2013) 647.
[122] A. Einstein, *Über einen die Erzeugung und Verwandlung des Lichtes betreffenden heuristischen Gesichtspunkt*, Ann. Phys. 322 (1905) 132.
[123] *The Nobel Prize in Physics*, (1921). https://www.nobelprize.org/prizes/physics/1921/summary/ (accessed May 13, 2019).
[124] A. Klein, T. Mayer, A. Thissen, W. Jaegermann, *Photoelectron Spectroscopy in Materials Science and Physical Chemistry*, Bunsen- Mag. (2008) 124.
[125] J.F. Moulder, W.F. Stickle, P.E. Sobel, K.D. Bomben, Handbook of X-ray Photoelectron Spectroscopy, in: Handb. X-Ray Photoelectron Spectrosc., 1995: p. 26.
[126] M.P. Seah, W.A. Dench, *Quantitative electron spectroscopy of surfaces: A standard data base for electron inelastic mean free paths in solids*, Surf. Interface Anal. 1 (1979) 2.
[127] W.H. Gries, *A Universal Predictive Equation for the Inelastic Mean Free Pathlengths of X-ray Photoelectrons and Auger Electrons*, Surf. Interface Anal. 24 (1996) 38.
[128] S. Tanuma, C.J. Powell, D.R. Penn, *Calculations of electron inelastic mean free paths*, Surf. Interface Anal. 20 (1993) 77.
[129] S. Tanuma, C.J. Powell, D.R. Penn, *Calculations of electron inelastic mean free paths. V. Data for 14 organic compounds over the 50-2000 eV range*, Surf. Interface Anal. 21 (1994) 165.
[130] D.A. Shirley, *High-Resolution X-Ray Photoemission Spectrum of the Valence Bands of Gold*, Phys. Rev. B. 5 (1972) 4709.
[131] M.P. Seah, Quantification in AES and XPS, in: J.T. Briggs, DGrant (Ed.), Surf. Anal. by Auger X-Ray Photoelectron Spectrosc., 2003: pp. 345–375.
[132] J.H. Scofield, *Hartree-Slater subshell photoionization cross-sections at 1254 and 1487 eV*, J. Electron Spectros. Relat. Phenomena. 8 (1976) 129.
[133] M. Kühn, Heterokontakte organischer Leuchtdioden : Schichtdickenabhängiges Strom-Spannungsverhalten, 2017.
[134] R. Holze, Surface and Interface Analysis, Springer, 2009.
[135] P. Schulz, L.L. Whittaker-Brooks, B.A. MacLeod, D.C. Olson, Y.-L. Loo, A. Kahn, *Electronic Level Alignment in Inverted Organometal Perovskite Solar Cells*, Adv. Mater. Interfaces. 2 (2015) 1400532.
[136] Jean-Nicolas Tisserant (Technical University of Brauschweig), *Personal communication*, (2018).
[137] A. Pizzi, K.L. Mittal, Handbook of Adhesive Technology, Revised and Expanded, 2003.
[138] A. Schutze, J.Y. Jeong, S.E. Babayan, Jaeyoung Park, G.S. Selwyn, R.F. Hicks, *The atmospheric-pressure plasma jet: a review and comparison to other plasma sources*, IEEE Trans. Plasma Sci. 26 (1998) 1685.
[139] J.C. De Jesus, I. González, A. Quevedo, T. Puerta, *Thermal decomposition of nickel acetate tetrahydrate: An integrated study by TGA, QMS and XPS techniques*, J. Mol. Catal. A Chem. 228 (2005) 283.
[140] Joint Committee on Powder Diffraction Standards, JCPDS Card No. 4-835, 1983.
[141] N. Talebian, M. Kheiri, *Sol–gel derived nanostructured nickel oxide films: Effect of solvent on crystallographic orientations*, Solid State Sci. 27 (2014) 79.
[142] F. Friedrich, Anpassung der Austrittsarbeit von aus Lösung hergestelltem Nickeloxid durch selbstorganisierende Monolagen, 2016.
[143] S. Hillebrandt, Infrarotspektroskopische Untersuchung von Elektrodenmodifikationen und deren Auswirkung auf die angrenzenden organischen Halbleiter, 2017.
[144] M. Scherer, Correlating structure and function in small molecule organic solar cells by means of scanning probe and electron microscopy, 2016.
[145] K. Itaka, M. Yamashiro, J. Yamaguchi, M. Haemori, S. Yaginuma, Y. Matsumoto, M. Kondo, H. Koinuma, *High-Mobility C60 Field-Effect Transistors Fabricated on Molecular- Wetting Controlled Substrates*, Adv. Mater. 18 (2006) 1713.

[146] A. Opitz, J. Wagner, W. Brütting, A. Hinderhofer, F. Schreiber, *Molecular semiconductor blends: Microstructure, charge carrier transport, and application in photovoltaic cells*, Phys. Status Solidi. 206 (2009) 2683.
[147] S.E. Koh, K.D. McDonald, D.H. Holt, C.S. Dulcey, J. a Chaney, P.E. Pehrsson, *Phenylphosphonic acid functionalization of indium tin oxide: surface chemistry and work functions.*, Langmuir. 22 (2006) 6249.
[148] N. Kedem, S. Blumstengel, F. Henneberger, H. Cohen, G. Hodes, D. Cahen, *Morphology-, synthesis- and doping-independent tuning of ZnO work function using phenylphosphonates.*, Phys. Chem. Chem. Phys. 16 (2014) 8310.
[149] F. Ullrich, S. Hillebrandt, S. Hietzschold, V. Rohnacher, T. Marszalek, W. Kowalsky, R. Lovrincic, S. Beck, E. Mankel, A. Pucci, *Correlation between Chemical and Electronic Properties of Solution-Processed Nickel Oxide*, ACS Appl. Energy Mater. 1 (2018) 3113.
[150] M.A. van Veenendaal, G.A. Sawatzky, *Nonlocal screening effects in 2 p x-ray photoemission spectroscopy core-level line shapes of transition metal compounds*, Phys. Rev. Lett. 70 (1993) 2459.
[151] K. Wandelt, *Photoemission studies of adsorbed oxygen and oxide layers*, Surf. Sci. Rep. 2 (1982) 1.
[152] M.W. Roberts, S.T.C. Smart, *The Defect Structure of Nickel Oxide Surfaces as Revealed by Photoelectron Spectroscopy*, J. Chem. Soc., Faraday Trans. 1. 80 (1984) 2957.
[153] A.P. Grosvenor, M.C. Biesinger, R.S.C. Smart, N.S. McIntyre, *New interpretations of XPS spectra of nickel metal and oxides*, Surf. Sci. 600 (2006) 1771.
[154] B.P. Payne, M.C. Biesinger, N.S. McIntyre, *The study of polycrystalline nickel metal oxidation by water vapour*, J. Electron Spectros. Relat. Phenomena. 175 (2009) 55.
[155] M. Atanasov, D. Reinen, *Non-local electronic effects in core-level photoemission , UV and optical electronic absorption spectra of nickel oxides 1*, J. Electron Spectros. Relat. Phenomena. 86 (1997) 185.
[156] H.A.. Hagelin-Weaver, J.F. Weaver, G.B. Hoflund, G.N. Salaita, *Electron energy loss spectroscopic investigation of Ni metal and NiO before and after surface reduction by Ar+ bombardment*, J. Electron Spectros. Relat. Phenomena. 134 (2004) 139.
[157] K.J. Gaskell, A. Starace, M.A. Langell, *Zn_x Ni_(1-x) O Rocksalt Oxide Surfaces: Novel Environment for Zn 2+ and its Effect on the NiO Band Structure*, 1 (2007) 13912.
[158] M.A. Langell, M.H. Nassir, *Stabilization of NiO(111) thin films by surface hydroxyls*, J. Phys. Chem. (1995) 4162. http://pubs.acs.org/doi/abs/10.1021/j100012a042.
[159] D.-J. Yun, S.-W. Rhee, *Deposition of NiOx thin films with radio frequency magnetron sputtering and their characteristics as a source/drain electrode for the pentacene thin film transistor*, J. Vac. Sci. Technol. B Microelectron. Nanom. Struct. Process. Meas. Phenom. 26 (2008) 1787.
[160] Y.A.K. Reddy, B. Ajitha, P.S. Reddy, *Influence of Growth Temperature on the Properties of DC Reactive Magnetron Sputtered NiO Thin Films*, (2014).
[161] Y. Chen, Y. Sun, X. Dai, B. Zhang, Z. Ye, M. Wang, H. Wu, *Tunable electrical properties of NiO thin films and p-type thin-film transistors*, Thin Solid Films. 592 (2015) 195.
[162] F. Behrouznejad, C.-M. Tsai, S. Narra, E.W.-G. Diau, N. Taghavinia, *Interfacial Investigation on Printable Carbon-Based Mesoscopic Perovskite Solar Cells with NiO_x /C Back Electrode*, ACS Appl. Mater. Interfaces. 9 (2017) 25204.
[163] R. Islam, G. Chen, P. Ramesh, J. Suh, N. Fuchigami, D. Lee, K.A. Littau, K. Weiner, R.T. Collins, K.C. Saraswat, *Investigation of the Changes in Electronic Properties of Nickel Oxide (NiO_x) Due to UV/Ozone Treatment*, ACS Appl. Mater. Interfaces. 9 (2017) 17201.
[164] X. Yan, J. Zheng, L. Zheng, G. Lin, H. Lin, G. Chen, B. Du, F. Zhang, *Optimization of sputtering NiOx films for perovskite solar cell applications*, Mater. Res. Bull. 103 (2018) 150.
[165] Z. Liu, J. Chang, Z. Lin, L. Zhou, Z. Yang, D. Chen, C. Zhang, S.F. Liu, Y. Hao, *High-Performance Planar Perovskite Solar Cells Using Low Temperature, Solution-Combustion-Based Nickel Oxide Hole Transporting Layer with Efficiency Exceeding 20%*, Adv. Energy Mater. 1703432 (2018) 1703432.
[166] H.-M. Kim, J. Kim, J. Jang, *Quantum-dot light-emitting diodes with a perfluorinated ionomer-doped copper-nickel oxide hole transporting layer*, Nanoscale. 10 (2018) 7281.
[167] Y. Nishihara, M. Chikamatsu, S. Kazaoui, T. Miyadera, Y. Yoshida, *Influence of O2 plasma treatment on NiOx layer in perovskite solar cells*, Jpn. J. Appl. Phys. 57 (2018) 04FS07.
[168] X. Zhao, J. Chen, N.-G. Park, *Importance of Oxygen Partial Pressure in Annealing NiO Film for High Efficiency Inverted Perovskite Solar Cells*, Sol. RRL. (2019) 1800339.

[169] T. Wang, D. Ding, X. Wang, R. Zeng, H. Liu, W. Shen, *High-Performance Inverted Perovskite Solar Cells with Mesoporous NiOx Hole Transport Layer by Electrochemical Deposition*, ACS Omega. 3 (2018) 18434.
[170] J.K. Kim, *PEG-assisted Sol-gel Synthesis of Compact Nickel Oxide Hole-Selective Layer with Modified Interfacial Properties for Organic Solar Cells*, Polymers (Basel). 11 (2019) 120.
[171] H. Lee, Y. Huang, M.W. Horn, S. Feng, *Engineered optical and electrical performance of rf – sputtered undoped nickel oxide thin films for inverted perovskite solar cells*, Sci. Rep. (2018) 1.
[172] M.B. Islam, N. Pant, M. Yanagida, Y. Shirai, K. Miyano, *Effect of hydroxyl groups in NiO x on the open circuit voltage of lead iodide perovskite solar cells*, Jpn. J. Appl. Phys. 57 (2018) 08RE06.
[173] J.H. Park, J. Seo, S. Park, S.S. Shin, Y.C. Kim, N.J. Jeon, H.-W. Shin, T.K. Ahn, J.H. Noh, S.C. Yoon, C.S. Hwang, S. Il Seok, *Efficient CH_3 NH_3 PbI_3 Perovskite Solar Cells Employing Nanostructured p-Type NiO Electrode Formed by a Pulsed Laser Deposition*, Adv. Mater. 27 (2015) 4013.
[174] W. Chen, F.Z. Liu, X.Y. Feng, A.B. Djurišić, W.K. Chan, Z.B. He, *Cesium Doped NiOx as an Efficient Hole Extraction Layer for Inverted Planar Perovskite Solar Cells*, Adv. Energy Mater. 7 (2017) 1.
[175] W. Chen, Y. Wu, J. Fan, A.B. Djurišić, F. Liu, H.W. Tam, A. Ng, C. Surya, W.K. Chan, D. Wang, Z.-B. He, *Understanding the Doping Effect on NiO: Toward High-Performance Inverted Perovskite Solar Cells*, Adv. Energy Mater. 8 (2018) 1703519.
[176] H. Kamal, E.K. Elmaghraby, S.A. Ali, K. Abdel-Hady, *Characterization of nickel oxide films deposited at different substrate temperatures using spray pyrolysis*, J. Cryst. Growth. 262 (2004) 424.
[177] A. Liu, G. Liu, H. Zhu, B. Shin, E. Fortunato, R. Martins, F. Shan, *Hole mobility modulation of solution-processed nickel oxide thin-film transistor based on high-k dielectric*, Appl. Phys. Lett. 108 (2016) 233506.
[178] P. Dubey, N. Kaurav, R.S. Devan, G.S. Okram, Y.K. Kuo, *The effect of stoichiometry on the structural, thermal and electronic properties of thermally decomposed nickel oxide*, RSC Adv. 8 (2018) 5882.
[179] L.M. Moroney, R.S.C. Smart, M.W. Roberts, *Studies of the thermal decomposition of βNiO(OH) and nickel peroxide by X-ray photoelectron spectroscopy*, J. Chem. Soc. Faraday Trans. 1 Phys. 79 (1983) 1769.
[180] B.P. Payne, M.C. Biesinger, N.S. Mcintyre, *Use of Oxygen/Nickel ratios in the XPS characterisation of oxide phases on nickel metal and nickel alloy surfaces*, J. Electron Spectros. Relat. Phenomena. 185 (2012) 159.
[181] Y. Wei, K. Yao, X. Wang, Y. Jiang, X. Liu, N. Zhou, F. Li, *Improving the efficiency and environmental stability of inverted planar perovskite solar cells via silver-doped nickel oxide hole-transporting layer*, Appl. Surf. Sci. 427 (2018) 782.
[182] S. Wheeler, F. Deledalle, N. Tokmoldin, T. Kirchartz, J. Nelson, J.R. Durrant, *Influence of Surface Recombination on Charge-Carrier Kinetics in Organic Bulk Heterojunction Solar Cells with Nickel Oxide Interlayers*, Phys. Rev. Appl. 4 (2015) 29.
[183] Y. Zhou, C. Fuentes-hernandez, J. Shim, J. Meyer, A.J. Giordano, H. Li, P. Winget, T. Papadopoulos, H. Cheun, J. Kim, M. Fenoll, A. Dindar, W. Haske, E. Najafabadi, T.M. Khan, H. Sojoudi, S. Barlow, S. Graham, J. Brédas, S.R. Marder, A. Kahn, B. Kippelen, *for Organic Electronics*, 873 (2012) 327.
[184] M. Alt, J. Schinke, S. Hillebrandt, M. Hänsel, G. Hernandez-Sosa, N. Mechau, T. Glaser, E. Mankel, M. Hamburger, K. Deing, W. Jaegermann, A. Pucci, W. Kowalsky, U. Lemmer, R. Lovrincic, *Processing follows function: Pushing the formation of self-assembled monolayers to high-throughput compatible time scales*, ACS Appl. Mater. Interfaces. 6 (2014) 20234.
[185] S. Hietzschold, Surface Functionalization of Nickel Oxide and Gallium Nitride for Hybrid Opto-Electronics, 2017.
[186] F.S. Benneckendorf, S. Hillebrandt, F. Ullrich, V. Rohnacher, S. Hietzschold, D. Jänsch, J. Freudenberg, S. Beck, E. Mankel, W. Jaegermann, A. Pucci, U.H.F. Bunz, K. Müllen, *Structure-Property Relationship of Phenylene-Based Self-Assembled Monolayers for Record Low Work Function of Indium Tin Oxide*, J. Phys. Chem. Lett. 9 (2018) 3731.
[187] B.C. Cornilsen, P.J. Karjala, P.L. Loyselle, *Structural models for nickel electrode active mass*, J. Power Sources. 22 (1988) 351.
[188] D.S. Hall, D.J. Lockwood, S. Poirier, C. Bock, B.R. MacDougall, *Applications of in Situ Raman*

Spectroscopy for Identifying Nickel Hydroxide Materials and Surface Layers during Chemical Aging, ACS Appl. Mater. Interfaces. 6 (2014) 3141.
[189] P.J. Gielisse, J.N. Plendl, L.C. Mansur, R. Marshall, S.S. Mitra, R. Mykolajewycz, A. Smakula, *Infrared Properties of NiO and CoO and Their Mixed Crystals*, J. Appl. Phys. 36 (1965) 2446.
[190] G. Dalmai-Imelik, J.C. Bertolini, J. Rousseau, *Relationship between vibrational states of O-Ni systems and their superficial structure on (100) face of nickel single crystal*, Surf. Sci. 63 (1977) 67.
[191] A.J. Hunt, T.R. Steyer, D.R. Huffman, *Infrared surface modes in small NiO particles*, Surf. Sci. 36 (1973) 454.
[192] R. Balasundaraprabhu, E.V. Monakhov, N. Muthukumarasamy, O. Nilsen, B.G. Svensson, *Effect of heat treatment on ITO film properties and ITO/p-Si interface*, Mater. Chem. Phys. 114 (2009) 425.
[193] J. Tauc, *Optical properties and electronic structure of amorphous Ge and Si*, Mater. Res. Bull. 3 (1968) 37.
[194] M.C. Biesinger, L.W.M. Lau, A.R. Gerson, R. St, C. Smart, *The role of the Auger parameter in XPS studies of nickel metal , halides and oxides*, Phys. Chem. Chem. Phys. 14 (2012) 2434.
[195] J. Kim, H.J. Park, C.P. Grigoropoulos, D. Lee, J. Jang, *Solution-processed nickel oxide nanoparticles with NiOOH for hole injection layers of high-efficiency organic light-emitting diodes - SI*, (2016).
[196] S.D. Chavhan, R. Hansson, L.K.E. Ericsson, P. Beyer, A. Hofmann, W. Brütting, A. Opitz, E. Moons, *Low temperature processed NiO x hole transport layers for efficient polymer solar cells*, Org. Electron. 44 (2017) 59.
[197] F. Jiang, W.C.H. Choy, X. Li, D. Zhang, J. Cheng, *Post-treatment-free solution-processed Non-stoichiometric NiOx nanoparticles for efficient hole-transport layers of organic optoelectronic devices*, Adv. Mater. 27 (2015) 2930.
[198] C.T. Campbell, *An XPS study of molecularly chemisorbed oxygen on Ag(111)*, Surf. Sci. Lett. 173 (1986) L641.
[199] K. Prabhakaran, C.N.. Rao, *A combined EELS-XPS study of molecularly chemisorbed oxygen on silver surfaces: Evidence for superoxo and peroxo species*, Surf. Sci. Lett. 186 (1987) 575.
[200] M. Vayer-Besançon, B. Rousseau, H. Estrade-Szwarckopf, *Oxygen adsorption on Cs-graphite intercalation compounds UV and X-ray photoelectron studies on CsC8 at 100 K: formation of oxide, peroxide and superoxide on the surface*, Surf. Sci. 318 (1994) 169.
[201] M.A. Henderson, *A surface science perspective on TiO2 photocatalysis*, Surf. Sci. Rep. 66 (2011) 228.
[202] J.W. Shim, C. Fuentes-Hernandez, A. Dindar, Y. Zhou, T.M. Khan, B. Kippelen, *Polymer solar cells with NiO hole-collecting interlayers processed by atomic layer deposition*, Org. Electron. Physics, Mater. Appl. 14 (2013) 2802.
[203] J.W. Schultze, M.M. Lohrengel, D. Ross, *Nucleation and growth of anodic oxide films*, Electrochim. Acta. 28 (1983) 973.
[204] A. Motori, F. Sandrolini, G. Davolio, *Electrical properties of nickel hydroxide for alkaline cell systems*, J. Power Sources. 48 (1994) 361.
[205] M.S. Wu, H.H. Hsieh, *Nickel Oxide/Hydroxide nanoplatelets synthesized by chemical precipitation for electrochemical capacitors*, Electrochim. Acta. 53 (2008) 3427.
[206] M.A. Green, M.J. Keevers, *Optical properties of intrinsic silicon at 300 K*, Prog. Photovoltaics Res. Appl. 3 (1995) 189.
[207] V. Rohnacher, Infrarotspektroskopische Untersuchung zur Charakterisierung und Oberflächenmodifikation von Nickeloxid, Iniversity of Heidelberg, 2017.
[208] W. Xing, F. Li, Z. Yan, G.Q. Lu, *Synthesis and electrochemical properties of mesoporous nickel oxide*, J. Power Sources. 134 (2004) 324.
[209] W.K. Liu, M.B. Santos, Thin Films: Heteroepitaxial Systems, WORLD SCIENTIFIC, 1999.
[210] UK National Measurement Institute (NPL), *Average Matrix Relative Sensitivity Factors (AMRSFs) for X-ray Photoelectron Spectroscopy (XPS)*, (2006). http://resource.npl.co.uk/nanoanalysis/xpsamrsf.pdf.
[211] C.D. Wagner, L.E. Davis, M. V. Zeller, J.A. Taylor, R.H. Raymond, L.H. Gale, *Empirical atomic sensitivity factors for quantitative analysis by electron spectroscopy for chemical analysis*, Surf. Interface Anal. 3 (1981) 211.
[212] M. Brendel, S. Krause, A. Steindamm, A.K. Topczak, S. Sundarraj, P. Erk, S. Höhla, N. Fruehauf, N. Koch, J. Pflaum, *The effect of gradual fluorination on the properties of FnZnPc thin films and FnZnPc/C60 bilayer photovoltaic cells*, Adv. Funct. Mater. 25 (2015) 1565.

[213] I.H. Campbell, J.P. Ferraris, T.W. Hagler, M.D. Joswick, I.D. Parker, D.L. Smith, *Measuring internal electric fields in organic light-emitting diodes using electroabsorption spectroscopy*, Polym. Adv. Technol. 8 (1997) 417.
[214] A. Wan, J. Hwang, F. Amy, A. Kahn, *Impact of electrode contamination on the α-NPD/Au hole injection barrier*, Org. Electron. 6 (2005) 47.
[215] A. Crispin, X. Crispin, M. Fahlman, M. Berggren, W.R. Salaneck, *Transition between energy level alignment regimes at a low band gap polymer-electrode interfaces*, Appl. Phys. Lett. 89 (2006) 213503.
[216] C. Tengstedt, W. Osikowicz, W.R. Salaneck, I.D. Parker, C.-H. Hsu, M. Fahlman, *Fermi-level pinning at conjugated polymer interfaces*, Appl. Phys. Lett. 88 (2006) 053502.
[217] H. Peisert, M. Knupfer, T. Schwieger, J.M. Auerhammer, M.S. Golden, J. Fink, *Full characterization of the interface between the organic semiconductor copper phthalocyanine and gold*, J. Appl. Phys. 91 (2002) 4872.
[218] I.G. Hill, A. Rajagopal, A. Kahn, Y. Hu, *Molecular level alignment at organic semiconductor-metal interfaces*, Appl. Phys. Lett. 73 (1998) 662.
[219] S. Braun, W.R. Salaneck, *Fermi level pinning at interfaces with tetrafluorotetracyanoquinodimethane (F4-TCNQ): The role of integer charge transfer states*, Chem. Phys. Lett. 438 (2007) 259.
[220] J. Hwang, A. Wan, A. Kahn, *Energetics of metal–organic interfaces: New experiments and assessment of the field*, 64 (2009) 1.
[221] L. Ley, Y. Smets, C.I. Pakes, J. Ristein, *Calculating the universal energy-level alignment of organic molecules on metal oxides*, Adv. Funct. Mater. 23 (2013) 794.
[222] H. Vázquez, F. Flores, A. Kahn, *Induced Density of States model for weakly-interacting organic semiconductor interfaces*, Org. Electron. 8 (2007) 241.
[223] H. Vázquez, R. Oszwaldowski, P. Pou, J. Ortega, R. Pérez, F. Flores, A. Kahn, *Dipole formation at metal/PTCDA interfaces: Role of the Charge Neutrality Level*, Europhys. Lett. 65 (2004) 802.
[224] J. Zhang, S. Wei, X. Wang, J. Xiang, W. Wang, *Experimental estimation of charge neutrality level of SiO2*, Appl. Surf. Sci. 422 (2017) 690.
[225] M.T. Greiner, M.G. Helander, W.-M. Tang, Z.-B. Wang, J. Qiu, Z.-H. Lu, *Universal energy-level alignment of molecules on metal oxides*, Nat. Mater. 11 (2012) 76.
[226] M. Oehzelt, N. Koch, G. Heimel, *Organic semiconductor density of states controls the energy level alignment at electrode interfaces*, Nat. Commun. 5 (2014) 4174.
[227] M.-S. Liao, S. Scheiner, *Electronic structure and bonding in metal phthalocyanines, Metal=Fe, Co, Ni, Cu, Zn, Mg*, J. Chem. Phys. 114 (2001) 9780.
[228] H. Peisert, M. Knupfer, T. Schwieger, J. Fink, *Strong chemical interaction between indium tin oxide and phthalocyanines*, Appl. Phys. Lett. 80 (2002) 2916.
[229] M. Schwarze, W. Tress, B. Beyer, F. Gao, R. Scholz, C. Poelking, K. Ortstein, A.A. Günther, D. Kasemann, D. Andrienko, K. Leo, *Band structure engineering in organic semiconductors.*, Science. 352 (2016) 1446.
[230] H. Brinkmann, C. Kelting, S. Makarov, O. Tsaryova, G. Schnurpfeil, D. Wöhrle, D. Schlettwein, *Fluorinated phthalocyanines as molecular semiconductor thin films*, Phys. Status Solidi. 205 (2008) 409.
[231] D.G. de Oteyza, A. El-Sayed, J.M. Garcia-Lastra, E. Goiri, T.N. Krauss, A. Turak, E. Barrena, H. Dosch, J. Zegenhagen, A. Rubio, Y. Wakayama, J.E. Ortega, *Copper-phthalocyanine based metal–organic interfaces: The effect of fluorination, the substrate, and its symmetry*, J. Chem. Phys. 133 (2010) 214703.
[232] T. Mayer, U. Weiler, C. Kelting, D. Schlettwein, S. Makarov, D. Wöhrle, O. Abdallah, M. Kunst, W. Jaegermann, *Silicon–organic pigment material hybrids for photovoltaic application*, Sol. Energy Mater. Sol. Cells. 91 (2007) 1873.
[233] C. Schünemann, C. Elschner, A.A. Levin, M. Levichkova, K. Leo, M. Riede, *Zinc phthalocyanine — Influence of substrate temperature, film thickness, and kind of substrate on the morphology*, Thin Solid Films. 519 (2011) 3939.
[234] Y. Gassenbauer, A. Klein, *Electronic and Chemical Properties of Tin-Doped Indium Oxide (ITO) Surfaces and ITO/ZnPc Interfaces Studied In-situ by Photoelectron Spectroscopy*, J. Phys. Chem. B. 110 (2006) 4793.
[235] H. Peisert, M. Knupfer, T. Schwieger, G.G. Fuentes, D. Olligs, J. Fink, T. Schmidt, *Fluorination of copper phthalocyanines: Electronic structure and interface properties*, J. Appl. Phys. 93 (2003) 9683.
[236] L. Pauling, *The nature of the chemical bond. IV The energy of single bonds and the relative*

electronegativity of atoms, J. Am. Chem. Soc. 54 (1932) 3570.
[237] H. Peisert, M. Knupfer, J. Fink, *Electronic structure of partially fluorinated copper phthalocyanine (CuPCF4) and its interface to Au(100)*, Surf. Sci. 515 (2002) 491.
[238] C. Shen, A. Kahn, J. Schwartz, *Role of metal–molecule chemistry and interdiffusion on the electrical properties of an organic interface: The Al–F16CuPc case*, J. Appl. Phys. 90 (2001) 6236.
[239] S. Stolz, Photoelektronenspektroskopie an organischen Charge-Transfer-Komplexen, Technical University Darmstadt, 2012.
[240] D.G. de Oteyza, I. Silanes, M. Ruiz-Osés, E. Barrena, B.P. Doyle, A. Arnau, H. Dosch, Y. Wakayama, J.E. Ortega, *Balancing Intermolecular and Molecule-Substrate Interactions in Supramolecular Assemblies*, Adv. Funct. Mater. 19 (2009) 259.
[241] H. Vázquez, Energy level alignment at organic semiconductor interfaces, 2006.
[242] P.J. John, J. Liang, *Initial metal fluoride formation at metal/fluorocarbon interfaces*, J. Vac. Sci. Technol. A Vacuum, Surfaces, Film. 12 (1994) 199.
[243] S. Duhm, G. Heimel, I. Salzmann, H. Glowatzki, R.L. Johnson, A. Vollmer, J.P. Rabe, N. Koch, *Orientation-dependent ionization energies and interface dipoles in ordered molecular assemblies*, Nat. Mater. 7 (2008) 326.
[244] W. Chen, H. Huang, S. Chen, Y.L. Huang, X.Y. Gao, A.T.S. Wee, *Molecular Orientation-Dependent Ionization Potential of Organic Thin Films*, Chem. Mater. 20 (2008) 7017.
[245] B.P. Rand, D. Cheyns, K. Vasseur, N.C. Giebink, S. Mothy, Y. Yi, V. Coropceanu, D. Beljonne, J. Cornil, J.-L. Brédas, J. Genoe, *The Impact of Molecular Orientation on the Photovoltaic Properties of a Phthalocyanine/Fullerene Heterojunction*, Adv. Funct. Mater. 22 (2012) 2987.
[246] J.S. Chappell, A.N. Bloch, W.A. Bryden, M. Maxfield, T.O. Poehler, D.O. Cowan, *Degree of charge transfer in organic conductors by infrared absorption spectroscopy*, J. Am. Chem. Soc. 103 (1981) 2442.
[247] H.G. McCann, *Reactions of Fluoride Ion with Hydroxyapatite*, J. Biol. Chem. 201 (1953) 247.
[248] E.C. Moreno, M. Kresak, R.T. Zahradnik, *Fluoridated Hydroxyapatite Solubility and Caries Formation*, Nature. 247 (1974) 64.
[249] E. Kemnitz, D.-H. Menz, *Fluorinated metal oxides and metal fluorides as heterogeneous catalysts*, Prog. Solid State Chem. 26 (1998) 97.
[250] W. Wu, A.J. Fisher, N.M. Harrison, *Theoretical modeling of the electronic structure and exchange interactions in a Cu(II)Pc one-dimensional chain*, Phys. Rev. B. 84 (2011) 024427.
[251] G. Dufour, C. Poncey, F. Rochet, H. Roulet, M. Sacchi, M. De Santis, M. De Crescenzi, *Copper phthalocyanine on Si(111)-7 × 7 and Si(001)-2 × 1 surfaces: an X-ray photoemission spectroscopy and synchrotron X-ray absorption spectroscopy study*, Surf. Sci. 319 (1994) 251.
[252] E.V. Tsiper, Z.G. Soos, W. Gao, A. Kahn, *Electronic polarization at surfaces and thin films of organic molecular crystals: PTCDA*, Chem. Phys. Lett. 360 (2002) 47.
[253] H. Yamane, Y. Yabuuchi, H. Fukagawa, S. Kera, K.K. Okudaira, N. Ueno, *Does the molecular orientation induce an electric dipole in Cu-phthalocyanine thin films?*, J. Appl. Phys. 99 (2006) 093705.
[254] S. Wang, D. Niu, L. Lyu, Y. Huang, X. Wei, C. Wang, H. Xie, Y. Gao, *Interface electronic structure and morphology of 2,7-dioctyl[1]benzothieno[3,2-b]benzothiophene (C8-BTBT) on Au film*, Appl. Surf. Sci. 416 (2017) 696.
[255] E. Mankel, C. Hein, M. Kühn, T. Mayer, *Electric potential distributions in space charge regions of molecular organic adsorbates using a simplified distributed states model*, Phys. Status Solidi. 211 (2014) 2040.
[256] S. Chen, J.R. Manders, S.-W. Tsang, F. So, *Metal oxides for interface engineering in polymer solar cells*, J. Mater. Chem. 22 (2012) 24202.
[257] J. Hou, X. Guo, Active Layer Materials for Organic Solar Cells, in: W. Choy (Ed.), Org. Sol. Cells. Green Energy Technol., Springer, London, 2013.
[258] S.R. Cowan, P. Schulz, A.J. Giordano, A. Garcia, B.A. MacLeod, S.R. Marder, A. Kahn, D.S. Ginley, E.L. Ratcliff, D.C. Olson, *Chemically Controlled Reversible and Irreversible Extraction Barriers Via Stable Interface Modification of Zinc Oxide Electron Collection Layer in Polycarbazole-based Organic Solar Cells*, Adv. Funct. Mater. 24 (2014) 4671.
[259] Y.E. Ha, M.Y. Jo, J. Park, Y.-C. Kang, S. Il Yoo, J.H. Kim, *Inverted Type Polymer Solar Cells with Self-Assembled Monolayer Treated ZnO*, J. Phys. Chem. C. 117 (2013) 2646.
[260] C. Fruböse, K. Doblhofer, *In situ quartz-microbalance study of the self-assembly and stability of*

aliphatic thiols on polarized gold electrodes, J. Chem. Soc., Faraday Trans. 91 (1995) 1949.
[261] C.D. Bain, E.B. Troughton, Y.T. Tao, J. Evall, G.M. Whitesides, R.G. Nuzzo, *Formation of monolayer films by the spontaneous assembly of organic thiols from solution onto gold*, J. Am. Chem. Soc. 111 (1989) 321.
[262] C.D. Bain, J. Evall, G.M. Whitesides, *Formation of Monolayers by the Coadsorption of Thiols on Gold: Valiation in the Head Group, Tail Group, and Solvent*, J. Am. Chem. Soc. 111 (1989) 7155.
[263] S.A. Paniagua, A.J. Giordano, O.L. Smith, S. Barlow, H. Li, N.R. Armstrong, J.E. Pemberton, J.-L. Brédas, D. Ginger, S.R. Marder, *Phosphonic Acids for Interfacial Engineering of Transparent Conductive Oxides*, Chem. Rev. 116 (2016) 7117.
[264] N. Beaumont, I. Hancox, P. Sullivan, R.A. Hatton, T.S. Jones, *Increased efficiency in small molecule organic photovoltaic cells through electrode modification with self-assembled monolayers*, Energy Environ. Sci. 4 (2011) 1708.
[265] S. a Paniagua, P.J. Hotchkiss, S.C. Jones, S.R. Marder, A. Mudalige, F.S. Marrikar, J.E. Pemberton, N.R. Armstrong, *Phosphonic Acid Modification of ITO Electrodes - Combined XPS - UPS - Contact Angle Studies*, J. Phys. Chem. C. 112 (2008) 7809.
[266] P.J. Hotchkiss, M. Malicki, A.J. Giordano, N.R. Armstrong, S.R. Marder, *Characterization of phosphonic acid binding to zinc oxide*, J. Mater. Chem. 21 (2011) 3107.
[267] X. Bulliard, S.-G. Ihn, S. Yun, Y. Kim, D. Choi, J.-Y. Choi, M. Kim, M. Sim, J.-H. Park, W. Choi, K. Cho, *Enhanced Performance in Polymer Solar Cells by Surface Energy Control*, Adv. Funct. Mater. 20 (2010) 4381.
[268] M. Gliboff, H. Li, K.M. Knesting, A.J. Giordano, D. Nordlund, G.T. Seidler, J.-L. Brédas, S.R. Marder, D.S. Ginger, *Competing Effects of Fluorination on the Orientation of Aromatic and Aliphatic Phosphonic Acid Monolayers on Indium Tin Oxide*, J. Phys. Chem. C. 117 (2013) 15139.
[269] M. Gliboff, L. Sang, K.M. Knesting, M.C. Schalnat, A. Mudalige, E.L. Ratcliff, H. Li, A.K. Sigdel, A.J. Giordano, J.J. Berry, D. Nordlund, G.T. Seidler, J.L. Br??das, S.R. Marder, J.E. Pemberton, D.S. Ginger, *Orientation of phenylphosphonic acid self-assembled monolayers on a transparent conductive oxide: A combined NEXAFS, PM-IRRAS, and DFT study*, Langmuir. 29 (2013) 2166.
[270] M. Timpel, M. V. Nardi, S. Krause, G. Ligorio, C. Christodoulou, L. Pasquali, A. Giglia, J. Frisch, B. Wegner, P. Moras, N. Koch, *Surface modification of ZnO(0001)-Zn with phosphonate-based self-assembled monolayers: Binding modes, orientation, and work function*, Chem. Mater. 26 (2014) 5042.
[271] L. Sang, A. Mudalige, A.K. Sigdel, A.J. Giordano, S.R. Marder, J.J. Berry, J.E. Pemberton, *PM-IRRAS Determination of Molecular Orientation of Phosphonic Acid Self-Assembled Monolayers on Indium Zinc Oxide*, Langmuir. 31 (2015) 5603.
[272] M.P. Seah, I.S. Gilmore, S.J. Spencer, *Quantitative XPS I . Analysis of X-ray photoelectron intensities from elemental data in a digital photoelectron database*, 120 (2001) 93.
[273] L. Romaner, G. Heimel, E. Zojer, *Electronic structure of thiol-bonded self-assembled monolayers: Impact of coverage*, Phys. Rev. B. 77 (2008) 045113.
[274] R. Cohen, S. Bastide, D. Cahen, J. Libman, A. Shanzer, Y. Rosenwaks, *Controlling surfaces and interfaces of semiconductors using organic molecules*, Opt. Mater. (Amst). 9 (1998) 394.
[275] W.E. McClain, P.R. Florence, A. Shu, A. Kahn, J. Schwartz, *Surface dipole engineering for conducting polymers*, Org. Electron. 14 (2013) 411.
[276] I. Lange, S. Reiter, M. Pätzel, A. Zykov, A. Nefedov, J. Hildebrandt, S. Hecht, S. Kowarik, C. Wöll, G. Heimel, D. Neher, *Tuning the work function of polar zinc oxide surfaces using modified phosphonic acid self-assembled monolayers*, Adv. Funct. Mater. 24 (2014) 7014.
[277] G. Heimel, L. Romaner, E. Zojer, J.-L. Brédas, *Toward Control of the Metal−Organic Interfacial Electronic Structure in Molecular Electronics: A First-Principles Study on Self-Assembled Monolayers of π-Conjugated Molecules on Noble Metals*, Nano Lett. 7 (2007) 932.
[278] G. Heimel, L. Romaner, E. Zojer, J.-L. Bredas, *The Interface Energetics of Self-Assembled Monolayers on Metals*, Acc. Chem. Res. 41 (2008) 721.
[279] F. Brodard-Severac, G. Guerrero, J. Maquet, P. Florian, C. Gervais, P.H. Mutin, *High-Field 17 O MAS NMR Investigation of Phosphonic Acid Monolayers on Titania*, Chem. Mater. 20 (2008) 5191.
[280] P.J. Hotchkiss, S.C. Jones, S.A. Paniagua, A. Sharma, B. Kippelen, N.R. Armstrong, S.R. Marder, *The Modification of Indium Tin Oxide with Tuning of Surface Properties , and Potential for*

Use in Organic Electronic Applications, 45 (2012) 337.
[281] B.H. Stuart, Experimental Methods, Wiley Online Library, 2005.
[282] Y. Yuan, T.R. Lee, Contact Angle and Wetting Properties, in: G. Bracco, B. Holst (Eds.), Surf. Sci. Tech., Springer-Verlag Berlin Heidelberg, 2013: pp. 3–34.
[283] H. Li, P. Paramonov, J.-L. Bredas, *Theoretical study of the surface modification of indium tin oxide with trifluorophenyl phosphonic acid molecules: impact of coverage density and binding geometry*, J. Mater. Chem. 20 (2010) 2630.
[284] S. Pawsey, K. Yach, L. Reven, *Self-Assembly of Carboxyalkylphosphonic Acids on Metal Oxide Powders*, Langmuir. 18 (2002) 5205.
[285] G.E. Poirier, *Coverage-Dependent Phases and Phase Stability of Decanethiol on Au(111)*, Langmuir. 15 (1999) 1167.
[286] R. Saive, C. Mueller, J. Schinke, R. Lovrincic, W. Kowalsky, *Understanding S-shaped current-voltage characteristics of organic solar cells: Direct measurement of potential distributions by scanning Kelvin probe*, Appl. Phys. Lett. 103 (2013) 243303.
[287] A. Wagenpfahl, D. Rauh, M. Binder, C. Deibel, V. Dyakonov, *S-shaped current-voltage characteristics of organic solar devices*, Phys. Rev. B - Condens. Matter Mater. Phys. 82 (2010) 1.
[288] S. Trost, K. Zilberberg, A. Behrendt, A. Polywka, P. Görrn, P. Reckers, J. Maibach, T. Mayer, T. Riedl, *Overcoming the "Light-Soaking" Issue in Inverted Organic Solar Cells by the Use of Al:ZnO Electron Extraction Layers*, Adv. Energy Mater. 3 (2013) 1437.
[289] W. Tress, K. Leo, M. Riede, *Influence of Hole-Transport Layers and Donor Materials on Open-Circuit Voltage and Shape of I-V Curves of Organic Solar Cells*, Adv. Funct. Mater. 21 (2011) 2140.
[290] W. Tress, *Open circuit voltage and IV curve shape of ZnPc:C60 solar cells with varied mixing ratio and hole transport layer*, J. Photonics Energy. 1 (2011) 011114.
[291] W. Tress, O. Inganäs, *Solar Energy Materials & Solar Cells Simple experimental test to distinguish extraction and injection barriers at the electrodes of (organic) solar cells with S-shaped current – voltage characteristics*, Sol. Energy Mater. Sol. Cells. 117 (2013) 599.
[292] A. Kumar, S. Sista, Y. Yang, *Dipole induced anomalous S-shape I-V curves in polymer solar cells*, J. Appl. Phys. 105 (2009) 094512.
[293] W. Tress, A. Petrich, M. Hummert, M. Hein, K. Leo, M. Riede, *Imbalanced mobilities causing S-shaped IV curves in planar heterojunction organic solar cells*, Appl. Phys. Lett. 98 (2011) 063301.
[294] J. Kim, H.R. Lee, H.P. Kim, T. Lin, A. Kanwat, A.R. bin Mohd Yusoff, J. Jang, *Effects of UV-ozone irradiation on copper doped nickel acetate and its applicability to perovskite solar cells*, Nanoscale. 8 (2016) 9284.
[295] J.H. Kim, P.-W. Liang, S.T. Williams, N. Cho, C.-C. Chueh, M.S. Glaz, D.S. Ginger, A.K.-Y. Jen, *High-Performance and Environmentally Stable Planar Heterojunction Perovskite Solar Cells Based on a Solution-Processed Copper-Doped Nickel Oxide Hole-Transporting Layer*, Adv. Mater. 27 (2015) 695.
[296] K.H. Kim, C. Takahashi, Y. Abe, M. Kawamura, *Effects of Cu doping on nickel oxide thin film prepared by sol–gel solution process*, Optik (Stuttg). 125 (2014) 2899.
[297] O.G. Palanna, Engineering Chemistry, Tata McGraw Hill Education Private Limited, New Delhi, 2009.
[298] H. Kuhlenbeck, G. Odörfer, R. Jaeger, G. Illing, M. Menges, T. Mull, FreundH.-J., *Molecular adsorption on oxide surfaces: Electronic structure and orientation of NO on NiO(100)/Ni(100) and on NiO(100) as determined from electron spectroscopies and ab initio cluster calculations*, Phys. Rev. B. 43 (1991) 1969.
[299] T. Robert, M. Bartel, G. Offergeld, *Characterization of oxygen species adsorbed on copper and nickel oxides by X-ray photoelectron spectroscopy*, Surf. Sci. 33 (1972) 123.
[300] A. Joiner, R.H. Mohr, J.N. Yukich, *High-resolution photodetachment spectroscopy from the lowest threshold of O^-*, Phys. Rev. A. 83 (2011) 035401.
[301] K.M. Ervin, I. Anusiewicz, P. Skurski, J. Simons, W.C. Lineberger, *The Only Stable State of O 2 - Is the X 2 Π g Ground State and It (Still!) Has an Adiabatic Electron Detachment Energy of 0.45 eV*, J. Phys. Chem. A. 107 (2003) 8521.
[302] D.R. Lide, Ionization potentials of atoms and atomic ions, in: Handb. Chem. Phys., 1992: pp. 10–211.
[303] R.G. Tonkyn, J.W. Winniczek, M.G. White, *Rotationally resolved photoionization of O2+ near threshold*, Chem. Phys. Lett. 164 (1989) 137.

[304] S. Berglund, *The Free Energy of Formation of Nickel Oxide*, Berichte Der Bunsen-Gesellschaft. 80 (1976) 862.
[305] D.D. Macdonald, M.L. Challingsworth, *Thermodynamics of Nickel-Cadmium and Nickel-Hydrogen Batteries*, 140 (1993) 606.
[306] J.D. Cox, D.D. Wagman, V.A. Medvedev, CODATA Key Values for Thermodynamics, Hemisphere Publishing Corp., New York, 1984.
[307] M.W. Chase, *NIST–JANAF Thermochemical Tables, Fourth Edition*, J. Phys. Chem. Ref. Data, Monogr. 9. (1998) 1.
[308] M. Kröger, Devive and Process Technology for Full-Color Active-Matrix OLED Displays, Technical University of Braunschweig, 2007.
[309] D. Nanova, Intermolecular ordering in organic semiconductor layers and its correlation to electronic properties, University of Heidelberg, 2015.
[310] Y. Liao, Practical Electron Microscopy and Database, 2018. www.globalsino.com/EM/.
[311] T. Glaser, Infrarotspektroskopische Untersuchung der p-Dotierung organischer Halbleiter mit Übergangsmetalloxiden, Universität Heidelberg, 2013.
[312] K.T. Queeney, M.K. Weldon, J.P. Chang, Y.J. Chabal, A.B. Gurevich, J. Sapjeta, R.L. Opila, *Infrared spectroscopic analysis of the Si/SiO2 interface structure of thermally oxidized silicon*, J. Appl. Phys. 87 (2000) 1322.
[313] J. Bombsch, Solution-processed nickel oxide as hole transport layer in organic solar cells, 2017.
[314] L. Dimesso, M. Stöhr, C. Das, T. Mayer, W. Jaegermann, *Investigation on the properties of hybrid CH3NH3SnxI3 (0.9 ≤ x ≤ 1.4) perovskite systems*, J. Mater. Res. 32 (2017) 4132.
[315] M. Timpel, M. V. Nardi, G. Ligorio, B. Wegner, M. Pätzel, B. Kobin, S. Hecht, N. Koch, *Energy-Level Engineering at ZnO/Oligophenylene Interfaces with Phosphonate-Based Self-Assembled Monolayers*, ACS Appl. Mater. Interfaces. 7 (2015) 11900.
[316] A. Ostapenko, T. Klöffel, B. Meyer, G. Witte, *Formation and Stability of Phenylphosphonic Acid Monolayers on ZnO: Comparison of In Situ and Ex Situ SAM Preparation*, Langmuir. 32 (2016) 5029.
[317] M.A. Peck, M.A. Langell, *Comparison of nanoscaled and bulk NiO structural and environmental characteristics by XRD, XAFS, and XPS*, Chem. Mater. 24 (2012) 4483.
[318] D. Nanova, Organische Charge-Transfer-Komplexe, University of Heidelberg, 2011.
[319] S. Beck, Infrarotspektroskopie an organischen Charge-Transfer-Komplexen, University of Heidelberg, 2011.

List of Abbreviations

AD	as-deposited
AFM	atomic force microscopy
AMRSF	average matrix relative sensitivity factor
ARXPS	angel-resolved X-ray photoelectron spectroscopy
ASF	atomic sensitivity factor
BB	band bending
BHJ	bulk heterojunction
CB	conduction band
CBM	conduction band maximum
CL	core level
CNL	charge neutrality level
CT	charge transfer
CYNOPPA	4-cyanophenylphosphonic acid ($C_7H_6NPO_3$)
DFT	density functional theory
DOS	density of states
EA	electron affinity
ELS	energy level shift
ETL	electron transport layer
EtOH	ethanol
F_4ZnPc	fluorinated tin phthalocyanin
FHJ	flat heterojunction
FIR	far-infrared
FTIR	Fourier-transform infrared spectroscopy
FTO	fluorine-dope tin oxide
GB	glove box
HOMO	highest occupied molecular orbital
HTL	hole transport layer
ICT	integer charge transfer
IDIS	induced density of interface states
IMFP	inelastic mean free path
ip	in-plane
IP	ionization potential
IR	infrared
ITO	indium tin oxide
KP	Kelvin probe
LI-ELS	light-induced energy level shift
LUMO	lowest unoccupied molecular orbital
MIR	mid-infrared
MPP	maximum power point
MSD	mean squared deviation
NEXAFS	near edge X-ray absorption fine structure
$Ni(OH)_2$	nickel hydroxide
NiO	nickel oxide
NiOOH	nickel oxyhydroxide
OLED	organic light-emitting diode
oop	out-of-plane
OP	oxygen plasma
OPV	organic photovoltaic cell

OSC	organic semiconductor
PA	phosphonic acid
PCE	power conversion efficiency
pcNiO	polycrystalline nickel oxide
PE	photoelectron
PES	photoelectron spectroscopy
PVSC	perovskite solar cell
RMS	root mean square
RSF	relative sensitivity factor
RT	room temperature
SAM	self-assembled monolayer
scNiO	single crystalline nickel oxide
SEC	secondary electron cutoff
SEM	scanning electron microscopy
sNiO	solution-processed nickel oxide
SP-to-MP ratio	side peak to main peak ratio
SSR	sum of squared residuals
TCO	transparent conductive oxide
TGA	thermogravimetric analysis
TMO	transition-metal oxide
UHV	ultra-high vacuum
UPS	ultraviolet photoelectron spectroscopy
VB	valence band
VBM	valence band maximum
WF	work function
XP	X-ray photoelectron
XPS	X-ray photoelectron spectroscopy

Publications and Conference Contributions

Publications

S. Hietzschold, S. Hillebrandt, F. Ullrich, J. Bombsch, V. Rohnacher, S. Ma, W. Liu, A. Köhn, W. Jaegermann, A. Pucci, W. Kowalsky, E. Mankel, S. Beck, R. Lovrincic, *Functionalized Nickel Oxide Hole Contact Layers: Work Function versus Conductivity*, ACS Appl. Mater. Interfaces. 9 (2017) 39821.

M. Ruscello, S. Stolz, D.L. Gonzalez Arellano, F. Ullrich, S. Hillebrandt, E. Mankel, A. Pucci, W. Kowalsky, T. Emrick, A.L. Briseno, G. Hernandez-Sosa, *Electron Injection and Interfacial Trap Passivation in Solution-Processed Organic Light-Emitting Diodes Using a Polymer Zwitterion Interlayer*, Org. Electron. 50 (2017) 384.

F.L. Geyer, S. Koser, M.N. Bojanowski, F. Ullrich, V. Brosius, S. Hahn, K. Brödner, E. Mankel, T. Marszalek, W. Pisula, F. Hinkel, U.H.F. Bunz, *Tetraazapentacene Constructs: Controlling Bulk-Morphology Through Molecular Dimensionality*, Chem. Commun. 54 (2017) 1045.

F. Ullrich, S. Hillebrandt, S. Hietzschold, V. Rohnacher, T. Marszalek, W. Kowalsky, R. Lovrincic, S. Beck, E. Mankel, A. Pucci, *Correlation between Chemical and Electronic Properties of Solution-Processed Nickel Oxide*, ACS Appl. Energy Mater. 1 (2018) 3113.

F.S. Benneckendorf, S. Hillebrandt, F. Ullrich, V. Rohnacher, S. Hietzschold, D. Jänsch, J. Freudenberg, S. Beck, E. Mankel, W. Jaegermann, A. Pucci, U.H.F. Bunz, K. Müllen, *Structure-Property Relationship of Phenylene-Based Self-Assembled Monolayers for Record Low Work Function of Indium Tin Oxide*, J. Phys. Chem. Lett. 9 (2018) 3731.

F. Zhang, F. Ullrich, S.H. Silver, R.A. Kerner, B.P. Rand, A. Kahn, *Complexities of Contact Potential Difference Measurements on Metal Halide Perovskite Surfaces*, J. Phys. Chem. Lett. 10 (2019) 890.

T. Auzelle, F. Ullrich, S. Hietzschold, S. Brackmann, S. Hillebrandt, W. Kowalsky, E. Mankel, R. Lovrincic, S. Fernández-Garrido, *Electronic Properties of Air-Exposed GaN(11-00) and (0001) Surfaces after Several Device Processing Compatible Cleaning Steps*, Appl. Surf. Sci. 495 (2019) 143514.

F. Zhang, S.H. Silver, N.K. Noel, F. Ullrich, B.P. Rand and A. Kahn, *Photoemission Spectroscopy and Kelvin Probe Measurements on Metal Halide Perovskites: Advantages and Pitfalls*, Adv. Energy Mater. (2020) 1903252

T. Auzelle, F. Ullrich, S. Hietzschold, C. Sinito, S. Brackmann, W. Kowalsky, E. Mankel, O. Brandt, R. Lovrincic, and S. Fernández-Garrido *External control of GaN band bending and work function using phosphanate self-assembled monolayers*, in preparation.

Conference Contributions

DPG 2016 in Berlin:	"Investigation of Solution-Processable Electron Injection Layers in Organic Light-Emitting Diodes"
DPG 2017 in Dresden:	"Multi-Analytical Study on Solution-Processed Nickel Oxide as Functional Layer in Organic Electronic Devices - X-ray Photoelectron Spectroscopy"
MRS 2017 in Boston:	"Analytical Study of Solution-Processed Nickel Oxide: New Insights into the Correlation of Chemical and Electronic Properties"

Acknowledgements

I would like to thank everyone who has contributed to the success of this work, by whatever means. In particular, I would like to thank…

…Prof. Wolfram Jaegermann for the supervision of the thesis and the possibility to benefit from both the profound knowledge on surfaces and interfaces of his group and the excellent experimental setting at the InnovationLab. I am grateful for the participation in several conferences and the opportunity of carrying out a research stay at Princeton.

…Prof. Robert Stark for his kind approval to act as second referee.

…Dr. Eric Mankel for the scientific discussions and his support regarding the enabling of the research stay.

…Dr. Thomas Mayer for the thorough proof-reading, the suggestions and scientific discussions.

…my colleagues from TU Darmstadt, in particular my office partners Patrick Reiser and Markus Frericks for the pleasant working atmosphere and the almost constant availability for spontaneous questions. Without you, the time would have been much harder.

…Prof. Antoine Kahn for hosting me at Princeton and the priceless experiences associated with the stay abroad.

…the project partners, especially Dr. Sebastian Hietzschold and Dr. Sabina Hillebrandt for the very constructive teamwork, which enabled the success of the project. It was a pleasure working with you. In particular, I would like to thank Dr. Sebastian Hietzschold for his support toward the end of my thesis and the proof-reading.

…all other office partners and members of the analytic team at the InnovationLab in Heidelberg, first and foremost my table neighbor Valentina Rohnacher, who directly contributed to numerous experiments by measurements, discussions and sample fabrication. I have always enjoyed working with you.

…all other collaborators and colleagues at the InnovationLab for the warm and friendly atmosphere.

Last but not least, I want to express my deep gratefulness to my family, who has always supported me in whatever I do. This refers especially to my parents, without whom I certainly would not have come so far, my grandparents, who have given me so much, and my brother, the best Dude I have ever met.

Thank you!